ANALYTICAL THEORY FOR TWO-PHASE, MULTICOMPONENT FLOW IN POROUS MEDIA WITH ADSORPTION

A DISSERTATION
SUBMITTED TO THE DEPARTMENT OF
ENERGY RESOURCES ENGINEERING
AND THE COMMITTEE ON GRADUATE STUDIES
OF STANFORD UNIVERSITY
IN PARTIAL FULFILLMENT OF THE REQUIREMENTS
FOR THE DEGREE OF
DOCTOR OF PHILOSOPHY

Carolyn Jennifer Seto
April 2007

I certify that I have read this thesis and that in my opinion it is fully adequate, in scope and in quality, as a dissertation for the degree of Doctor of Philosophy.

_____

(Prof. Franklin M. Orr, Jr.)
Principal Advisor

I certify that I have read this thesis and that in my opinion it is fully adequate, in scope and in quality, as a dissertation for the degree of Doctor of Philosophy.

_____

(Margot G. Gerritsen)

I certify that I have read this thesis and that in my opinion it is fully adequate, in scope and in quality, as a dissertation for the degree of Doctor of Philosophy.

_____

(Anthony R. Kovscek)

I certify that I have read this thesis and that in my opinion it is fully adequate, in scope and in quality, as a dissertation for the degree of Doctor of Philosophy.

_____

(Hamdi A. Tchelepi)

Approved for the University Committee on Graduate Studies:

Abstract

Gas injection is an effective method for enhanced recovery of oil and gas When dissipative effects such as diffusion or capillary crossflow are negligible, conservation equations describing multicomponent flow are described by a set of first order hyperbolic equations. Analytical theory to solve these problems using the method of characteristics is well established. In this dissertation, the analytical theory for multiphase, multicomponent flow is extended to consider the effects adsorption and desorption of gas species from the solid surface. Changes in local flow velocity as components transfer between gas and liquid phases are also considered. The theory developed in this work is applied to enhanced coalbed methane recovery (ECBM) and CO_2 sequestration in deep unminable coalbeds.

Transport in coal is a multistep process. CH_4 production is a balance between diffusive and convective transport and the slower process dominates production behaviour. While coal reservoirs are complex and highly heterogeneous, the solutions developed in this work are applied to coals with large diffusion coefficients and small fracture spacing. This analysis focuses on the interaction of gas components with the solid phase and the flowing phases. Recovery of CH_4 is solely the result of changes in gas compositions as mixtures propagate through the coal. Adsorption is described by the extended Langmuir isotherm. Mixtures of N_2, CH_4, CO_2 and H_2O are used to represent flue gas injection into a water saturated coalbed. Solutions were constructed for a variety

of injection compositions encountered in ECBM. When injection gas is rich in N_2, fast recovery of CH_4 occurs. Because more molecules of CH_4 are desorbed for every molecule of N_2 adsorbed, volume is added to the flowing phase resulting in an increase in local flow velocity. Because N_2 is less strongly adsorbing than CH_4, displacement of CH_4 occurs through a continuous variation and the resulting production stream is a mixture of N_2 and CH_4. When injection gas is rich in CO_2, slow recovery of CH_4 occurs. Because CO_2 is more strongly adsorbing than CH_4, displacement of CH_4 occurs through a shock and distinct banks of CH_4 and CO_2 are produced. A decrease in local flow velocity occurs when CO_2 is adsorbed onto the coal surface, resulting in a slow displacement. When mixtures of gas are injected into a coalbed, gas components are chromatographically separated based on relative adsorption strength and volatility. Stronger adsorbing and less volatile components propagate more slowly than weaker adsorbing and more volatile components.

A new composition path for certain injection gas mixtures consisting of the most volatile component and least volatile intermediate component is reported. This path requires an additional tie line, the degenerate tie line, along which a degenerate shock occurs. This new solution structure includes other features, such as a switch between two nontie-line paths, a degenerate shock and nontie-line path that follows the increasing saturation branch of the nontie-line path, which were previously unreported.

If nonlinear functions are present in the accumulation term of the governing equation, shocks into and out of the two-phase region no longer occur along the extension of the tie line. This work presents the first investigation into undersaturated systems of this kind. Together with the degenerate structure, established algorithms developed for determining composition paths must be modified to include there new features.

The analytical solutions are validated by high resolution 1-D finite difference simulations with single point upstream weighting. Features such as equal-eigenvalue points, zones of constant state and path switches from nontie-line path to tie-line path are difficult for a first order numerical scheme to resolve. High resolution finite difference simulations are required to capture the fine features of the analytical solutions.

Acknowledgments

I would like to thank my advisor, Professor Lynn Orr for his patience, encouragement, guidance, and tolerance of cultural idiosyncrasies during my period at Stanford. I would also like acknowledge the contributions of Kristian Jessen to my research, for the interesting and fruitful discussions and also use of his finite difference code to confirm, and convince myself of the validity of my solutions.

I would like to thank my parents, Ray and Dawn Seto, and my grandmother, Sybil Chin, for their love and encouragement.

Financial support from the Global Climate and Energy Project, at Stanford University, is gratefully acknowledged.

Contents

List of Tables

List of Figures

Chapter 1

Introduction and Literature Survey

1.1. Background and Problem Statement

Atmospheric concentrations of CO_2 have increased significantly from pre-industrial levels of 280 ppm to current concentrations of 385 ppm (Carbon Dioxide Information Analysis Centre, 2003). This increase is attributed to human activity, the majority of which is attributed to fossil fuel combustion and is believed to be responsible for current global warming trends (Intergovernmental Panel on Climate Change, 2001). World CO_2 emissions are predicted to increase annually by 1.9 %. The United States is responsible for approximately 25% of world CO_2 emissions. Approximately 85% of its energy needs are supplied by combustion of fossil fuels (Energy Information Administration, 2003). Clearly, stabilisation of atmospheric CO_2 concentrations without significant negative impact on world economies is a tremendous challenge. The Intergovernmental Panel on Climate Change outlined four options to stabilise greenhouse gas levels, while minimising economic impact:

- use of less carbon intensive fuels,
- increased energy efficiency,
- carbon sequestration, and
- increased conservation.

Enhanced coalbed methane (ECBM) is a promising technology for greenhouse gas stabilisation. Simultaneous recovery of CH_4 while CO_2 is sequestered in coal seams is an attractive option because it addresses the issue of increasing atmospheric CO_2 concentrations while offsetting some of the costs of capture, storage, compression and transportation of CO_2 by production of CH_4. Due to this synergy, coalbed reservoirs may be more attractive as initial sequestration sites over candidates such as saline aquifers where there is no offset of operational costs. Moreover, coalbed reservoirs have been long recognised as a significant source of CH_4 due to the occurrence of mine explosions and outbursts. Due to the large internal surface area, on which gas is adsorbed, coal reservoirs may contain 6 to 7 times more gas than an equivalent rock volume from a conventional gas reservoir. Global coal bed methane (CBM) resources are estimated to range from 3010 to 7840 Tcf. Of this, 510 Tcf are considered technically recoverable. Significant reserves are present in China and the United States (Kuuskraa, 1998). Figure 1-1 shows the location of major coalbed methane resources in the lower 48 region of the United States.

Gas injection has been widely used in the oil industry to enhance hydrocarbon recovery. When gas is injected into a reservoir, the injected gas mixes with the fluid initially in place and multiphase mixtures may form once thermodynamic equilibrium is established. This procedure is repeated as newly formed mixtures propagate through the reservoir. Different phases propagate through the reservoir at different velocities depending on their multiphase flow

properties. Phase behaviour partitions components between liquid and gaseous phases dependent on relative volatility. ECBM is an application of gas injection, where the injected gas and subsequent intermediate gas mixtures produced interact with components in the aqueous and solid phases.

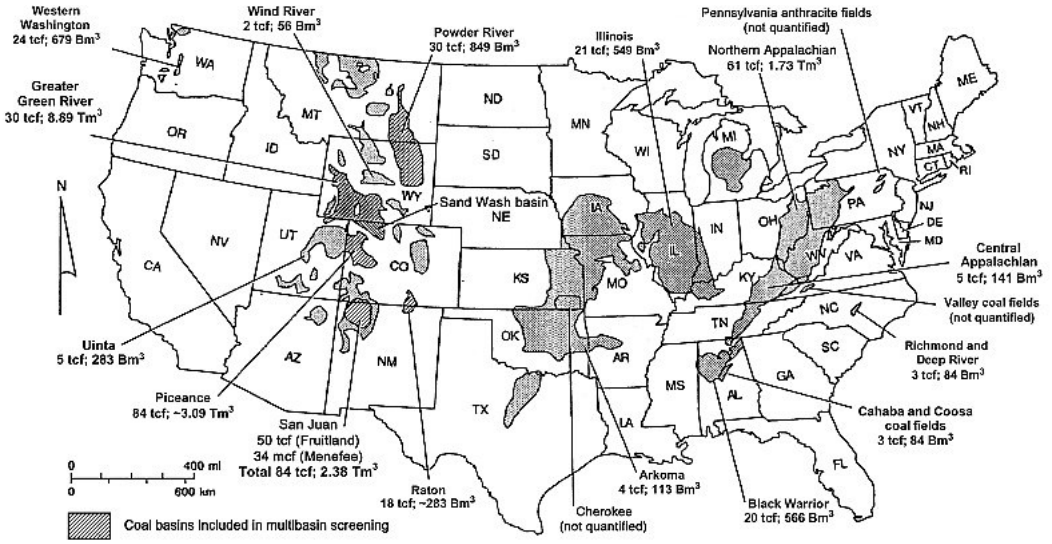

Figure 1-1: Location of major coal bearing basins in the United States, lower 48 (from USGS, 1997).

ECBM recovery is controlled by a combination of gravity, capillary and viscous forces. The resulting equations to describe flow in these systems are nonlinear, and are typically solved through numerical techniques. When numerical methods are used to investigate displacement mechanisms, truncation error in space and time may make it difficult to isolate key mechanisms affecting transport. Because gas injection is inherently a compositional problem, computational requirements may make simulation of these systems computationally prohibitive depending on the number of components and number of gridblocks used. In these settings, analytical models, the subject of this dissertation, are useful for isolating the key physics controlling the displacement, providing improved understanding of the physics and aid in interpreting laboratory experiments and field observations. Analytical solutions can be used as benchmarks against which higher order numerical techniques can be compared, ensuring that information propagation in

the displacement is honoured adequately. Combined with streamline simulation methods, analytical solutions can be extended to model displacements in higher dimensional systems (Seto *et al.*, 2003). In this work, simplified limiting case analytical models are applied to understand the key physics involved in transport in coal and ECBM recovery.

1.2. Coal Reservoirs

Coal is a complex porous medium, consisting of a high permeability fracture network and low permeability matrix. The majority of the gas stored in coal reservoirs is contained in the matrix (> 95%), while the fractures provide the conduits for production. Both diffusion and convection are important components of transport in coal and in ECBM processes. Although coals are recognised as significant sources of CH_4, production from these reservoirs in the United States did not begin in earnest until the 1980s with the Section 29 subsidies for unconventional gas production in the Crude Oil Windfall Profits Tax Act of 1980. In 1985, less than 10 Bcf was produced in the United States (approximately 1% of total domestic gas production). This volume grew to 1003 Bcf by 1996 (approximately 6% of total domestic gas production), and by 2004 CBM production was 1720 Bcf (Petroleum Technology Transfer Council, 1999).

Coal reservoirs are a unique class of reservoir, in that they are both the source and the reservoir. Coals are low energy sedimentary deposits composed from peat, a mixture of organic and inorganic material. Coal reservoirs are formed in a very narrow environment. Rapid burial and a low oxygen environment are necessary for the coalification process to occur. As peat is compacted by the overburden, water is driven out and material is converted into a sedimentary rock. Pressure and temperature increase with increasing burial depth, further compacting and dewatering the system. Coalification slowly converts plant material into coal (Levine, 1993), altering physical chemical properties of the reservoir. During this process, two important features of coal reservoirs result: natural gas generation

and cleat formation. Significant amounts of CH_4 are generated during the coalification process; ranging from 150 to 200 cm^3/g of coal, dependent on organic content of peat, temperature and pressure of burial and maturation time (Rice, 1993). Higher molecular weight hydrocarbons and CO_2 may also be produced during the coalification process; however, CH_4 is usually the major constituent, 88 to 98% (Diamond *et al*., 1986). CO_2 is also a by-product of the coalification process; however, it is more soluble in water and more reactive than CH_4, and other mechanisms such as thermal decomposition of carbonates (Hunt, 1979), carbonate dissolution associated with silicate hydrolysis (Smith and Ehrenberg, 1989), bacterial oxidation of hydrocarbons (Carothers and Kharaka, 1980), or migration from magma chambers (Kotarba, 1989), may be responsible for CO_2 generation. As a consequence, CO_2 present in coal reservoirs may have different origins, and can vary from compositions on the order of trace amounts to greater than 99% (Hunt, 1979). Naturally occurring coalbeds with high CO_2 concentrations, such as the Rhur Basin, Germany (Colombo *et al.*, 1970) and the Silesia Basin, Poland (Kotarba, 1989), further support the case that coal reservoirs are good candidates for geological sequestration of CO_2, demonstrating the CO_2 can be safely sequestered in coal beds for geological time scales.

Coals are classified according to rank. This is a measure of thermal maturity and carbon content (higher rank coals are more mature, and have higher carbon content). Higher rank coals typically have lower permeability, lower porosity and lower adsorption capacity (Meissner, 1984). Trends in type of porosity are also functions of rank: in low rank coals, porosity is due to macropores; in medium rank coals, porosity is due to micropores and mesopores; in high rank coals, porosity is due to micropores (Gan *et al.*, 1972).

Cleats formed during the coalification process are believed to be formed through mode I (opening mode) failure (Pollard and Aydin, 1988, Pollard and Fletcher, 2005). In opening mode failure, development of cleats is caused by

matrix shrinkage due to moisture loss during the coalification process. This is more complex than simple desiccation because it involves the rearrangement of the coal structure rather than just loss of interstitial water (Close, 1993). Two sets of cleats dominate: face cleats and butt cleats. Face cleats dominate the fracture network. These are identified as planar and continuous features, oriented in the direction of maximum compressive stress during regional folding, or perpendicular to fold axis. Butt cleats are secondary features, formed parallel to the axial trends of the folds. These are commonly discontinuous and nonplanar, typically oriented orthogonal to the face cleats. Cleat spacing is controlled by bed thickness, rank and composition. For any rank coal, cleat spacing decreases as bed thickness decreases. Higher rank coals (vitrinite rich, with low ash content) have smaller cleat spacing than lower rank coals (Close, 1993). Table 1-1 lists measured cleat spacing for a range of coal samples. Fractures in coal tend to be open, acting as conduits for flow. Gamson *et al.* (1993) measured fracture widths ranging from 0.1-2 mm in calcite infilled coal cores from the Bowen Basin. Table 1-2 lists measured permeabilities for a range of coal basins.

Permeability changes as gases adsorb onto and desorb from the coal surface have been observed by a number of researchers (Lin, 2006). Matrix shrinkage occurs when gases desorb from the surface and matrix swelling occurs when gases adsorb onto the coal. The enlarged cleat structure associated with shrinkage may enhance fracture permeability, while the reduced fracture area open to flow associated with swelling may decrease permeability. Harpalani and Schraufnagel (1990) observed volumetric shrinkage of 0.4% when the gas pressure was reduced from 6.9 MPa to atmospheric pressure. St. George and Barakat (2001) conducted gas desorption experiments and observed matrix shrinkage and stress increases associated with CH_4 desorption.

Table 1-1: Measured cleat spacing for a range of coal samples.

rank	location	cleat spacing	source
lignite	Rocky Mountain basin, U.S.	2 cm	Law (1991)
medium-volatile bituminous	Rocky Mountain basin, U.S.	0.08 cm	Law (1991)
sub-bituminous to high-volatile C bituminous	Fruitland coal, San Juan Basin	2.5-6.3 cm	Tremain *et al.* (1991)
high-volatile B bituminous	Fruitland coal, San Juan Basin	0.6-1.2 cm	Tremain *et al.* (1991)
high-volatile A bituminous	Fruitland coal, San Juan Basin	0.3-0.6 cm	Tremain *et al.* (1991)
high-volatile C bituminous	Lethbridge coal, Alberta Basin	1-2 cm	Beaton (2004)
sub-bituminous	Ardley coal, Alberta Basin	face: 2 cm butt: 5 cm	Beaton (2004)
high-volatile bituminous to semi-anthracite	Bowen Basin, Australia	0.3-2 cm	Gamson *et al.* (1993)
bituminous	Arkoma Basin, Oklahoma	5 – 24 cm	Friedman (2001)
bituminous	Wind River Basin, WY	0.25-2.5 cm	Johnson *et al.* (1993)

Table 1-2: Measured permeabilities for a range of coal samples.

basin	permeability (md)	source
Bowen Basin, Australia	2	Enver *et al.*, 1994
San Juan, NM	2-35, local values reaching 800	Sawyer *et al.*, 1987 Oldaker, 1991,
Green River, WY	local values reaching 1500	Tyler *et al.*, 1995

At deeper depths, permeability of the coals decreases exponentially due to the increase in effective stress (McKee *et al.*, 1988), resulting in very low permeability reservoirs at these depths. Stresses orthogonal to face cleats reduce the permeability, while stresses parallel to face cleats may enhance permeability by partially opening the cleat (Mavor and Vaughn, 1998). It is estimated that

production from coals may be limited to depths less than 1524-1829 m if structural permeability enhancement interventions, such as massive hydraulic fractures, are not performed (Scott, 2000). If the permeability enhancement due to CH_4 desorption is insufficient to offset the permeability reduction from pore pressure reduction due to production, CO_2 injection and CH_4 production from deep coals may not be feasible (Cui and Bustin, 2005).

1.3. Production from Coal

In coal reservoirs, natural gas is adsorbed onto the internal surfaces of the coal. Gas is bound to the surface through weak intermolecular van der Waals forces (van Krevelen, 1954). The majority of the gas exists in an adsorbed state, with small amounts present as a free gas phase in the micropores and cleats and dissolved in the aqueous phase (De Bruin and Lyman, 1999). Adsorption capacity is a function of pressure and temperature and is typically described by the Langmuir and extended Langmuir isotherm models (Yang, 1987, Arri *et al.*, 1992, Yee *et al.*, 1993). At higher pressures, a larger amount of gas is adsorbed.

Coal reservoirs are characterised by dual porosity systems, consisting of a low permeability matrix and high permeability fracture network. In the matrix, transport is controlled by diffusion, where the rate of transport is dependent on concentration gradients. In the fracture, Darcy flow dominates and flow is controlled by pressure gradients (Cervik, 1969). Some researchers propose an additional porosity system (Reeves and Pekot, 2001, Shi and Durucan, 2003), where transport is a three step process: diffusion from micropores to macropores, diffusion from macropores to fracture network, convection in the fracture network. In systems where diffusion is fast, the single porosity model is sufficient to model gas production behaviour (Seidle and Arri, 1990), while coals that are diffusion limited require a triple porosity model (Reeves and Pekot, 2001).

In conventional CBM production, gas is produced through reduction of reservoir pressure. This is usually achieved through dewatering of the reservoir. During this primary stage, large volumes of water are produced. There may also be some small volumes of gas produced. Once the pressure has decreased sufficiently such that gas desorbs from the matrix and accumulates to form a free gas phase, stable production occurs. The final stage of a CBM project is the decline stage. After the gas rate has peaked, production declines until the economic limit is reached.

In many coals that are water saturated, significant volumes of water must be extracted and disposed of. In some basins, this water is saline (salinity of San Juan Basin produced water: 14,000 – 40,000 ppm), creating a water disposal issue. From 1989 to 1992, water production in the Fruitland Formation increased from 40,000 bbls/d to 115,000 bbls/d (Ayers, 2000). In some basins, dewatering for depressurisation has significantly decreased the water table (in the Powder River basin, some areas of water table have been drawn down in the hundreds of feet), negatively affecting the hydrology of the area. One or more stages of compression are required to sufficiently reduce bottom hole pressure of the production well to induce gas desorption and migration to the well. In conventional CBM production, compression and water disposal costs are high, placing an economic constraint on recovery. Typical recovery factors for CBM projects range from 20-50%.

In ECBM production, gas is injected to reduce the partial pressure of CH_4 in the coal (Figure 1-2). Reservoir pressure is maintained, preserving high production flow rates. ECBM could reduce the need to produce and dispose of water, and minimise the adverse effects on the water table. When CO_2 is injected, CO_2 is preferentially adsorbed onto the surface, displacing CH_4 from the coal surface. Replacement ratios of CO_2:CH_4 vary from 2:1 to 10:1 (Stanton *et al.*, 2001), making CO_2-ECBM a potential low-emissions technology. When N_2 is injected, CH_4 is still the preferentially adsorbed gas species. Reduction of partial

pressure of CH_4 in the fractures provides the driving force for desorption in N_2 displacements. Pilots of both CO_2-ECBM and N_2-ECBM have successfully demonstrated the feasibility ECBM (Reeves, 2001), and several more are planned (van Bergen and Pagnier, 2006, Wong *et al.*, 2006, Quattrocchi *et al.*, 2006).

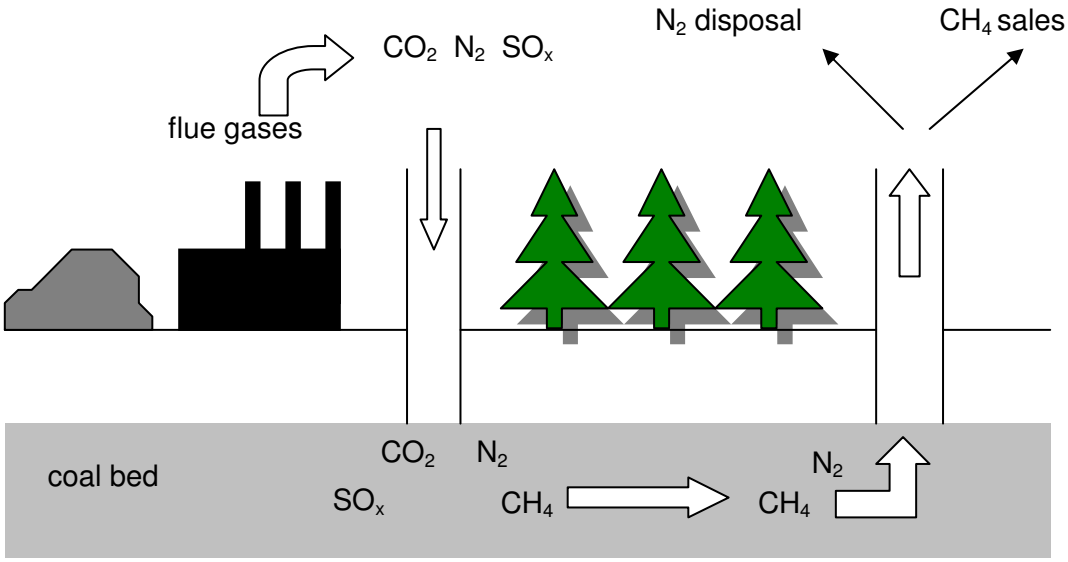

Figure 1-2: Schematic of ECBM production.

1.4. Analytical Theory for Gas Injection

If the dissipative effects of capillarity, diffusion, and dispersion are negligible, transport in convection-dominated systems is described by a system of nonlinear, hyperbolic, first-order differential algebraic equations. When injection and initial conditions are constant and uniform, the flow problem is a Riemann problem. Analytical solutions to particular injection and initial states can be obtained using the method of characteristics (MOC). The mathematical theory of the Riemann problem for solving generalised initial value problems is well established and has been applied to solving systems of equations ranging from areas of gas dynamics to electromagnetics to multicomponent chromatography to traffic flow. The resulting solutions to Riemann problems are self-similar and depend on a single

parameter. Injection and initial states are connected piecewise by rarefactions (continuous solutions), shocks (discontinuous solutions) or zones of constant states.

This technique has been employed in solving similar classes of problems pertaining to transport in porous media, and its use is well established in the petroleum industry (Larson, 1979, Pope *et al.*, 1978, Pope, 1980, Hirasaki, 1981, Johns and Orr, 1996, Gonzalez and Araujo, 2002, Jessen *et al.*, 2002, Zhu *et al.* 2004, Johns *et al*., 2004, Juanes and Patzek, 2004, LaForce and Johns, 2005). When applied to modelling subsurface flows, the system of equations describing flow is converted into an eigenvalue problem. The resulting eigenvalues represent the velocities at which characteristic compositions propagate through the reservoir as the displacement evolves. The corresponding eigenvectors are the directions in composition space along which compositions may vary as allowed by the differential equations. In this dissertation, analysis is limited to nonstrictly hyperbolic systems, where the eigenvalues are real but are not distinct everywhere. In multicomponent systems, equal-eigenvalue points occur, and the system becomes weakly hyperbolic. These are important in constructing solutions for enhanced oil recovery applications. Equal-eigenvalue points represent points where the solution may switch eigenvectors, changing direction in composition space. The presence of equal-eigenvalue points complicates solutions to the Riemann problem because the eigenvalues are no longer able to be ordered. When these systems are solved numerically, these points are difficult to resolve because small amounts of dispersion will cause the solution to overshoot or undershoot this point. To resolve these points, a high resolution grid or higher order scheme is required. If there are a large number of components present, accurate numerical simulations may become computationally prohibitive.

Buckley and Leverett (1941) presented an analytical solution for modelling displacement of oil by water. In this system, oil and water were immiscible and

incompressible. Multivalued saturations were resolved by applying mass conservation across a shock. This work provided the basis for subsequent development of the two-phase, multicomponent, analytical theory. Welge (1952) simplified the water-oil displacement problem with a graphical method to construct the shock. Shocks were resolved by a tangent construction from the injection or initial states to the fractional flow curve. Isaacson (1980) generalised the Riemann problem for a nonadsorbing polymer, water, and oil system. Polymer was soluble in the water phase, essentially acting like a passive tracer and the system was reduced to a 2×2 system. Oil and water phases were immiscible. Helfferich (1981) generalised the theory for multiphase, multicomponent flow into a mathematical framework. In this analysis, ideal mixing was assumed. No change in volume occurred as components transferred between phases. Example solutions presented in Helfferich's analysis were limited to ternary systems. Dumore *et al.* (1984) extended the theory developed by Helfferich to include the effects of volume change as components transfer between phases.

The first solutions to quaternary systems with and without volume change on mixing were developed by Monroe *et al*. (1990). With this solution, the concept of the crossover tie line was introduced, laying the foundations for solving systems with more components and more realistic representation of gas and oil mixtures. The crossover tie line is used to construct a unique solution connecting injection and initial states. In the solutions developed by Monroe, only classes of problems where tie lines were connected by shocks were considered. Johns (1992) applied this theory to analyse the behaviour of gas injection processes. Components with high volatility were displaced faster than components with lower volatility. Dindoruk (1992) performed an extensive analysis on the quaternary system to completely classify displacements in two-phase, four-component systems with and without volume change on mixing. Analysis of the geometry of the key tie lines provided insight into displacement mechanisms in condensing, vaporising and combined gas drives (Dindoruk *et al.*, 1992, Johns *et al*., 1993). Wang (1998)

used the tie line intersection concept to develop a fast and efficient algorithm to obtain analytical solutions for multicomponent systems with an arbitrary number of components in the injection gas and initial oil, extending this theory to more realistic representation of gas and oil mixtures. In this analysis, only shock segments across a sequence of key tie lines were assumed. Ermakov (2000) and Jessen (1999) considered the effect of volume change in systems with an arbitrary number of components. Jessen *et al.* (2001) introduced the concept of the primary key tie line from which solution construction is initiated for a system with an arbitrary number of components.

A number of researchers have investigated problems pertaining to adsorption of species to the solid surface as the displacement proceeds. Johansen and Winther (1988, 1989) considered the Riemann problem to model single component and multicomponent polymer flooding. In their analysis, the polymer dissolved in the aqueous phase. Oleic and aqueous phases were immiscible. Ideal mixing was assumed. This is a reasonable assumption for polymer and surfactant systems because relatively small volume change occurs when these compounds are dissolved in the aqueous phase. Rhee *et al*. (1971) applied this technique to model exchange in multicomponent chromatography. In their analysis, Riemann invariants were used to solve equations when the Langmuir isotherm controlled mass transfer. Dahl *et al*. (1990) extended the analysis to model multicomponent chromatography in a two-phase system. Again, ideal mixing was assumed. Zhu (2003) (see also Zhu *et al.*, 2003) applied this technique to model ECBM in single phase systems. Gas was the mobile phase. Any water present was assumed to be below critical saturations and was immobile. In this analysis, adsorption and desorption of gas from the coal played a key role in transport in these systems. Changes in molar density were considered through an equation of state.

In this chapter, a brief introduction into the development of the theory of multicomponent, multiphase flow was presented. The complex structure of

coalbeds, and mechanisms for transport in and exploitation of this resource was discussed.

Chapter 2 presents an analysis into the relative magnitude of physics involved in transport in ECBM. Identifying the key physical mechanisms involved in transport allows development of efficient simulation techniques for modelling flow in coalbeds. In this analysis, diffusion timescale is shown to be short relative to the convection timescale if the coal is well cleated and has a large diffusion coefficient, and hence, the local equilibrium assumption is reasonable for some coals. In these settings, the coalbed is modelled as a single porosity medium and the analytical theory for gas injection can be applied to modelling ECBM displacements.

Chapter 3 presents the analytical theory for the dispersion-free limit of two-phase, multicomponent flow with adsorption/desorption effects and volume change as components transfer between gas and liquid phases is developed. Assumptions in the mathematical model are discussed and a generalised formulation of conservation equations is presented. Using the procedure presented by Dindoruk, local flow velocity is decoupled from the composition problem and the system is converted to a generalised eigenvalue problem. Conditions eliminating unrealistic solutions are discussed.

Chapter 4 presents solutions for ECBM in binary and ternary systems. The analysis presented is for an analogue system with constant K-values, phase densities and mobility ratio. The extended Langmuir formulation is used to describe adsorption and desorption of gas species from the coal surface. Parameters used are model parameters, allowing a clear view of composition path behaviour. Example solutions are presented for a variety of injection and initial conditions that may be encountered in ECBM projects. The solutions presented are confirmed by finite-difference simulations

Chapter 5 extends the analysis of the ternary system to quaternary systems. Solutions were constructed for a variety of injection and initial conditions, delineating the structures encountered in ECBM recovery. The analytical model was used to assess the sensitivity of solution structures to model parameters such as relative permeability and adsorption strength, demonstrating the power of simplified analytical models in developing insight into the physics of displacement.

Chapter 6 summarises this research and provides some insights to extend this work.

Chapter 2

Transport in Coal

In this chapter, the physical processes involved in transport in coalbeds are investigated through a series of scaling analyses and simplified analytical models. Enhanced coal bed methane (ECBM) recovery is a multistep process (Figure 2-1). When gas is injected into a coalbed, the injected gas diffuses from the fracture network, through the matrix and macropores to the internal surfaces of the coal. At the coal surface, partial pressure with respect to the adsorbed gas is reduced, causing desorption, and gas exchange takes place. The desorbed gas diffuses through the matrix and micropores, out to the fracture network where it flows to the production well. The rate of production of coal reservoirs is controlled by the slower of these two processes. To predict performance accurately in ECBM recovery, key physical mechanisms controlling transport in these systems must be captured adequately.

In this section, the effect of diffusion in transport in the cleat and matrix systems is considered. In cases where convection dominates, the local equilibrium assumption is reasonable and the matrix is in equilibrium with the fracture network. For these conditions, the cleat network controls flow in the coalbed.

Matrix diffusion effect need not be considered and the coal can be effectively modelled as a single porosity system. The next sections examine the relative importance of dispersion on flow in the cleat system and diffusion into and out of the matrix.

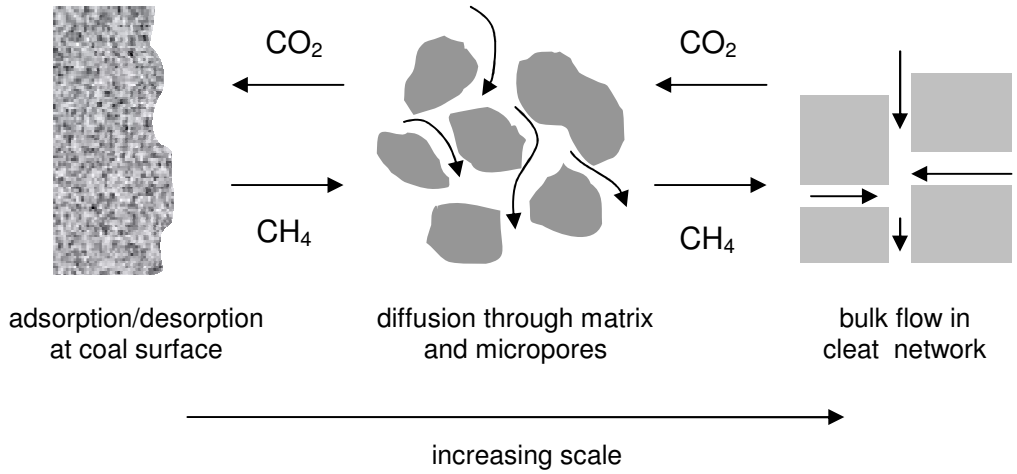

Figure 2-1: Schematic of transport in ECBM recovery.

2.1. Transport in the Cleat System

In the cleat system, flow is controlled by pressure gradients. Flow is described by Eq. 2-1. The Peclet number, *Pe* (Eq. 2-2), is a ratio of the characteristic time for convection to the characteristic time for diffusion. If *Pe* is large, diffusion times are small relative to convection, and flow in the cleat system is convection-dominated.

$$\frac{\partial C_f}{\partial \tau} + \frac{\partial C_f}{\partial \xi} - \frac{1}{Pe_f}\frac{\partial^2 C_f}{\partial \xi^2} = 0\,, \tag{2.1}$$

where:

$$Pe_f = \frac{vL_f}{\phi_f D_f}\,, \tag{2.2}$$

$$\tau = \frac{vt}{\phi_f L}, \tag{2.3}$$

and

$$\xi = \frac{x}{L}. \tag{2.4}$$

Table 2-1 summarises Pe_f for a range of matrix properties found in coals. The range of fracture lengths is taken from Table 1-1. Fracture porosity in coals ranges from 0.5 to 2.5 % (Puri *et al*., 1991, Gash, 1992, Chen and Harpalani, 1995). A typical gas-liquid diffusion coefficient is 10^{-5} cm^2/s (Unver and Himmelblau, 1964, Tewes and Boury, 2005, Yang *et al.*, 2006). Because the diffusion coefficient is several orders of magnitude smaller than the other terms in Pe_f, this value is large. The assumption of convection-dominated flow in the cleats is a reasonable assumption.

Table 2-1: Pe_f of typical fracture scale displacements encountered in coals.

v (m/d)	0.33	0.33	0.33	0.33
L_f (m)	0.01	0.01	0.01	0.05
ϕ_f	0.001	0.005	0.01	0.01
D_f (cm^2/s)	10^{-5}	10^{-5}	10^{-5}	10^{-5}
Pe_f	3.82×10^4	7.64×10^4	3.82×10^3	1.91×10^4

2.2. Transport in the Matrix

In the matrix system, diffusion is the sole mechanism of transport (Eq. 2-5). Diffusion times were calculated for two cases: dry matrix and wet matrix.

$$\frac{\partial C_m}{\partial t} = \nabla \cdot D_m \nabla C_f . \tag{2.5}$$

2.2.1. Dry Matrix

In the dry matrix analysis, diffusion through a single matrix block was considered. To simplify the coordinate system, the system was reduced to an equivalent spherical system (Figure 2-2, Eqs. 2-6 to 2-8). In this analysis the diffusion coefficient is constant. All diffusion mechanisms, Fickian, Knudsen and surface diffusion (Thimons and Kissell, 1973), are lumped into a single effective diffusion coefficient. The time required for the centre of the system to reach a concentration of 95% was calculated.

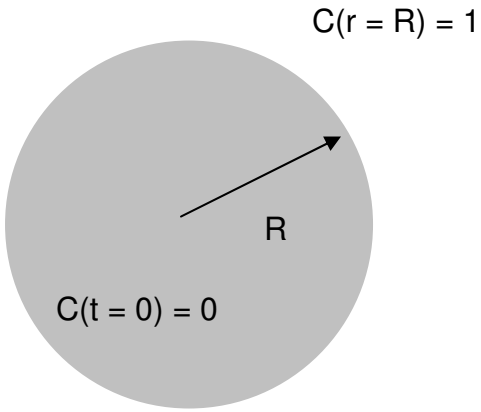

Figure 2-2: Schematic of dry matrix system modelled.

$$\frac{\partial C}{\partial t} = \frac{D_{eff}}{r^2}\frac{\partial}{\partial}\left(r^2\frac{\partial D}{\partial r}\right), \tag{2.6}$$

$$C\left(r = R, t\right) = 1, \tag{2.7}$$

$$C\left(r < R, t = 0\right) = 0. \tag{2.8}$$

$$C = 1 - 2\left(\sum_{n=1}^{\infty} -1^{n+1}\frac{\sin n\pi r / R}{n\pi r / R}\exp\left(-\frac{n^2\pi^2 D_{eff}\tau}{R^2}\right)\right) \tag{2.9}$$

Diffusion time as a function of effective diffusion coefficient and sphere radius is shown in Figure 2-3, Eq. 2.9. Cleat spacings considered reflect typical spacing observed in geological analogues. Typical gas-solid diffusion coefficients for coals vary widely. Laboratory measurements on pulverised coals were found to range from 10^{-5}-10^{-9} cm^2/s (Smith and Frank, 1984, Shi and Durucan, 2003). For large diffusion coefficients, equilibration times for all sphere radii considered are on the order of days. When the diffusion coefficient is small, equilibration time is a function of the radius, ranging from a few days for spheres with a 1 cm radius, to months for spheres with a 5 cm radius. Sphere radius is analogous to cleat spacing. Larger cleat spacings require a longer path length for diffusion, while small cleat spacings require a short path length for diffusion.

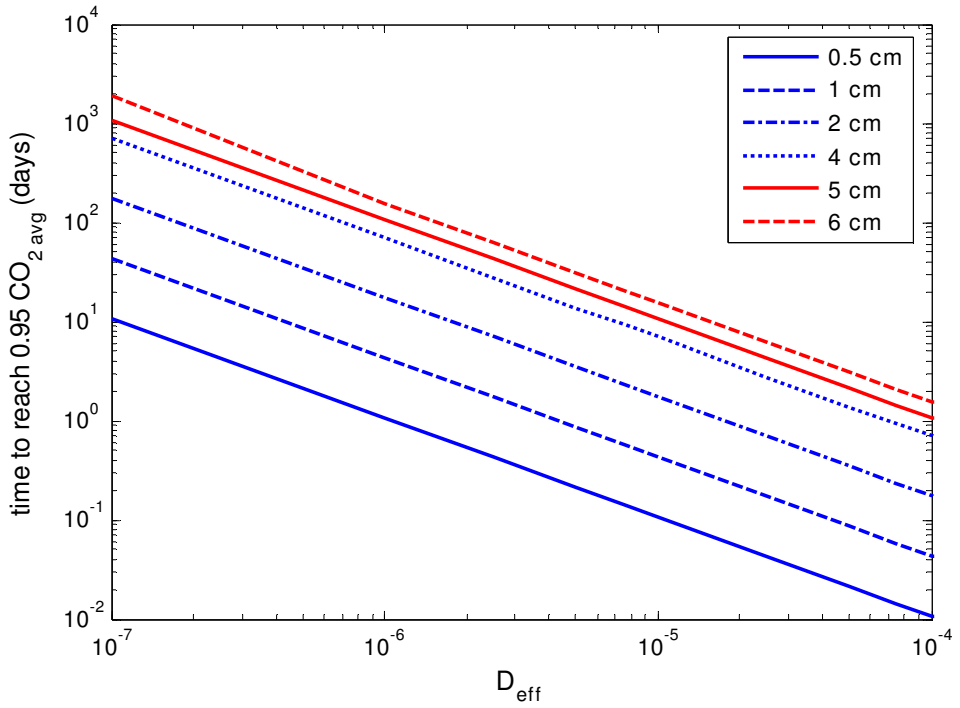

Figure 2-3: Diffusion time for a spherical system as function of effective diffusion coefficient and sphere radius.

2.2.2. Wet Matrix

In many settings, coal reservoirs are water saturated and are commonly active aquifer systems, such as in the Powder River Basin, WY, (Flores, 2004) and the Black Warrior Basin, AL (Pashin *et al.*, 1991). If the coal surface is water wet, additional resistance to mass transfer between the matrix and cleat system is created by the presence of a thin film of water through which gas must diffuse. The rate of mass transfer is affected because the concentration gradient between the outer edge of coal matrix block is limited by the solubility of gas in water.

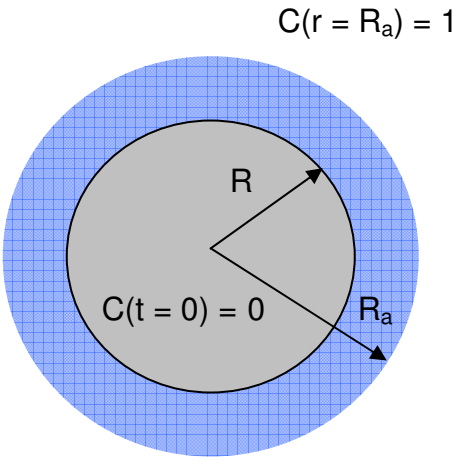

Figure 2-4: Schematic of simplified wet coal system.

To model this effect, the wet matrix was approximated as a spherical film of constant thickness, surrounding the matrix (Figure 2-4). Time to reach 99% of the solubility concentration at R as a function of diffusion coefficient and film thickness is presented in Figure 2-5. Measured cleat apertures range from 0.01 mm to 0.2 mm (Close and Mavor, 1991). For the range of thicknesses and diffusion coefficients considered, film equilibration times are very short, ~O(minutes), compared to matrix equilibration times, ~O(days). The diffusion distance through the film is small, ~O(mm), relative to the diffusion distance through the matrix, ~O(cm) and the diffusion of gas through the relatively thin

water layer has a small effect on the time required for gas to diffuse into the matrix.

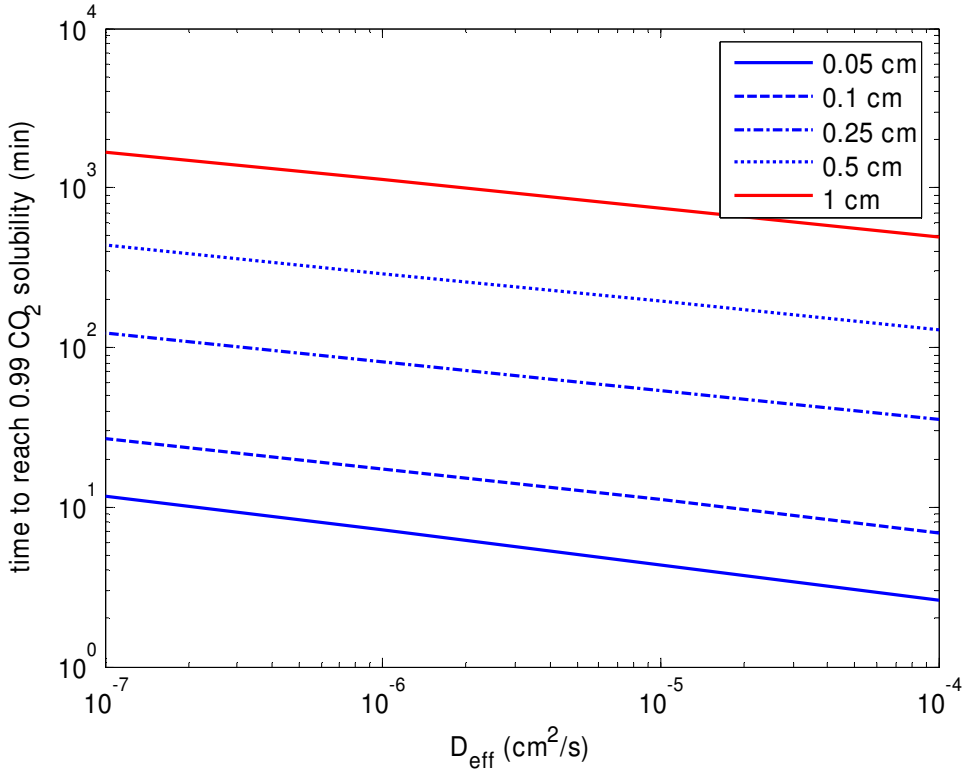

Figure 2-5: Time required for diffusion through a thin film as a function of film thickness and diffusion coefficient. Diffusion times for other gas species, CH_4 and N_2, are of similar order of magnitude.

2.2.3. 1-D Displacement Simulations

Simple one-dimensional displacement simulations of a dual porosity system were performed to observe the interplay between cleat spacing and diffusion time between the matrix and fracture system. The compositional simulator GEM (Computer Modelling Group, 2005) was used in this analysis. A sample input deck is provided in Appendix A. In a dual porosity system (Warren and Root, 1963), the porous medium is modelled as a dual continuum, with a set of governing equations for the matrix system and a corresponding set of governing

equations for the fracture system. Mass transfer between the matrix and fracture network is coupled via a matrix-fracture transfer function. For modelling coalbeds, the matrix-fracture transfer function is analogous to the diffusion time from the internal surfaces of the coal to the cleat network.

Figure 2-6 shows recoveries for a fixed diffusion coefficient as a function of fracture spacing. For a large diffusion coefficient, recovery curves are similar and fracture spacing does not affect recovery. For a small diffusion coefficient, the recovery curves differ. In this setting, fracture spacing affects recovery and the system must be modelled as a dual porosity system. Recoveries for a range of diffusion coefficients for a fixed fracture length (0.5 cm) are plotted in Figure 2-7. If the cleat spacing is small and the diffusion coefficient is large (10^{-4}-10^{-6}), recoveries are similar and a single porosity model is sufficient to model transport in the coalbed.

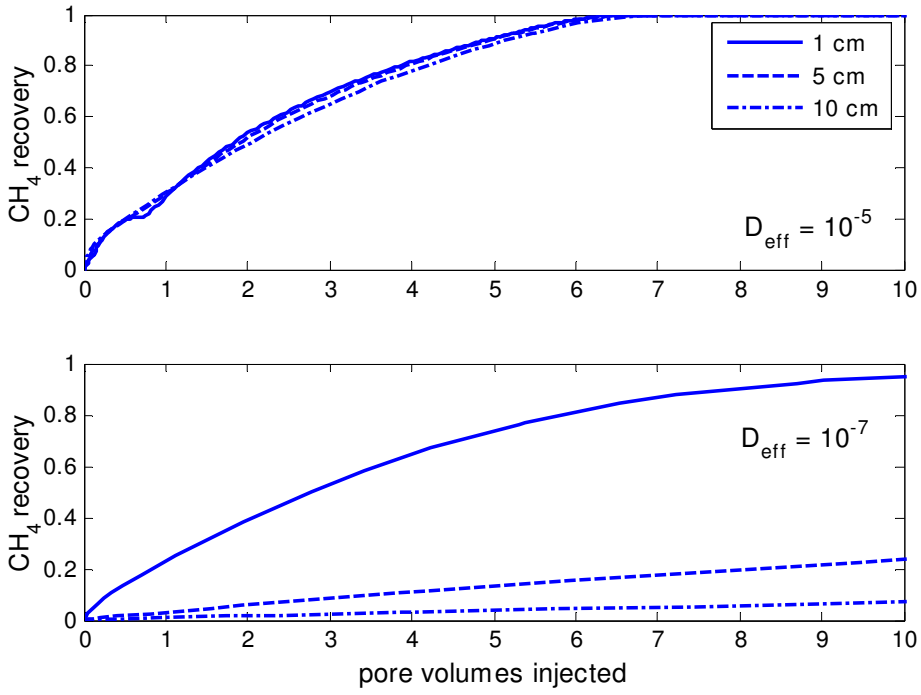

Figure 2-6: Recovery curves for large (top) and small (bottom) effective diffusion coefficients as a function of fracture spacing.

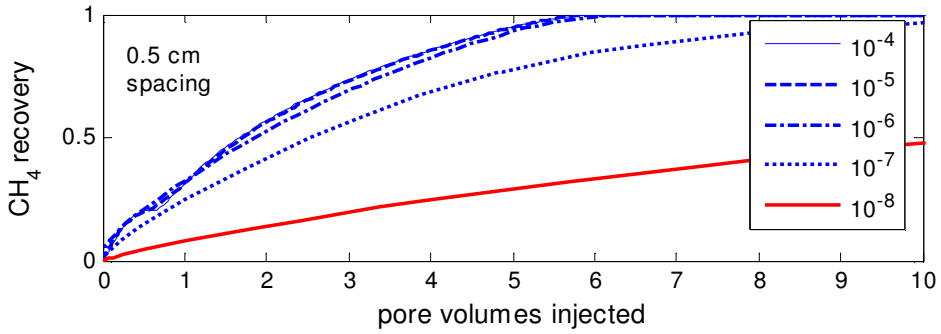

Figure 2-7: Recovery curves for a 0.5 cm fracture spacing as a function of diffusion coefficient.

2.3. Summary

Transport in coal is a balance between convection and diffusion. In the fracture system, flow is dominated by convection. In the matrix, the timescale for diffusion is dependent on fracture spacing and diffusion coefficient. In poorly cleated coals (large fracture spacings), the diffusion path length is long, resulting in slow diffusion times. In well cleated coals (small fracture spacings), the diffusion path length is short and diffusion times are small. Therefore, for well cleated coals with small fracture spacings and large diffusion coefficients, diffusion times are short relative to advection, and it is reasonable to make the assumption that the matrix is in equilibrium with the fluid in the cleat network. In these systems, the coal can be modelled as a single porosity medium and the analytical theory for multiphase, multicomponent flow in porous media can be applied to model ECBM processes.

The following chapter extends the analytical theory to include mass transfer between the flowing phases and the solid phase. The generalised governing equations describing flow in convection-dominated systems are developed, and the analytical solution technique to solve gas injection in coals is presented.

Chapter 3

Mathematical Model

In this chapter, the mathematical model for convection dominated flow in multicomponent, multiphase systems with adsorption using the method of characteristics is presented. The governing equations describing flow are developed, and the underlying physical assumptions and simplifications are discussed. The solutions consist of continuous and discontinuous variations of state variables. For continuous variation, the system of conservation equations describing flow is converted into an eigenvalue problem. Across the discontinuity, the step change in state variables must also obey conservation of mass. The weak form of the material balance is formulated.

3.1. Assumptions

To model displacement gas injection into a water saturated coal, the following assumptions are made:

- one-dimensional flow,
- local equilibrium,

- no hydrodynamic dispersion or molecular diffusion,
- homogenous and fixed properties of the porous medium,
- negligible capillary and gravity effects,
- constant pressure, for the purposes of evaluating phase behaviour,
- small solubility of gas in the aqueous and water in the gas phase. Henry's Law is reasonable for modelling component partitioning between gas and aqueous phases in the coalbed,
- constant phase densities and viscosities, and
- isothermal conditions.

Instantaneous equilibrium between gas, liquid and solid phases is assumed. Implicit in this analysis is that the matrix and fracture systems are in equilibrium with each other and can be modelled as a single porosity system. Coals are complex porous media, consisting of a complex, high permeability fracture network and a low permeability matrix that may contain varying degrees of macroporosity and microporosity (Gan *et al.*, 1972). Equilibration times vary significantly between coal basins (Gray, 1987, Kissell and Bielicky, 1972). In coals with short equilibration times, the assumption of local equilibrium is reasonable, and flow is convection-dominated.

Porosity and permeability are assumed constant as gas species adsorb onto and desorb from the coal surface. In this analysis, the effects of shrinkage and swelling are not considered. Both laboratory experiments and field pilots reported changes in permeability during ECBM production (Harpalani and Zhao, 1989, Pekot and Reeves, 2002, Mazumder *et al.*, 2006). Researchers developed a Karmen-Kozeney type relationship between permeability and porosity to describe

matrix shrinkage and swell effects (Palmer and Mansoori, 1996, Shi and Durucan, 2005), inclusion of this phenomenon will affect the overall concentration of components because changes in porosity influence the degree to which gases interact with solid surface and the flowing phase. Incorporation of this effect does not affect the quasilinear structure of the governing equation. The same techniques to construct analytical solutions are still valid.

The constant pressure assumption states that the exchange of components between the solid phase and mobile phases is purely due to changes in partial pressure as compositions propagate through the coalbed. For small pressure gradients, crossflow effects are negligible. Srivastava (2004) performed a detailed investigation of the errors associated with making this assumption. In that analysis, it was found that the effect of a pressure gradient on recovery was small. This was attributed to the low viscosity gas transmitting pressure between injection and producer, maintaining high pressure at the displacement front.

3.2. Material Balance Formulation

For a system with N_c components and N_p phases, the conservation equations to describe one-dimensional, multiphase flow in porous media with adsorption for each component are:

$$\frac{\partial}{\partial t}\sum_{j=1}^{N_p}\phi x_{ij}\rho_j S_j + (1-\phi)a_i + \frac{\partial}{\partial x}\sum_{j=1}^{N_p} x_{ij}\rho_j u_j = 0, \quad i = 1,\ldots,N_c \quad j = 1,\ldots,N_p\,, \tag{3.1}$$

where:

ϕ = porosity of the porous medium,

x_{ij} = mole fraction of component i in phase j,

ρ_j = molar density of phase j,

S_j = saturation of phase j,

a_i = amount of component i adsorbed on the coal per unit volume of coal and

u_j = local flow velocity of phase j.

Introducing fractional flow as

$$f_j = \frac{u_j}{u}, \tag{3.2}$$

where f_j is the volumetric fractional flow of phase j, and u is the overall local flow velocity, the conservation equations are expressed in terms of overall molar concentration and overall molar flux (Dumore *et al.*, 1984):

$$\frac{\partial G_i}{\partial t} + \frac{\partial H_i}{\partial x} = 0, \quad i = 1,\ldots,N_c\ , \tag{3.3}$$

where

$$G_i = \sum_{j=1}^{N_c} x_{ij}\rho_j S_j + \frac{1-\phi}{\phi} a_i\ , \tag{3.4}$$

and

$$H_i = u\sum_{j=1}^{N_p} x_{ij}\rho_j f_j\ . \tag{3.5}$$

Substituting the following dimensionless variables into Eq. 3.3:

$$\xi = \frac{x}{L}, \tag{3.6}$$

$$\tau = \frac{u_{inj}t}{\phi L}, \tag{3.7}$$

$$u_D = \frac{u}{u_{inj}}, \tag{3.8}$$

$$\rho_{jD} = \frac{\rho_j}{\rho_{inj}}, \tag{3.9}$$

$$a_{iD} = \frac{a_i}{\rho_{inj}}, \tag{3.10}$$

where:

ξ = dimensionless distance,

τ = dimensionless time,

u_D = dimensionless overall local flow velocity,

u_{inj} = injection velocity,

ρ_{jD} = dimensionless molar density of phase j,

ρ_{inj} = molar density of injected fluid,

a_{iD} = dimensionless adsorbed amount of component i, and

L = system length,

the conservation equations, in dimensionless form, become:

$$\frac{\partial G_{iD}}{\partial \tau} + \frac{\partial H_{iD}}{\partial \xi} = 0, \quad i = 1, \ldots N_c \tag{3.11}$$

and Eqs. 3.3 and 3.4 are now:

$$G_{iD} = \phi \sum_{j=1}^{N_c} x_{ij} \rho_{jD} S_j + \frac{(1-\phi)}{\phi} a_{iD}, \tag{3.12}$$

$$H_{iD} = u_D \sum_{j=1}^{N_c} x_{ij} \rho_{jD} f_j \ . \tag{3.13}$$

Initial and boundary conditions are uniform and constant:

$$z_i(\xi,0)=\begin{cases} z_i^{inj}, & \xi=0 \\ z_i^{init}, & \xi>0 \end{cases}, \tag{3.14}$$

$$u_D(\xi,\tau)=\begin{cases} 0 & \xi=0,\tau=0 \\ 1 & \xi=0,\tau>0 \end{cases}, \tag{3.15}$$

where *inj* refers to the injection state and *init* refers to the initial state. Together with the hyperbolic nature of the conservation equations, a Riemann problem is specified and is solved by the method of characteristics.

3.3. Eigenvalue Problem and Continuous Variation

For a system with N_c components, N_c independent material balance equations are formulated. In terms of overall molar compositions, there are N_c independent relations. Local flow velocity changes as components transfer between phases and is unknown, resulting in a total of N_c unknowns. Mole fractions and saturations sum to one. The system is fully specified, and N_c unknowns are solved through N_c material balance equations. Once the overall molar compositions and local flow velocity are solved, other variables, such as saturations and equilibrium phase compositions are calculated by performing an equilibrium flash calculation.

Defining η to combine ξ and τ,

$$\eta=\frac{\xi}{\tau}, \tag{3.16}$$

solutions to the Riemann problem are expressed in terms of a single variable and are self-similar. Because G_i, H_i, and u_D are functions of composition, let η be a function of composition:

$$\frac{dG_{iD}}{d\tau}=\left[\sum_{k=1}^{N_c}\frac{\partial G_{iD}}{\partial z_k}\frac{\partial z_k}{\partial \eta}\right]\frac{\partial \eta}{\partial \tau}, \tag{3.17}$$

$$\frac{dH_{iD}}{d\xi} = \left[\sum_{k=1}^{N_c} \frac{\partial H_{iD}}{\partial z_k}\frac{\partial z_k}{\partial \eta}\right]\frac{\partial \eta}{\partial \xi}, \tag{3.18}$$

where

$$\frac{\partial \eta}{\partial \tau} = -\frac{\xi}{\tau^2}, \tag{3.19}$$

and

$$\frac{\partial \eta}{\partial \xi} = \frac{1}{\tau}. \tag{3.20}$$

Substitution of Eqs. 3.19 and 3.20 into 3.17 and 3.18 yields the following expression for the conservation equations:

$$-\left[\sum_{k=1}^{N_c} \frac{\partial G_{iD}}{\partial z_k}\frac{\partial z_k}{\partial \eta}\right]\frac{\xi}{\tau^2} + \left[\sum_{k-1}^{N_c} \frac{\partial H_i}{\partial z_k}\frac{\partial z_k}{\partial \eta}\right]\frac{1}{\tau} = 0 \quad i = 1,\ldots,N_c\,. \tag{3.21}$$

The system of equations is expressed in terms an eigenvalue problem, where η represents the characteristic wave speed of compositions,

$$\eta = \lambda\left(\overline{U}(\eta)\right), \tag{3.22}$$

where $\overline{U}(\eta)$ is a vector of state variables.

In matrix form, the system of conservation equations is written as:

$$\begin{bmatrix} \frac{\partial H_1}{\partial \zeta_1} & \cdots & \frac{\partial H_1}{\partial \zeta_{N_c-1}} & \frac{\partial H_1}{\partial u_D} \\ \vdots & \cdots & \vdots & \vdots \\ \frac{\partial H_{N_c-1}}{\partial \zeta_1} & \cdots & \frac{\partial H_{N_c-1}}{\partial \zeta_{N_c-1}} & \frac{\partial H_{N_c-1}}{\partial u_D} \\ \frac{\partial H_{N_c}}{\partial \zeta_1} & \cdots & \frac{\partial H_{N_c}}{\partial \zeta_{N_c-1}} & \frac{\partial H_{N_c}}{\partial u_D} \end{bmatrix} \begin{bmatrix} \frac{d\zeta_1}{d\eta} \\ \vdots \\ \frac{d\zeta_{N_c-1}}{d\eta} \\ \frac{du_D}{d\eta} \end{bmatrix} - \lambda \begin{bmatrix} \frac{\partial G_1}{\partial \zeta_1} & \cdots & \frac{\partial G_1}{\partial \zeta_{N_c-1}} & 0 \\ \vdots & \cdots & \vdots & \vdots \\ \frac{\partial G_{N_c-1}}{\partial \zeta_1} & \cdots & \frac{\partial G_{N_c-1}}{\partial \zeta_{N_c-1}} & 0 \\ \frac{\partial G_{N_c}}{\partial \zeta_1} & \cdots & \frac{\partial G_{N_c}}{\partial \zeta_{N_c-1}} & 0 \end{bmatrix} \begin{bmatrix} \frac{d\zeta_1}{d\eta} \\ \vdots \\ \frac{d\zeta_{N_c-1}}{d\eta} \\ \frac{du_D}{d\eta} \end{bmatrix} = \overline{0}\,. \tag{3.23}$$

For compositions with a particular wave velocity, components must have the same local flow velocity. Normalised component fluxes are introduced:

$$H_i = u_D \alpha_i \quad i = 1, \ldots, N_c \,, \tag{3.24}$$

where,

$$\alpha_i = \sum_{j=1}^{N_p} x_{ij} \rho_j f_j \quad i = 1, \ldots, N_c \,, \tag{3.25}$$

and the system of conservation equations becomes:

$$\begin{bmatrix} u_D \dfrac{\partial \alpha_1}{\partial \zeta_1} & \cdots & u_D \dfrac{\partial \alpha_1}{\partial \zeta_{N_c-1}} & \alpha_1 \\ \vdots & \cdots & \vdots & \vdots \\ u_D \dfrac{\partial \alpha_{N_c-1}}{\partial \zeta_1} & \cdots & u_D \dfrac{\partial \alpha_{N_c-1}}{\partial \zeta_{N_c-1}} & \alpha_{N_c-1} \\ u_D \dfrac{\partial H_{N_c}}{\partial \zeta_1} & \cdots & u_D \dfrac{\partial \alpha_{N_c}}{\partial \zeta_{N_c-1}} & \alpha_{N_c} \end{bmatrix} \begin{bmatrix} \dfrac{d\zeta_1}{d\eta} \\ \vdots \\ \dfrac{d\zeta_{N_c-1}}{d\eta} \\ \dfrac{du_D}{d\eta} \end{bmatrix} - \lambda \begin{bmatrix} \dfrac{\partial G_1}{\partial \zeta_1} & \cdots & \dfrac{\partial G_1}{\partial \zeta_{N_c-1}} & 0 \\ \vdots & \cdots & \vdots & \vdots \\ \dfrac{\partial G_{N_c-1}}{\partial \zeta_1} & \cdots & \dfrac{\partial G_{N_c-1}}{\partial \zeta_{N_c-1}} & 0 \\ \dfrac{\partial G_{N_c}}{\partial \zeta_1} & \cdots & \dfrac{\partial G_{N_c}}{\partial \zeta_{N_c-1}} & 0 \end{bmatrix} \begin{bmatrix} \dfrac{d\zeta_1}{d\eta} \\ \vdots \\ \dfrac{d\zeta_{N_c-1}}{d\eta} \\ \dfrac{du_D}{d\eta} \end{bmatrix} = \bar{0}. \tag{3.26}$$

In this analysis, the procedure outlined by Dindoruk (1992) is used to decouple local flow velocity from other dependent variables. The eigenvalue problem is split into two subsystems: one which solves for N_c-*1* unknowns in composition space and other which solves for the local flow velocity. Setting independent variables as S_g and $y_1, \ldots, y_{Nc-1}$, the eigenvalue system becomes:

$$\begin{bmatrix} F - \lambda^* G & \bar{0} \\ \bar{F}^T - \lambda^* \bar{G}^T & \dfrac{1}{u_D} \end{bmatrix} \begin{bmatrix} \bar{e} \\ \dfrac{du_D}{d\eta} \end{bmatrix} = \begin{bmatrix} \bar{0} \\ 0 \end{bmatrix}, \tag{3.27}$$

$$F = \frac{\partial \alpha_i}{\partial \zeta_j} - \frac{\alpha_i}{\alpha_{N_C}} \frac{\partial \alpha_{N_c}}{\partial \zeta_j}, \tag{3.28}$$

$$G = \frac{\partial G_i}{\partial \zeta_j} - \frac{\alpha_i}{\alpha_{N_c}} \frac{\partial G_{N_c}}{\partial \zeta_j}, \tag{3.29}$$

$$F^T = \frac{1}{\alpha_{N_c}} \frac{\partial \alpha_i}{\partial \zeta_j}, \tag{3.30}$$

$$G^T = \frac{1}{\alpha_{N_c}} \frac{\partial G_{N_c}}{\partial \zeta_j}, \tag{3.31}$$

$$\lambda^* = \frac{\lambda}{u_D}, \tag{3.32}$$

$$\bar{e} = \left[\frac{\partial S_g}{\partial \eta}, \frac{\partial y_1}{\partial \eta} \ldots, \frac{\partial y_{N_c-1}}{\partial \eta} \right]^T. \tag{3.33}$$

The eigenvalues of the composition subsystem represent the characteristic wave propagation speeds of compositions through the system, and the corresponding eigenvectors are the directions of variation in composition space that satisfy the differential equations. The eigenvalue of the local flow velocity subsystem is infinite. Therefore, variations in local flow velocity are propagated instantaneously throughout the system.

Once the composition subsystem has been solved, the local flow velocity is solved by integrating

$$\left[\bar{F}^T - \lambda^* \bar{G}^T \quad \frac{1}{u_D} \right] \left[\begin{matrix} \bar{e} \\ \frac{du_D}{d\eta} \end{matrix} \right] = 0. \tag{3.34}$$

and taking small increments along the composition path

$$u_D = u_0 \, exp\left[-\eta \left(\bar{F}^T - \lambda^* \bar{G}^T \right) \bar{e} \right]. \tag{3.35}$$

3.4. Discontinuous Solution and Solution Construction

The Riemann problem consists of an infinite number of states specified by the dependent variables of the composition subsystem and the local flow velocity. Each of these states propagates at a fixed wave velocity specified by the eigenvalues and in the direction of their corresponding eigenvectors. Continuous variation from the injection state to the initial state may result in non-monotonic variation of wave velocity, resulting in a multivalued state for a specific wave

velocity. Existence of such states is unphysical, and therefore additional constraints are applied to construct unique and physical solutions: the velocity rule and entropy condition.

The velocity rule specifies that faster travelling states lie downstream of slower moving states. In situations where a continuous variation violates the velocity rule, a shock must be introduced to resolve the multivalued state. Shock segments are discontinuous, therefore, the shock must satisfy the integral form of the material balance. This is achieved by applying the Rankine-Hugoniot condition (Eq. 3.36). For each component, the integral balance across a shock is

$$\Lambda = \frac{H_i^u - H_i^d}{G_i^u - G_i^d} \quad i = 1, \ldots, N_c \ , \tag{3.36}$$

where Λ is the shock velocity and u and d represent conditions upstream and downstream of the shock.

For a shock solution to remain stable, the entropy condition must be satisfied. This condition requires that the velocity immediately downstream of the shock is slower than the shock velocity and that the velocity immediately upstream of the shock is faster than the shock velocity:

$$\lambda^d < \Lambda < \lambda^u \tag{3.37}$$

Under a small perturbation, the shock remains self-sharpening as it propagates through the displacement. If velocities on either side of the shock do not satisfy the aforementioned requirements, the shock is unstable and collapses under a small perturbation.

Three types of shocks are possible: genuine shock, semishock and degenerate shock. These are classified by the velocities immediately upstream and downstream of the shock. Genuine shocks are those in which the velocities immediately upstream and downstream of the shock are unequal to the shock

velocity. Upstream and downstream states are connected to the shock through zones of constant state. Semishocks (also referred to as tangent shocks) occur when the velocity immediately upstream or immediately downstream of the shock is equal to the shock velocity. The state on the opposite side of the shock is connected by a zone of constant state. Degenerate shocks are those where the velocities immediately upstream and downstream of the shock are equal to the shock velocity. Table 3-1 summarises the shock types.

Table3-1: Summary of shock types.

shock type	configuration
genuine shock	$\lambda^u < \Lambda < \lambda^d$
semishock	$\lambda^u < \Lambda = \lambda^d$ or $\lambda^u = \Lambda < \lambda^d$
degenerate	$\lambda^u = \Lambda = \lambda^d$

Because the governing equations are expressed in differential form, discontinuous solutions are taken only when continuous variation violates the velocity rule. In addition to continuous and discontinuous variations, the solutions to the Riemann problem also include zones of constant state. In these states, dependent variables are constant, and the zones propagate downstream to connect continuous and discontinuous variations in a coherent manner.

These three types of variation: continuous variation, discontinuous variation and zones of constant state, can be combined to construct solutions to the Riemann problem. These segments must be arranged in a fashion whereby when combined, they obey the velocity rule. For changes in injection or initial state, the solution structure will vary in a consistent manner. In the following sections, these procedures are applied to construct solutions modelling gas injection in coals for ECBM recovery, in binary, ternary and quaternary systems for a variety of injection and initial states.

Chapter 4

Binary and Ternary Solutions for Enhanced Coalbed Methane Recovery

In this chapter, analytical solutions for modelling gas injection into reservoirs with adsorption and desorption of gases are developed. Such solutions are applicable to ECBM recovery and shale gas systems where gas components adsorb onto and desorb from the solid surface as gas mixtures propagate through the reservoir. Applying analytical models to these systems is of interest because the effects of phase behaviour, multiphase flow and adsorption/desorption effects are coupled. Analytical models allow isolation of these effects to provide enhanced understanding of the physical mechanisms involved in these processes.

4.1. Solution Construction

In this analysis, solutions for binary and ternary systems are constructed. These are modelled by mixtures of N_2, CH_4, CO_2 and H_2O. Constant K-values are used to represent component partitioning between gas and aqueous phases. Model parameters are used for clear display of solution structures. The K-values were

chosen to represent relative vapour-liquid volatility of the model system. Solutions were evaluated at a pressure of 1000 kPa. Model parameters are summarised in Table 4-1. In $N_2/CH_4/CO_2/H_2O$ systems, K values of CO_2, CH_4 and N_2 are much higher, while that of H_2O is much lower. This results in even lower solubilities of CO_2, CH_4 and N_2 in the aqueous phase, increasing the size of the two phase region. When more realistic values are used, the features of the displacement (shocks, rarefactions and zones of constant state) remain the same. These features scale appropriately to the phase behaviour of the system. A solution with more realistic fluid properties and equation of state modelling of phase behaviour is presented in Section 5.10 of Chapter 5. The extended Langmuir isotherm is used to model adsorption and desorption behaviour of gases. Gas adsorption strength is ordered opposite to vapour-liquid volatility; gases with higher volatility are weaker adsorbing than gases with lower volatility.

Table 4-1: Model parameters used in example solutions presented.

ρ_{GD}	1
ρ_{LD}	2
ρ_{inj} (mol/m^3)	1
ρ_r (kg/m^3)	1536
K_{N2}	5
K_{CH4}	3
K_{CO2}	1.2
K_{H2O}	0.1
M	10

4.1.1. Adsorption Model

Adsorption is the primary storage mechanism in coals. Gases are bound to the coal surfaces through weak intermolecular van der Waals forces. Because there are no chemical bonds between the adsorbed molecules and the solid surface, adsorption is a reversible process. Most of the adsorption experiments of gases on coals have been limited to N_2, CH_4 and CO_2 at relatively low pressures and low

temperatures (Chaback *et al.*, 1992, Arri *et al.*, 1992, Seidel *et al.*,1995). Adsorption capacity is a function of temperature and pressure; increased pressure results in higher volumes of gas adsorbed, while higher temperatures results in a decrease in gas adsorbed (Wymann, 1984). At low pressures, it is believed that adsorption occurs as a monolayer. Chaback *et al*. (1992) measured isotherms for N_2, CH_4 and CO_2 on wet bituminous coals under in situ conditions and concluded that the Langmuir equation adequately described experimental adsorption measurements for both pure gases and binary mixtures.

The Langmuir model assumes monolayer adsorption. Molecules are adsorbed on a fixed number of localized sites, each of which holds one adsorbed molecule, and are energetically equivalent with no interaction between adsorbed molecules and neighbouring sites. Markham *et al*. (1931) extended the Langmuir isotherm to account for adsorption of multicomponent gas mixtures, where the fractional coverage of individual components, θ, is a function of a Langmuir constant for a given temperature, B_i, for a pure gas species and the partial pressure of that species, p_i:

$$\theta_i = \frac{B_i p_i}{1 + \sum_{j=1}^{N_c} B_j p_j}. \tag{4.1}$$

Partial pressure of component *i* is calculated using the ideal gas relation:

$$p_i = P y_i, \tag{4.2}$$

where y_i is the equilibrium gas concentration of component *i* and *P* is the reservoir pressure. In terms of molar concentration of adsorbed components, a_i, Eq. 4.1 is expressed as

$$a_i = \frac{\rho_i \rho_r V_{mi} B_i p_i}{1 + \sum_{j=1}^{N_c} B_j p_j}, \tag{4.3}$$

where ρ_r is the mass density of the coalbed, ρ_i is the molar density of component i at standard conditions and V_{mi} is the Langmuir constant at a specified temperature for component i. Adsorption constants used in this analysis are summarised in Table 4-2. They are based on the experimental work of Greaves *et al.* (1993) and are the same as those used in the analysis of Zhu (2003). In this analysis, water is assumed not to adsorb. While moisture content affects the gas sorption capacity, Joubert *et al.* (1974) found that the amount of adsorbed CH_4 decreased with moisture content up to a critical value. Moisture in excess of the critical value had no additional effect on CH_4 adsorption.

Table 4-2: Summary of adsorption constants used in the example solutions presented.

component	V_{mi} (scf/ton)	B_i (psi^{-1})
N_2	222	0.0017
CH_4	444	0.0034
CO_2	707	0.0066
H_2O	0	0

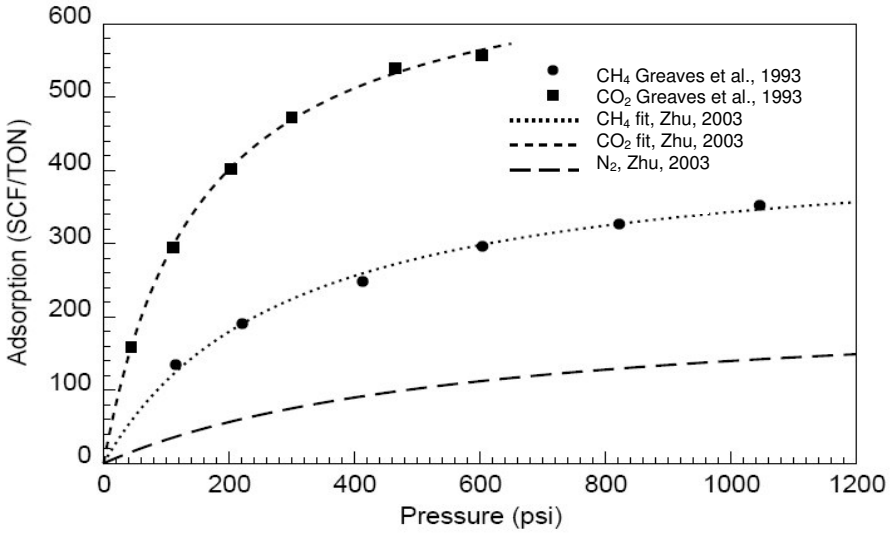

Figure 4-1: Adsorption isotherm used in the solutions presented in this analysis (from Zhu, 2003).

4.1.2. Multiphase Flow Model

Multiphase flow is represented by quadratic relative permeability functions,

$$k_{rg} = k_{rgo}\left(\frac{S_g - S_{gc}}{1 - S_{gc} - S_{wr}}\right)^n, \quad S_{gc} < S_g < 1 - S_{wr}\,, \tag{4.4}$$

$$k_{rg} = 0, \quad S_g < S_{gc}\,, \tag{4.5}$$

$$k_{rg} = 1, \quad S_g > 1 - S_{wr}\,, \tag{4.6}$$

$$k_{rw} = k_{rwo}\left(\frac{1 - S_g - S_{wr}}{1 - S_{gc} - S_{wr}}\right)^n, \quad S_{gc} < S_g < 1 - S_{wr}\,, \tag{4.7}$$

$$k_{rw} = 1, \quad 1 - S_g > 1 - S_{gc}\,, \tag{4.8}$$

and

$$k_{rw} = 0, \quad 1 - S_g < S_{wr}\,. \tag{4.9}$$

S_{gc} is the critical gas saturation. Below this saturation, the gas phase is immobile. S_{wr} is the residual water saturation. Below this saturation, the water phase is immobile and only gas is mobile. n is the Corey exponent (Brooks and Corey, 1964). In the solutions presented, this is 2. Expressing two-phase flow in terms of fractional flow, f_g:

$$f_g = 0, \quad S_g < S_{gc}\,, \tag{4.10}$$

$$f_g = \frac{k_{rgo}\left(S_g - S_{gc}\right)^2}{k_{rgo}\left(S_g - S_{gc}\right)^2 + k_{rwo}\left(1 - S_g - S_{wr}\right)^2 / M}, \quad S_{gc} < S_g < 1 - S_{wr}\,, \tag{4.11}$$

$$f_g = 1, \quad S_g > 1 - S_{wr}\,, \tag{4.12}$$

$$M = \frac{\mu_w}{\mu_g}\,. \tag{4.13}$$

M is the viscosity ratio, where μ_w is the water phase viscosity, and μ_g is the gas phase viscosity. Phase viscosities are assumed constant. In this analysis, residual saturations of gas and water are set to zero, end point relative permeabilities (k_{rgo} and k_{rwo}) are unity and M equals 10.

4.2. Binary Displacement

The solution to the eigenvalue problem for the binary system is presented in Appendix A. When only two components are present, the eigenvalue (normalised by the local flow velocity) in the two-phase region is

$$\lambda^* = \frac{\lambda}{u_D} = \frac{df}{dS}. \tag{4.14}$$

In this system, compositions vary only along tie lines, along which

$$\frac{dS}{d\eta} = 1. \tag{4.15}$$

In the single phase region, the normalized eigenvalue is

$$\lambda^* = \frac{\rho_D\left(1+\frac{z_1}{z_2}\right)}{\rho_D\left(1+\frac{z_1}{z_2}\right)+\frac{1-\phi}{\phi}\frac{da_{1D}}{dz_1}}. \tag{4.16}$$

Figure 4-2 shows the variation of the eigenvalue along a tie line. At phase boundaries, the eigenvalue in the two-phase region approaches zero, while the eigenvalue of the single phase region does not. Because the adsorption function used in this analysis is positive and concave, the normalized eigenvalue in the single phase region will always be greater than zero. Therefore, a shock must occur as compositions enter and leave the two phase region.

The landing point from the single phase region into the two phase region is found through solution of the shock balance,

$$\Lambda = \frac{H_1^u - H_1^d}{G_1^u - G_1^d} = \frac{H_2^u - H_2^d}{G_2^u - G_2^d}, \tag{4.17}$$

where u is the upstream state and d is the downstream state. Solving for the velocity ratio as components transfer between phases gives (Orr, 2007)

$$\frac{u_D^d}{u_D^u} = \frac{\alpha_1^u \left(G_2^u - G_2^d\right) - \alpha_2^u \left(G_1^u - G_1^d\right)}{\alpha_1^d \left(G_2^u - G_2^d\right) - \alpha_2^d \left(G_1^u - G_1^d\right)}, \tag{4.18}$$

and the shock velocity is expressed as a function of equilibrium composition

$$\Lambda = \frac{\alpha_1^u - \frac{u_D^d}{u_D^u}\alpha_1^d}{G_1^u - G_1^d}. \tag{4.19}$$

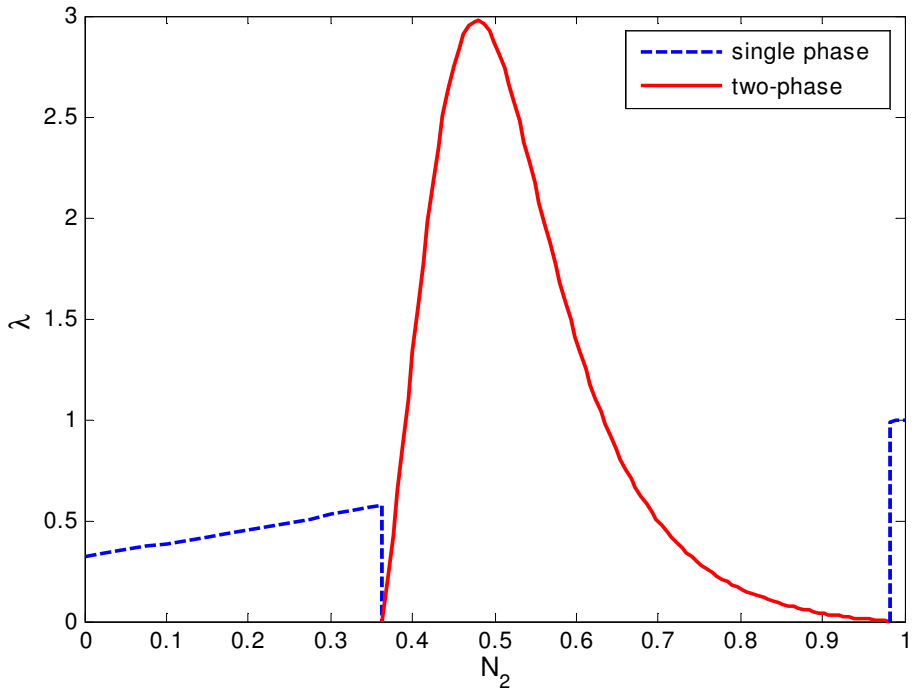

Figure 4-2: Variation of the eigenvalue along a tie line in a binary system.

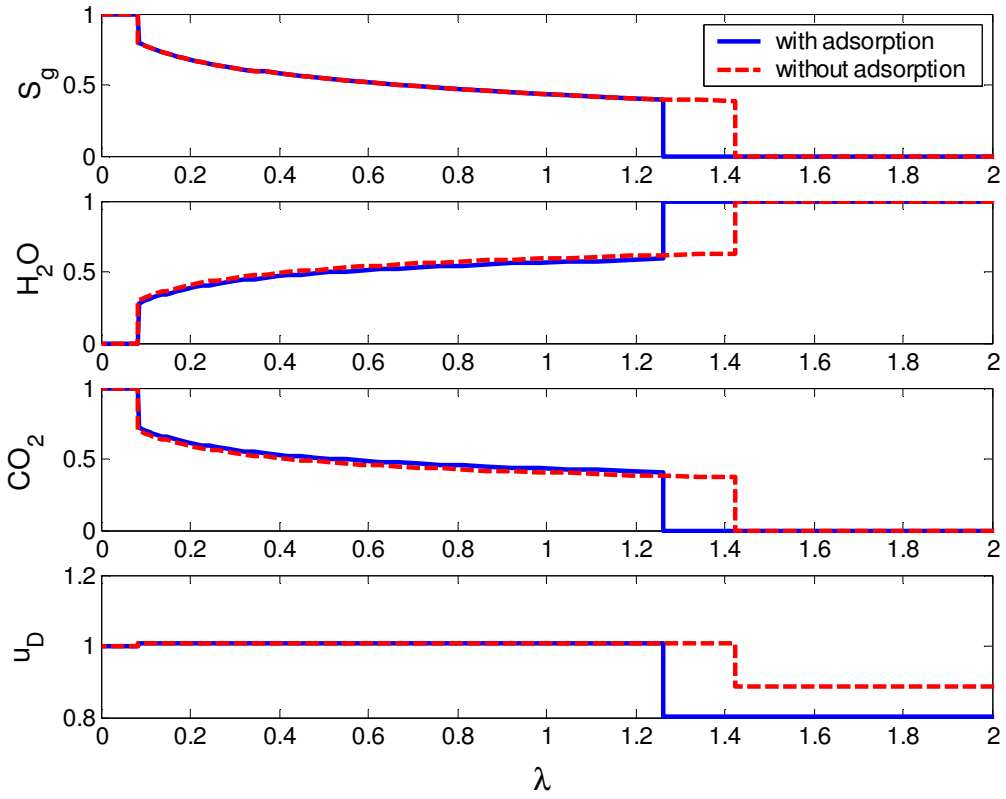

Figure 4-3: Solution profile for a binary system of CO_2 injection into a water saturated coal.

The solution profile for injection of CO_2 into a water-saturated core is shown in Figure 4-3. Also shown is the solution for the corresponding nonadsorbing system. The solution structure is similar to the nonadsorbing solution presented by Helfferich (1981). However, now the location of the shocks is determined by a combination of phase behaviour and adsorption. The leading shock saturation is low due to the unfavourable mobility ratio between injection gas and reservoir fluid. A slow trailing shock occurs at the upstream end of the displacement. Due to the low solubility of H_2O in the vapour phase, many pore volumes of CO_2 must be injected to vaporise the remaining portion of H_2O. It should also be noted that there is a large decrease in flow velocity between injection conditions and initial

conditions. Adsorption of CO_2 onto the surface, with the accompanying volume change, reduces the shock velocity. A small increase in flow velocity at the trailing shock is observed. When gas is injected into the wet coal, a two-phase mixture is produced and a small amount of H_2O vaporises into the gas phase and a small amount of CO_2 dissolves in the aqueous phase.

4.3. Ternary Displacements

The eigenvalue problem for the ternary system is formulated in Appendix A. The key features of the binary displacement are preserved when the number of components is increased to three. In the two-phase region of the displacement, the eigenvalues and corresponding eigenvectors are:

$$\lambda_t^* = \frac{df}{dS}, \quad \lambda_{nt}^* = \frac{f - \chi_1}{S - \chi_1 - \chi_2}, \tag{4.20}$$

and

$$\bar{e}_t = \begin{bmatrix} 1 \\ 0 \end{bmatrix}, \quad \bar{e}_{nt} \begin{bmatrix} 1 \\ \dfrac{\lambda_{nt}^* - \lambda_t^*}{dH_1 / d\eta} \end{bmatrix}. \tag{4.21}$$

Where:

$$\chi_1 = \frac{\left(\frac{\partial \beta_1}{\partial y_1} - \frac{\alpha_1}{\alpha_3}\frac{\partial \gamma_3}{\partial y_1}\right)\left(\gamma_2 - \frac{\alpha_2}{\alpha_3}\gamma_3\right) - \left(\frac{\partial \beta_2}{\partial y_1} - \frac{\alpha_2}{\alpha_3}\frac{\partial \gamma_3}{\partial y_1}\right)\left(\gamma_1 - \frac{\alpha_1}{\alpha_3}\gamma_3\right)}{\left(\frac{\partial \gamma_1}{\partial y_1} - \frac{\alpha_1}{\alpha_3}\frac{\partial \gamma_3}{\partial y_1}\right)\left(\gamma_2 - \frac{\alpha_2}{\alpha_3}\gamma_3\right) - \left(\frac{\partial \gamma_2}{\partial y_1} - \frac{\alpha_2}{\alpha_3}\frac{\partial \gamma_3}{\partial y_1}\right)\left(\gamma_1 - \frac{\alpha_1}{\alpha_3}\gamma_3\right)}, \tag{4.22}$$

$$\chi_2 = \frac{\left(\frac{\partial \delta_1}{\partial y_1} - \frac{\alpha_1}{\alpha_3}\frac{\partial \delta_3}{\partial y_1}\right)\left(\gamma_2 - \frac{\alpha_2}{\alpha_3}\gamma_3\right) - \left(\frac{\partial \delta_2}{\partial y_1} - \frac{\alpha_2}{\alpha_3}\frac{\partial \delta_3}{\partial y_1}\right)\left(\gamma_1 - \frac{\alpha_1}{\alpha_3}\gamma_3\right)}{\left(\frac{\partial \gamma_1}{\partial y_1} - \frac{\alpha_1}{\alpha_3}\frac{\partial \gamma_3}{\partial y_1}\right)\left(\gamma_2 - \frac{\alpha_2}{\alpha_3}\gamma_3\right) - \left(\frac{\partial \gamma_2}{\partial y_1} - \frac{\alpha_2}{\alpha_3}\frac{\partial \gamma_3}{\partial y_1}\right)\left(\gamma_1 - \frac{\alpha_1}{\alpha_3}\gamma_3\right)}, \tag{4.23}$$

$$\gamma_i = \rho_{GD} y_i - \rho_{LD} x_i \,, \tag{4.24}$$

$$\beta_i = \rho_{LD} x_i \,, \tag{4.25}$$

$$\delta_i = \frac{1-\phi}{\phi} a_{iD} \,. \tag{4.26}$$

When another component is added, another eigenvalue, λ^*_{nt}, and corresponding eigenvector, $\bar{e}_{nt}$, satisfy the system of equations. This path allows continuous variation between tie lines, which may be allowed, provided the velocity rule is satisfied. For each point in composition space, there are two possible directions for variation. The allowable path is determined by applying the velocity rule and entropy condition discussed in Chapter 3. χ_1 describes the variation in composition and χ_2 describes the variation in adsorption, and along a tie line, these are constant (Appendix A). χ_1 and χ_2 are analogous to the envelope curve intersection parameter in nonadsorbing systems (Dindoruk, 1992), allowing similar geometric constructions and path analysis in systems with adsorption. Similar to nonadsorbing systems, the tie-line eigenvalue is the derivative of the fractional flow with respect to saturation. However, the denominator of the nontie-line eigenvalue is now a function of both phase behaviour and adsorption. At the phase boundary, the presence of the adsorption term, χ_2, in the denominator prevents the nontie-line eigenvalue from equalling the numerator at the phase boundaries and equivelocity point. At these points, the nontie-line eigenvalue is no longer unity, as it is in the nonadsorbing case, and these points are no longer paths, as they are in systems without adsorption (Orr, 2007). Figures 4-3 and 4-4 show the variation of eigenvalues and eigenvectors in saturation and mobile composition space, where

$$G_{i\,norm} = \frac{G_i - \dfrac{1-\phi}{\phi} a_{Di}}{\displaystyle\sum_{j=1}^{N_c} G_j - \frac{1-\phi}{\phi} a_{Dj}} \,. \tag{4.27}$$

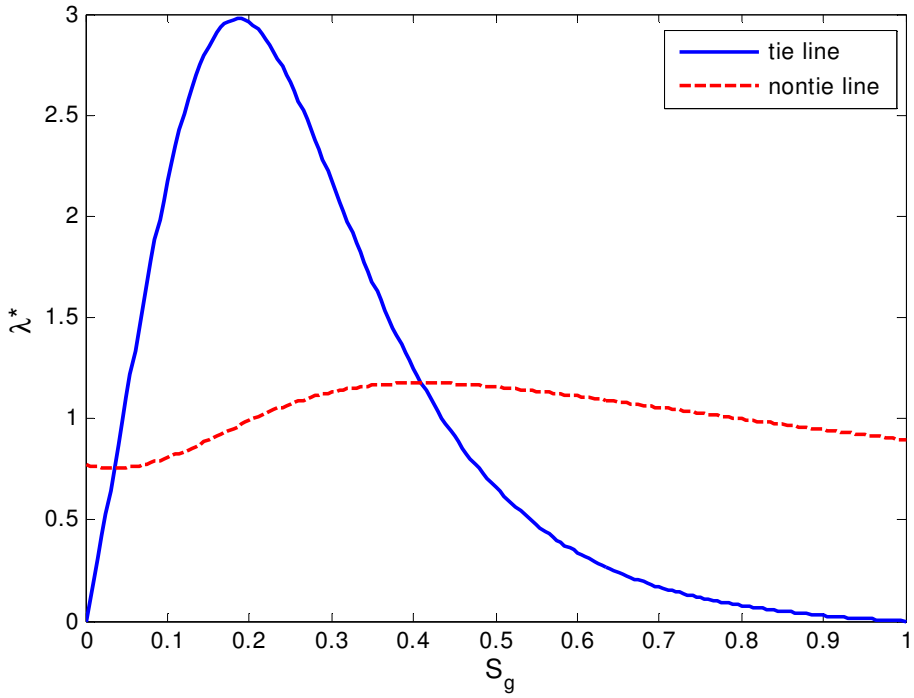

Figure 4-4: Eigenvalue variation along a tie line in the two-phase region of a ternary system.

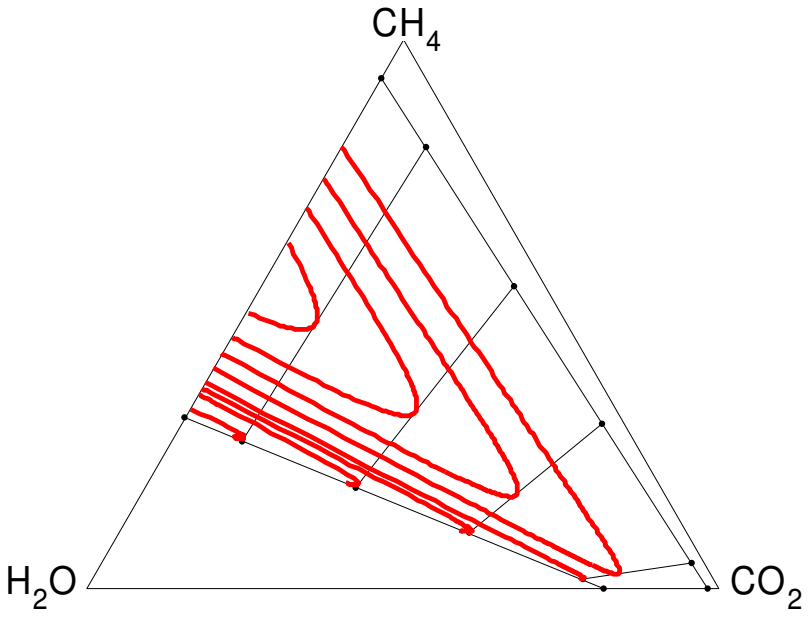

Figure 4-5: Integral curves of the eigenvectors (paths) in the two phase region, in mobile composition space.

In ternary displacements, two types of solutions result: designated Type I and Type II in the discussion that follows. These are classified based on the type of composition variation that connects initial and injection tie lines. The following two examples illustrate these solutions.

The analytical solutions were confirmed by 1-D finite difference simulations. The simulator was modified from a model developed by Jessen in Tang *et al.* (2005). An explicit, single point upstream weighting scheme was used to discretise the governing equations:

$$G_{i,k}^{n+1} = G_{i,k}^{n} - \frac{\Delta t}{\Delta x}\left[H_{i,k}^{n} - H_{i,k-1}^{n}\right] \tag{4.28}$$

At each time step, an equilibrium calculation was performed for each gridblock. For a given overall composition, components were distributed between gas, aqueous and solid phases. Changes in local flow velocity correspond to changes in molar density as components were mixed. For the composition paths presented, analytical solutions were compared to finite difference solutions. 1000 gridblocks were used, with a Courant number, $\frac{\Delta t}{\Delta x}$, of 0.09.

4.3.1. Type I: Shock

Type I solutions are characterised by a semishock connecting the injection and initial tie lines. This type of solution occurs when the injected gas adsorbs more strongly than the gas component present initially and is more soluble in the liquid water phase (e.g. CO_2 displacing CH_4). To illustrate this solution, pure CO_2 is injected into a coalbed saturated with a mixture of 0.3103 CH_4 and 0.6987 H_2O. Compositions are listed in terms of mole fractions. The composition path and solution profile for this displacement are presented in Figures 4-6 and 4-7.

Eigenvalues decrease as compositions vary from the injection tie line to the initial tie line (Figure 4-8), and hence, continuous variation violates the velocity

rule. Therefore, a shock is required to connect injection and initial tie lines. Compositions upstream and downstream of the shock are found by solving the Rankine-Hugoniot condition (Eq. 3.36).

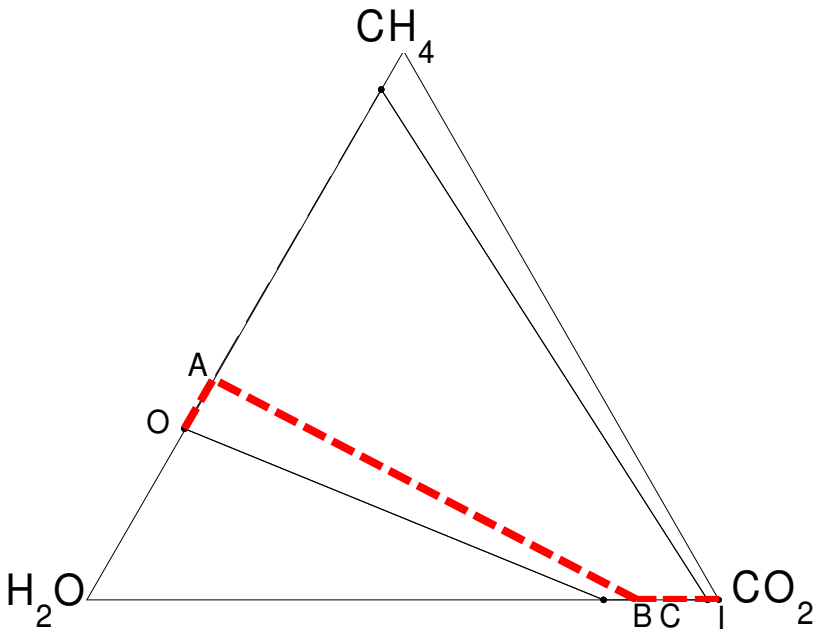

Figure 4-6: Composition path of Type I displacement.

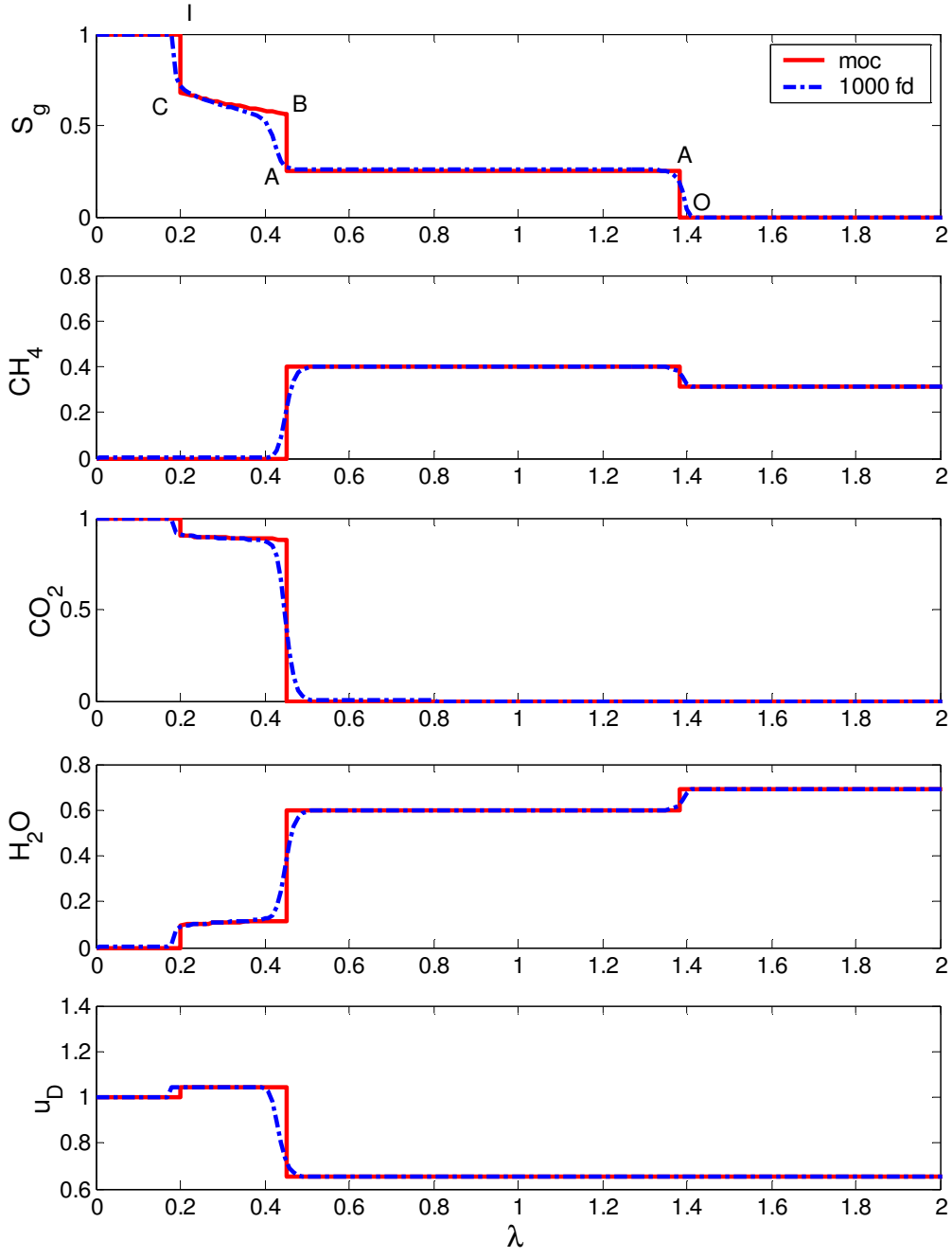

Figure 4-7: Solution profile of Type I displacement. The numerical solution agrees well with the analytical solution.

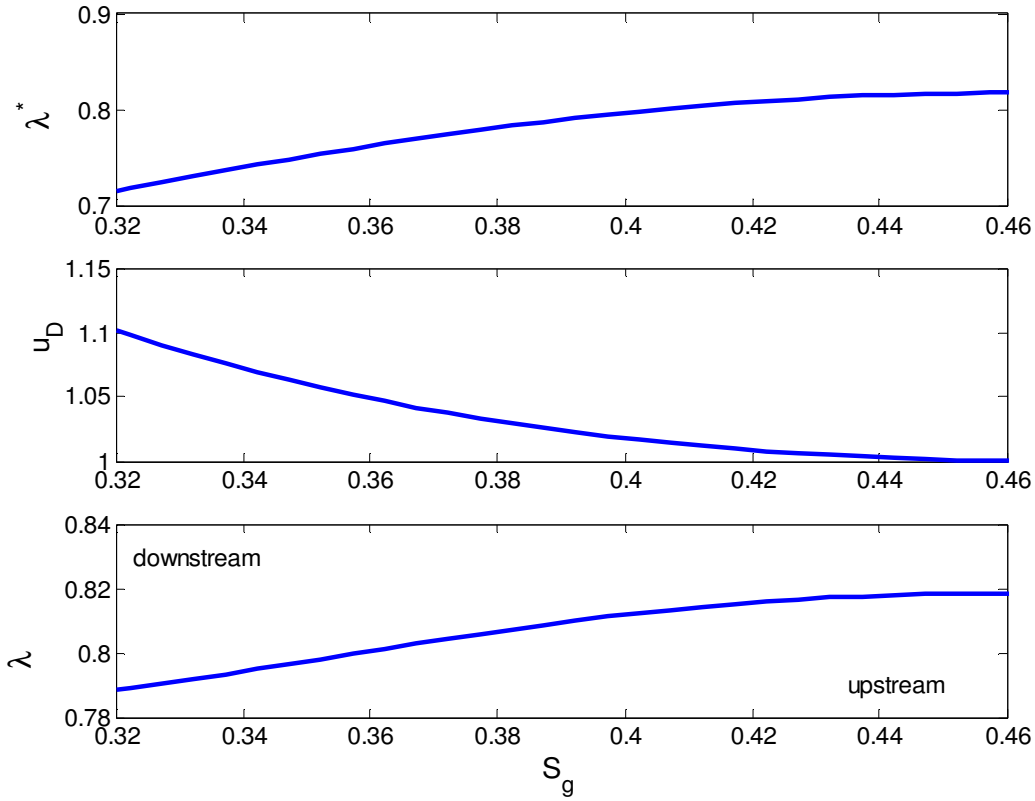

Figure 4-8: Variation of eigenvalues from injection tie line to initial tie line.

Table 4-3: Summary of shock velocity and tie-line eigenvalues for shock from initial to injection tie line.

Λ^*	0.4349
λ_{tl}^* injection ($S_g = 0.5633$)	0.4349
λ_{tl}^* initial ($S_g = 0.2565$)	2.6020
$u_{D\ initial}/\ u_{D\ injection}$	0.6264

Table 4-3 summarises the shock velocity that satisfies the Rankine-Hugoniot condition and the velocity rule at the jump and landing points for the semishock connecting injection and initial tie lines. The velocity upstream of the shock is equal to the shock velocity, while the velocity downstream of the shock is greater than the shock velocity.

Similar to solution construction algorithms in nonadsorbing cases (Orr, 2007) solution construction begins at the shortest tie line of the displacement, the injection tie line. The solution includes a semishock from the injection composition (I) into the two-phase region (C). This shock is followed by a rarefaction along the injection tie line from C to B. A shock connects injection and initial tie lines from B to A. The landing point of the semishock (A) is faster than the velocity of the phase change shock from the two-phase region to the initial conditions, and hence a genuine shock from A to the initial composition O completes the composition path. At point A, a zone of constant state connects the semishock velocity (B to A) with the leading shock velocity (A to O). Parameters of key points in the displacement are summarised in Table 4-4.

Table 4-4: Summary of key points in Type I displacement.

composition label	composition (mol fraction)			S_g	total flow velocity	wave velocity (λ)
	CH_4	CO_2	H_2O			
I	0.0	1.0	0.0	1.0	1.0	0.0-0.2077
C	0.0	0.9019	0.0981	0.6710	1.0418	0.2077
B	0.0	0.8823	0.1177	0.5633	1.0418	0.4531
A	0.4017	0.0	0.5983	0.2565	0.6526	0.4531-1.3826
O	0.3103	0.0	0.6897	0.0	0.6526	1.3826

A significant decrease in local flow velocity occurs as CO_2 adsorbs onto the coal and is removed from the flowing gas phase, delaying CO_2 breakthrough at the outlet. A faster moving bank of CH_4 propagates ahead of the CO_2 bank. Chromatographic separation of components is observed, with more strongly adsorbing and less volatile components propagating more slowly than less strongly adsorbing and more volatile components.

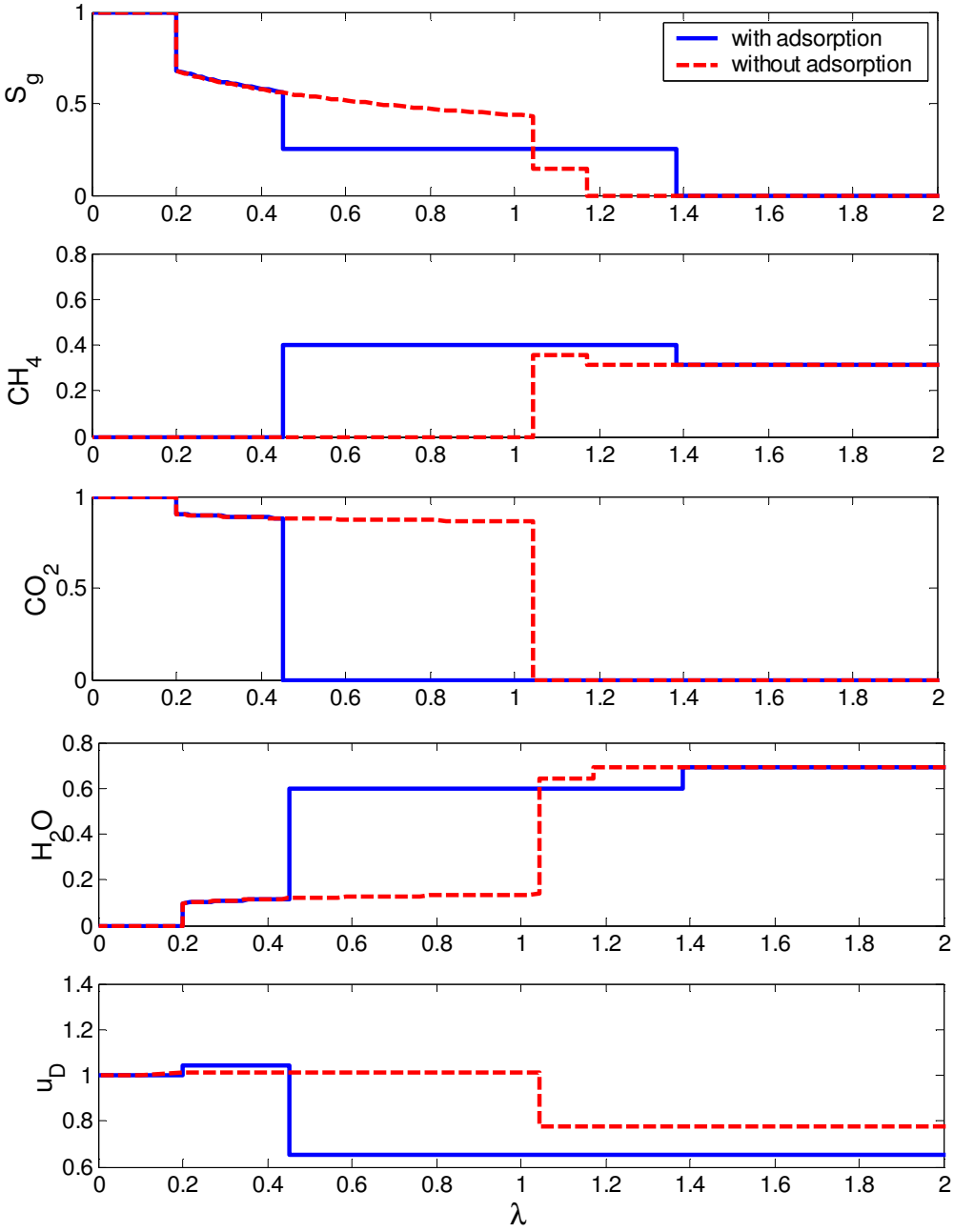

Figure 4-9: Comparison of the Type I solution with and without adsorption.

When initial and injection compositions are saturated, shocks in and out of the two-phase region occur along a tie line, as they do in gas displacements in the absence of adsorption (Larson, 1979). Because the extended Langmuir function is dependent on the equilibrium gas phase composition, adsorption along a tie line is constant. If initial or injection compositions are saturated, the adsorption term cancels, and the shock occurs along the tie line.

Analogous to the binary system, the structure of the Type I solution with adsorption is similar to that of a nonadsorbing system. Shock velocities are functions of both phase behaviour and adsorption. Because adsorption reduces shock velocity, the displacement in the adsorbing system is slower relative to the nonadsorbing system. In the system with adsorption, there is an additional phase that gas components interact with, the solid phase. Significant volume change occurs as CO_2 is adsorbed onto the coal surface, compared to the volume change due to dissolution of CO_2 into the aqueous phase. A comparison of the solution profiles for the adsorbing and nonadsorbing system is presented in Figure 4-9.

4.3.2. Type II: Rarefaction

Type II solutions are characterised by a continuous variation connecting initial and injection tie lines. These solutions occur when a less strongly adsorbing gas is injected to displace a more strongly adsorbing gas. Because the initial gas is the preferentially adsorbed gas species, a decrease in partial pressure is required to displace the gas initially adsorbed. To illustrate this solution structure, pure N_2 is injected into a coalbed saturated with 0.3103 CH_4 and 0.6987 H_2O. The composition path and solution profile for a Type II displacement are shown in Figures 4-10 and 4-11, again for typical ordering of component solubilities and strengths of adsorption.

In this system, the initial tie line is the shortest tie line and solution construction begins at the initial tie line. As the composition path is traced from initial tie line to injection tie line, eigenvalues decrease, satisfying the velocity rule, and hence, a continuous variation along a nontie-line path is allowed (Figure 4-12). Entry into the two phase region occurs with a shock from O to A. This is followed by a rarefaction along the initial tie line from A to B. A path switch occurs at the equal-eigenvalue point, B, from the tie-line path to the nontie-line path. The nontie-line rarefaction from B to C connects the initial and injection tie lines. A second path switch at C from the nontie-line path to the injection tie line is manifested as a zone of constant state in the solution profile. This is followed by a short rarefaction along the injection tie line to D. A semi-shock from D to I is required to exit the two-phase region. Parameters of key points in the displacement are summarised in Table 4-5.

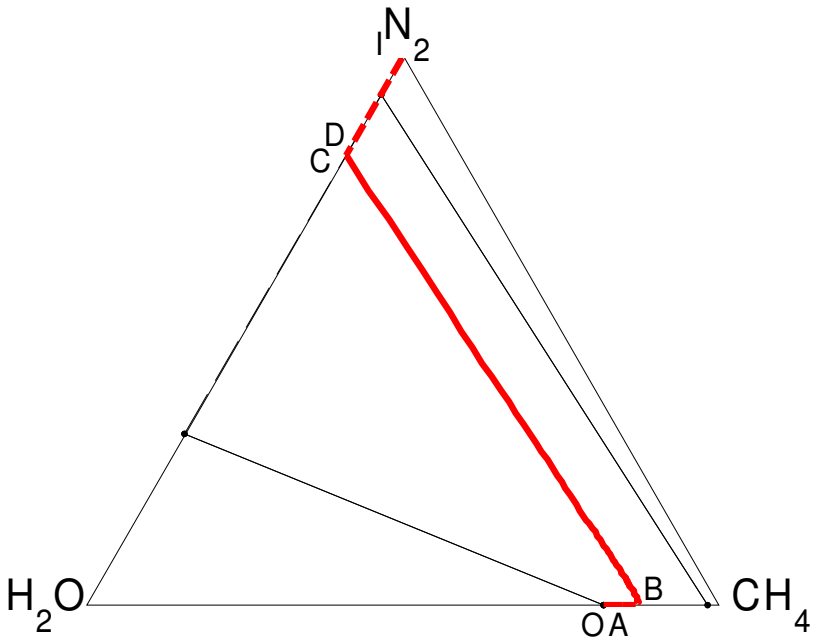

Figure 4-10: Composition path for Type II displacement.

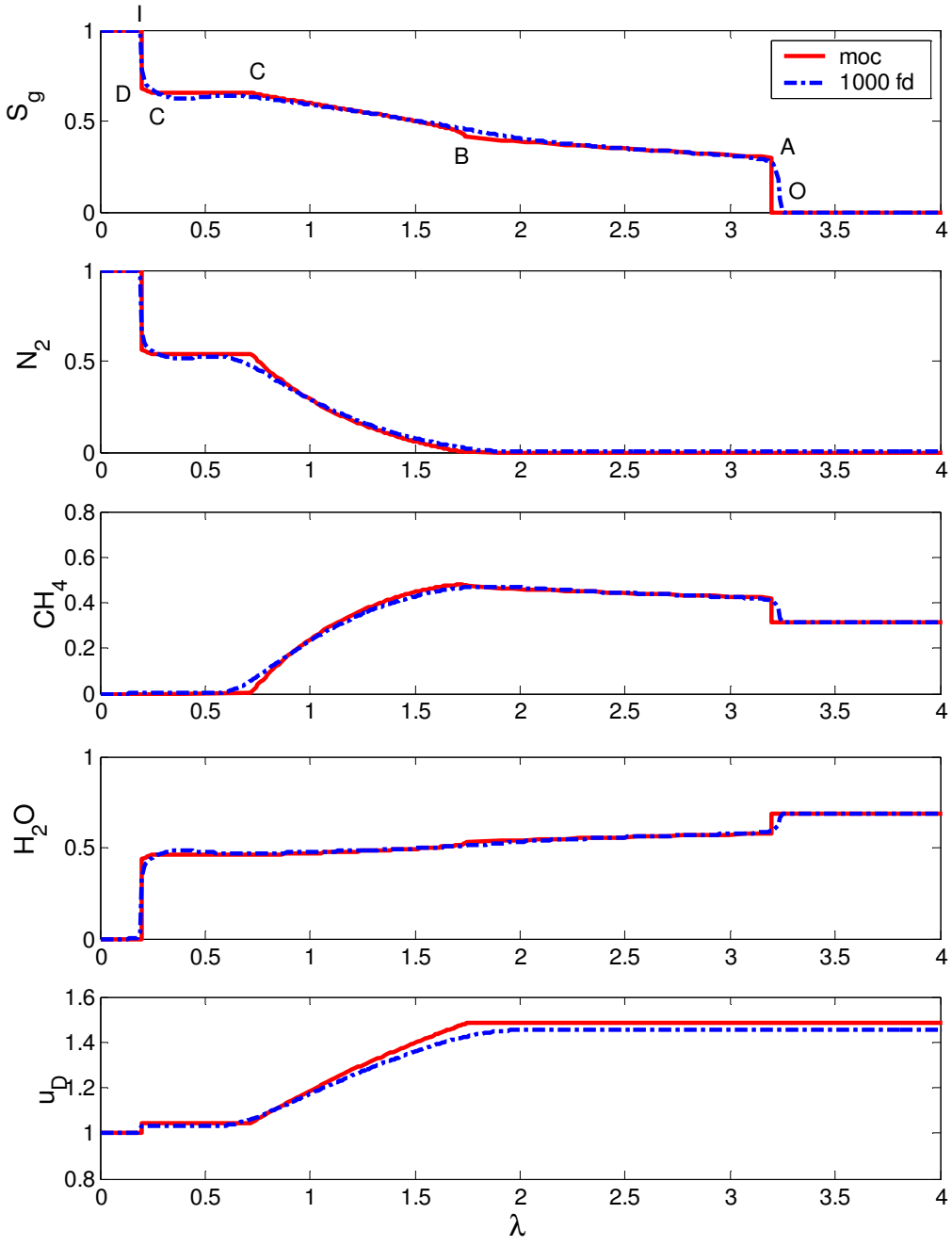

Figure 4-11: Solution profile for Type II displacement.

Table 4-5: Summary of key points in a Type II displacement.

composition label	composition (mol fraction)			S_g	total flow velocity	wave velocity (λ)
	N_2	CH_4	H_2O			
I	1.0	0.0	0.0	1.0	1.0	0.0-0.1995
D	0.5594	0.0	0.4406	0.6767	1.0420	0.1995
C	0.5411	0.0	0.4586	0.6549	1.0420	0.2423-0.0759
B	0.0	0.4704	0.5296	0.4099	1.4826	1.7427
A	0.0	0.4205	0.5795	0.3015	1.4826	3.1994
O	0.0	0.3103	0.6897	0.0	1.4826	3.1994

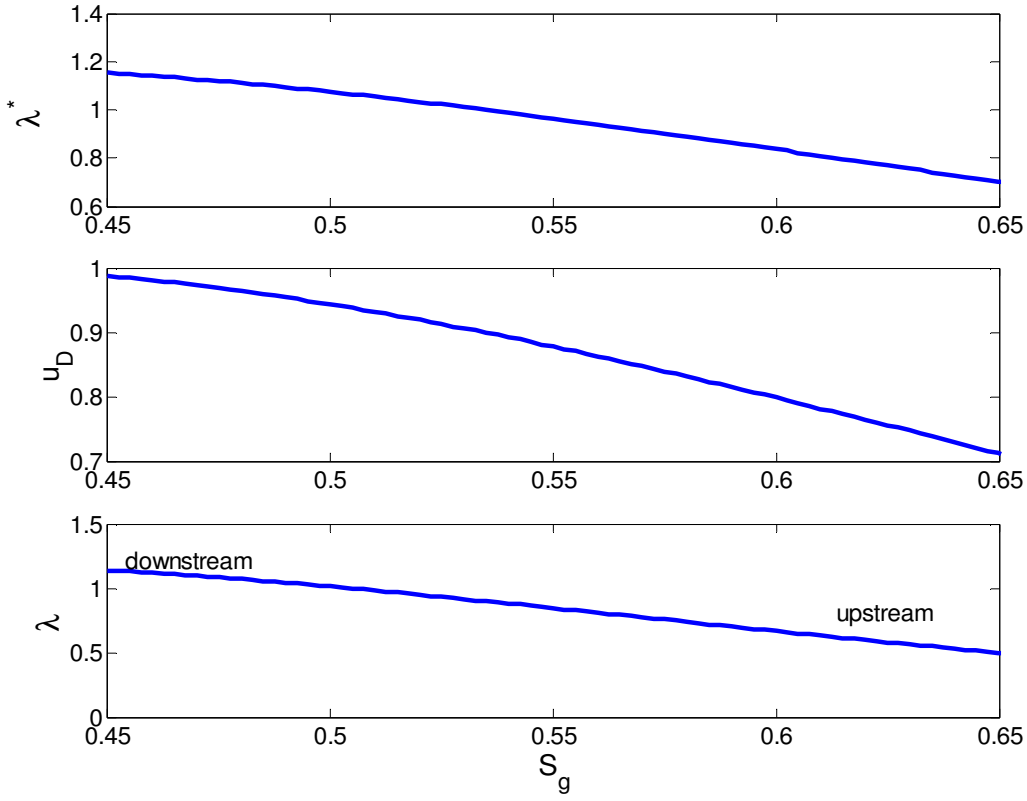

Figure 4-12: Variation of eigenvalues from the initial tie line to the injection tie line.

Because N_2 is more volatile and less strongly adsorbing than CH_4, it travels quickly through the system, causing CH_4 desorption to occur earlier than when CO_2 is injected to recover CH_4. A large bank of N_2 propagates through the system, with a faster moving mixture of desorbed CH_4 ahead. Because more molecules of CH_4 are desorbed per molecule of N_2 adsorbed, volume is added to the flowing vapour phase. Local flow velocity increases as CH_4 desorbs, resulting in the fast arrival of the leading shock. A mixture of CH_4 and N_2 is produced at the outlet, requiring separation of the produced gas stream prior to use. Complete recovery of CH_4 is achieved as the partial pressure of CH_4 is driven to zero by continued injection of pure N_2.

Figure 4-13 compares the Type II solution with and without adsorption. The solution structures remain the same, but the features of the displacement are shifted according to adsorption and desorption. Adsorption retards the trailing edge of the displacement as N_2 adsorbs onto the surface as it propagates through the coalbed. The leading edge of the displacement is fast relative to the system without adsorption. The velocity increase in the system with adsorption is more significant as CH_4 desorbs from the coal surface. Some CH_4 vaporised from the aqueous phase also contributes to the velocity increase.

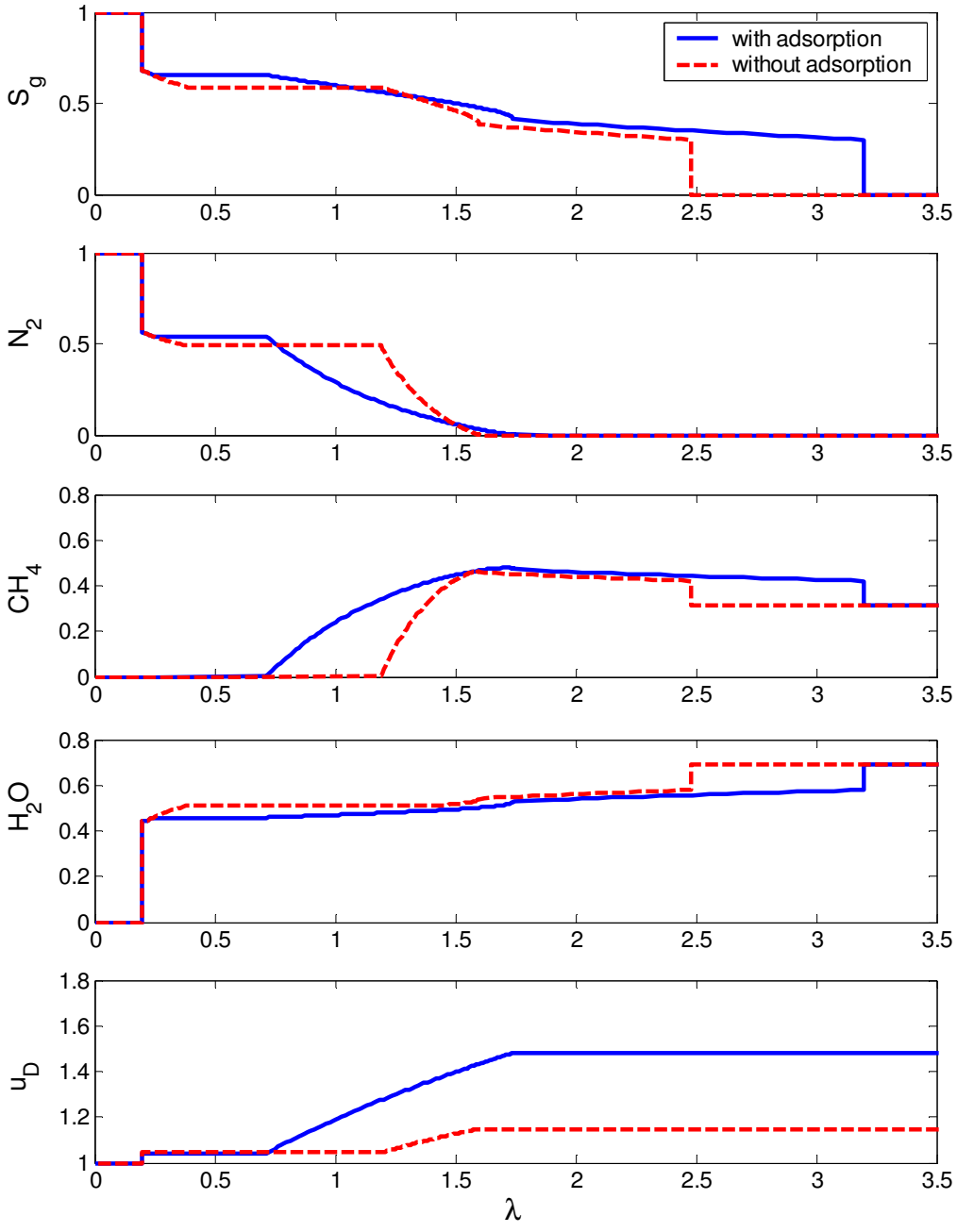

Figure 4-13: Comparison of the Type II solution with and without adsorption.

4.3.3. Undersaturated Systems

When the initial or injection conditions are undersaturated, entry from the single phase region into the two phase region no longer occurs along the tie-line extension, as they do in nonadsorbing systems (Larson,). Figure 4-14 shows the corresponding initial tie lines for a variety of undersaturated initial conditions. Nonlinearities in the accumulation term of the governing equation (i.e. the adsorption function), prevent cancellation of the adsorption terms in the shock balance

$$x_i^I = \frac{1-\phi}{\phi}\Lambda\frac{a_i^{II}-a_i^I}{\rho_D^I\left(\Lambda-u_D^I\right)} + x_i^{II}\rho_{LD}^{II}\frac{\Lambda\left(1-S^{II}\right)+\left(u_D^{II}f^{II}-1\right)}{\rho_D^I\left(\Lambda-u_D^I\right)} + y_i^{II}\rho_{LD}^{II}\frac{\Lambda S^{II}+u_D^{II}f^{II}}{\rho_D^I\left(\Lambda-u_D^I\right)}. \quad (4.29)$$

The shock balance for undersaturated systems is derived in Appendix A. Solutions are constructed by solving the tie-line composition and saturation that satisfy the Rankine-Hugoniot condition. As in the nonadsorbing system, solution construction starts at the shortest tie line. Table 4-6 compares adsorbed concentrations obtained from the equilibrium composition that satisfies the Rankine-Hugoniot condition and those from the tie-line extension against the adsorbed amount for a range of undersaturated conditions. The adsorbed amount of CH_4 solved by the shock balance is lower than the adsorbed amount from the tie-line extension equilibrium compositions. Less CH_4 is adsorbed on the coal when it is undersaturated than when initial conditions are saturated. Figure 4-15 shows the location of undersaturated conditions relative to the adsorption isotherm. When conditions are undersaturated, the pressure must be decreased to bring the coal surface to a saturated state prior to desorption.

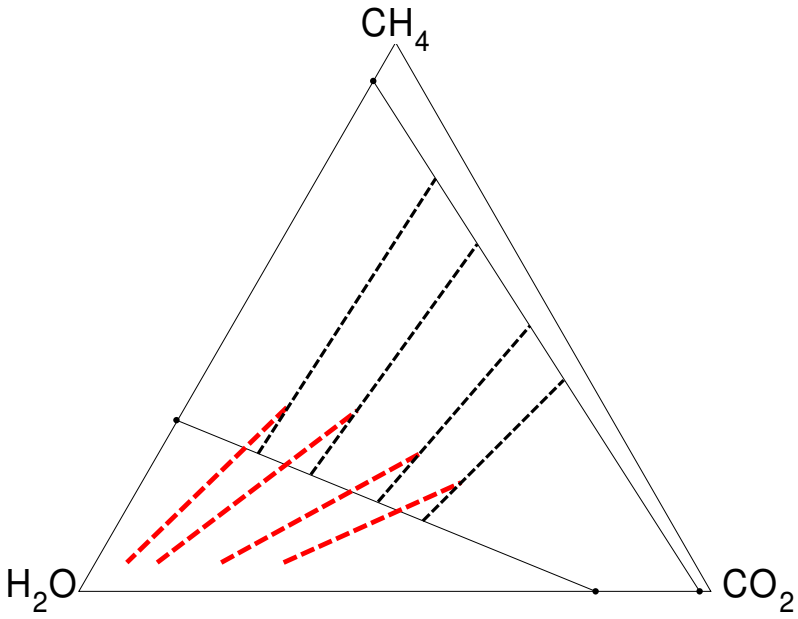

Figure 4-14: Phase change shock from undersaturated initial compositions into the two-phase region. The phase change shock no longer occurs along a tie-line extension.

Table 4-6: Comparison of adsorbed amounts satisfied by the Rankine-Hugoniot condition and the tie-line extension.

z_{CH4}	z_{CO2}	undersaturated		Rankine-Hugoniot condition		tie-line extension	
		a_{CH4}	a_{CO2}	a_{CH4}	a_{CO2}	a_{CH4}	a_{CO2}
0.05	0.05	0.1014	0.1260	0.1414	0.1101	0.1700	0.0397
0.05	0.10	0.0805	0.1998	0.1147	0.1759	0.1546	0.0777
0.05	0.20	0.0569	0.2828	0.0840	0.2532	0.1258	0.1486
0.05	0.30	0.0440	0.3282	0.0633	0.3025	0.0995	0.2134

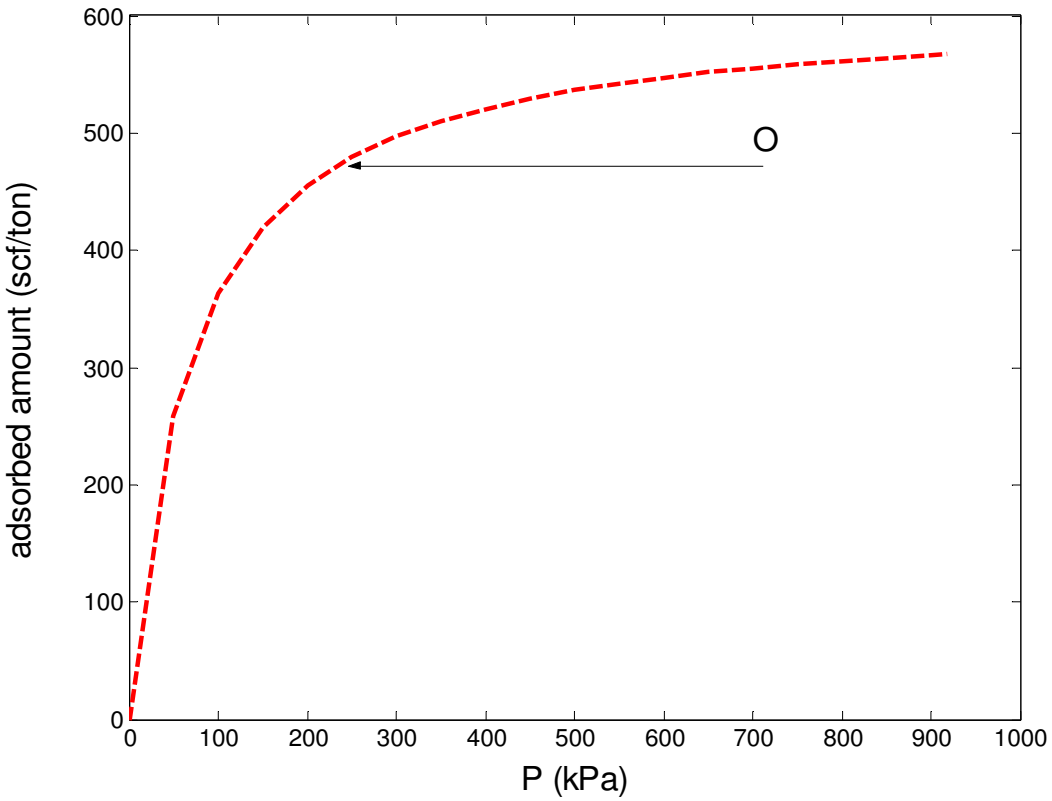

Figure 4-15: Location of undersaturated conditions relative to saturated conditions. To reach saturation, partial pressure must be lowered. This is achieved by injecting more CO_2 than in the saturated case.

A Type I solution with an undersaturated initial composition is presented (0.05 CH_4, 0.05 CO_2 and 0.9 H_2O) in Figures 4-16 and 4-17. In the undersaturated system, less CH_4 is available to be recovered than in the saturated case. The tie line that satisfies the shock balance has a lower equilibrium concentration than that of the tie-line extension, reflecting that the tie line controlling the initial equilibrium concentrations is lower in CH_4 compared to the saturated system. Injection and initial tie lines are identified. In this example, the injection tie line is still the shortest tie line, and solution construction starts at the injection tie line. A rarefaction occurs along the injection tie line. The new tie line to which a tangent shock connecting injection and initial tie lines is closer, resulting in a slower shock

at a higher S_g. This is followed by a genuine shock from the landing point to initial undersaturated conditions.

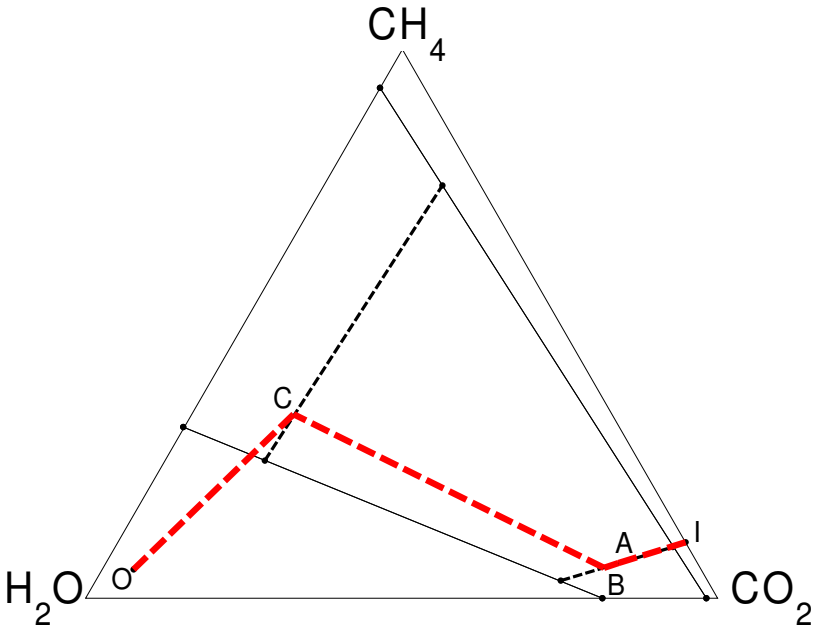

Figure 4-16: Composition path of Type I solution with undersaturated initial conditions.

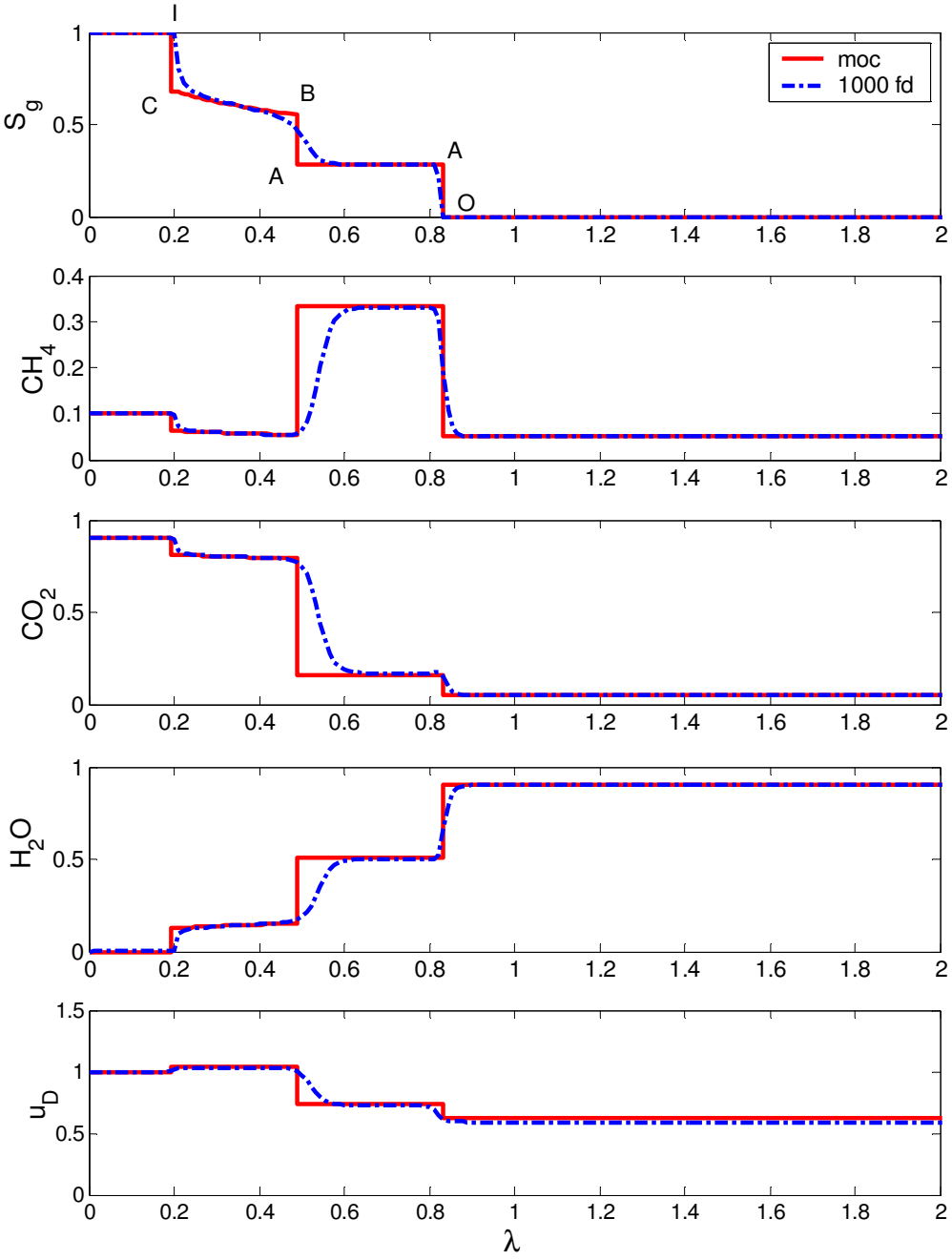

Figure 4-17: Solution profile of Type I solution with undersaturated initial conditions.

Figures 4-18 and 4-19 compare the composition paths and solution profiles for the saturated and undersaturated displacements. Because the injection tie line is the same in both systems, the trailing edge of the solution is unchanged. Initial compositions of CH_4 and CO_2 in the undersaturated case are much lower than in the saturated case. Banking behaviour is observed in the undersaturated CH_4 profile, while in the saturated system, this bank is less pronounced. The undersaturated displacement is slower than the saturated displacement because more gas must be injected to saturate the system before desorption can occur. This results in a slower initial recovery in undersaturated coals (Figure 4-20). If CO_2 sequestration is the goal of the project, injection into undersaturated coalbeds are preferable to saturated coals because of the delay of gas breakthrough. More CO_2 can be injected into the reservoir prior to gas breakthrough in undersaturated coals. If accelerating CH_4 recovery is the objective, then injection into undersaturated coals is not attractive because of the delayed production response associated with bringing the coal to saturated conditions before CH_4 desorption occurs.

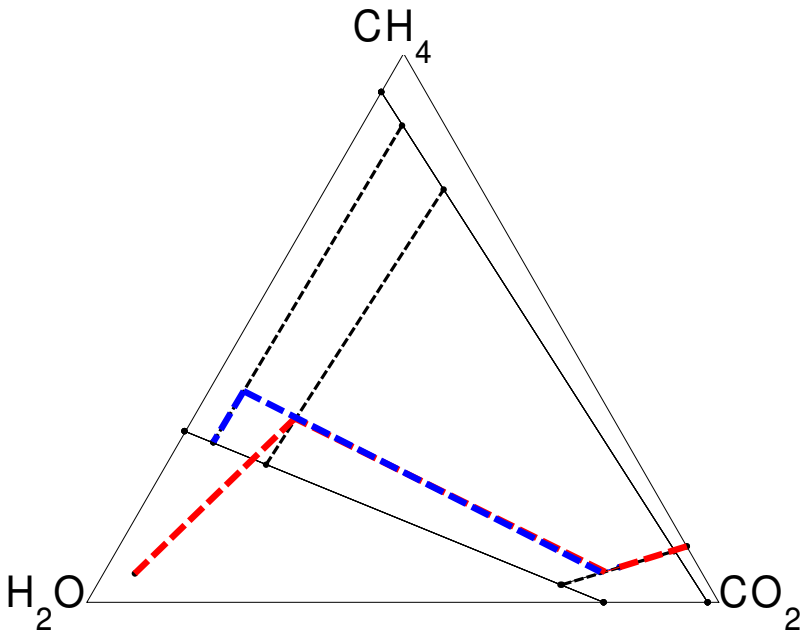

Figure 4-18: Comparison of composition paths for saturated (blue) and undersaturated (red) Type I solutions.

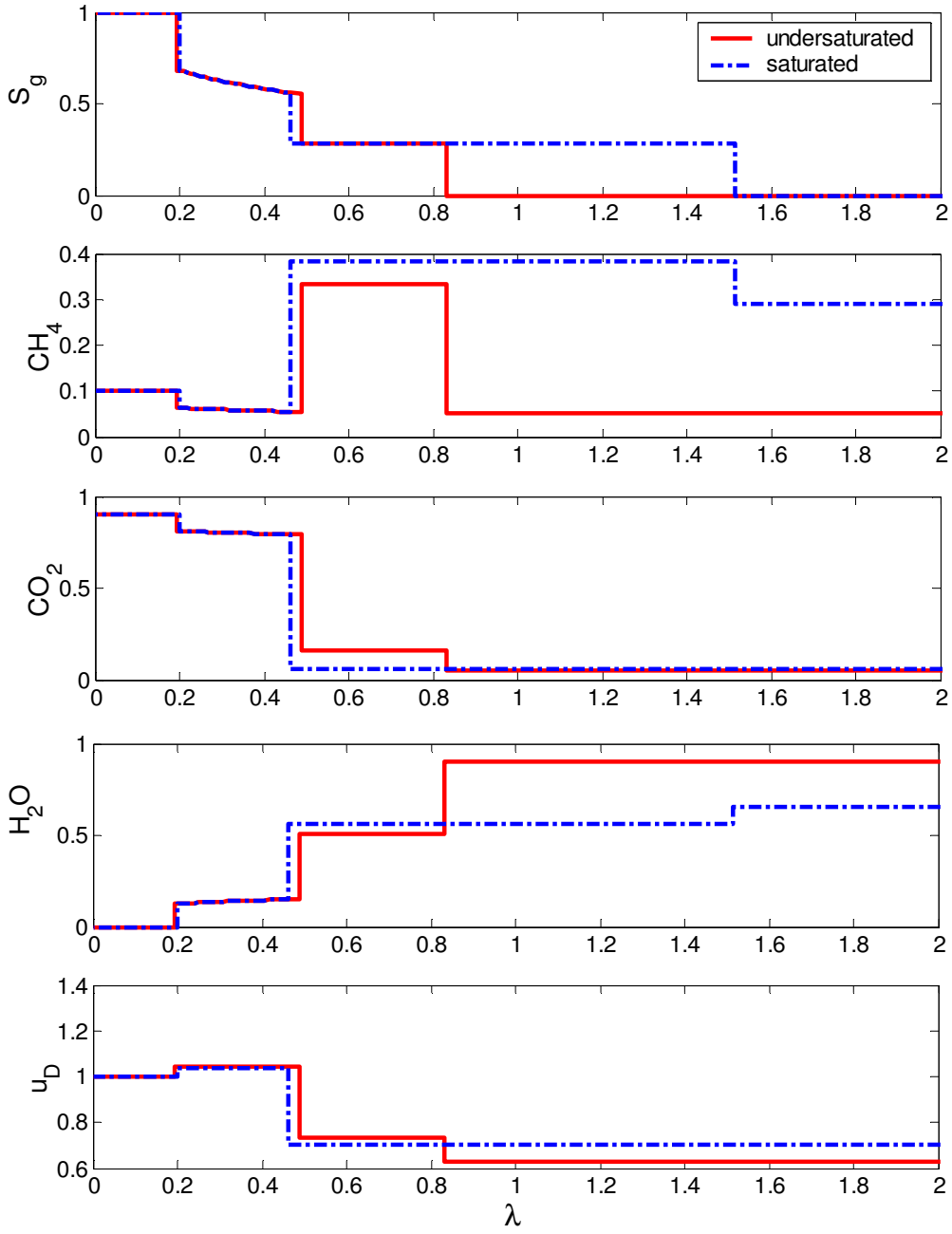

Figure 4-19: Comparison of solution profiles for saturated (blue) and undersaturated (red) Type I solutions.

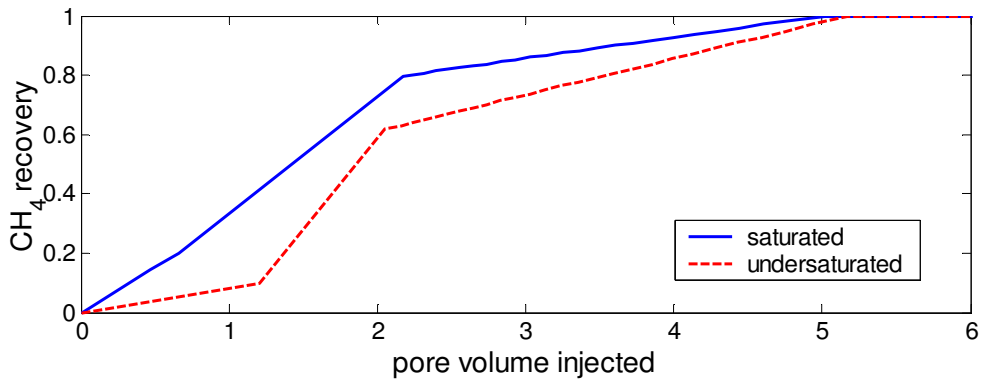

Figure 4-20: Comparison of CH_4 recovery for saturated (blue) and undersaturated (red) Type I solutions.

4.4. Summary

In this chapter, analytical solutions for binary and ternary component, two-phase flow in adsorbing systems with volume change on mixing were developed. Solution structures are strongly dependent on initial and injection compositions. Displacement of more strongly adsorbing and less volatile components by less strongly adsorbing and more volatile components occurs through a continuous variation (rarefaction). Displacement of a less strongly adsorbing and more volatile components by more strongly adsorbing and less volatile components occurs through a discontinuous variation (shock). Chromatographic separation of components based on adsorption strength and volatility occurs as compositions propagate through the coal. More volatile and less strongly adsorbing components propagate faster than less volatile and more strongly adsorbing components.

The solution construction procedure follows that of nonadsorbing systems, starting with the identification of key tie lines. When injection or initial conditions are saturated, entry into and exit from the two-phase region occurs along the tie line extension. If there are nonlinear functions in the accumulation term of the

governing equation, e.g. adsorption function, is nonlinear, entry into and exit from the two-phase region to undersaturated conditions no longer occurs along the tie line extension.

In the following section, solution construction is extended to quaternary displacements with two-phase flow, adsorption and volume change on mixing. A range of solutions is presented for conditions covering realistic injection conditions is investigated. Analytical solutions are used to investigate the effect of system parameters on solution structures. Understanding these effects provides an improved understanding of the physics of the displacement and aids in interpreting experimental results.

Chapter 5

Quaternary Solutions for Enhanced Coalbed Methane Recovery

This chapter presents analytical solutions for two-phase, four-component systems with adsorption and volume change effects. Quaternary systems are of interest because flue gases from industrial power generation activities are significant point sources of anthropogenic CO_2. In some settings, it is expensive to obtain pure CO_2 streams, and it is possible that a mixture of CO_2 and N_2 could be injected. Understanding how gas mixtures propagate during the displacement and the effect of mixed gas injection on recovery is important for design of sequestration projects that maximise recovery while minimising costs.

The eigenvalue problem for the quaternary system is formulated in Appendix A. An additional eigenvalue results with the addition of a fourth component. Eigenvalues for a typical tie line are shown in Figure 5-1. The structure of the integral curves in the system with adsorption is similar to those found in nonadsorbing systems. For each composition, there are three possible paths along

which compositions may vary: one along the tie line (tie-line path) and two between tie lines (nontie-line paths). The tie line path remains the same as in the nonadsorbing case, but now the nontie-line paths are functions of phase behaviour and the relative strength of adsorption between adsorbing components. As in the ternary system, adsorption reduces the nontie-line eigenvalues, so their values at the phase boundaries and equivelocity point are less than 1. Similar to nonadsorbing systems, there are four equal-eigenvalue points at each tie line where path switches between tie line and nontie-line path may occur. For the system shown in Figure 5-1, gas adsorption is strong enough that there is no longer an equal-eigenvalue point between the two nontie-line eigenvalues, as there is in nonadsorbing systems. The degree to which these separate is dependent on the relative adsorption strength for a given tie line. The separation between nontie-line eigenvalues is larger the greater the difference in adsorption strength. Corresponding integral curves of the eigenvectors are shown in Figure 5-2.

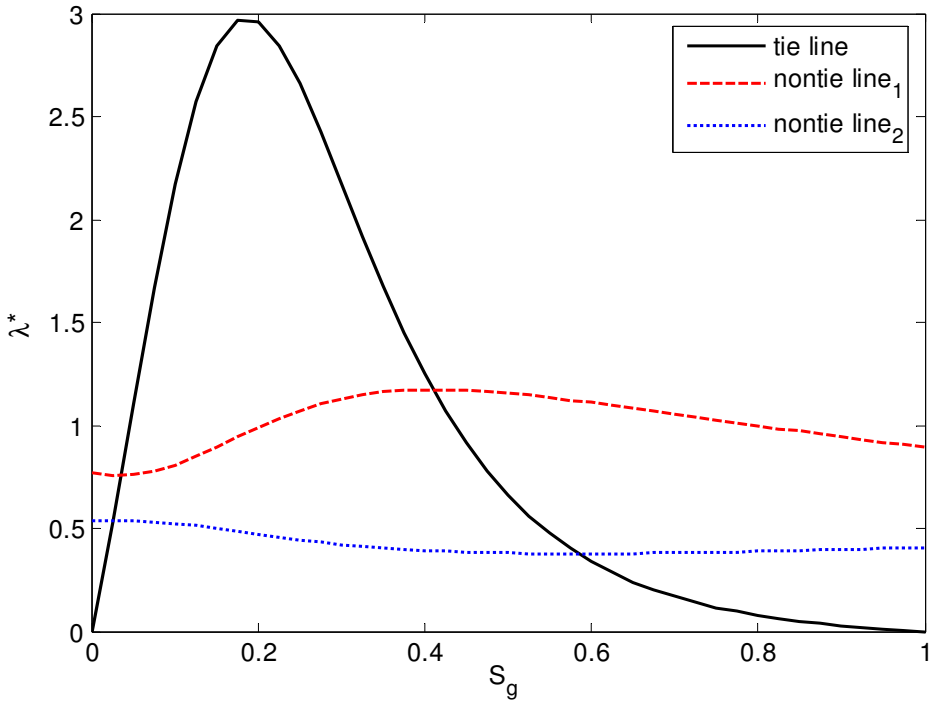

Figure 5-1: Eigenvalue variation along a tie line in a quaternary system.

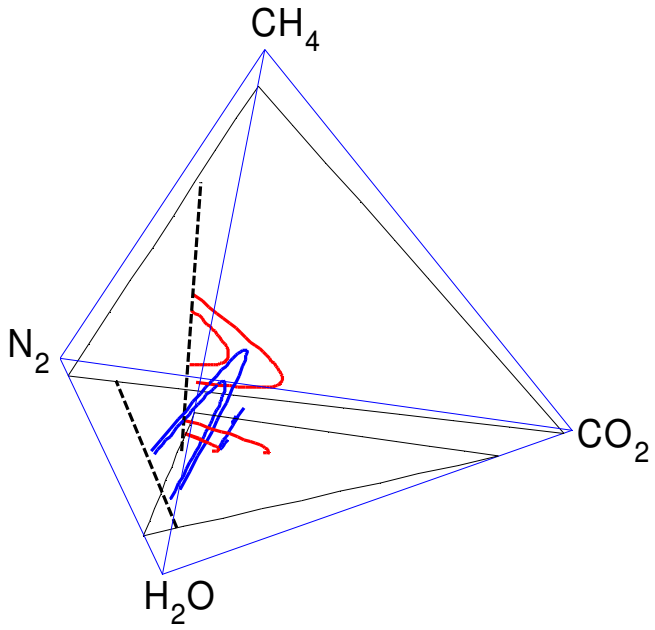

Figure 5-2: Integral curves of the eigenvectors in a quaternary system.

5.1. Solution Construction

Solution construction procedures for the quaternary systems with adsorption extend those developed for binary and ternary systems presented in Chapter 4. Quaternary solution structures are extensions of ternary systems. Resident mixtures displaced by weaker adsorbing and more volatile gases occur through a continuous variation, and resident mixtures that are displaced by stronger adsorbing and less volatile gases occur through a shock. When mixtures of gases are injected, they separate into banks ordered by relative adsorption strength and volatility. As the displacement propagates through the coalbed, stronger adsorbing gases, such as CO_2, travel slower than weaker adsorbing gases, such as N_2. The next sections delineate the solution structures encountered in quaternary composition space. A sequence of injection and initial conditions representative

of ECBM processes (pure gas injection, flue gas and acid gas injection) is considered. The analysis presented is for constant K-values and fixed mobility ratio. Model parameters are summarised in Tables 4-1 and 4-2. For each of the composition paths presented, analytical solutions were compared to finite difference solutions. 5000 gridblocks was used, with a Courant number of 0.09.

5.2. Type I: Double Shock

A fully self-sharpening solution occurs when all components in the injection gas are more strongly adsorbing than those in the initial gas. Preferential adsorption of the injected gas provides the recovery mechanism. In these systems, the injection tie line is the shortest tie line, and the initial tie line is the longest tie line. In the example solution shown in Figures 5-3 and 5-4, a mixture of 0.3 CH_4 and 0.7 CO_2 displaces an initial composition of 0.1605 N_2, 0.0391 CH_4 and 0.8004 H_2O. The numerical solution is in good agreement with the analytical solution. Because the initial composition is located on the phase boundary, entry into the two phase region from the initial composition occurs along a tie-line extension. Although CH_4 injection is unrealistic in a practical setting, such a displacement illustrates what would happen in a sour gas injection scheme (CO_2 and H_2S mixtures).

Solution construction starts at the injection tie line. Entry into the two-phase region from the injection composition, I, occurs via a shock. A rarefaction along the injection tie line occurs from D to C. At point C, a semishock connects the injection and crossover tie lines. At the crossover tie line, the strongest adsorbing component is removed from the mobile phase and a ternary composition remains. This shock velocity is faster than the semishock construction connecting the crossover and initial tie lines. Therefore, a genuine shock from the landing point on the crossover tie line, B, to the landing point on the initial tie line, A, connects crossover and initial tie lines. These wave velocities are connected by a zone of constant state. The landing point on the initial tie line, A, is faster than the landing point of a tangent phase change shock from the initial composition to the two

phase region. Another genuine shock is required to complete the composition path. Parameters of key points in the displacement are summarised in Table 5-1.

Table 5-1: Summary of key points in Type I quaternary displacement.

component label	component (mol fraction)				S_g	local flow velocity	wave velocity (λ)
	N_2	CH_4	CO_2	H_2O			
I	0.0	0.3	0.7	0.0	1.0	1.0	0.0-0.2077
D	0.0	0.1865	0.6314	0.1821	0.6709	1.0416	0.2077
C	0.0	0.1666	0.6191	0.2144	0.5686	1.0416	0.4370
B	0.0	0.4312	0.0	0.5688	0.3259	0.7642	0.5804
A	0.2407	0.0489	0.0	0.7104	0.2219	0.5806	1.1736
O	0.1605	0.0391	0.0	0.8004	0.0	0.5806	1.1736

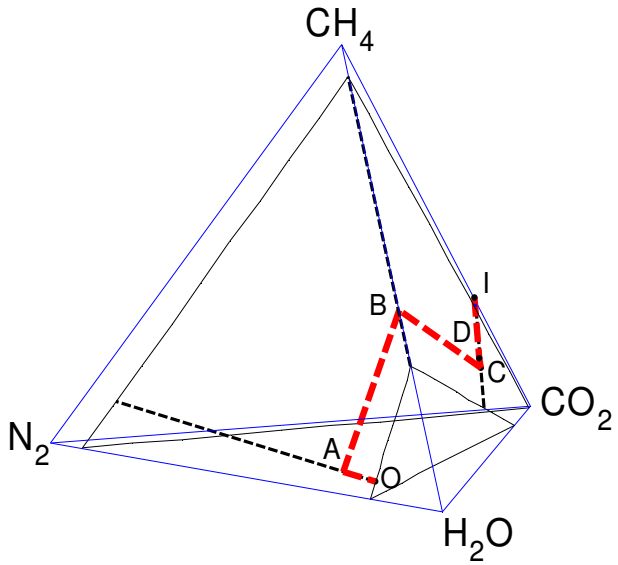

Figure 5-3: Composition path for Type I quaternary displacement.

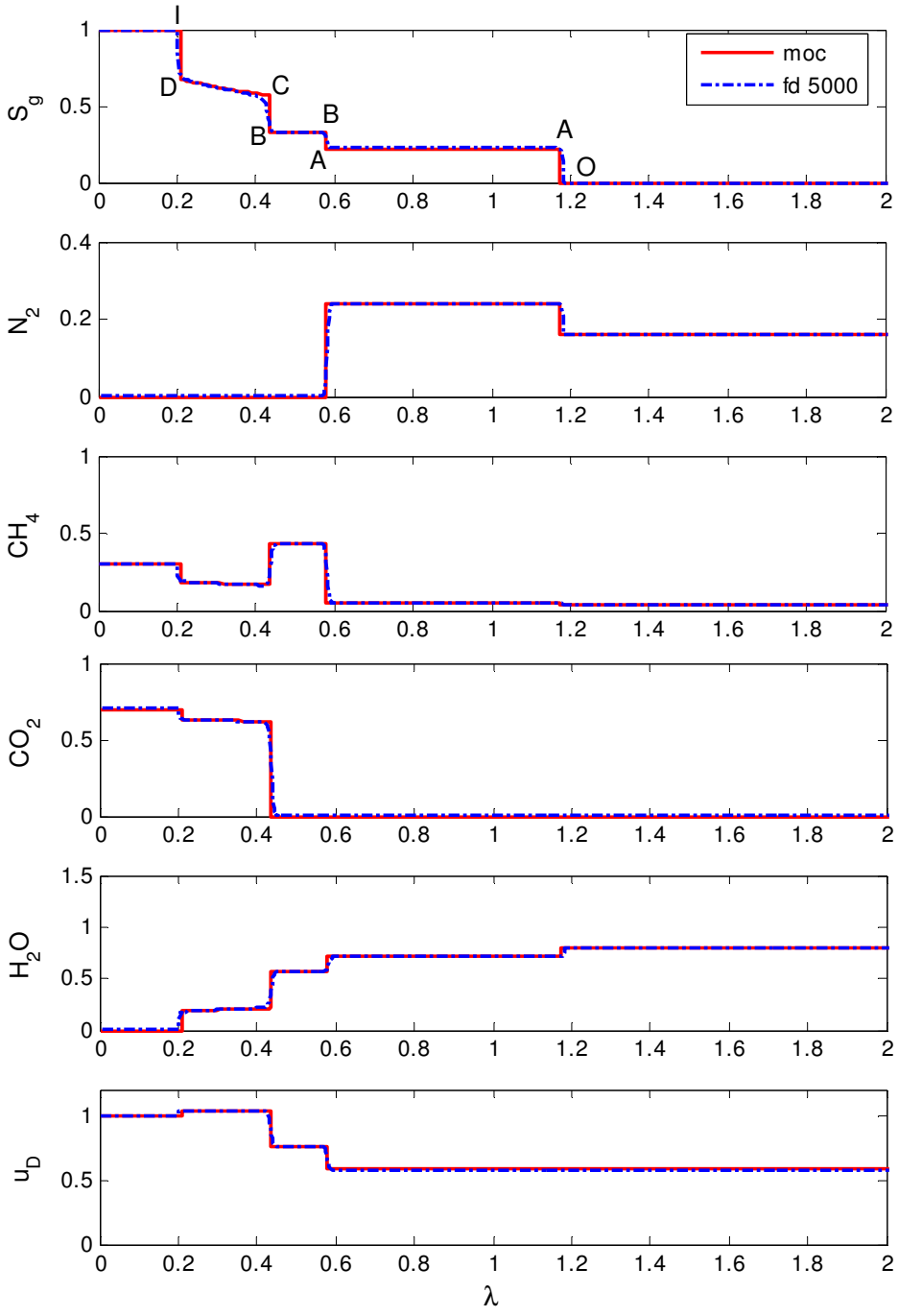

Figure 5-4: Solution profile for Type I quaternary displacement. The numerical solution is in good agreement with the analytical solution.

At each shock, one component is removed from the displacement. This fully self-sharpening displacement results in distinct banks of gas species propagating through the coal ordered according to relative adsorption strength and volatility, with more strongly adsorbing and less volatile gases propagating slower than weaker adsorbing and more volatile gases. The combined effects of preferential adsorption and differences in solubility result in natural separation of gas species as they propagate through the coalbed. Injected gases are preferentially adsorbed at a higher replacement ratio than the initial gas, resulting in a net removal of gas molecules from the mobile phase. At each shock, the local flow velocity is significantly reduced, resulting in a retardation of the overall displacement.

5.3. Type II: Double Rarefaction

Double rarefaction solutions occur when the injection components are less strongly adsorbing than the initial gas composition. Displacement of initial gas occurs through partial pressure reduction. This composition path is analogous to the Type II displacement in the ternary system. In these systems, the initial tie line is the shortest tie line and the injection tie line is the longest. To illustrate this example, pure N_2 is injected into a coalbed saturated with 0.1939 CH_4, 0.3070 CO_2 and 0.4991 H_2O. Initial compositions are located on the phase boundary. Solution profiles and composition path are shown in Figures 5-5 and 5-6. The numerical solution is in good agreement with the analytical solution. Key points of the displacement are summarised in Table 5-2.

Table 5-2: Summary of key points in Type II quaternary displacement.

component label	component (mol fraction)				S_g	local flow velocity	wave velocity (λ)
	N_2	CH_4	CO_2	H_2O			
I	1.0	0.0	0.0	0.0	1.0	1.0	0.0-0.2209
D	0.6505	0.0	0.0	0.3487	0.7778	1.0406	0.2209-0.3603
C	0.4077	0.0	0.2470	0.3449	0.6797	1.2293	0.5743-0.8829
B	0.0	0.2931	0.3226	0.3843	0.4072	1.6979	2.0300
A	0.0	0.2628	0.3178	0.4194	0.3015	1.6979	3.6645
O	0	0.1939	0.3069	0.4991	0.0	1.6979	3.6645

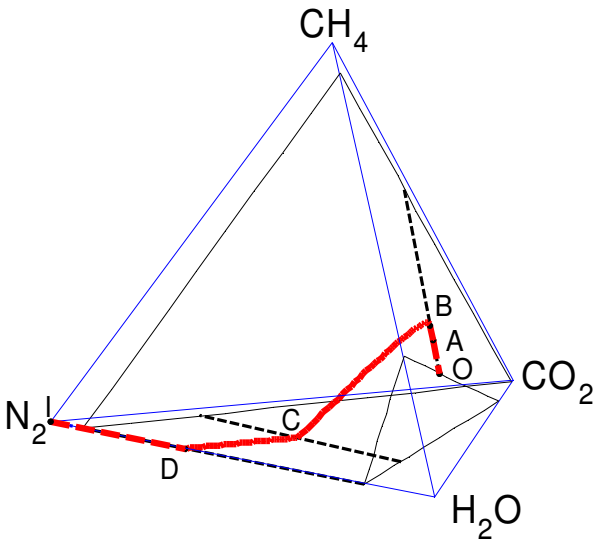

Figure 5-5: Composition path for Type II quaternary displacement.

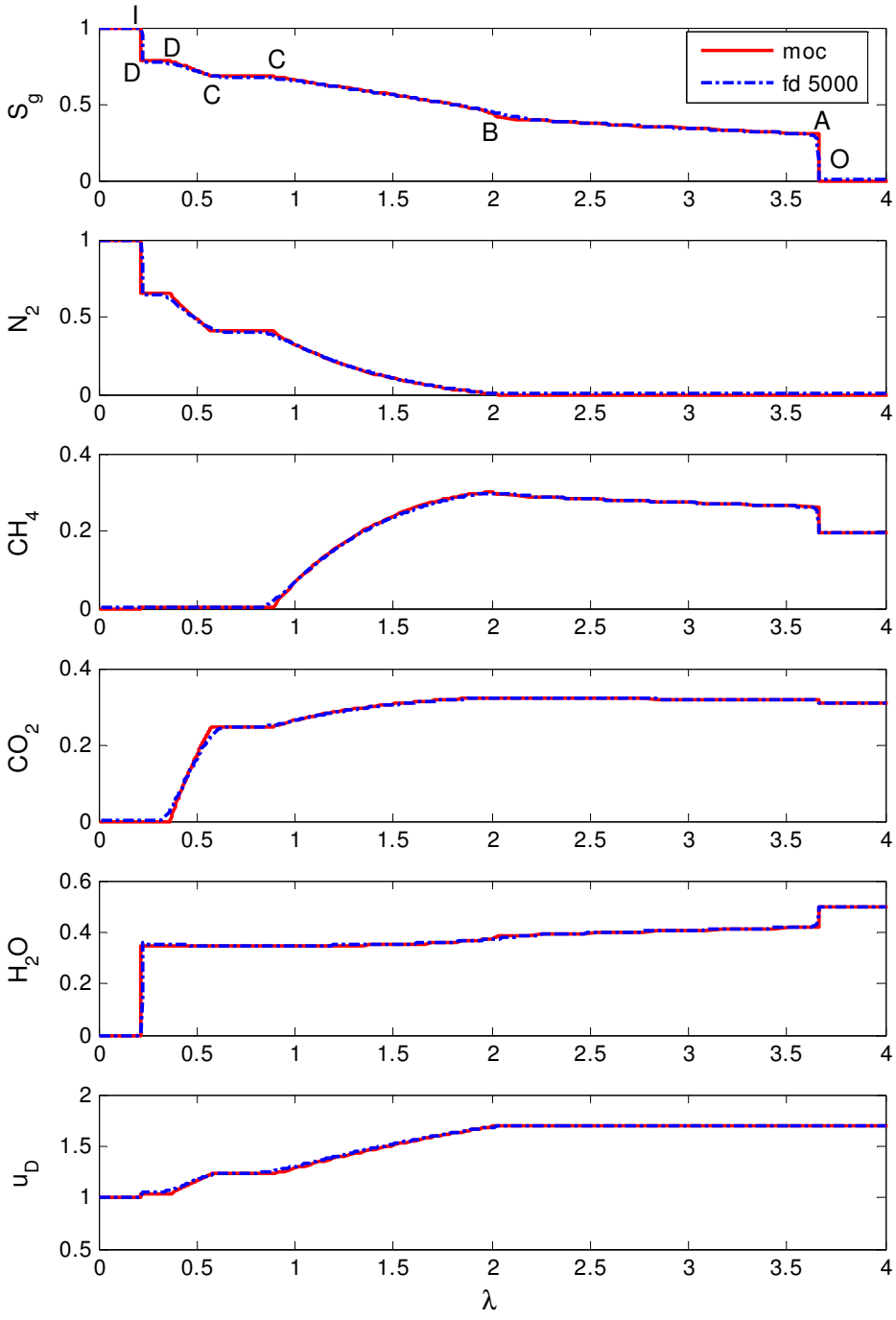

Figure 5-6: Solution profile for Type II quaternary displacement. The numerical solution agrees well with the analytical solution.

Construction begins with a phase change shock from the initial composition, O, to a point on the initial tie line, A. This is followed by a continuous variation along the initial tie line to the equal-eigenvalue point, B. At the equal-eigenvalue point, there is a switch from the tie-line path to the nontie-line path. The nontie-line variation connects the initial tie line to the crossover tie line. At point C, there is a switch from the nontie-line path from the initial segment to the nontie-line path of the injection segment. These states are connected through a zone of constant state. For these injection and initial conditions, there is an immediate switch between nontie-line paths. For other injection and initial conditions, a tie-line variation to the equal-eigenvalue point connecting the injection segment is required to complete the solution.

From C to D, a nontie-line variation connects the crossover tie line to the injection tie line. The landing point on the injection tie line, D, is slower than the tangent point of the phase change shock from injection composition into two-phase region, and a genuine shock out to injection composition, from D to I, completes the solution.

As N_2 propagates through the system, gas desorbs from the coal surface, adding volume to the flowing gas. Local flow velocity increases as the displacement proceeds, resulting in a fast production response from N_2 injection. CO_2 is the most strongly adsorbing gas and travels through the coal the slowest. It is the last component to be completely recovered from the coalbed. The injection gas travels quickly through the coalbed contaminating the resident gas produced. A final separation stage prior to sales is required.

5.4. Type III: Mixed Structures

In the solutions presented in this section, the injection gas composition is more strongly adsorbing than the intermediate gas composition, and the intermediate gas composition is less strongly adsorbing than the initial gas composition. The crossover tie line is the longest tie line. The solutions show a combination of Type I and Type II structures.

5.4.1. Type III-A

To illustrate this composition path, a mixture of 0.9 N_2 and 0.1 CO_2 was injected into a coalbed with initial conditions of 0.3103 CH_4 and 0.6987 H_2O. Composition path and solution profiles for this example are shown in Figures 5-7 and 5-8. The numerical solution is in good agreement with the analytical solution. Table 5-3 summarises key points in this displacement.

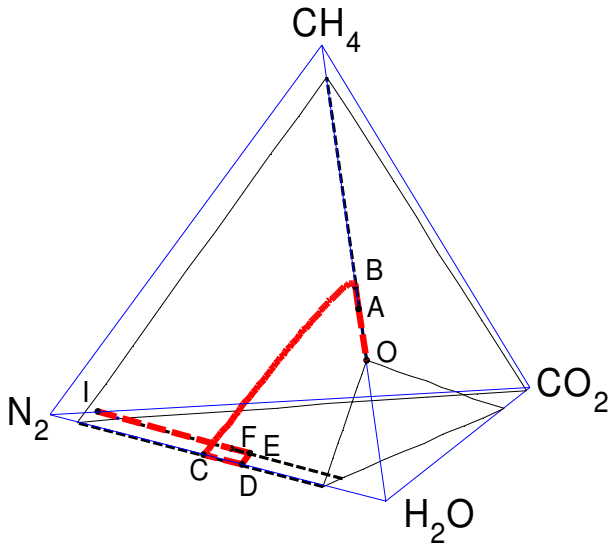

Figure 5-7: Composition path of Type III-A displacement.

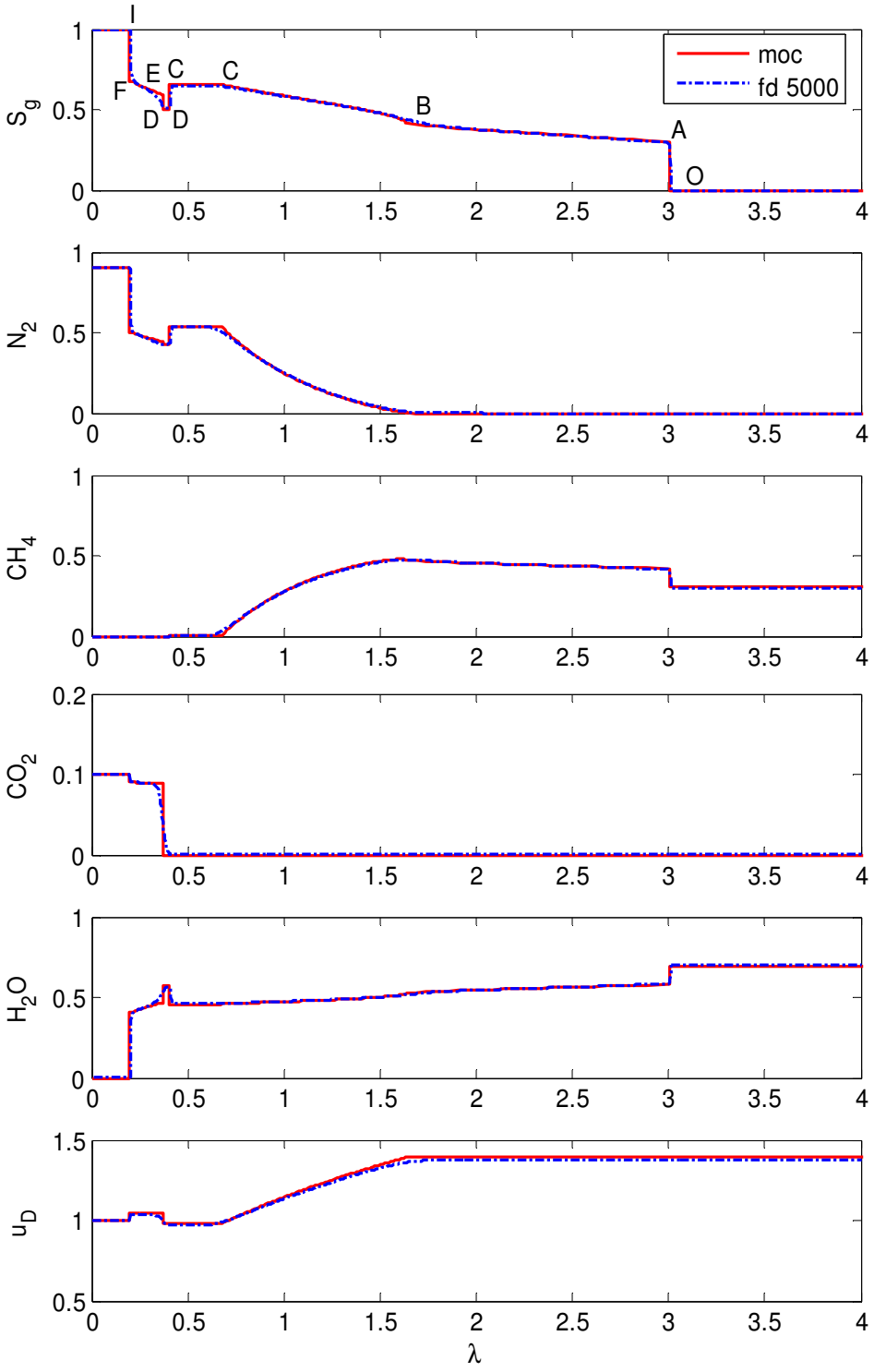

Figure 5-8: Solution profile of Type III-A displacement. The numerical solution agrees well with the analytical solution.

Table 5-3: Summary of key points in Type III-A displacement.

component label	component (mol fraction)				S_g	local flow velocity	wave velocity (λ)
	N_2	CH_4	CO_2	H_2O			
I	0.9	0.0	0.1	0.0	1.0	1.0	0.0-0.1995
F	0.5034	0.0	0.0902	0.4063	0.6767	1.0429	0.1995
E	0.4445	0.0	0.0887	0.4668	0.5938	1.0429	0.3694
D	0.4274	0.0	0.0	0.5725	0.4984	0.9821	0.3694-0.4045
C	0.5411	0.0	0.0	0.4585	0.6549	0.9821	0.4045-0.6747
B	0.0	0.4704	0.0	0.5296	0.4099	1.3930	1.6373
A	0.0	0.4205	0.0	0.5795	0.3015	1.3930	3.0065
O	0.0	0.3103	0.0	0.6897	0.0	1.3930	3.0065

In this system, the crossover tie line coincides with the N_2-H_2O axis. Because the crossover tie line is the longest key tie line, injection and initial segments to the crossover tie line are constructed independently. Injection solution starts with a tangent shock into the two phase region, I to F, followed by continuous variation along the injection tie line to E. Eigenvalues increase as the composition varies from the injection tie line to the crossover tie line, and therefore a shock is necessary to connect these tie lines, E to D. The initial segment starts with a tangent shock from the initial conditions into the two phase region, O to A. This is followed by a rarefaction along the initial tie line to the equal-eigenvalue point, B. At the equal-eigenvalue point, a path switch from the tie-line path to the nontie-line path occurs. Continuous variation along the nontie-line path connects the initial and crossover tie lines, B to C. At the crossover tie line, landing points of these segments, C and D, are connected by a genuine shock. A continuous variation between these two points would violate the velocity rule because the velocity decreases as the composition is traced from upstream, D, to downstream, C (Figure 5-9). This solution structure is similar to the $CH_4/C_4/C_{10}$

displacement by a mixture of N_2 and C_4H_{10} presented by Dindoruk (1992) for a displacement without adsorption.

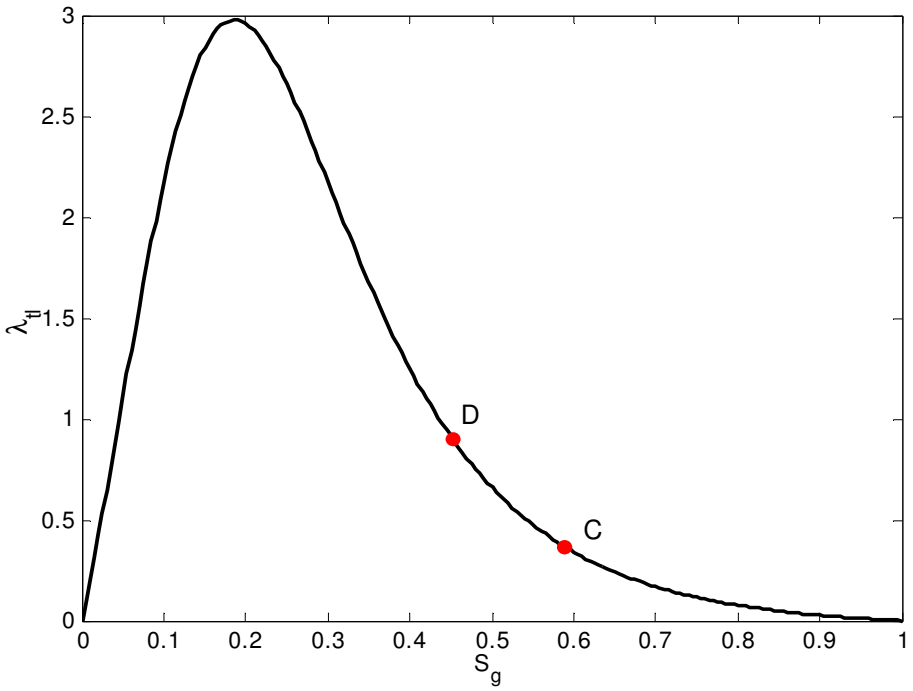

Figure 5-9: Variation along the crossover tie line from D to C violates the velocity rule.

At the leading edge of the displacement, there is a bank of two-phase flow of CH_4 and water. Upstream of this zone is a region in which N_2, CH_4, and water flow simultaneously, B to C, but CO_2 is absent. Gas mixtures from this region of the displacement would require separation before the CH_4 could be sold. All of the CH_4 present initially upstream of point C moves in these leading banks. In the zone of constant state, C, only water and N_2 are flowing at constant saturation. CO_2 is the most strongly adsorbing component, and it is also the most soluble in the aqueous phase, and hence it appears only upstream of the shock from D to E. The self-sharpening nature of CO_2 adsorption removes all the CO_2 from the mobile phase at the shock from D to E. Upstream of this shock the fractions of N_2

and CO_2 increase, reaching the injection composition at the very slow-moving trailing shock from F to I. Removal of CO_2 creates a small intermediate bank of water, D. Because N_2 is the least adsorbing gas, and the most volatile component, it propagates quickly through the system creating a bank of gas, B to C, that flows simultaneously with water. As N_2 propagates through the coal, the partial pressure of CH_4 is reduced, causing CH_4 desorption. A mixture of N_2 and CH_4 is produced at the outlet until CO_2 breakthrough occurs. Separation of the CO_2 in the injection gas mixture is achieved, but at the expense of contamination of the produced CH_4 with N_2.

5.4.2. Type III-B

As the CO_2 concentration in the injection gas is increased, a greater proportion of the vapour phase flowing upstream of the shock connecting the injection and crossover tie lines is removed. Figure 5-10 shows that the velocity of the genuine shock along the crossover tie line increases as CO_2 concentration in the injection gas increases. For high concentrations of CO_2, the velocity of the genuine shock will be faster than the landing point of the nontie-line path, as shown in Figure 5-11. This results in a multivalued region. Such a composition route violates the velocity rule. Therefore, a new path structure to connect injection and initial segments is required.

The velocity of the genuine shock connecting initial and injection composition paths is represented by the line segment connecting C and D. The landing point of the initial nontie-line path on the crossover tie line, C, remains unchanged as injection gas composition is manipulated. As the landing point of the injection segment on the fractional flow curve of the crossover tie line decreases, the slope of the CD line segment increases. Point P (Eq. 4-20) is the analogue of the intersection of the tie-line extension with the envelope curve in nonadsorbing systems from Dindoruk (1992), Eq. B-1. Presence of adsorption shifts P off the diagonal. The slope of the line segment from P to C represents the

nontie-line eigenvalue of the landing point of the initial path on the crossover tie line. The velocity rule is violated once the slope of the CD line segment exceeds the slope of the PC line segment.

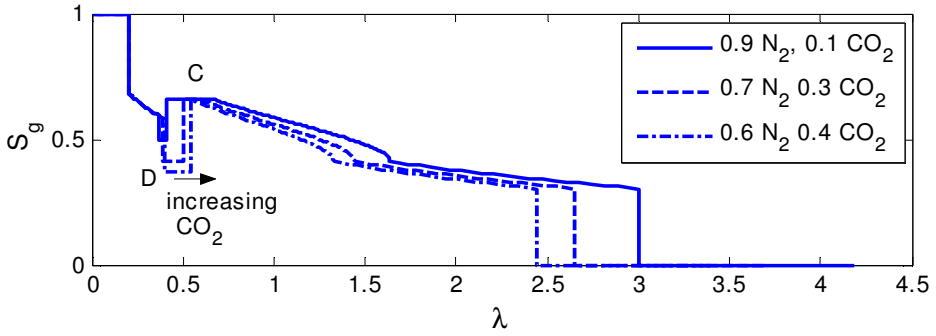

Figure 5-10: Genuine shock velocity increases are CO_2 concentration in the injection gas increases.

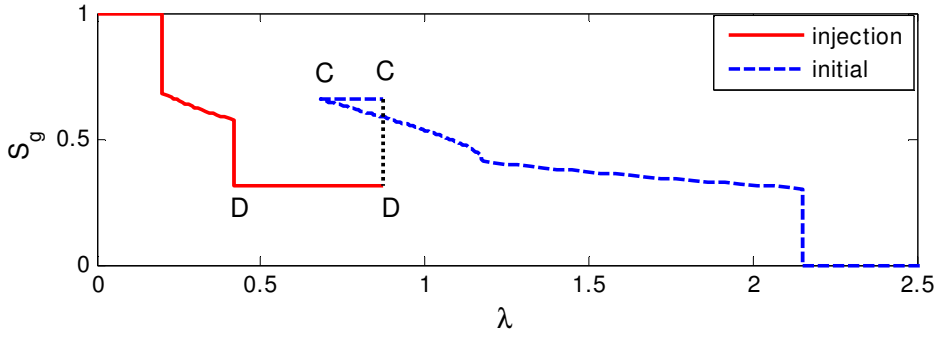

Figure 5-11: Genuine shock along the crossover tie line violates the velocity rule for high concentrations of CO_2 in the injection gas.

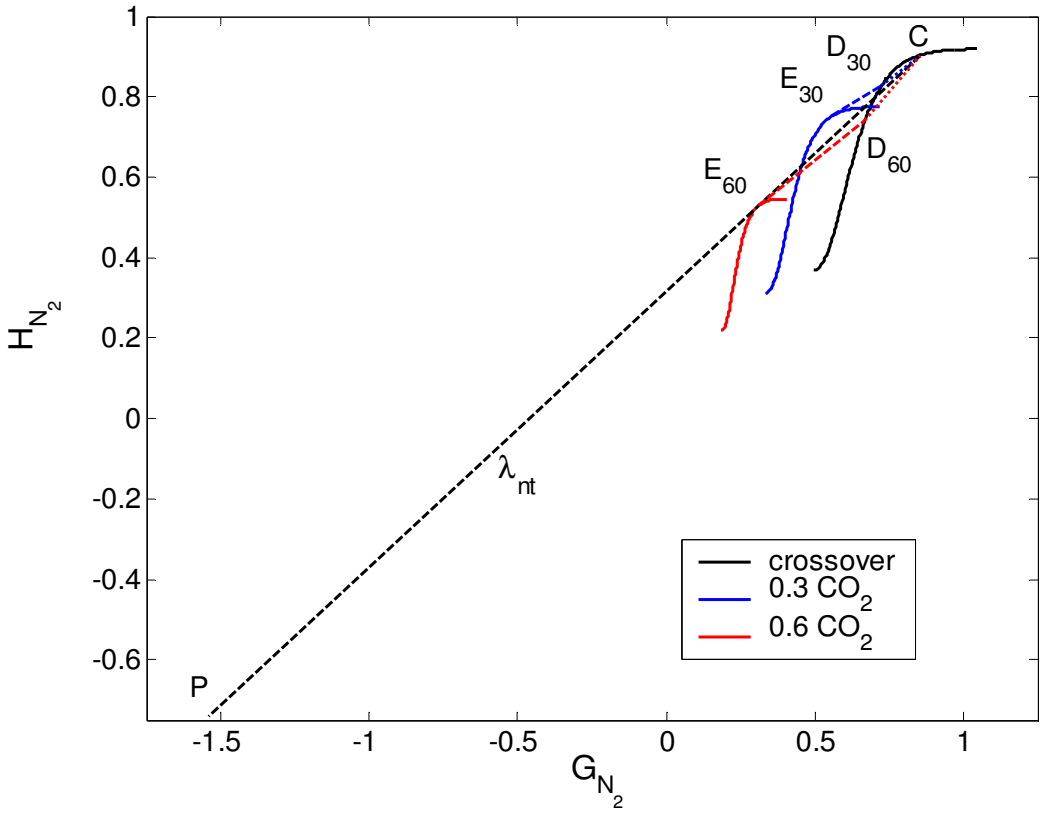

Figure 5-12: Fractional flow construction for the velocity rule violation by the genuine shock for increasing CO_2 concentration in the injection gas.

To illustrate this new structure, a mixture of 0.4 N_2 and 0.6 CO_2 is injected into a coalbed saturated with 0.3103 CH_4 and 0.6987 H_2O. The initial condition is located on the phase boundary. As in the Type III-A construction procedure, injection and initial segments are constructed independently. Composition path and solution profiles are shown in Figures 5-13 and 5-14. The numerical solution is in good agreement with the analytical solution. Starting from the injection segment, a phase change shock from the injection composition, I, to the two-phase region is required. This is followed by a rarefaction along the injection tie line to point F. At F, a semishock connects the injection tie line with the crossover tie line. Figure 5-15 shows the location of the Hugoniot locus that satisfies the material balance with the landing point on the crossover tie line, D, relative to the

location of the nontie-line path traced from the initial tie line, B. The Hugoniot locus from D does not intersect the initial tie line. Therefore, a shock directly from point D to a location on the nontie-line path does not satisfy the material balance.

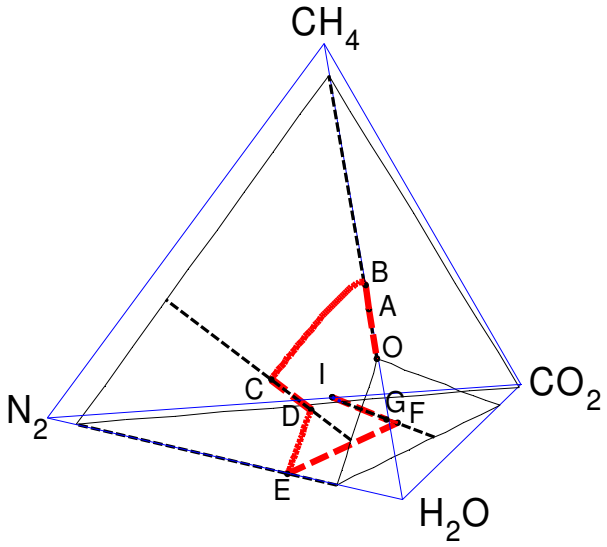

Figure 5-13: Composition path for Type III-B displacement.

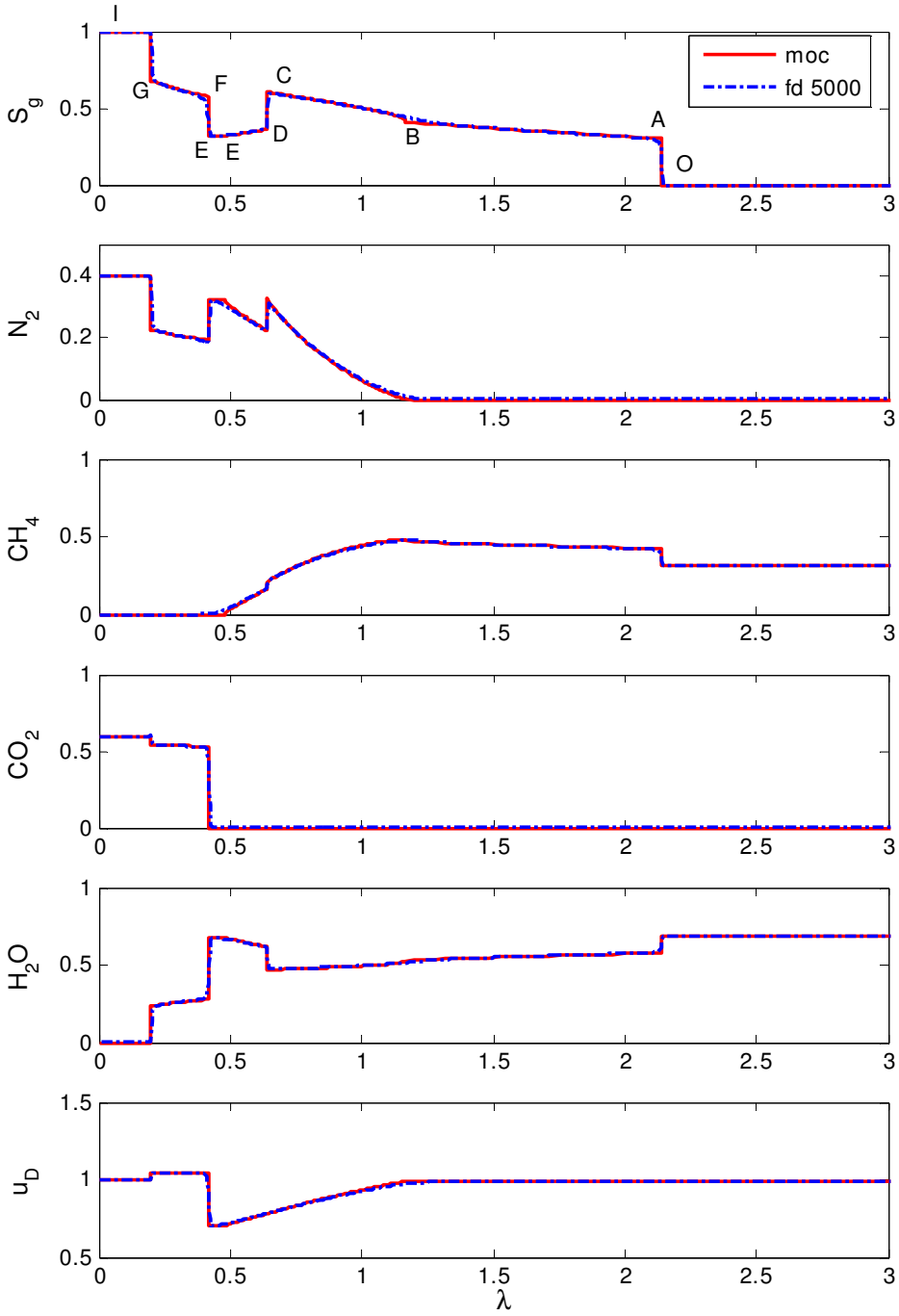

Figure 5-14: Solution profiles for Type III-B displacement. The numerical solution converges to the analytical solution.

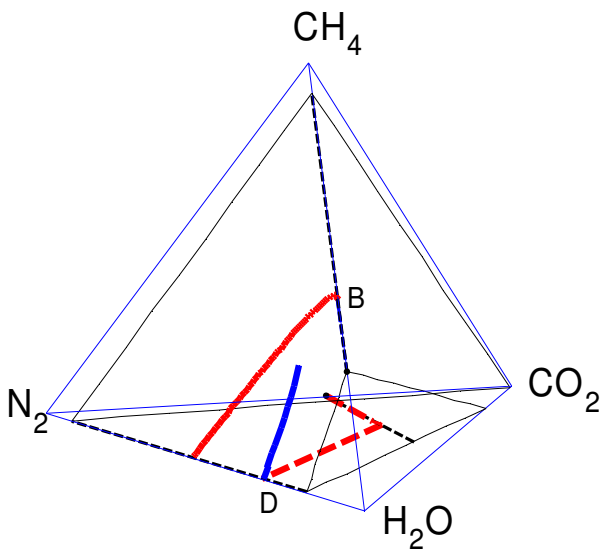

Figure 5-15: Location of the Hugoniot locus traced from D (blue) relative to the initial nontie-line path (red). A shock from D to a location on the initial tie line does not satisfy the material balance.

At the landing point on the crossover tie line of the injection segment, E, the path switches to the nontie-line path. The nontie-line path traced from the injection segment is nested in the nontie-line path of the initial segment (Figure 5-16). As the eigenvalues are traced along the nontie-line path from D, they increase up toward the equal-eigenvalue point, obeying the velocity rule. Past the equal-eigenvalue point, the nontie-line eigenvalue decreases, violating the velocity rule. This nonmonotonic variation is shown in Figure 5-17. For gas saturations less than the equal-eigenvalue point, $\frac{\partial \lambda_{nt}}{\partial S} > 0$. For gas saturations greater than the equal-eigenvalue point, $\frac{\partial \lambda_{nt}}{\partial S} < 0$. Eigenvalues increase from upstream to downstream conditions; therefore, both branches are allowable paths. However, direct, continuous variation along the nontie-line path to connect the two nontie-line paths is not possible. A shock is required to complete the composition path.

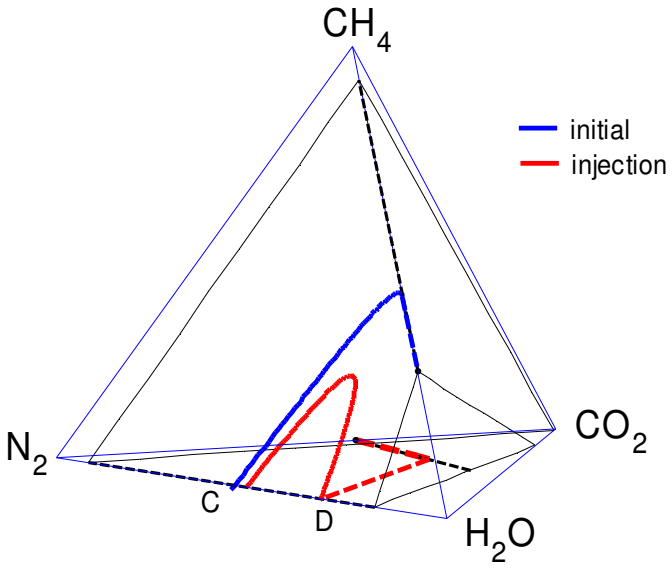

Figure 5-16: Nontie-line path of injection segment is nested in the nontie-line path of the initial segment.

As the nontie-line paths are traced, the eigenvalues vary in such a way that there exists a tie line where both the initial and injection nontie-line eigenvalue normalised by the local flow velocity are equal. This variation is shown in Figure 5-18. At this tie line, a path switch between injection and initial segments from nontie-line path to tie-line path is allowable for injection and initial segments. Continuous variation connecting along the tie line violates the velocity rule (Figure 5-19); therefore, a shock is from C to D is required. For this shock to remain stable throughout the displacement, its velocity must be the same velocity as the nontie-line eigenvalues at this tie line. This type of shock where the velocity immediately upstream of the shock and the velocity immediately downstream of the shock are equal to the shock velocity is classified as a degenerate shock (Jeffrey, 1976). The tie line along which the degenerate shock occurs is called the degenerate tie line. Because this shock is along a tie line, the local flow velocity of the injection eigenvalue is equal to the local flow velocity of the initial

eigenvalue at the degenerate tie line. Similar to the nonadsorbing case (Dumore *et al.*, 1984), a proof that the local flow velocity is constant along a tie line in systems with adsorption is presented in Appendix A.

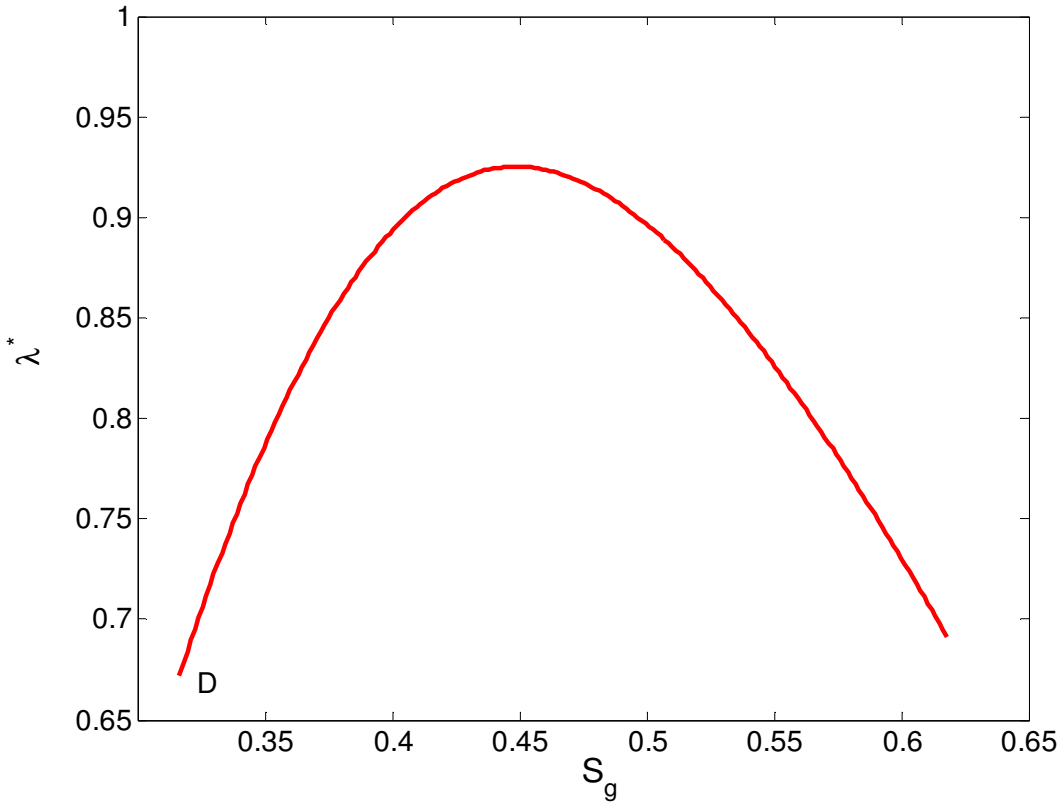

Figure 5-17: Variation of eigenvalues along the nontie-line path traced from D. Eigenvalues vary nonmonotonically along the nontie-line path.

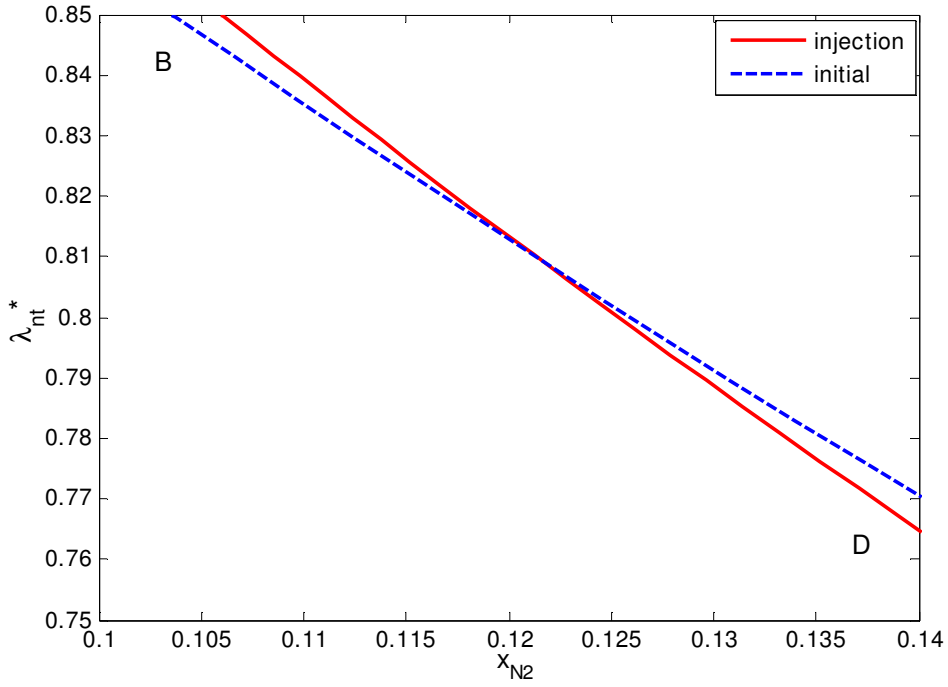

Figure 5-18: Variation of normalized eigenvalues along nontie-line paths.

Figure 5-20 shows potential tie lines connecting injection and initial segments along the $N_2/CH_4/H_2O$ face. If a shock at along a tie line longer than the tie line on which the degenerate shock occurs is considered, the shock velocity for tie lines longer than the degenerate tie line (e-f) is faster than the nontie-line eigenvalue on the initial segment, creating a multivalued region on the initial segment. As tie lines higher up on the $N_2/CH_4/H_2O$ face are selected for the switch between injection to initial nontie-line paths, the degenerate shock velocity decreases. For tie lines shorter than the degenerate tie line (a-b), the shock velocity is slower than the injection segment. A degenerate shock along this tie line also creates a multivalued region on the injection segment. Therefore, the only allowable tie line connecting initial and injection segments is the one where initial and injection nontie-line eigenvalues and the tie line shock velocity are equal (c-d).

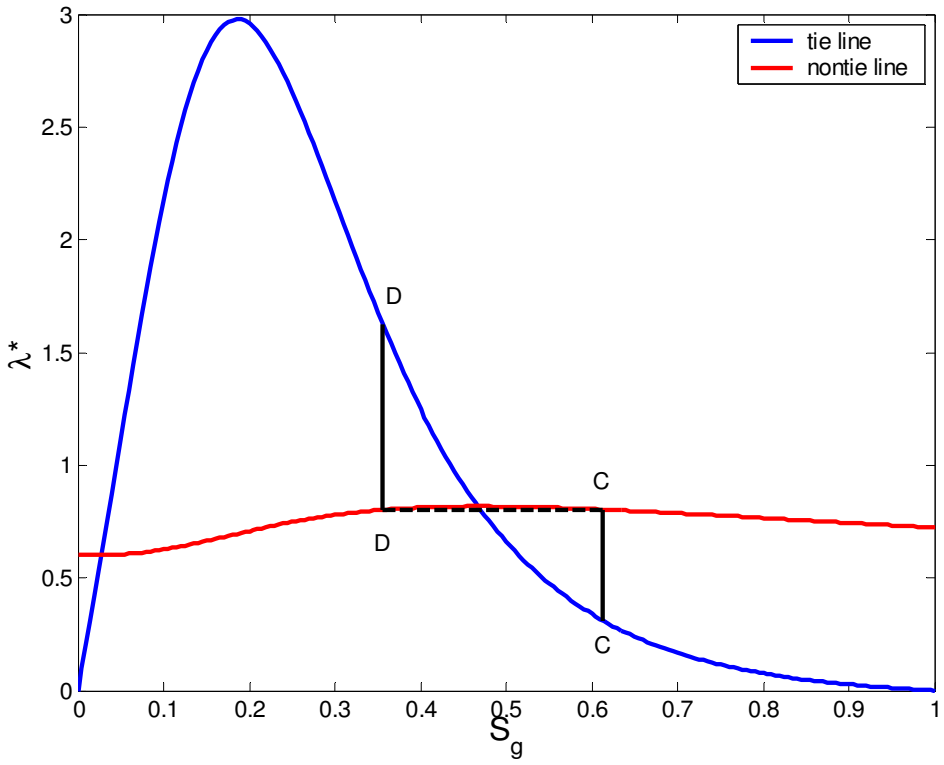

Figure 5-19: Path switch from nontie-line path to tie line path at the degenerate tie line obeys the velocity rule. The continuous variation from injection switch point (D) to initial switch point (C) violates the velocity rule.

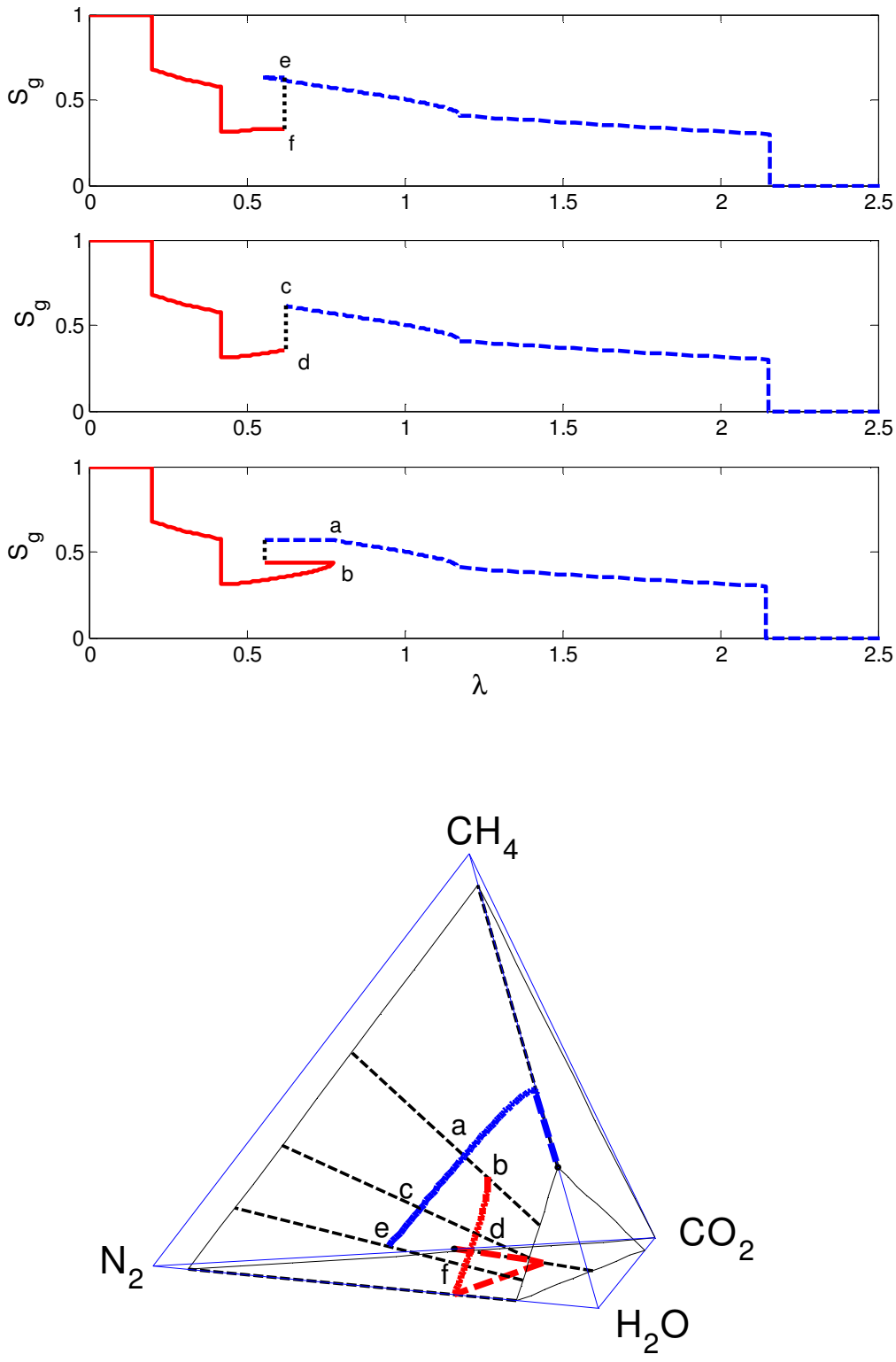

Figure 5-20: Analysis of tie line shocks connecting injection and initial nontie-line paths.

Continuing with the remaining elements of solution construction (Figures 5-13 and 5-14), a path switch to the nontie-line path occurs at point C. Because the shock velocity and eigenvalues immediately upstream and downstream of the shock are all equal, there is no zone of constant state connecting discontinuous and continuous variation. The nontie-line path is traced up to the initial tie line, B. At the equal-eigenvalue point, B, there is a path switch from the nontie-line path to the tie-line path. This is followed by a rarefaction along the initial tie line to A. A tangent shock from A to the initial conditions, O, completes the composition path. Key points of this displacement are summarised in Table 5-4.

Table 5-4: Summary of key points in Type III-B displacement.

component label	component (mol fraction)				S_g	local flow velocity	wave velocity (λ)
	N_2	CH_4	CO_2	H_2O			
I	0.4	0.0	0.6	0.0	1.0	1.0	0.0-0.1994
G	0.2237	0.0	0.5411	0.2351	0.6767	1.0420	0.1994
F	0.1919	0.0	0.5305	0.5746	0.5746	1.0420	0.4199
E	0.3217	0.0	0.0	0.6783	0.3164	0.7017	0.4199-0.4617
D	0.2321	0.1432	0.0	0.6246	0.3554	0.7748	0.6215
C	0.3442	0.1883	0.0	0.4674	0.6124	0.7748	0.6215
B	0.0	0.4704	0.0	0.5296	0.4099	0.9970	1.1719
A	0.0	0.4205	0.0	0.5795	0.3015	0.9970	2.1519
O	0.0	0.3103	0.0	0.6897	0.0	0.9970	2.1519

Figure 5-21 shows the location of key points of the displacement on the relative permeability curve. After CO_2 is adsorbed and removed from the flowing phase, E, gas is no longer the most mobile phase. The nontie-line variation from E to D corresponds to desorption of CH_4 from the coal by N_2, resulting in an increase in gas saturation. The degenerate shock from D to C corresponds to situation where gas switches from the least mobile phase to the most mobile phase.

In this displacement, a larger fraction of the injection gas is removed from the mobile phase when CO_2 is adsorbed. Comparison of Type III-A and Type III-B solutions indicates that there is less N_2 available for desorption of CH_4. The lower N_2 concentration in the Type III-B displacement leads to a smaller intermediate N_2-H_2O bank. The interplay of CH_4 desorption and preferential flow of the aqueous phase creates a secondary bank of N_2, from D to E. As in the Type III-A solution, differential adsorption strength separates the injection gas into a fast moving bank of N_2 followed by a slow moving bank of CO_2. A significant reduction in flow velocity results as CO_2 is adsorbed onto the coal. This reduction is offset by the volume increase associated with desorption of CH_4 downstream for the adsorption parameters used in this analysis.

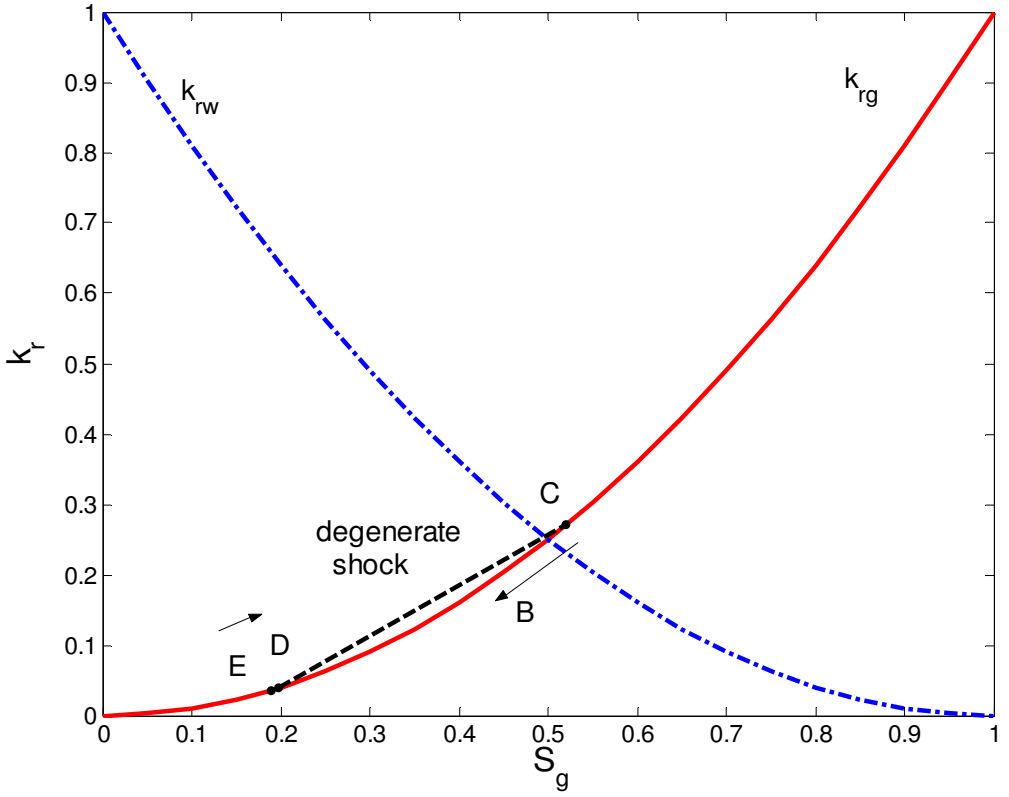

Figure 5-21: Location of key points of the degenerate shock on the relative permeability curve.

The Type III-B solution differs from those reported previously for two-phase four-component displacements in that this solution involves than N_c key tie lines, instead of N_c-*1* identified by a series of investigators of gas-oil displacements. This composition path utilises continuous variation along the $\frac{\partial \lambda_{nt}}{\partial S} > 0$ branch of the nontie-line path, also previously unobserved by earlier researchers. These new key tie lines may also exist in the absence of adsorption when the injection gas is a mixture of the most volatile component and least volatile intermediate component. Appendix B contains an analysis of the analogous composition path for systems without adsorption.

5.4.3. Type III-C

As CO_2 concentration is further increased in the injection gas, the velocity of the semishock connecting injection and crossover tie lines increases, while the nontie-line eigenvalue at the landing point decreases (Figure 5-22). Eventually the wave velocity of the nontie-line eigenvalue on the crossover tie line will be slower than the shock velocity, C-D, violating the velocity rule (Figure 5-23). This violation of the velocity rule is due to the large decrease in flowing volume as CO_2 is adsorbed. When the normalised eigenvalue (Eq. 4-14) is used to plot the saturation profile, the multivalued region on the zone of constant state, E, disappears.

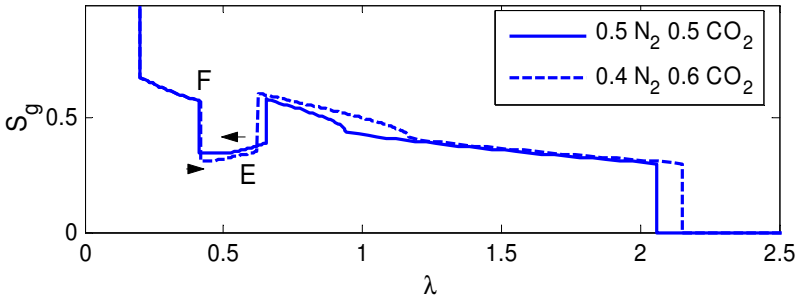

Figure 5-22: Change in shock velocity for increasing CO_2 concentrations.

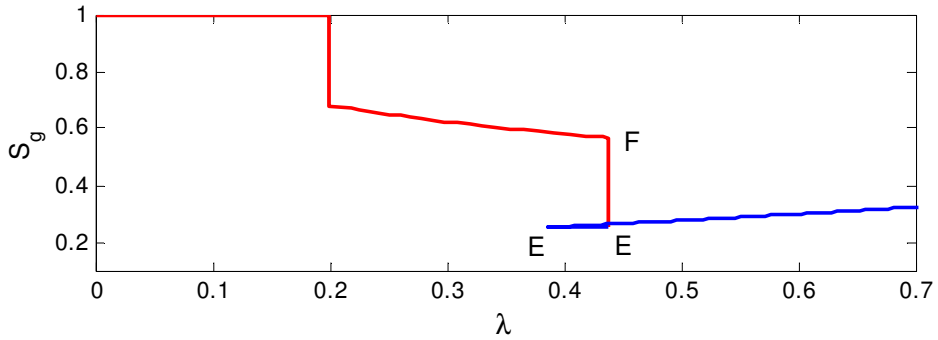

Figure 5-23: Semishock velocity is greater than the nontie-line eigenvalue on the crossover tie line, violating the velocity rule.

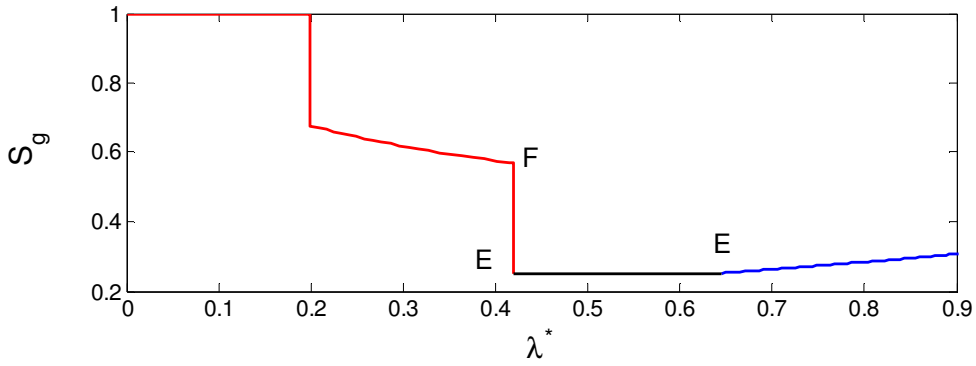

Figure 5-24: The velocity rule violation of the path switch at E disappears if changes in local flow velocity are not considered. The Type III-C structure is unique to systems where significant volume change effects due to mass transfer between liquid and gas phases are considered.

The changes in shock velocity as a function of injection tie line are illustrated in Figure 5-25. The slope of the line segment J to L, where J is the jump point from the injection tie line and L is the landing point on the crossover tie line, represents the velocity of the tangent shock connecting the injection tie line and the crossover tie line. As the injection tie line shortens and becomes more rich in CO_2, a greater proportion of gas is adsorbed and removed from the mobile phase. This results in a lower gas saturation at the landing point on the crossover

tie line and faster shock velocity, as shown by the steeper slope of the JL line segment. The nontie-line eigenvalue is equal to the slope of the line segment from C to L. As N_2 concentration decreases, the injection tie line shortens and shifts lower to the left of the crossover tie line. Point L decreases and reduces the slope of the CL line segment and the nontie-line eigenvalue at the landing point of the crossover tie line. A new path connecting the injection system to the initial system is required.

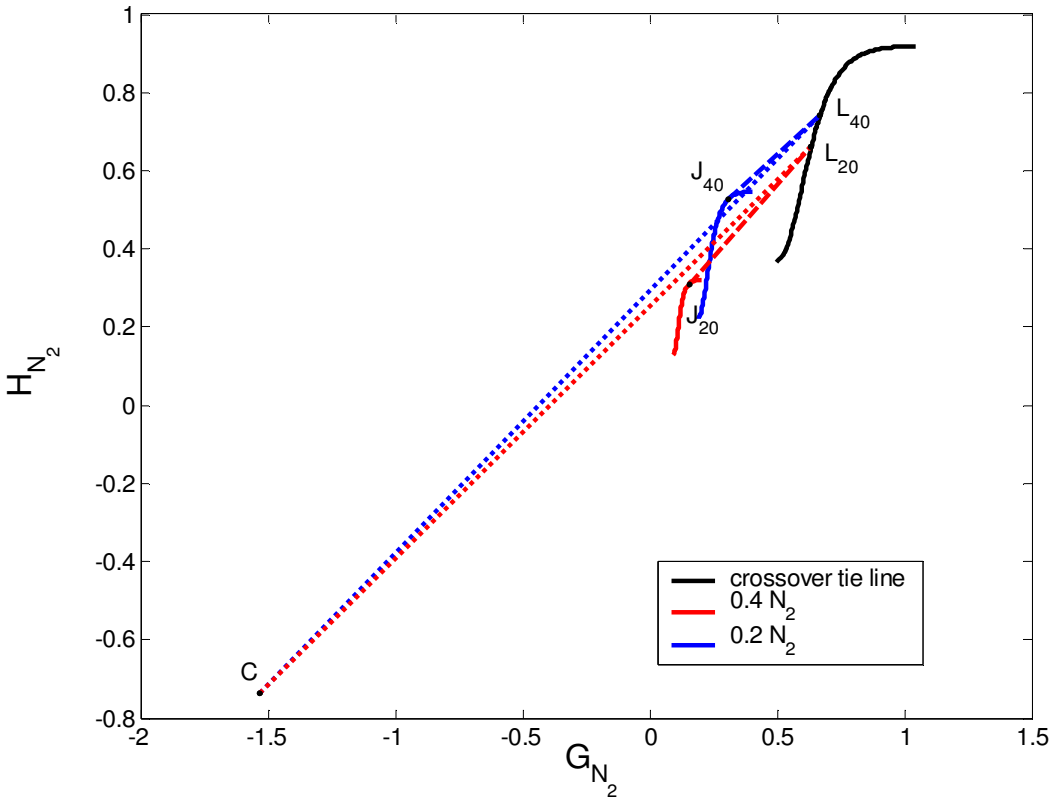

Figure 5-25: Semishock and nontie-line eigenvalue construction from injection tie line to crossover tie line.

Because available paths for continuous variation at point E have been exhausted, a shock is required. Injection and initial tie lines remain fixed. A new crossover tie line must be utilised in this composition path. A shock from the injection tie line to a tie line on the $N_2/CH_4/H_2O$ face resolves this problem. Figure 5-26 illustrates this construction. Equilibrium concentrations of N_2 on the $N_2/CH_4/H_2O$ face are lower than those on the N_2/H_2O axis. Overall concentrations of N_2 in the displacement are lower, and the crossover tie line on the $N_2/CH_4/H_2O$ face is shorter than the N_2/H_2O axis. As the crossover tie line moves up the $N_2/CH_4/H_2O$ face, point C moves closer to the composition space and the slope of the CL line segment increases, becoming faster than the tangent shock velocity.

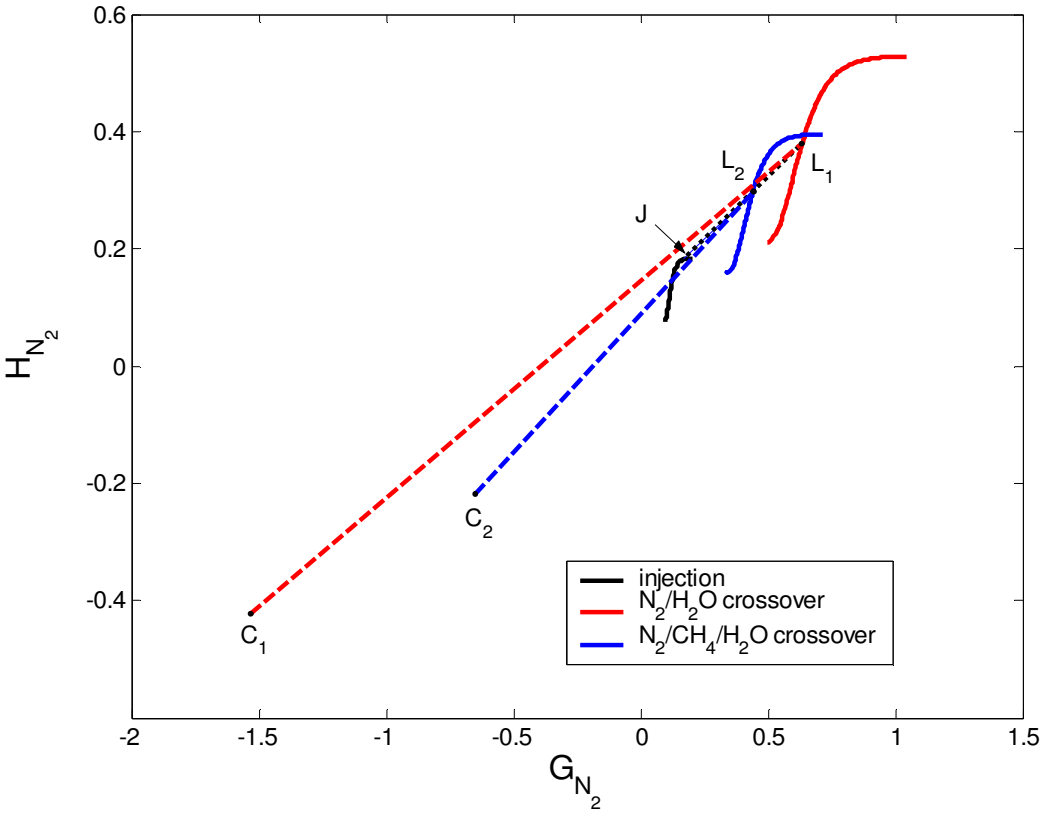

Figure 5-26: Semishock and nontie-line eigenvalue construction from injection tie line (0.2 N_2 mol fraction) to N_2/H_2O crossover tie line (red) and the $N_2/CH_4/H_2O$ crossover tie line (blue).

An example of this solution structure is presented in Figures 5-27 and 5-28. The numerical solution agrees well with the analytical solution. A mixture of 0.2 N_2 and 0.8 CO_2 is injected into coalbed saturated with 0.3103 CH_4 and 0.6987 H_2O. The solution construction procedure for the Type III-C composition path is similar to the Type III-B path. Entry into the two phase region occurs through a shock from the injection condition, I, to the tangent point on the injection tie line, G. This is followed by continuous variation along the injection tie line to point F. A semishock from F to E connects the injection tie line to the crossover tie line. Compared to the previous solution where the crossover tie line is a binary mixture of N_2 and H_2O, the crossover tie line for this composition path is a ternary mixture of N_2, CH_4 and H_2O. As in the Type III-B solution, the injection path switches to a nontie-line path at the landing point, E, and continues along this path up to the degenerate tie line, D. At the degenerate tie line, injection and initial segments are connected by the degenerate shock, C-D, providing a unique and allowable path from injection state to initial state. At point C, there is a path switch to the nontie-line path. This path is traced up to the equal-eigenvalue point of the initial tie line, B. Here, the composition path switches from nontie-line path to tie-line path. This is followed by a tie-line rarefaction to A and a tangent shock out to the initial conditions, O. Table 5-5 summarises key points in the Type III-C displacement.

As in previous displacements, CH_4 and CO_2 remain separated from each other, but N_2 flows with both of the other components. In this displacement, the N_2 concentration in the injection gas is no longer large enough to create an intermediate N_2 bank, and is always produced with other gases. The intermediate aqueous bank is wider than that of previous injection gas mixtures. For this injection gas mixture, the crossover tie line is no longer the N_2-H_2O axis. Because the N_2 concentration in the injection gas is not high enough to create an isolated N_2 bank prior to CH_4 desorption, the composition path includes a shock from the injection tie line to a crossover tie line that is a mixture of $N_2/CH_4/H_2O$. CO_2 in the injection mixture transfers into the slower moving aqueous phase and

immobile solid phase, retarding the entire displacement. The volume increase produced by CH_4 desorption no longer offsets the initial volume decrease caused by CO_2 adsorption for the adsorption constants considered.

Table 5-5: Summary of key points in Type III-C displacement.

component label	component (mol fraction)				S_g	local flow velocity	wave velocity (λ)
	N_2	CH_4	CO_2	H_2O			
I	0.2	0.0	0.8	0.0	1.0	1.0	0.0-0.1994
G	0.1119	0.0	0.7215	0.1666	0.6767	1.0419	0.1994
F	0.0951	0.0	0.7065	0.1984	0.5686	1.0419	0.4372
E	0.2076	0.1273	0.0	0.6652	0.2757	0.6511	0.4372-0.4958
D	0.0623	0.3638	0.0	0.5739	0.3557	0.7680	0.8031
C	0.0794	0.4298	0.0	0.4908	0.5139	0.76680	0.8031
B	0.0	0.4704	0.0	0.5296	0.4099	0.8285	0.9739
A	0.0	0.4205	0.0	0.5795	0.3015	0.8285	1.7881
O	0.0	0.3103	0.0	0.6897	0.0	0.8285	1.7881

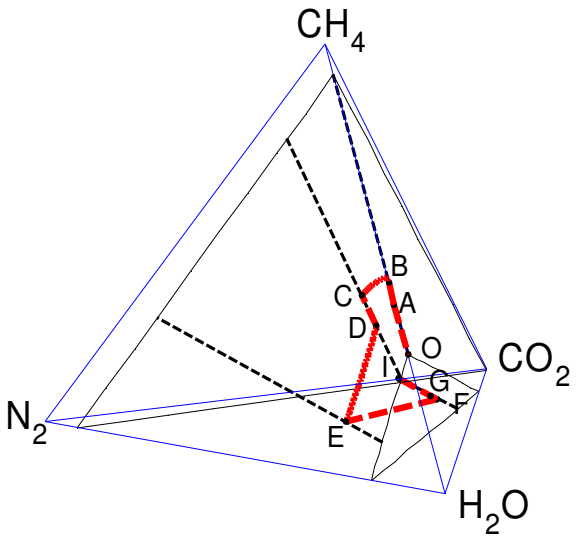

Figure 5-27: Composition path for Type III-C displacement.

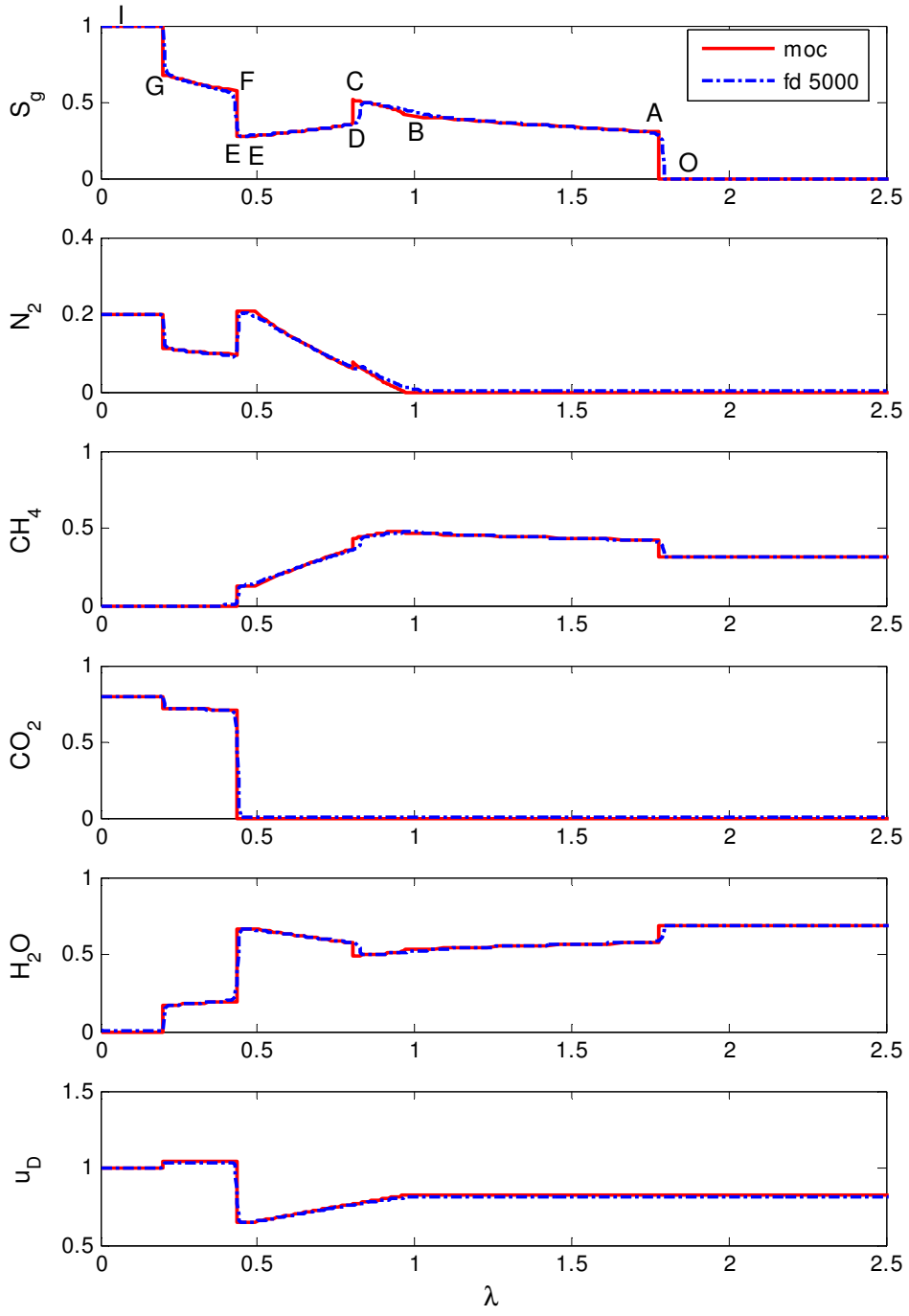

Figure 5-28: Solution profile for Type III-C displacement. The numerical solution is in good agreement with the analytical solution.

5.4.4. Type III-D

With additional increases in CO_2 concentration, it becomes possible to trace the injection nontie-line path from the landing point on the crossover tie line directly up to the initial tie line. Figures 5-29 and 5-30 illustrate this solution structure. In this example, a mixture of 0.05 N_2 and 0.95 CO_2 is injected into a coalbed with an initial composition of 0.3103 CH_4 and 0.6987 H_2O. The initial composition is located on the phase boundary. The numerical solution is in good agreement with the analytical solution. Table 5-6 summarises key points in the Type III-D displacement.

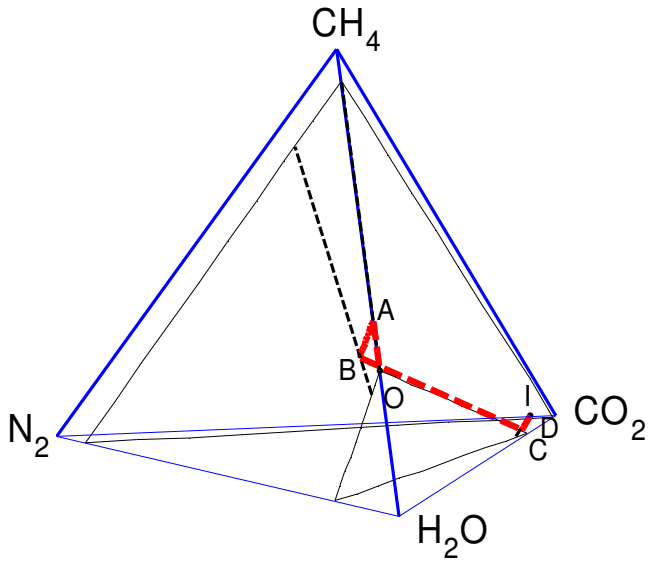

Figure 5-29: Composition path for Type III-D displacement.

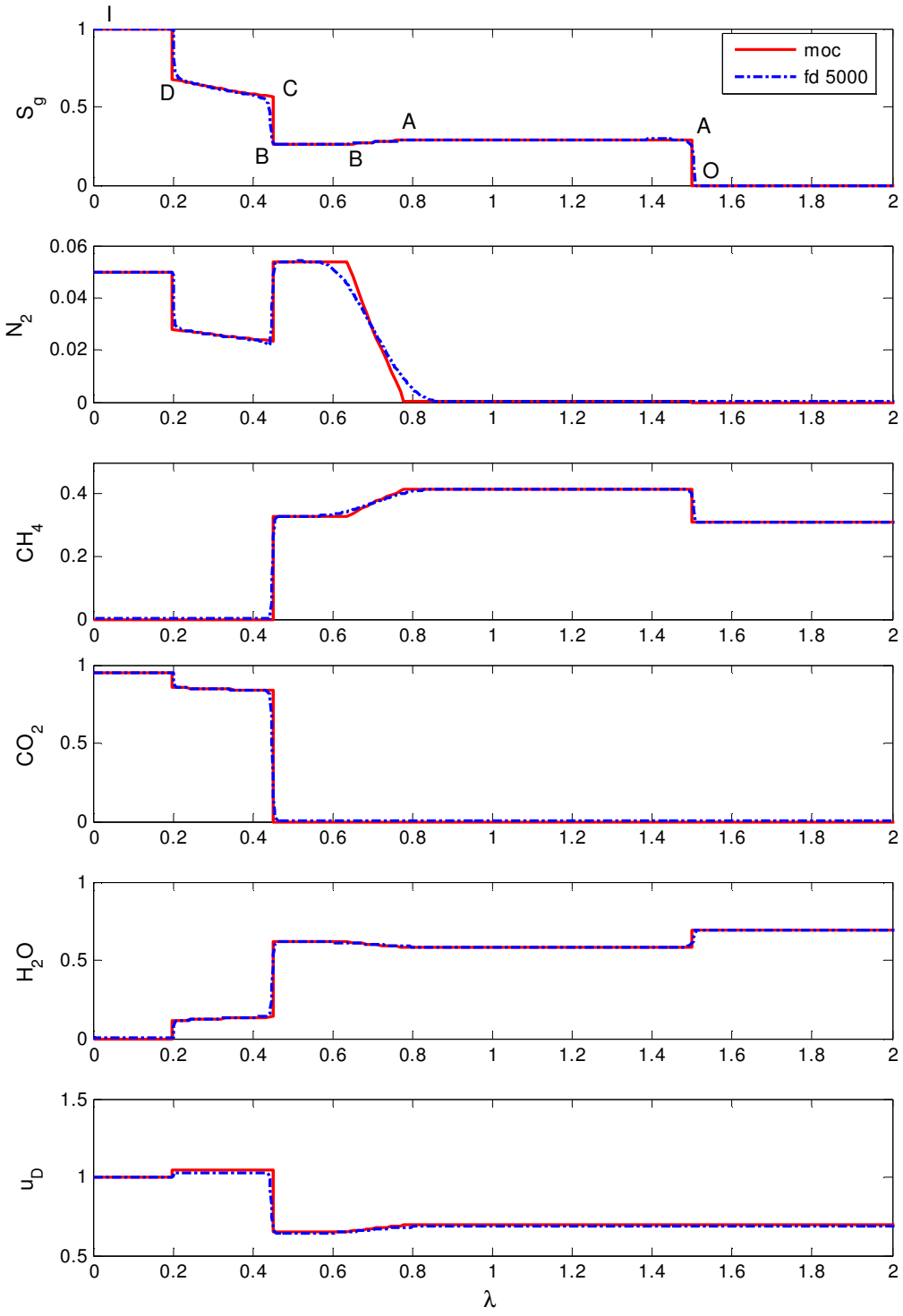

Figure 5-30: Solution profile for Type III-D displacement. The numerical solution is in good agreement with the analytical solution.

Table 5-6: Summary of key points in Type III-D displacement.

component label	component (mol fraction)				S_g	local flow velocity	wave velocity (λ)
	N_2	CH_4	CO_2	H_2O			
I	0.05	0.0	0.95	0.0	1.0	1.0	0.0-0.1995
D	0.0280	0.0	0.8568	0.1153	0.6767	1.0418	0.1995
C	0.0236	0.0	0.8384	0.1379	0.5645	1.0418	0.4492
B	0.0536	0.3301	0.0	0.6163	0.2615	0.6521	0.4492-0.6369
A	0.0	0.4155	0.0	0.5839	0.2915	0.6947	0.7792-1.4982
O	0.0	0.3103	0.0	0.6897	0	0.6947	1.4982

In this composition path, there is no nontie-line path from the initial tie line. Unlike the other Type III solution structures where injection and initial segments can be constructed independently, solution construction must begin at the injection tie line. Solution construction starts at the shortest tie line, where a tangent shock from I to D enters the two phase region. This is followed by a rarefaction along the injection tie line to C. A semishock from C to B connects the injection tie line to the crossover tie line. At point B, a path switch occurs, and the nontie-line path connects B to A on the initial tie line. At point A there is another path switch from the nontie-line path to the tie-line path. The solution is completed by a shock from A to initial conditions, O.

Figures 5-31 and 5-32 summarise composition paths and solution profiles for all Type III solutions. In all of the Type III paths shown, the crossover tie line is the longest tie line. For low concentrations of CO_2 in the injection gas, the displacement behaviour of N_2 dominates, and the solution looks more like a spreading wave solution (Type II). For injection gases with high concentrations of CO_2, the nontie-line component of the displacement shortens, and the solution has characteristics similar to a self-sharpening solution (Type I). The large reduction in flow velocity due to removal of CO_2 from the flowing phase results in a very

slow displacement. When very small amounts of N_2 are present in the injection gas, the N_2 is unable to propagate quickly enough through the coalbed to create an intermediate binary mixture of N_2 and H_2O. The N_2 concentrations present are unable to desorb sufficient gas to increase gas saturations to make it the preferential flowing phase after the tangent shock connecting injection and crossover tie lines where CO_2 is separated from the injection gas. When gas is not the preferential flowing phase, wave velocities are slow, further retarding the displacement.

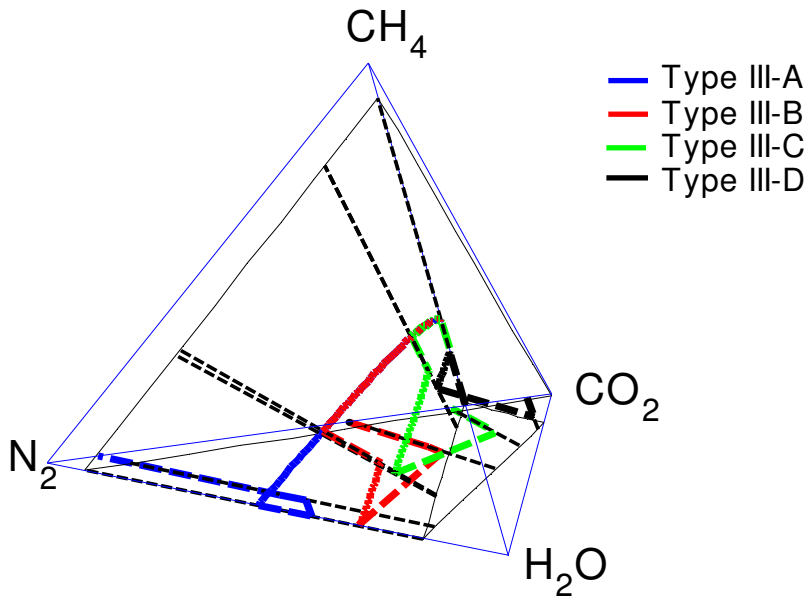

Figure 5-31: Summary of Type III composition paths.

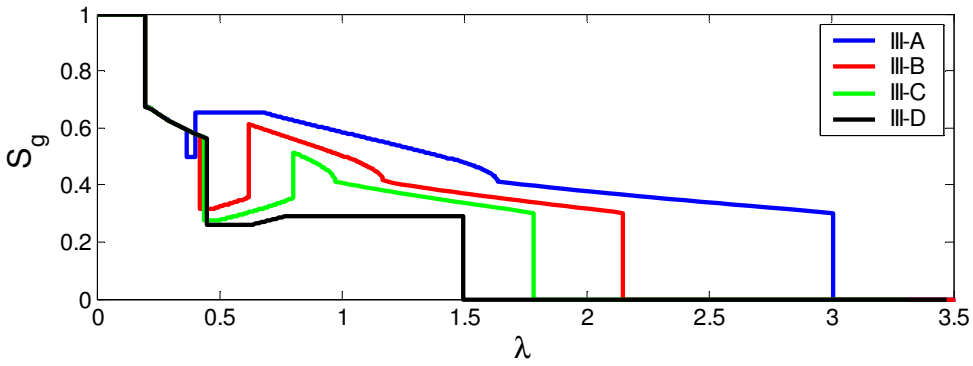

Figure 5-32: Summary of gas saturation profiles for the Type III solution structures.

Figure 5-33 shows the effect of injection gas composition on recovery. For all injection gas compositions, efficient recovery of CH_4 is achieved. Injection gases rich in N_2 recover CH_4 faster than injection gases rich in CO_2. Figure 5-34 compares the change in local flow velocity as a function of injection gas composition. Gases rich in CO_2 experience a greater decrease in local flow velocity. CO_2 is more strongly adsorbing than CH_4. More CO_2 molecules are adsorbed onto the coal surface and removed from the mobile phase than CH_4 molecules are desorbed and added to the mobile phase. This results in a net decrease in local flow velocity as CO_2 desorbs CH_4. Displacements with injection gas compositions rich in CO_2 propagate through the coal more slowly than displacements with injection gas compositions rich in N_2. Although gas is recovered faster when N_2 is present in the injection gas, the resulting production stream is contaminated with N_2 and requires an additional separation step prior to sales. When CO_2 is present in the injection gas, CH_4 is recovered more slowly, but CO_2 is segregated from the produced CH_4 stream. For all gas mixtures presented, CH_4 is recovered within a reasonable number of pore volumes injected. Depending on the goal of the gas injection project, to accelerate CH_4 production or delay CO_2 breakthrough, the injection gas composition can be tailored to meet those objectives.

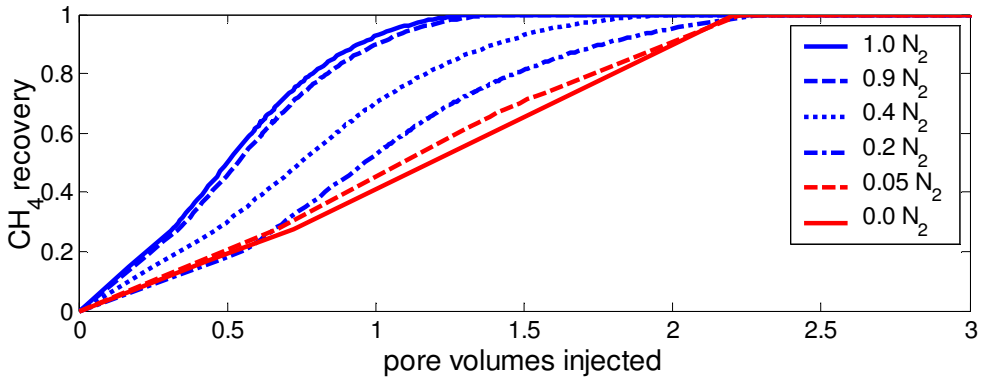

Figure 5-33: CH_4 recovery as a function of injection gas composition.

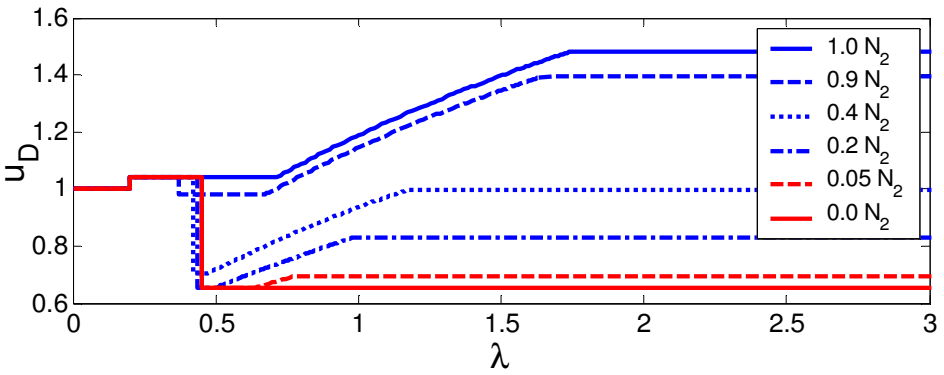

Figure 5-34: Local flow velocity profile as a function of injection gas composition.

5.5. Type IV: Mixed Structure

The Type IV solution occurs when the crossover tie line is the shortest tie line. In this system, components in the injection gas are less strongly adsorbing than gas components in the initial composition, while components in the intermediate gas are more strongly adsorbing than those in the initial gas. Like the Type III solutions, this solution structure exhibits Type I and Type II features, however the order in which segments are connected is reversed. The Type IV structure is

illustrated with an injection gas mixture of 0.9 N_2 and 0.1 CH_4 displacing a coalbed saturated with 0.1721 N_2, 0.0518 CO_2 and 0.7761 H_2O. Again, the initial condition is located on the phase boundary. Composition path and solution profiles for this displacement are presented in Figures 5-35 and 5-36. The numerical solution is in good agreement with the analytical solution. Table 5-7 summarises key points in this displacement.

Solution construction begins at the crossover tie line. From the crossover tie line, connections to the initial and injection tie lines are made. This section describes the construction of the initial segment of the solution. Eigenvalues decrease as they are traced from the crossover tie line to the initial tie line, and hence a continuous variation would violate the velocity rule. Therefore, a semishock from C to B connects the crossover tie line to the initial tie line. This is followed by a continuous variation from B to A along the initial tie line. A tangent shock along the initial tie line connects the two phase region to initial conditions from A to O.

Construction of the composition path of the injection segment is described in the following section. Eigenvalues decrease as the nontie-line path is traced from the crossover tie line to the injection tie line, and a continuous variation is allowed. At the equal-eigenvalue point on the crossover tie line, D, there is a path switch from the crossover tie line to the nontie-line path. The nontie-line path is traced down to the injection tie line. At the point E, there is a path switch from nontie-line path to tie-line path. These segments are connected by a zone of constant state. This is followed by a short rarefaction along the injection tie line to point F. A tangent shock from the two phase region to injection conditions completes the solution from F to I. Injection and initial segments are connected by a tie line rarefaction along the crossover tie line from D to C.

Table 5-7: Summary of key points in Type IV displacement.

component label	component (mol fraction)				S_g	local flow velocity	wave velocity (λ)
	N_2	CH_4	CO_2	H_2O			
I	0.9	0.1	0.0	0.0	1.0	1.0	0.0-0.1994
F	0.5035	0.0628	0.0	0.4338	0.6767	1.0421	0.1994
E	0.4976	0.0629	0.0	0.4394	0.6697	1.0421	0.2184-0.3634
D	0.4113	0.0521	0.0587	0.4779	0.5865	1.0839	0.3634-0.4042
C	0.3547	0.0469	0.0577	0.5407	0.4887	1.0839	0.7716
B	0.3579	0.0	0.0546	0.5875	0.4253	1.0510	0.7716-1.1231
A	0.2942	0.0	0.0537	0.6521	0.31015	1.0510	2.2681
O	0.1720	0.0	0.0518	0.7761	0.0	1.0510	2.2681

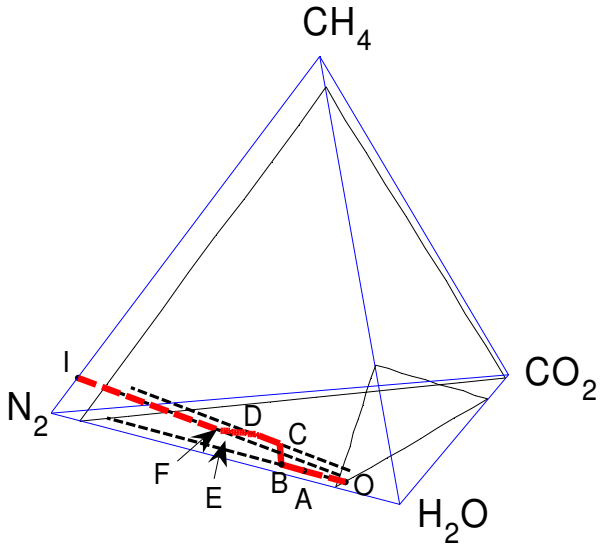

Figure 5-35: Composition path for Type IV displacement.

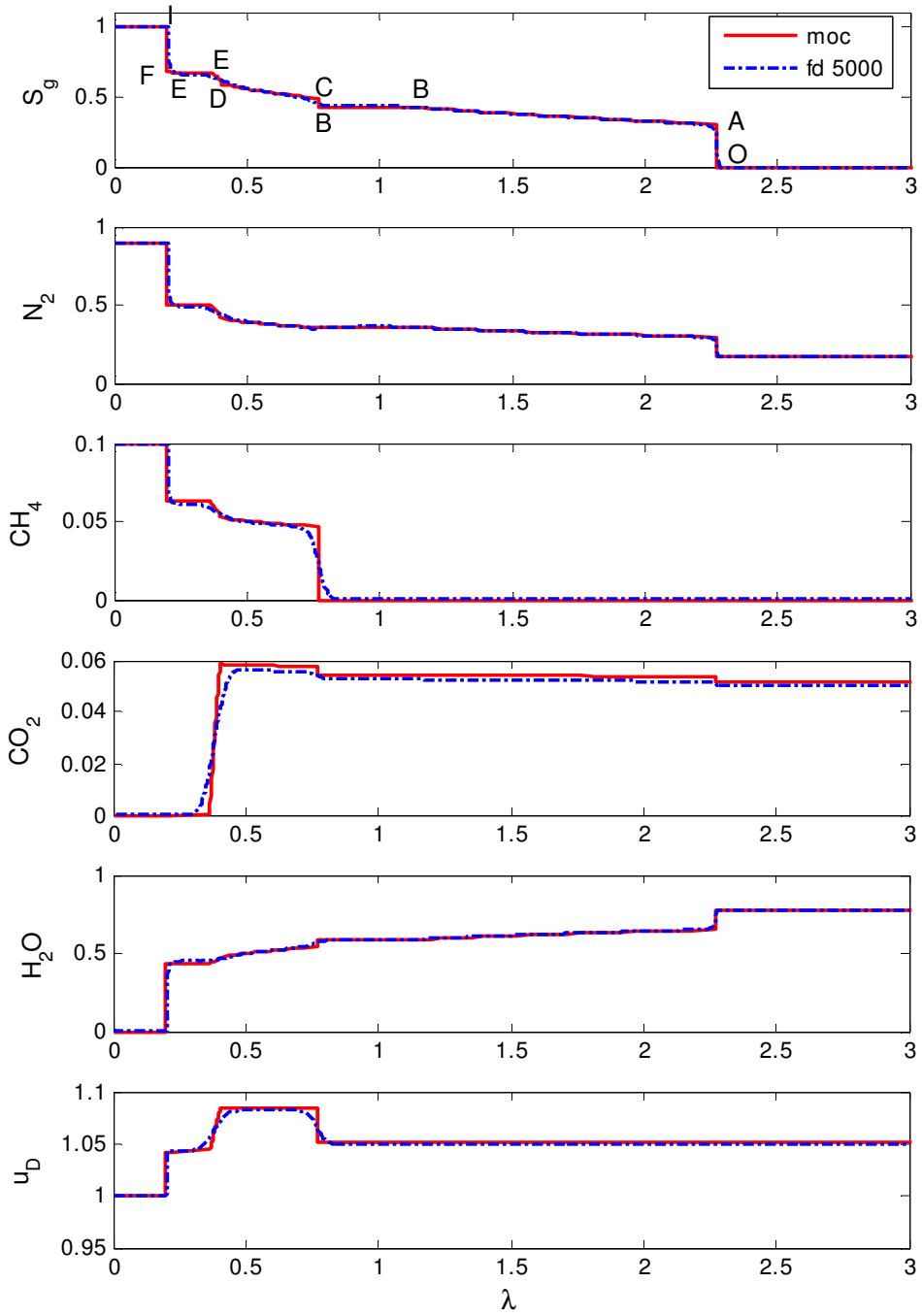

Figure 5-36: Solution profile for Type IV displacement. The numerical solution is in good agreement with the analytical solution.

The least strongly adsorbing and most volatile component, N_2, quickly propagates through the displacement to displace completely the CO_2. Volume increase associated with desorption of CO_2 accelerates the trailing edge of the displacement, while the volume decrease associated with adsorption of previously desorbed CO_2 and CH_4 as these stronger adsorbing components propagate downstream retards the leading edge of the displacement. Differential adsorption strength and solubility between N_2 and CH_4 in the injection gas mixture once again result in chromatographic separation of injection gas components based on their adsorption strength and volatility.

Solution structures for a variety of injection and initial conditions encountered in ECBM processes were presented. Components that are more strongly adsorbing and less volatile propagate through the coalbed at slower wave velocities than components that are less strongly adsorbing and more volatile. Solution structures can be classified into four categories. These are summarised in Table 5-8. The following section applies these analytical solutions to investigate the effect of model parameters, such as relative permeability and adsorption strength, on composition path.

Table 5-8: Summary of solution structures encountered in ECBM operations.

solution type	injection→ crossover tie line	crossover→ initial tie line	comment
I	shock	shock	Both components in the injection gas are more strongly adsorbing than those initially in the coal. The injection tie line is the shortest tie line, and the initial tie line is the longest.
II	rarefaction	rarefaction	Both components in the injection gas are less strongly adsorbing than those initially in the coal. The injection tie line is the longest tie line, and the initial tie line is the shortest.
III-A	shock	rarefaction	A genuine shock along the crossover tie line connects injection and initial landing points. Only the $\frac{\partial \lambda_{nt}}{\partial S} < 0$ branch of the nontie-line variation is used. Crossover tie line is the longest tie line.
III-B	shock	rarefaction→ shock→ rarefaction	A nontie-line rarefaction from the injection landing point up to the degenerate tie line, followed by a degenerate shock, is required to connect the injection and initial paths. Both $\frac{\partial \lambda_{nt}}{\partial S} > 0$ and $\frac{\partial \lambda_{nt}}{\partial S} < 0$ variation are required. The crossover tie line is the longest tie line.
III-C	shock	rarefaction→ shock→ rarefaction	The crossover tie line no longer lies in the ruled surface of the injection and initial tie lines; only in the ruled surface of the initial tie line. Switch from injection nontie-line path to initial nontie-line path follows Type III-B construction. Both $\frac{\partial \lambda_{nt}}{\partial S} > 0$ and $\frac{\partial \lambda_{nt}}{\partial S} < 0$ variation are required. The crossover tie line is the longest tie line.
III-D	shock	rarefaction	Continuous variation from the landing point on the crossover tie line up to the initial tie line occurs without the need for the degenerate tie line. Only the $\frac{\partial \lambda_{nt}}{\partial S} > 0$ variation is required. The crossover tie line is the longest tie line and the injection tie line is the shortest.
IV	rarefaction	shock	The crossover tie line is the shortest tie line.

5.6. Convergence of Numerical Solutions

The analytical solutions developed in this section are in good agreement with numerical simulations. Small differences between the numerical and analytical solution are caused by numerical dispersion. Numerical solutions at gridblock resolutions of 100, 500, 1000 and 5000 were obtained for all analytical solutions to assess the level of resolution required for the different solution structures. Composition paths and solution profiles are shown in Figures 5-37 to 5-50.

All of the composition routes presented have paths removed from the dilution line. The lowest resolution numerical simulations are strongly affected by numerical dispersion. For this resolution, features of the displacement, such as the equal-eigenvalue point and the path switch between tie-line and nontie-line path, are completely obscured by dispersion. In all cases, the leading shock velocity is over predicted, while the trailing shock velocity is under predicted. An order of magnitude increase in resolution is required to capture the fine scale features of the displacement.

The highest resolution simulations converge to most features of the displacements; however, the highest resolution numerical simulations still have difficulties resolving some features. Solutions with a tangent shock connecting injection and crossover tie lines (Type I and Types III) have difficulty capturing the jump point of this shock. The jump point is where the tie line eigenvalue is equal to the shock velocity. Numerical dispersion causes the simulation to overshoot this point. The numerical solution self corrects, and subsequent shock segments are captured well.

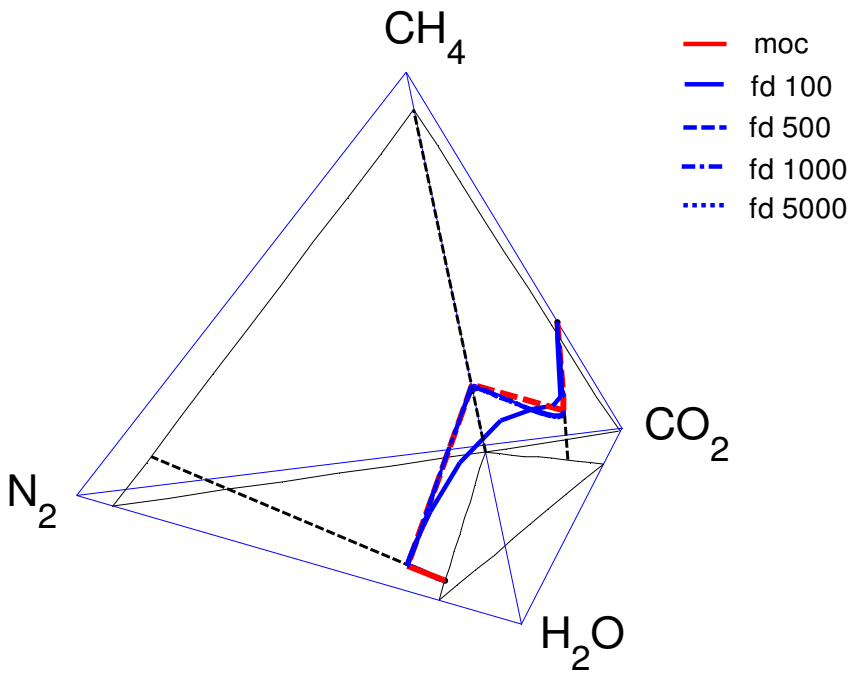

Figure 5-37: Comparison of composition paths calculated from the numerical solution for resolutions of 100, 500, 1000 and 5000 gridblocks against the Type I analytical solution.

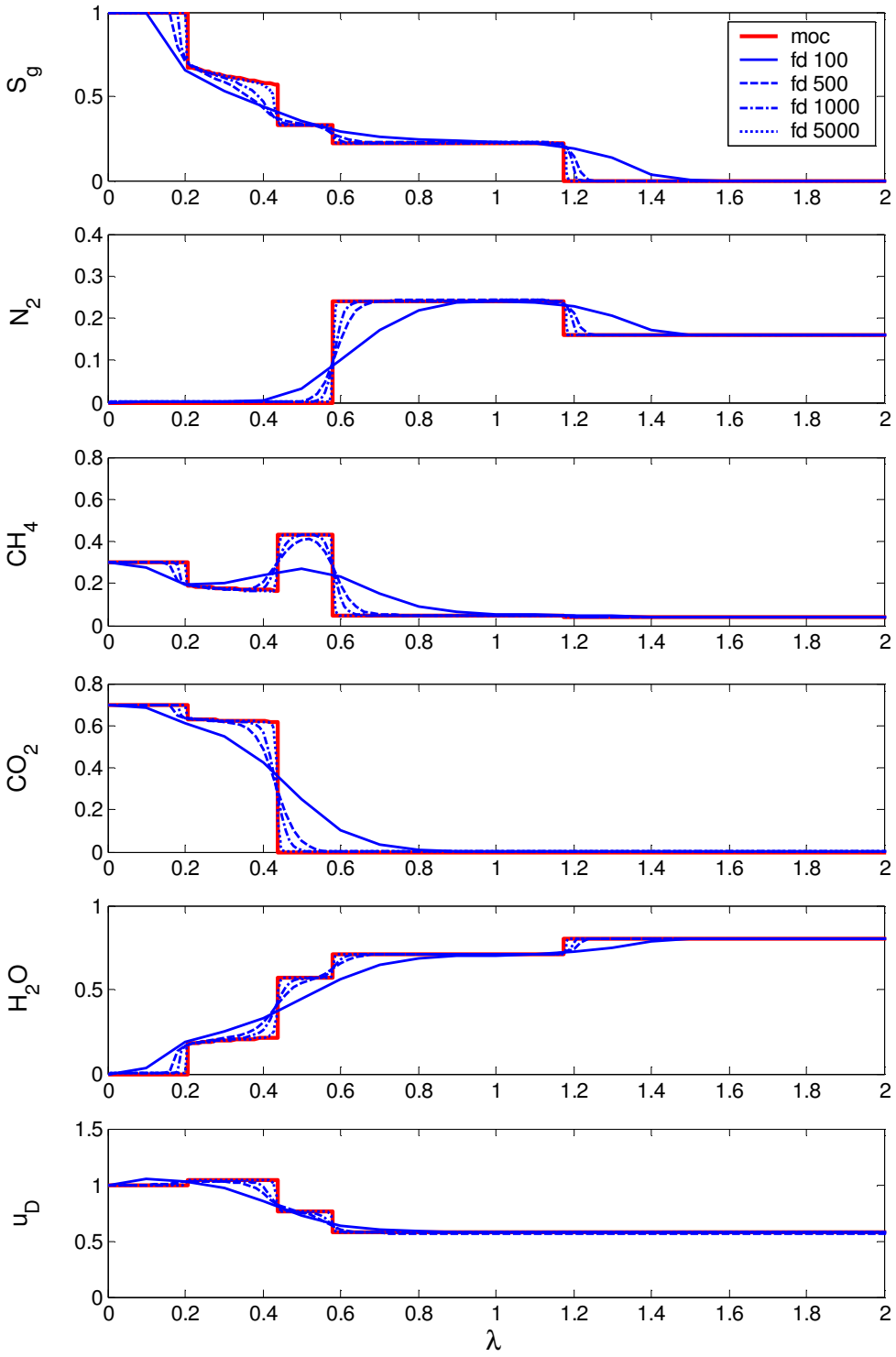

Figure 5-38: Comparison of solution profiles calculated from the numerical solution for resolutions of 100, 500, 1000 and 5000 gridblocks against the Type I analytical solution.

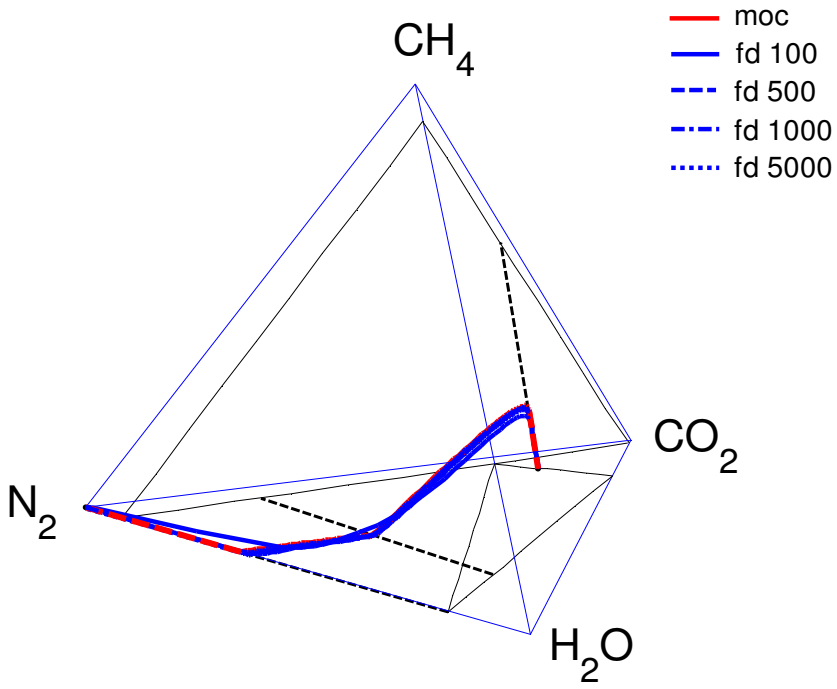

Figure 5-39: Comparison of composition paths calculated from the numerical solution for resolutions of 100, 500, 1000 and 5000 gridblocks against the Type II analytical solution.

Difficulties are also encountered in capturing path switches: from the tie-line path to the nontie-line path at the equal-eigenvalue points (Type II, Types III and Type IV paths), and from the nontie-line path to the tie-line path. The degenerate shock pulls the composition path away from the dilution line. High resolution finite difference simulation is also required to capture the degenerate shock structure.

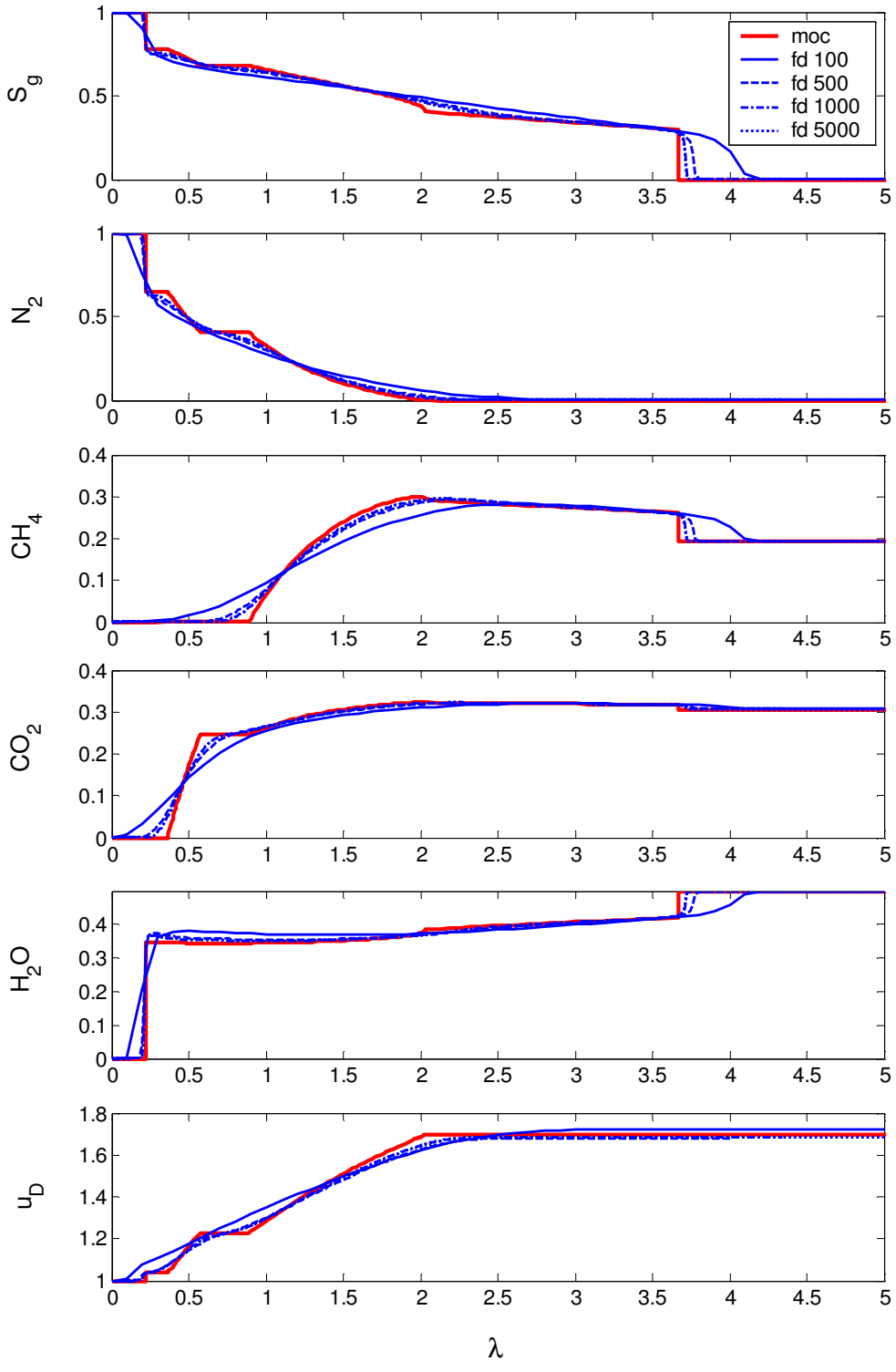

Figure 5-40: Comparison of solution profiles calculated from the numerical solution for resolutions of 100, 500, 1000 and 5000 gridblocks against the Type II analytical solution.

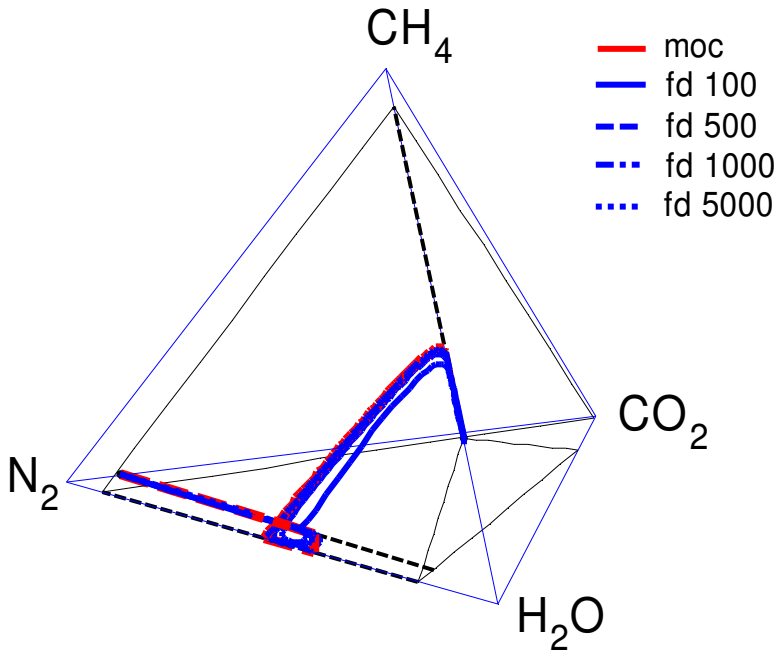

Figure 5-41: Comparison of composition paths calculated from the numerical solution for resolutions of 100, 500, 1000 and 5000 gridblocks against the Type III-A analytical solution.

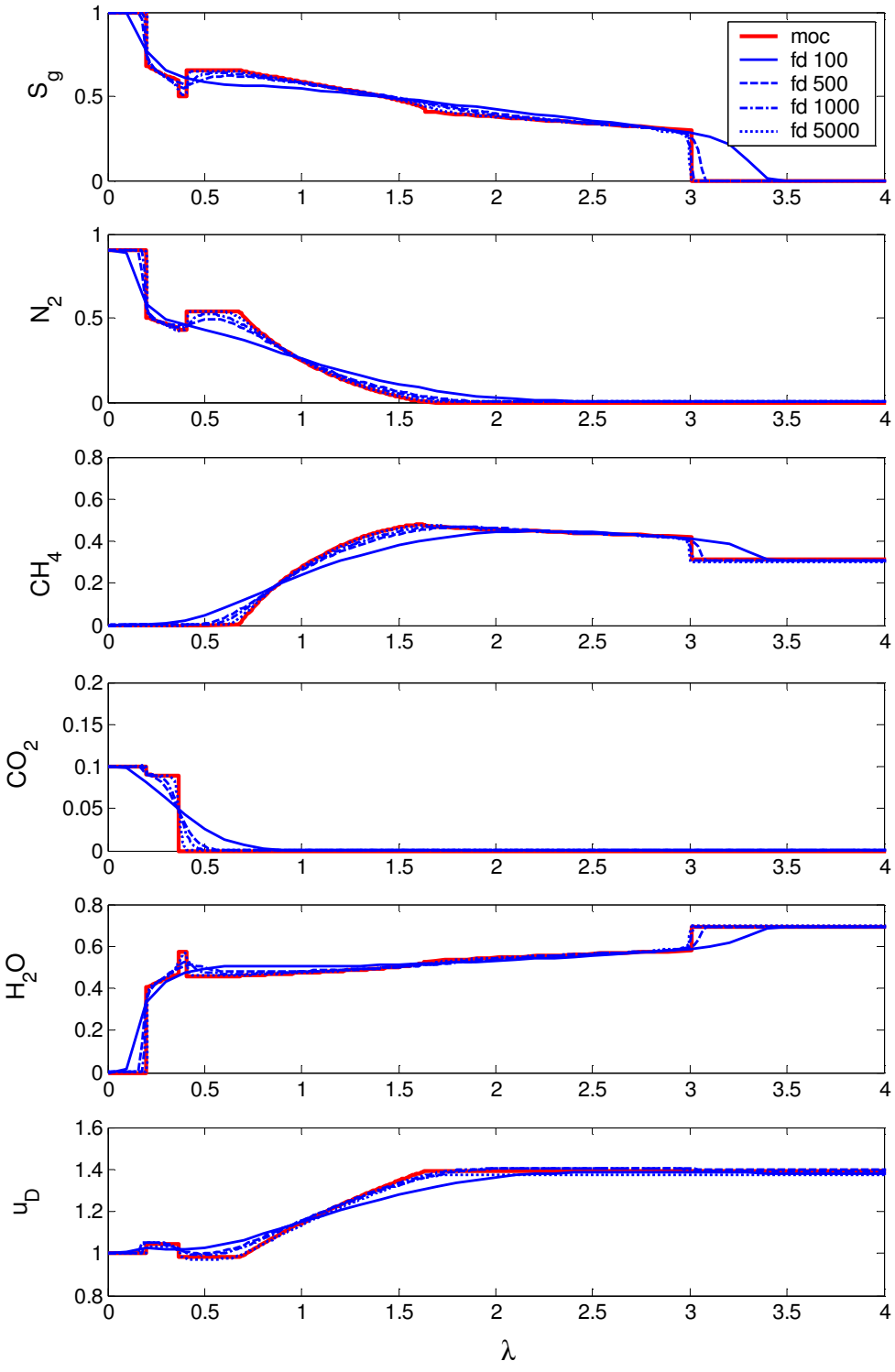

Figure 5-42: Comparison of solution profiles calculated from the numerical solution for resolutions of 100, 500, 1000 and 5000 gridblocks against the Type III-A analytical solution.

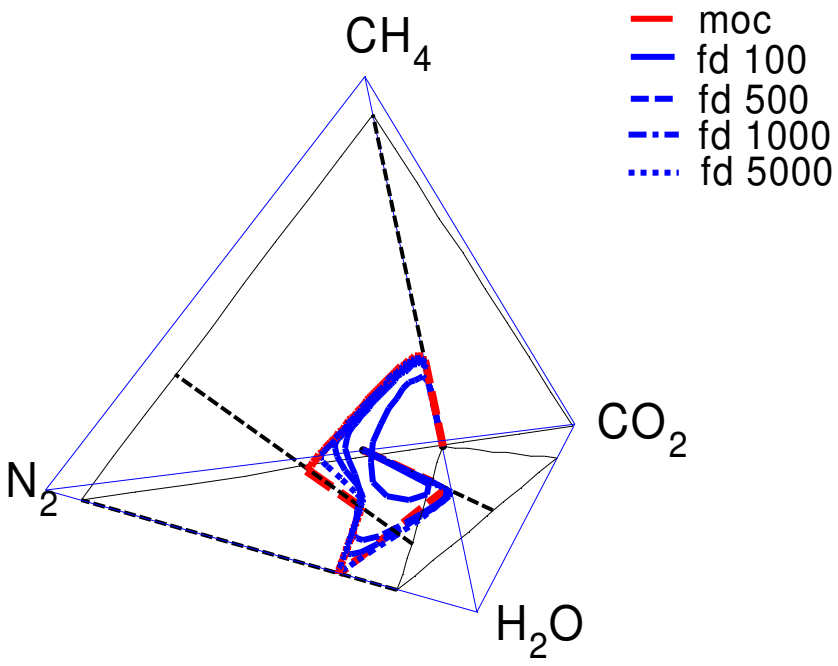

Figure 5-43: Comparison of composition paths calculated from the numerical solution for resolutions of 100, 500, 1000 and 5000 gridblocks against the Type III-B analytical solution.

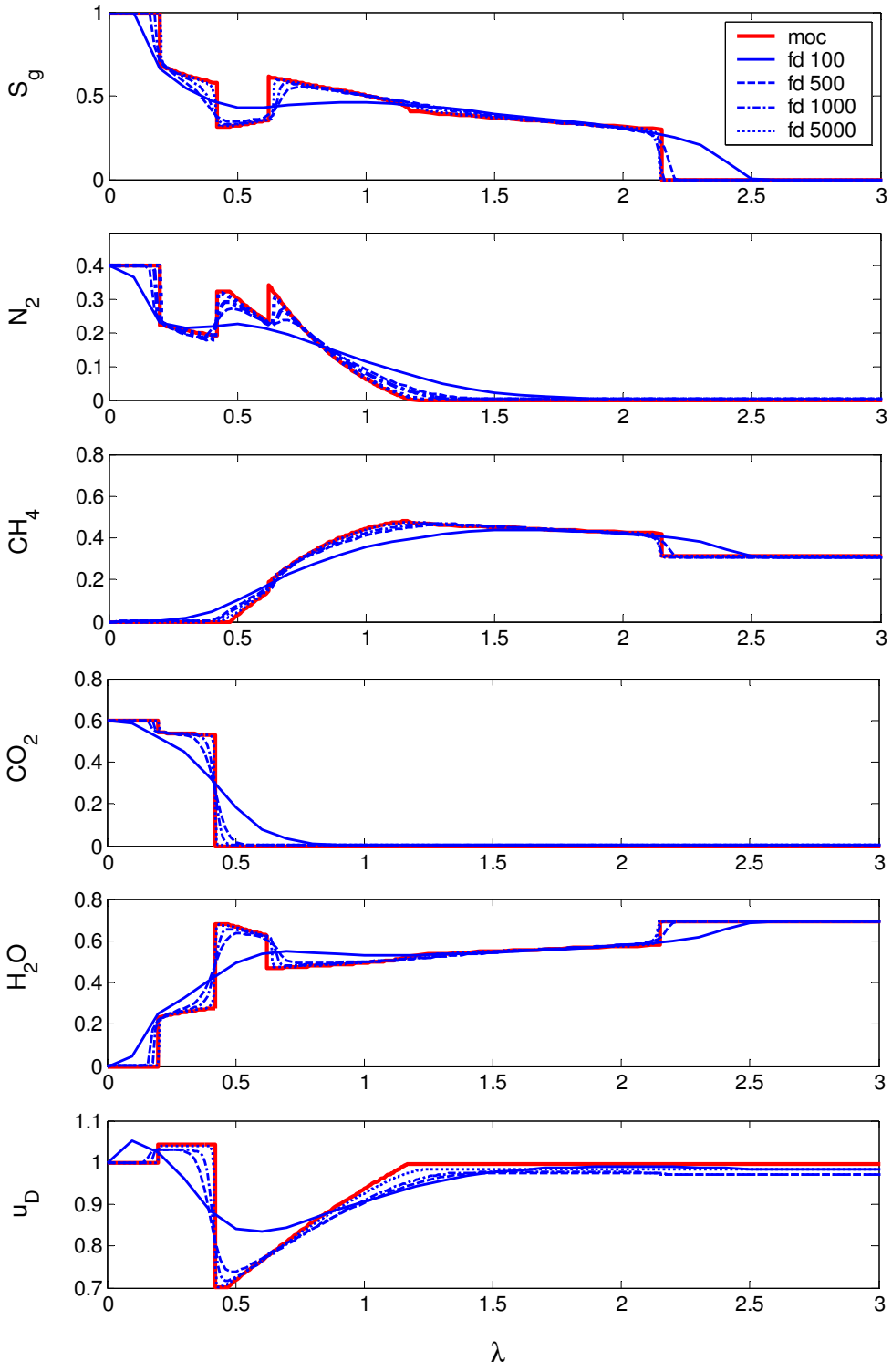

Figure 5-44: Comparison of solution profiles calculated from the numerical solution for resolutions of 100, 500, 1000 and 5000 gridblocks against the Type III-B analytical solution.

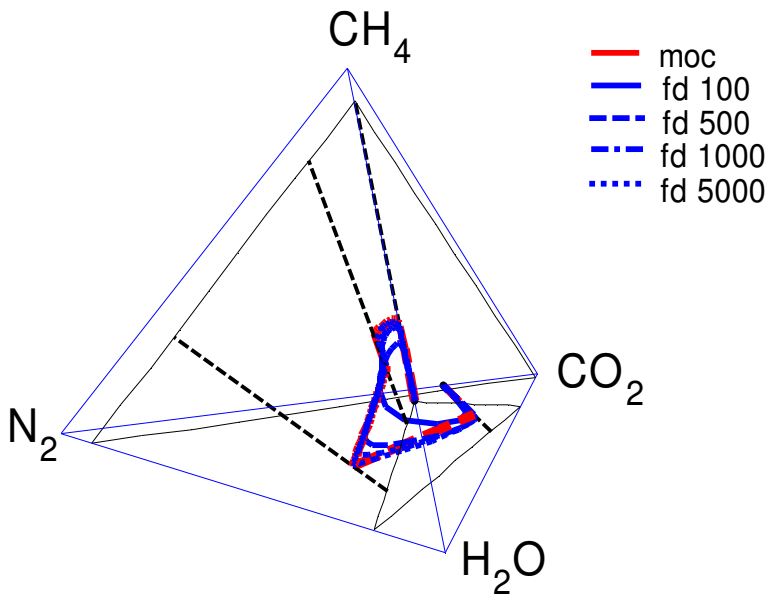

Figure 5-45: Comparison of composition paths calculated from the numerical solution for resolutions of 100, 500, 1000 and 5000 gridblocks against the Type III-C analytical solution.

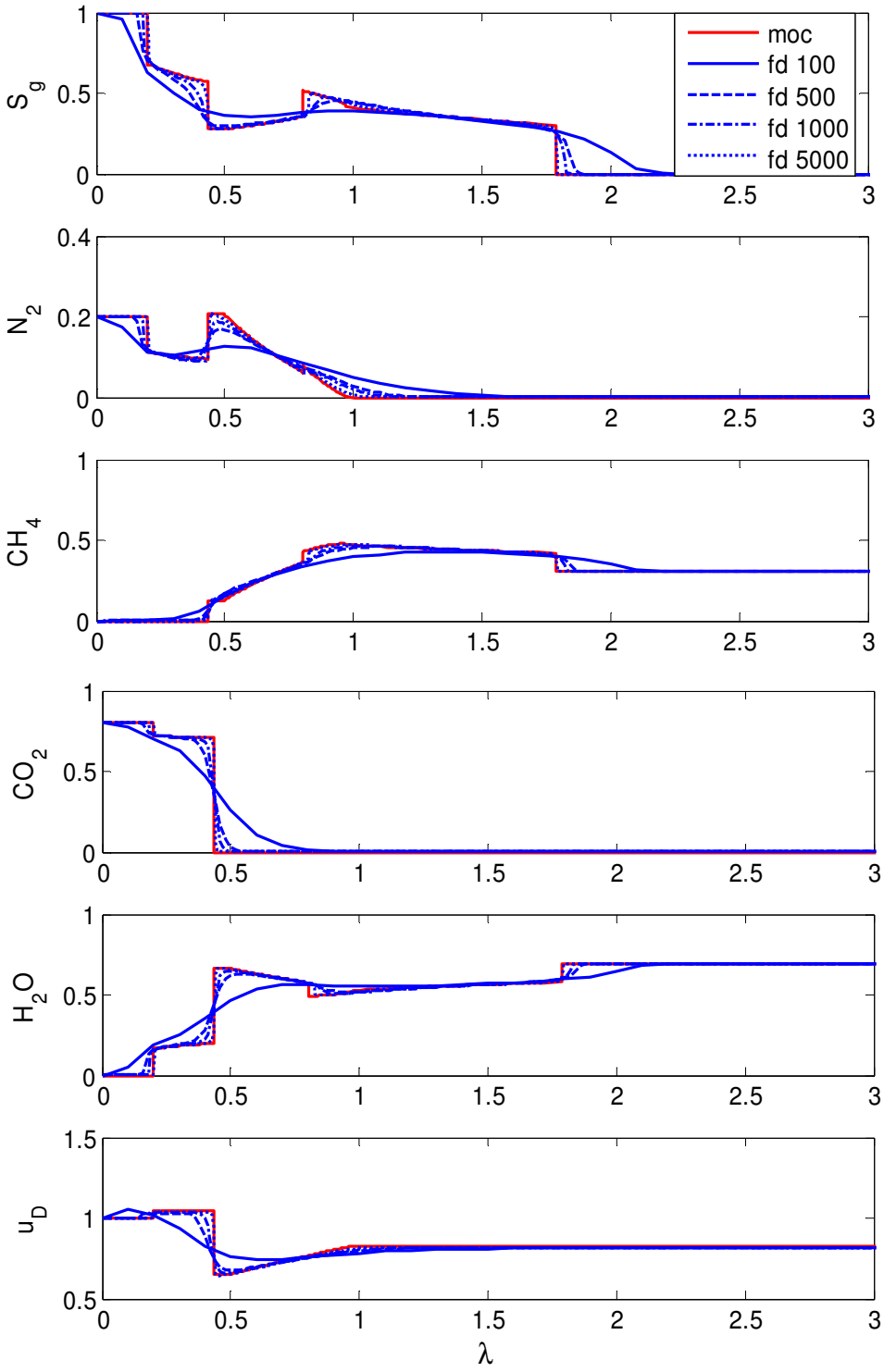

Figure 5-46: Comparison of solution profiles calculated from the numerical solution for resolutions of 100, 500, 1000 and 5000 gridblocks against the Type III-C analytical solution.

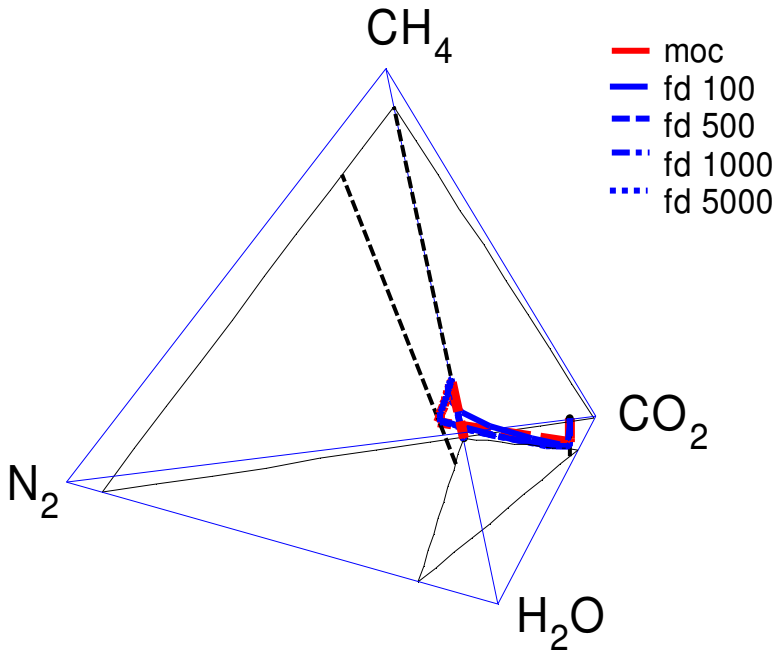

Figure 5-47: Comparison of composition paths calculated from the numerical solution for resolutions of 100, 500, 1000 and 5000 gridblocks against the Type III-D analytical solution.

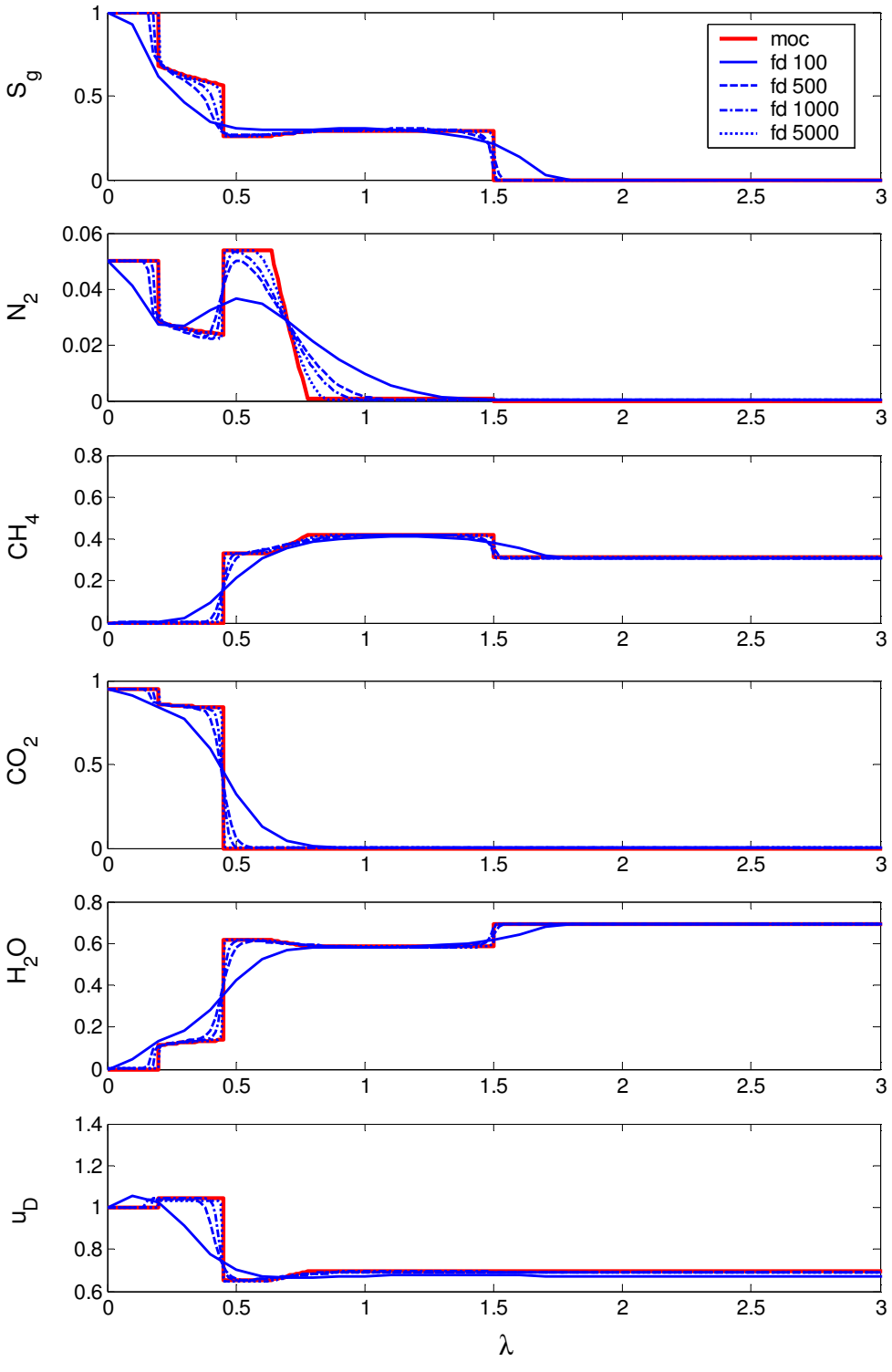

Figure 5-48: Comparison of solution profiles calculated from the numerical solution for resolutions of 100, 500, 1000 and 5000 gridblocks against the Type III-D analytical solution.

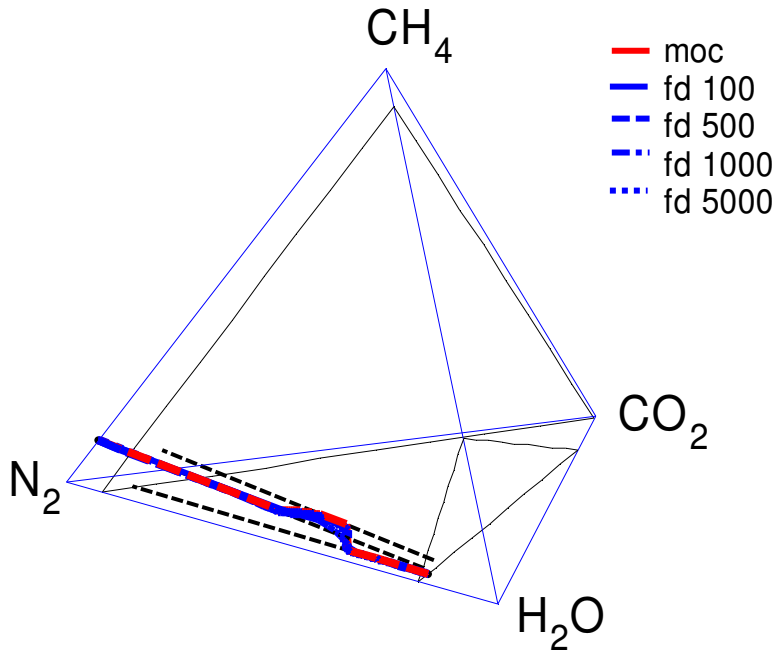

Figure 5-49: Comparison of composition paths calculated from the numerical solution for resolutions of 100, 500, 1000 and 5000 gridblocks against the Type IV analytical solution.

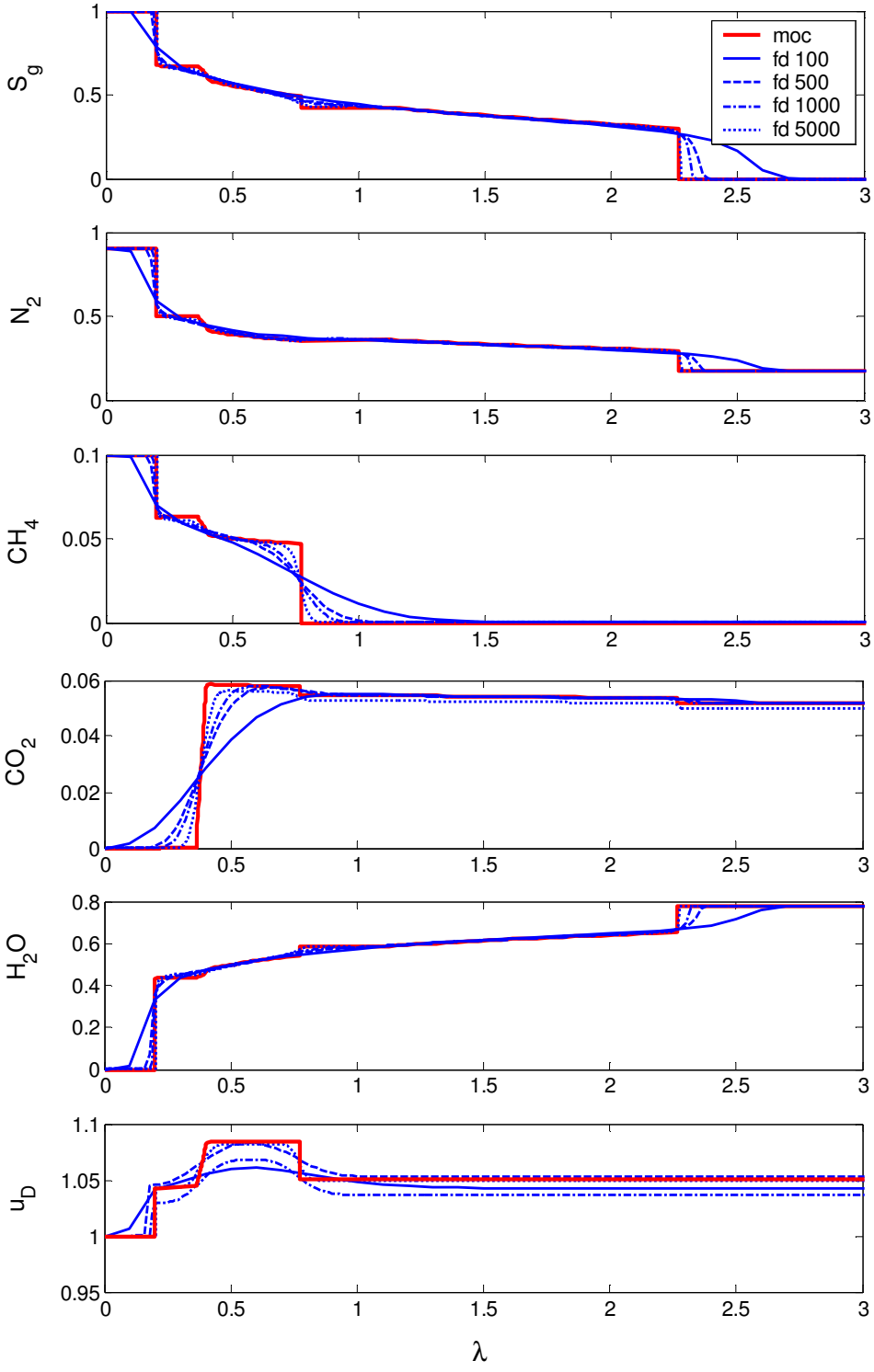

Figure 5-50: Comparison of solution profiles calculated from the numerical solution for resolutions of 100, 500, 1000 and 5000 gridblocks against the Type IV analytical solution.

5.7. Effect of Variations in Relative Permeability

Many coalbeds are water-saturated. Multiphase flow effects are important in modelling transport in these systems. In this section, the effect of variations in relative permeability on displacement is investigated. Experimental evidence suggests that the coal surface changes from gas wet to water wet during CO_2 injection and high pressure injection (Mazumder *et al.*, 2003, Chaturvedi, 2006). Changes in wettability can be modelled through the relative permeability function, which in turn affects the fractional flow function that models multiphase flow. To examine this effect, two examples are presented: the first examines the influence of the location of the crossover point, and the second shows the effect of curvature of the relative permeability curves. To demonstrate the effect of multiphase flow parameters on recovery, a gas mixture of 0.5 N_2 and 0.5 CO_2 injected into a coal saturated with 0.3103 CH_4 and 0.6987 H_2O is considered. Displacement follows a Type III-B composition path for the injection and initial compositions used.

Relative permeability model parameters for Eqs. 4-4 to 4-9 are summarized in Table 5-9, and the curves are shown in Figure 5-51 to 5-53. RP-1 and RP-2 represent a changing crossover point by changing S_{gc} and S_{wr}, while RP-3 and RP-4 illustrate the effect of curvature by comparing different exponents. RP-5 is representative of relative permeability curves measured by Chaturvedi (2006). RP-1 represents a gas wet system. RP-2 represents a water wet system. In all relative permeability models considered, the structure of the fractional flow curve remains the same: single inflection point, convex to concave for increasing gas saturation. The mobility ratio is fixed at 10.

Table 5-9: Relative permeability cases considered.

case	S_{gc}	S_{wr}	exponent	k_{rgo}	k_{rwo}
RP-1	0.25	0.025	2	1	1
RP-2	0.05	0.35	2	1	1
RP-3	0	0	2	1	1
RP-4	0	0	4	1	1
RP-5	0	0	2	0.15	1

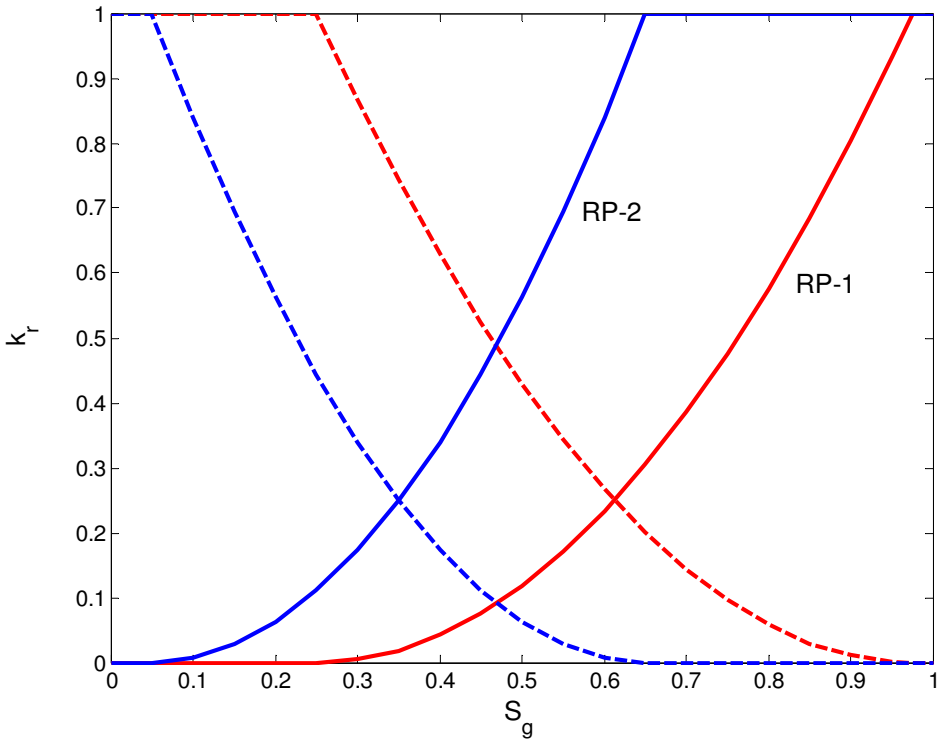

Figure 5-51: RP-1 (gas wet) and RP-2 (water wet) relative permeability curves.

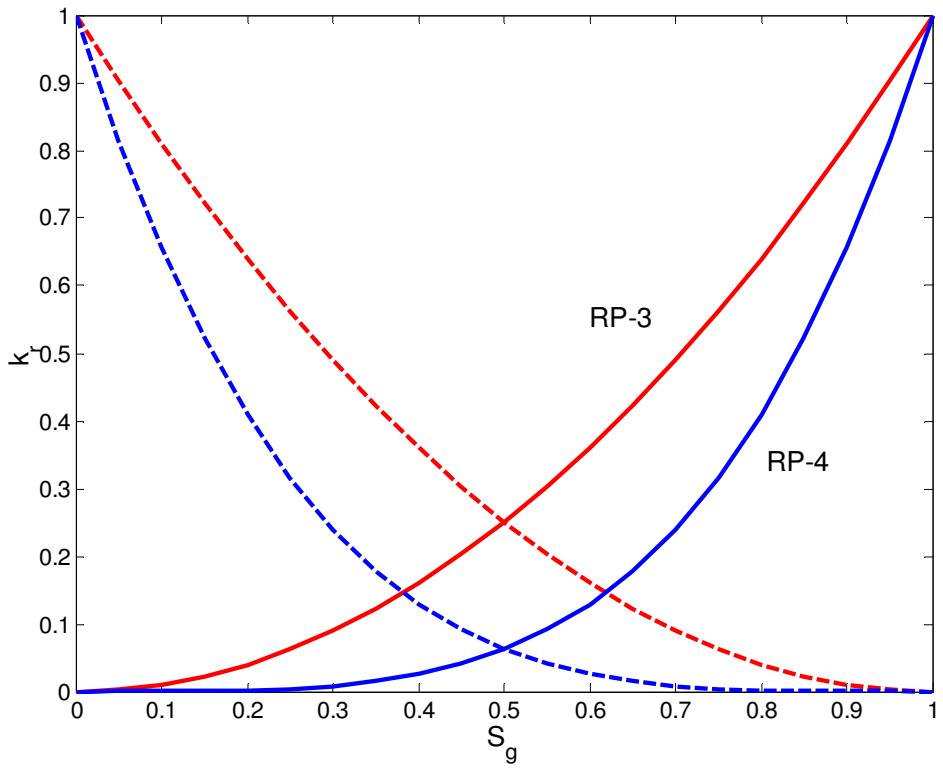

Figure 5-52: RP-3 and RP-4 relative permeability curves.

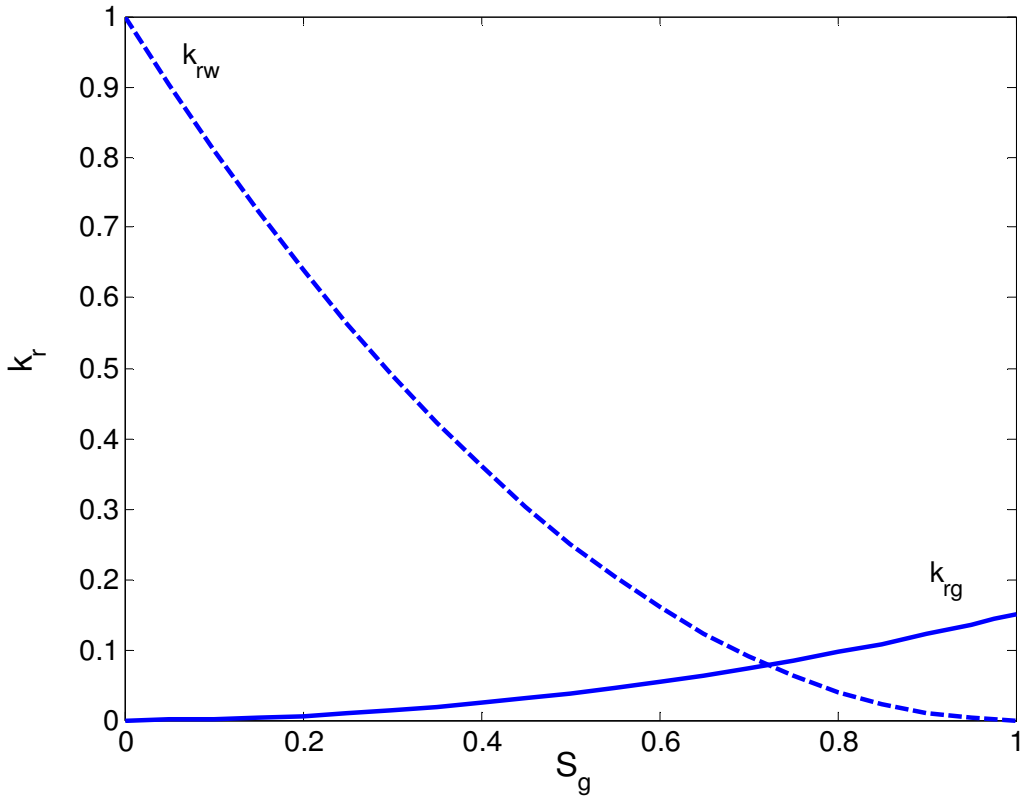

Figure 5-53: RP-5 relative permeability curve.

5.7.1. Influence of Wettability

The crossover point between gas and liquid relative permeability for RP-2 occurs at a lower gas saturation than that of RP-1 (Figure 5-51). Gas is more mobile at lower saturations in RP-2 than in RP-1. Chaturvedi (2006) observed changes in wettability as a function of pH. When CO_2 is injected into a water saturated coal, CO_2 forms H_2CO_3, decreasing the pH of the brine. At high pH, coal was observed to be more water wet than at low pH. This is manifested in the relative permeability curves as a shift of the crossover point to a lower gas saturation. Fractional flow models are shown in Figure 5-54. Figure 5-55 compares solution profiles for the two wettability cases. The solution profile of RP-1 is compressed relative to the solution profile of RP-2. In Figure 5-56, the region of gas mobility

for the RP-1 model is narrower and shifted to higher gas saturations than the window of gas mobility for RP-2. This translation is reflected in the higher gas saturations accessed in the solution profile. Because the mobile region of the fractional flow function of RP-1 is shifted to the higher gas saturations, the tangent construction for the leading shock results slower velocities than those of RP-2. The critical gas saturation in RP-2 is lower than that of RP-1. Gas is more mobile at lower saturations in RP-2 than RP-1, resulting in a faster displacement because gas is mobile at earlier saturations. There is a small effect on the upstream segments of the solution. At high gas saturations encountered in the trailing edge of the displacement, the variation of wave velocities is relatively narrow compared to the range that occurs at lower gas saturations. When gas is more mobile at lower gas saturations, the leading edge of the displacement moves faster than for a relative permeability model where gas is less mobile.

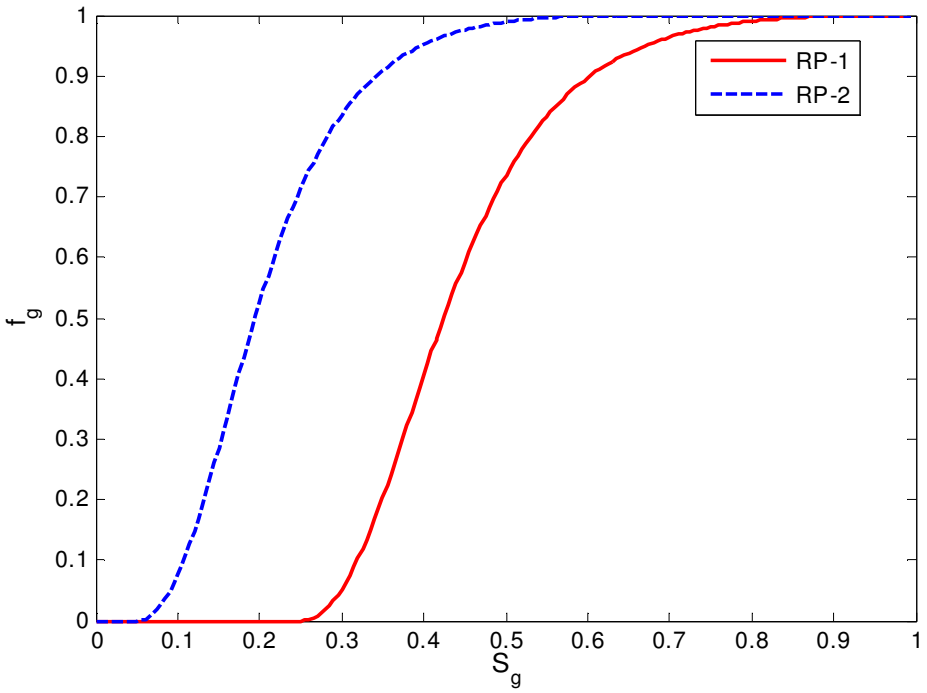

Figure 5-54: Fractional flow curves for RP-1 and RP-2.

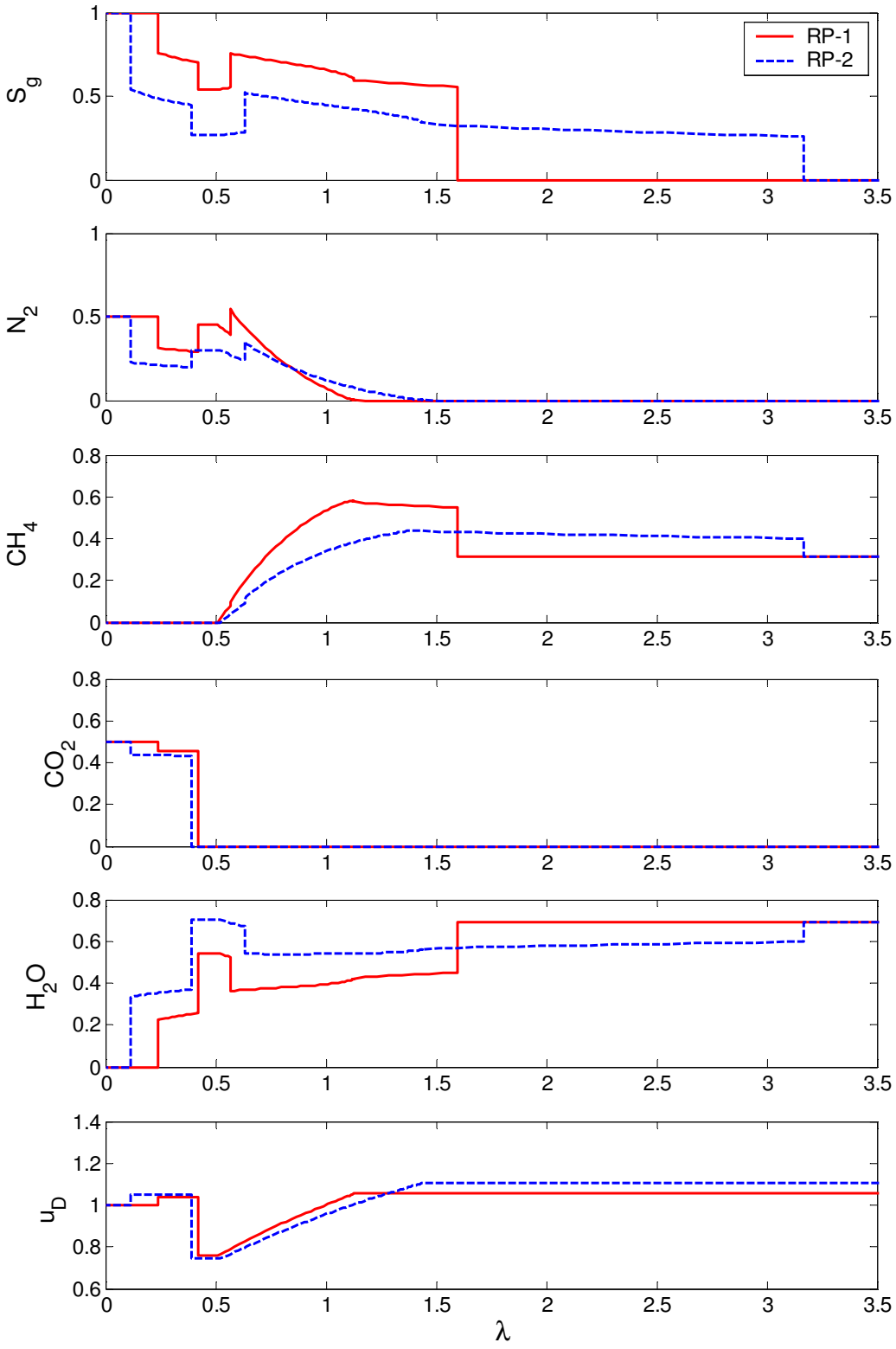

Figure 5-55: Comparison of solution profiles for RP-1 and RP-2 relative permeability models.

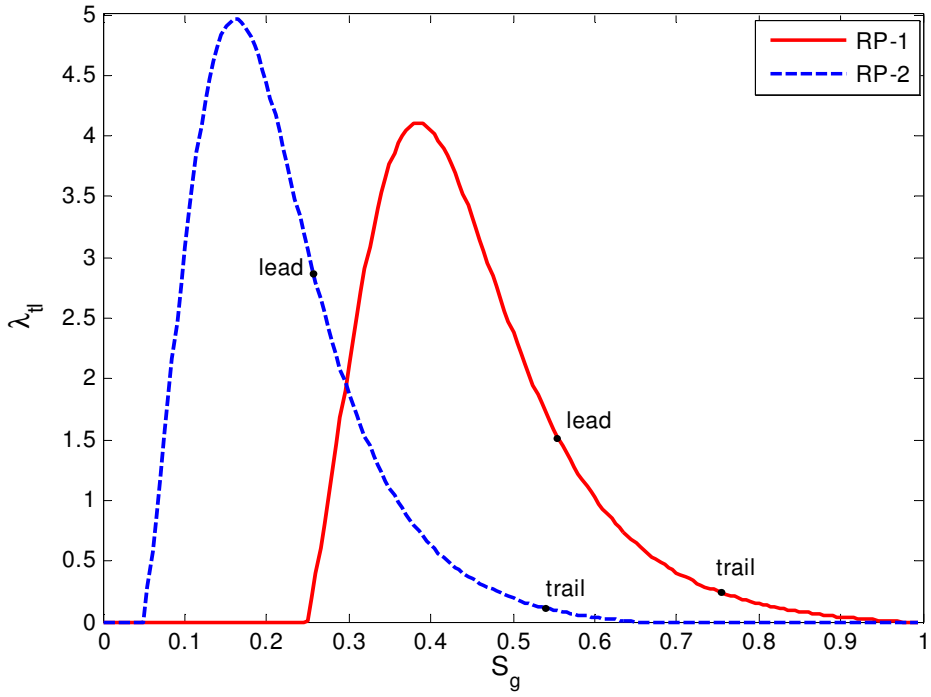

Figure 5-56: Comparison of regions of gas saturations and wave velocities accessed in the displacement.

5.7.2. Curvature of Relative Permeability Model

The curvature of relative permeability curves describes the degree of interference that one phase has with respect to flow of another phase. Models with steep curvature (RP-4) indicate more interference to flow than those with shallow curvature (RP-3), as shown in Figure 5-52. Fractional flow curves for the two cases are shown in Figure 5-57. Effect of curvature on solution structure is shown in Figure 5-58. The displacement using the RP-4 model is slower than that obtained using RP-3. Gas is less mobile at lower saturation in RP-4 than for RP-3 parameters. As in the previous example, the mobile region of RP-4 is shifted to higher gas saturations. Velocities at higher gas saturations for RP-4 are lower than those of RP-3, resulting in a slower displacement, as expected when there is more interference between flowing phases.

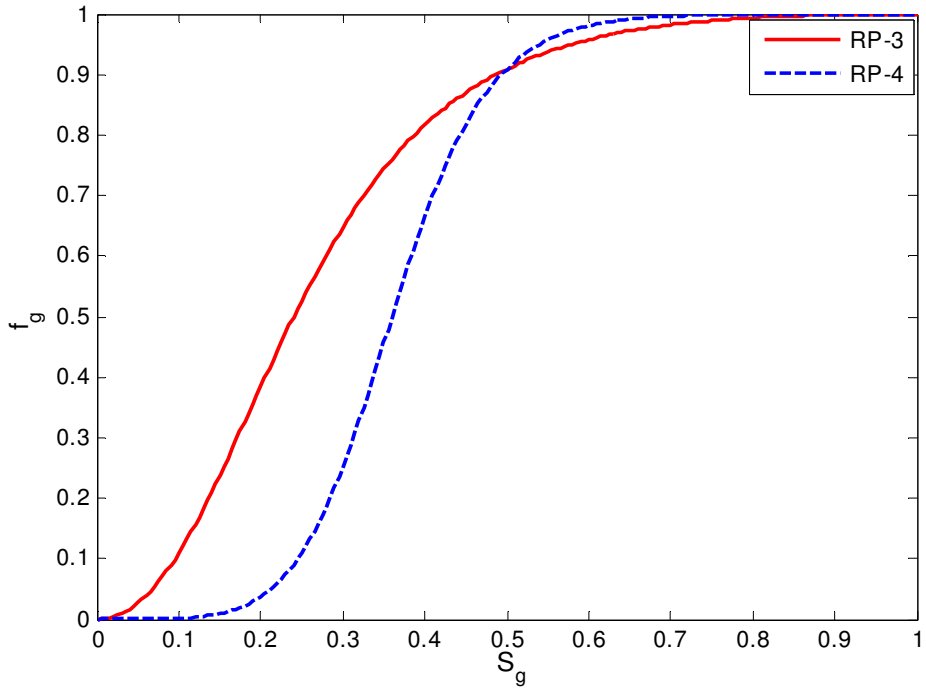

Figure 5-57: Fractional flow curves: RP-3 and RP-4.

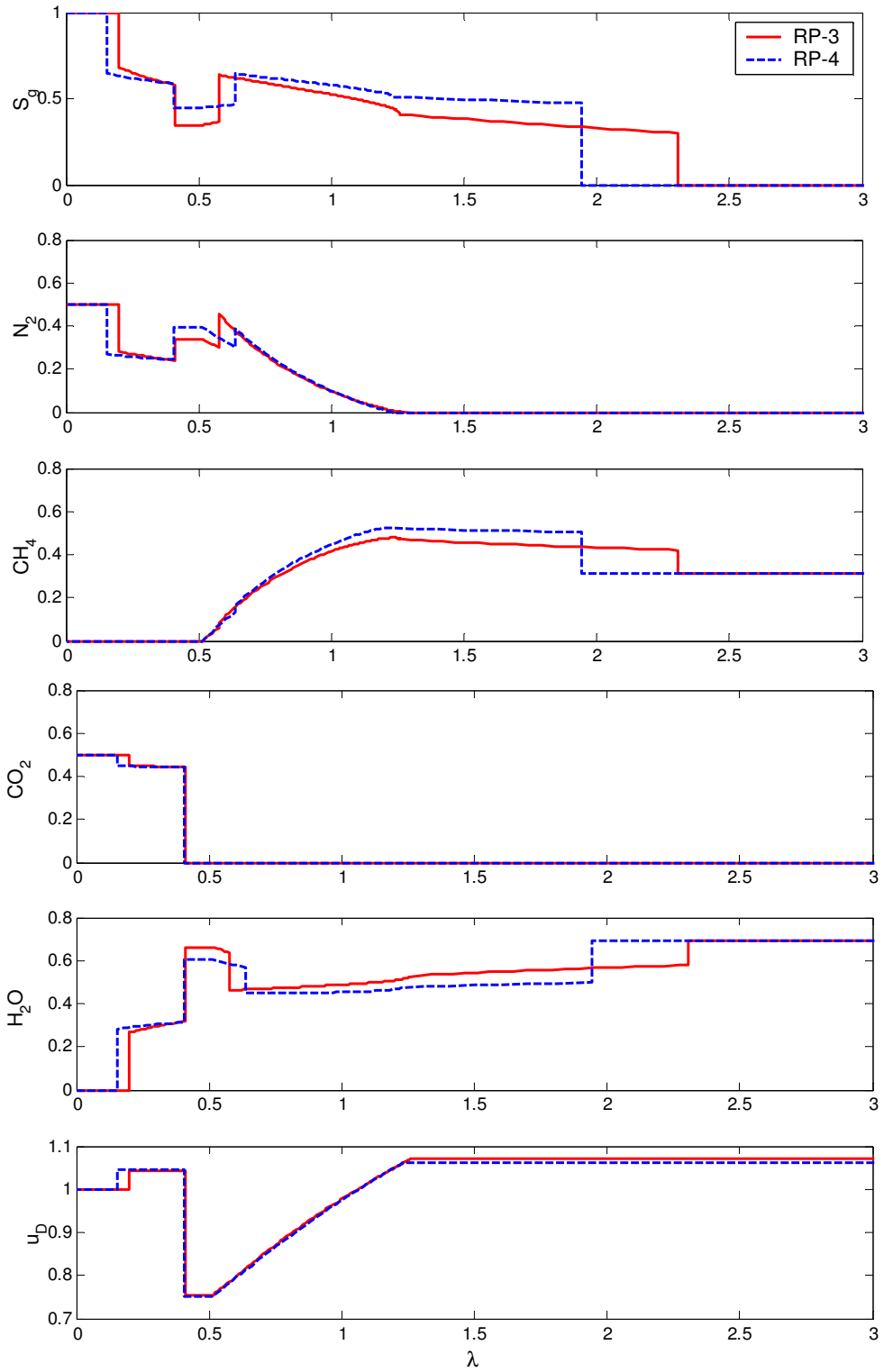

Figure 5-58: Comparison of solution profiles for RP-3 and RP-4 relative permeability models.

5.7.3. Low Endpoint Relative Permeability

Low gas mobility is modelled by a low gas endpoint relative permeability. Fractional flow curves for the RP-5 and RP-3 models are compared in Figure 5-59. Gas becomes mobile at higher gas saturations. Solution profiles for the low endpoint relative permeability model is shown in Figure 5-60. Because gas mobility is reduced, the displacement propagates slowly through the coal.

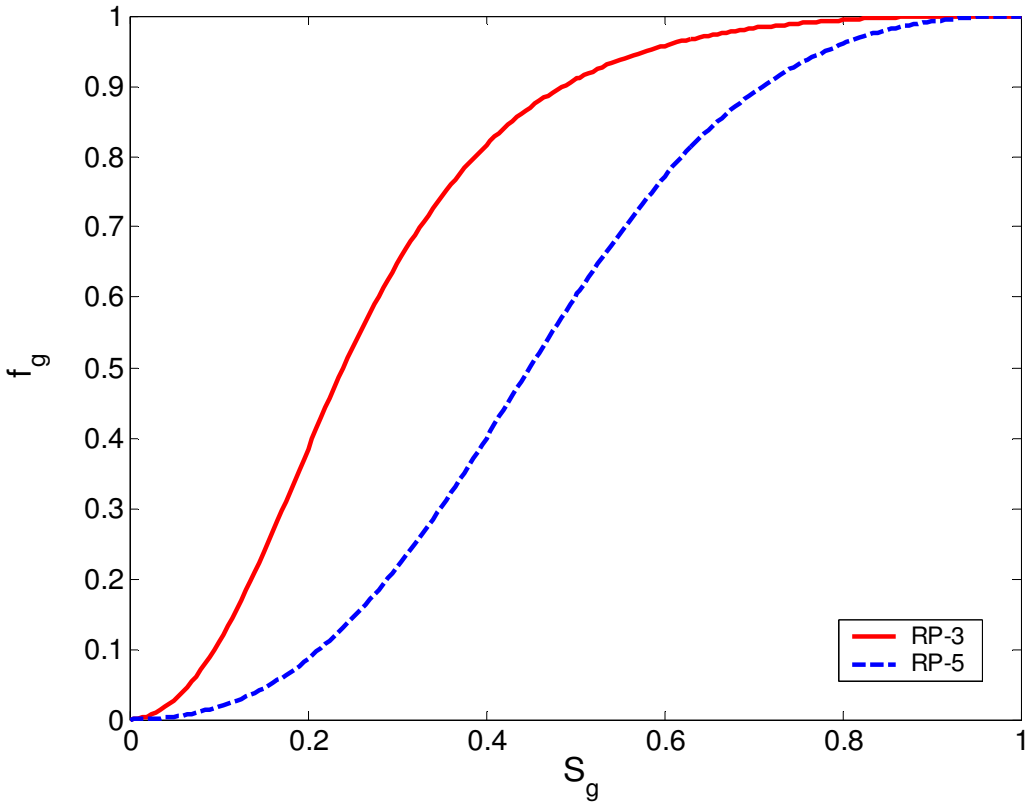

Figure 5-59: Comparison of fractional flow curves for RP-3 (high gas endpoint) and RP-5 (low gas endpoint).

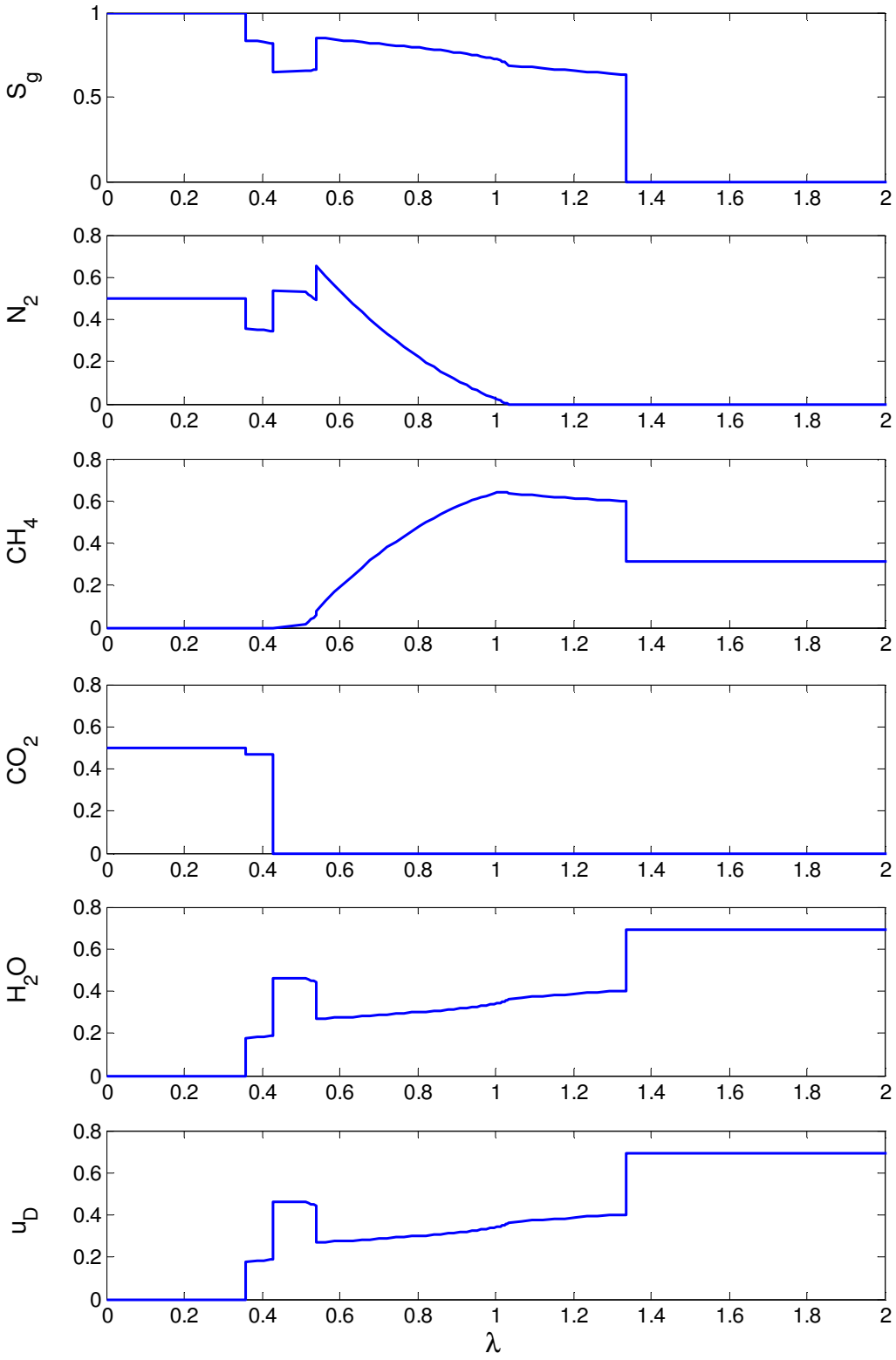

Figure 5-60: Solution profile for the RP-5 relative permeability model.

For all relative permeability models, solution structures remain the same. Injection, initial, and crossover tie lines remain unaffected because the initial and injection states are the same. There is a collection of compositions that satisfy the Rankine-Hugoniot condition compatible with the jump point on the injection tie line. These compositions create a curved surface in composition space. The crossover tie line is the intersection of the nontie-line path from the initial tie line with this curved surface. Because the injection and initial tie lines are unchanged, the crossover tie line remains unchanged.

The injection composition used in this example results in composition paths that include the degenerate tie line. This tie line is dependent on the relative permeability because it is affected by the nontie-line eigenvalues. The relative permeability parameters adjust the windows of mobile saturation and the tie-line eigenvalues. This affects the location of equal-eigenvalue points and tangent shock construction. For lower mobility gas displacements, the tangent shocks are slower and shocks occur at higher gas saturations. The degenerate shock is also slower, resulting in tie lines richer in N_2 where this shock occurs. Table 5-10 summarises the compositions of the degenerate tie line for the relative permeability cases considered. The degenerate tie line is dependent on the nontie-line paths traced from the equal-eigenvalue point of the initial tie line and the landing point of the tangent shock on the crossover tie line. The velocities of the key points change significantly, as do the saturation ranges spanned by the various solutions.

Table 5- 10: Summary of the composition of the degenerate tie line for the relative permeability cases considered.

case	x_{N2}	x_{CH4}	x_{CO2}	x_{H2O}	S_g	Λ
RP-1	0.1566	0.0457	0	0.7977	0.5513	0.5674
RP-2	0.1446	0.0659	0	0.7232	0.2859	0.6310
RP-3	0.1587	0.0420	0	0.7989	0.3653	0.5772
RP-4	0.1352	0.0817	0	0.7827	0.5490	0.6362
RP-5	0.1658	0.0302	0	0.8040	0.6621	0.5402

5.8. Adsorption Strength

Replacement ratio of CO_2 to CH_4 varies between coal types, ranging from 2:1 to 10:1 (Stanton *et al.*, 2001). Differences in gas affinity to the coal surface will determine the amount of gas added to or removed from the flowing phase as compositions propagate through the coalbed. This affects local flow velocity and speed of the displacement. Adsorption strength appears in the accumulation term of the material balance expression. In the continuous solution, adsorption strength affects the nontie-line eigenvalue. The accumulation term is also present in the shock balance, affecting shock velocities if discontinuous segments are required. This section describes the effect of adsorption strength on composition path. Injection and initial compositions are fixed at 0.4 N_2 and 0.6 CO_2 and 0.3103 CH_4 0.6987 H_2O respectively. A range of CO_2 to CH_4 and CO_2 to N_2 replacement ratios are considered. Table 5-11 summarises the adsorption cases presented.

Table 5-11: Adsorption cases considered in adsorption strength investigation.

case	N_2		CH_4		CO_2	
	V_m (scf/ton)	B (psi^{-1})	V_m (scf/ton)	B (psi^{-1})	V_m (scf/ton)	B (psi^{-1})
A-1	200	0.002	300	0.003	1000	0.01
A-2	200	0.002	400	0.004	1000	0.01
A-3	200	0.002	500	0.005	1000	0.01
A-4	200	0.002	400	0.004	600	0.006
A-5	200	0.002	400	0.004	800	0.008
A-6	200	0.002	400	0.004	1000	0.01

5.8.1. Varying CO_2-CH_4 Replacement Ratio

Figure 5-61 shows the effect of varying adsorption strength of CO_2 relative to CH_4 on the solution profile. The key tie lines in the displacement remain constant. Because there is no CH_4 in the injection gas mixture, the trailing edge of the displacement remains unchanged. As CH_4 affinity increases, a larger amount of CH_4 is desorbed for the same amount of CO_2 injected, resulting in a greater

increase in local flow velocity. The velocity of the leading edge of the displacement is increased. Varying CH_4 adsorption affects the nontie-line path of the initial segment.

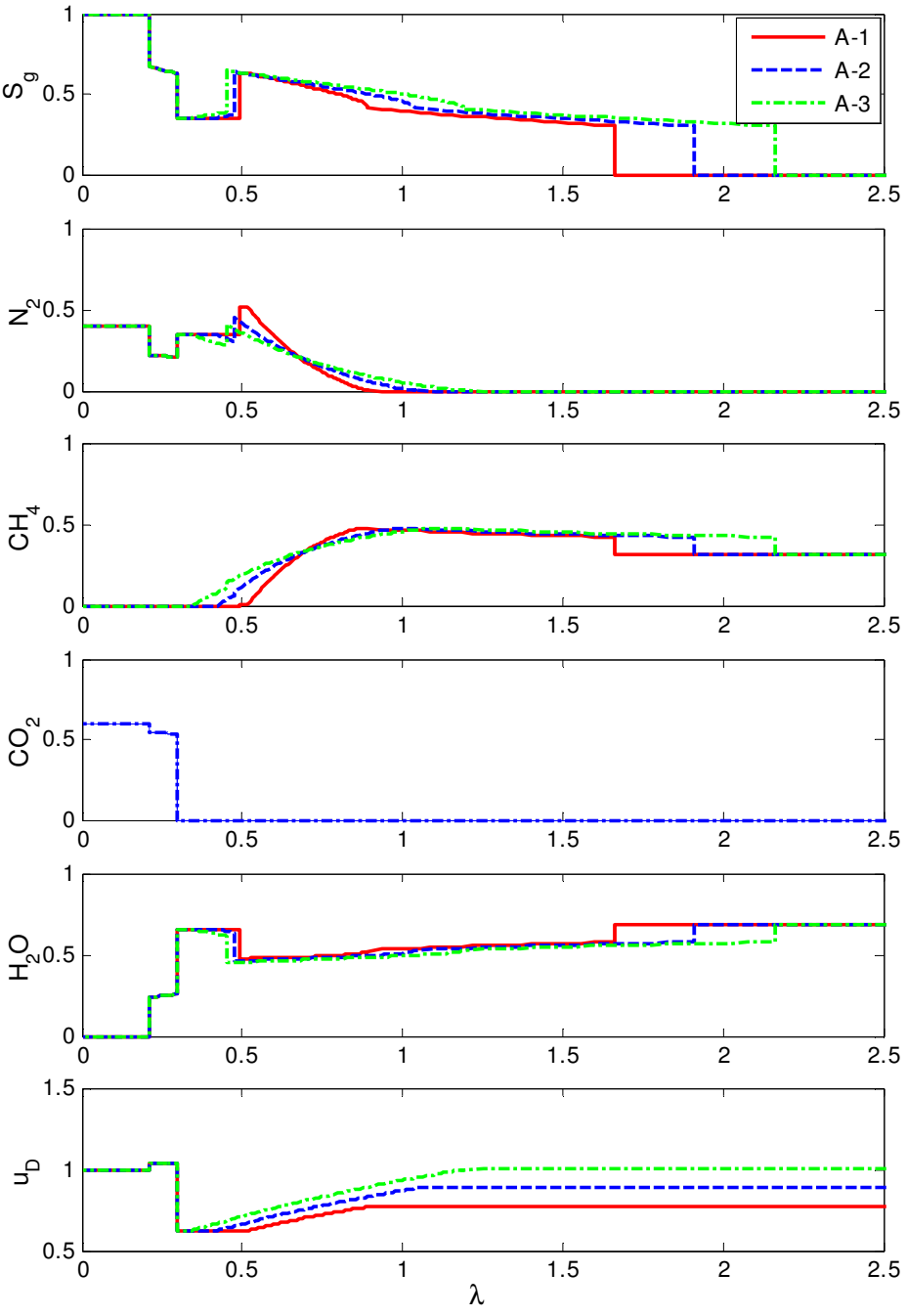

Figure 5-61: Effect of varying CO_2-CH_4 replacement ratio on solution profile.

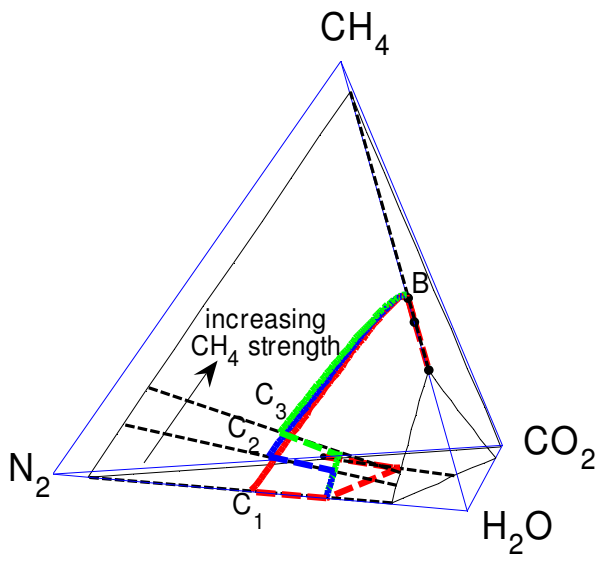

Figure 5-62: Effect of varying CO_2-CH_4 replacement ratio on composition path.

Figure 5-62 shows the effect of CH_4 adsorption strength on composition path. Stronger CH_4 adsorption offsets the effect of CO_2 strength, resulting in slower nontie-line paths in the $N_2/CH_4/H_2O$ ternary system (B to C). Increasing the CH_4 adsorption strength relative to CO_2 strength moves the location of the degenerate tie line closer to the initial tie line, farther away from the ruled surface of the injection tie line. For the lowest CO_2 to CH_4 replacement ratio used in this analysis, the nontie-line path wave velocities are sufficiently reduced that the genuine shock along the crossover tie line is slow enough that Type III-A composition path is allowed. Due to the increased adsorption strength of CH_4 relative to N_2, the eigenvalues of nontie-line path are reduced, producing a longer nontie-line rarefaction up to the degenerate tie line, resulting in a longer time to recover the CH_4 in the coalbed completely.

5.8.2. Varying CO_2-N_2 Replacement Ratio

Figures 5-63 and 5-64 shows the effect of varying the CO_2 to N_2 replacement ratio on solution profile and composition path. Key tie lines in the displacement remain the same. Adsorption is a function of gas phase composition; changes to the adsorption function affect the nontie-line eigenvalues. Figure 5-65 shows the effect of increased CO_2 adsorption strength on the nontie-line eigenvalue. As CO_2 adsorption strength is increased, the wave velocities of the nontie-line paths are decreased. The degenerate tie line occurs at a slower eigenvalue, pulling it closer to the crossover tie line. CO_2 adsorption strength also affects the trailing edge of the displacement. For higher CO_2 adsorption strengths, the jump point of the tangent shock occurs at a higher gas saturation than for lower CO_2 adsorption strengths because CO_2 is more readily adsorbed onto the coal surface. Stronger CO_2 adsorption results in a slower semishock velocity connecting injection and crossover tie lines. Increased CO_2 adsorption strength results in a larger proportion of the injection gas adsorbed onto the coal, producing a larger decrease in local flow velocity and a slower displacement. Significant differences in breakthrough times and solution structure (A-1) are observed when adsorption strengths are manipulated, demonstrating the need for confidence in the values of these parameters.

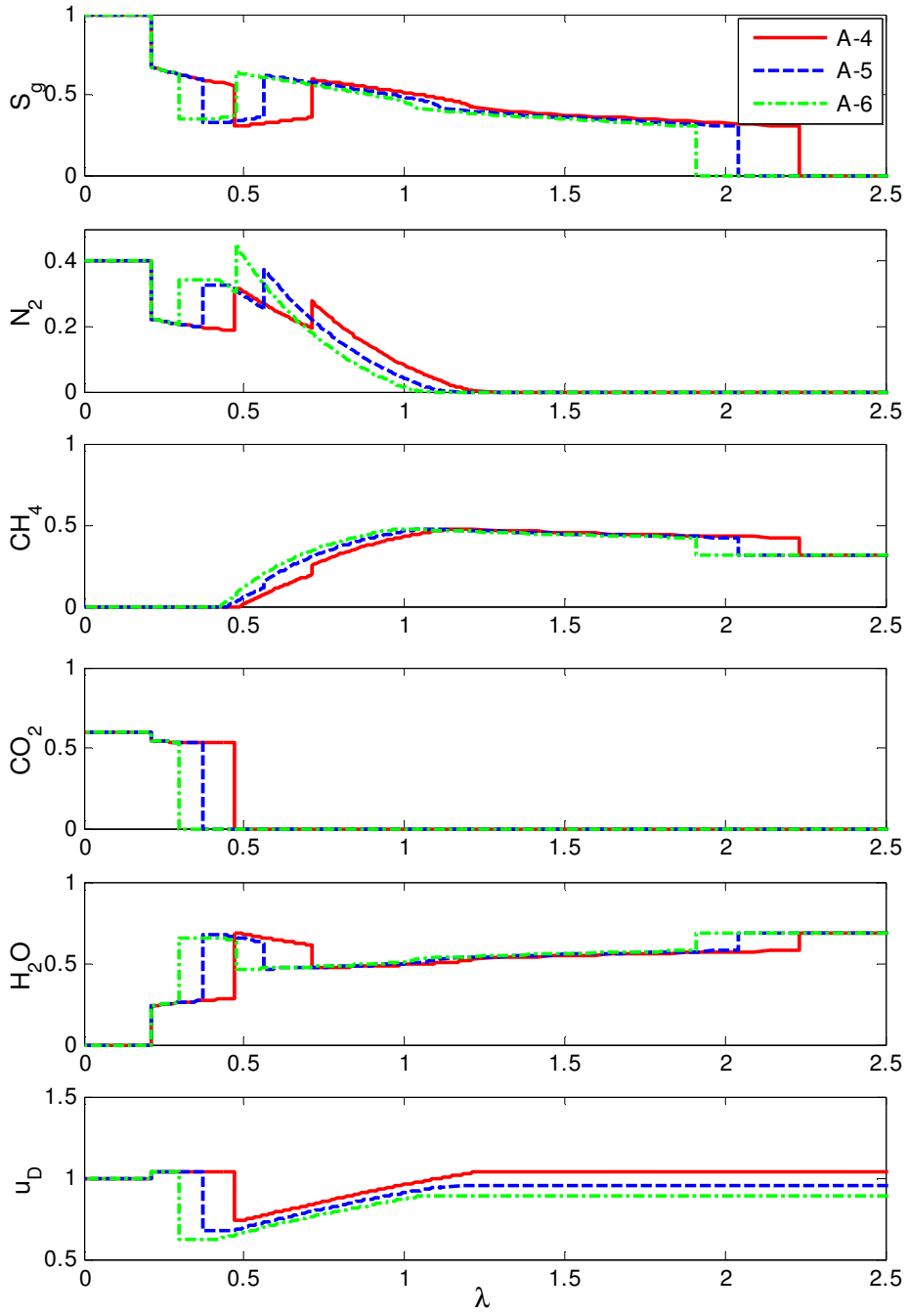

Figure 5-63: Effect of varying CO_2-N_2 replacement ratio on solution profile.

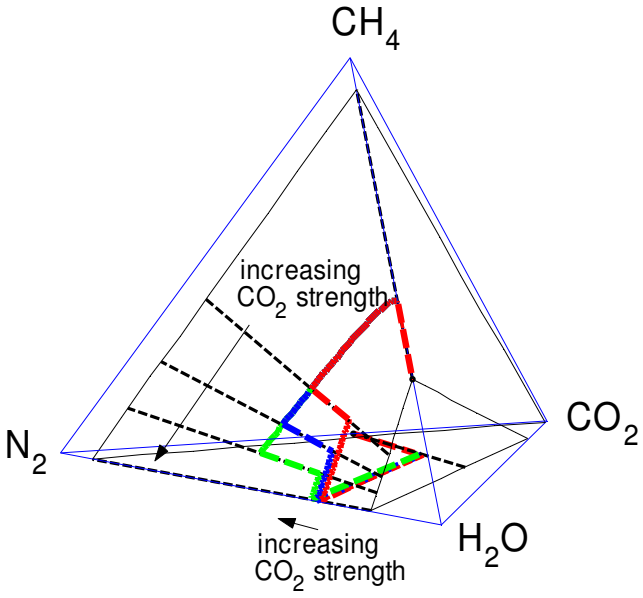

Figure 5-64: Effect of varying CO_2-N_2 replacement ratio on composition path.

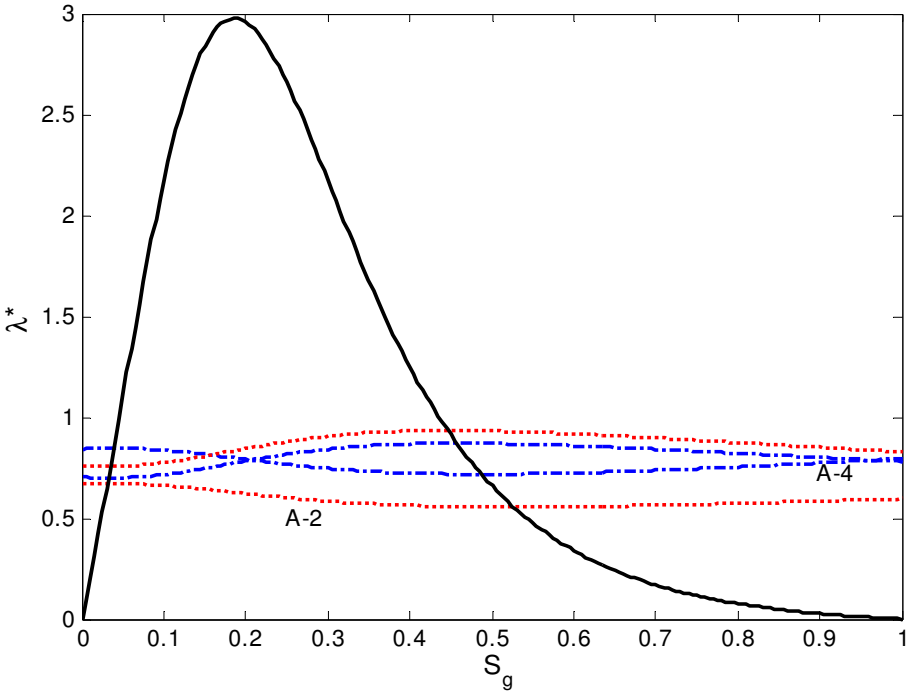

Figure 5-65: Effect of adsorption on nontie-line eigenvalues.

5.8.3. Effect of Adsorption on Solution Structure

The example solutions provided thus far show adsorption effects overprinting and reinforcing solution structures controlled by volatility effects. This section examines the effect of adsorption strength and volatility on solution structure. This is illustrated in a simple three component system. K-values and adsorption constants are summarized in Table 5-12. Pure C_2 is injected into initial composition of 0.3103 C_1 and 0.6987 C_3.

Table 5-12: Summary of adsorption constants and K-values used in the adsorption strength investigation.

	K_i	V_{mi} (scf/ton)	B_i (psi^{-1})
C_1	3	707	0.0066
C_2	1.2	444	0.0034
C_3	0.1	0	0

C_2 is less strongly adsorbing than C_1, so a rarefaction is expected for C_2 displacing C_1. If only volatility effects are considered, a shock is expected when a low volatility intermediate is injected to displace a higher volatility component. Solution construction commences at the shortest tie line, and in this case, it is the injection tie line. Eigenvalues increase as the nontie-line path is traced from the injection tie line to the initial tie line (Figure 5-66), and a continuous variation is allowed by the velocity rule. A nontie-line rarefaction connects injection and initial states, resulting in a solution that contrasts with the behaviour of the Type I solution presented in Chapter 4, where a shock connects injection and initial tie lines. Composition path and solution profile are shown in Figures 5-67 and 5-68. Because C_2 is less strongly adsorbing, partial pressure reduction is required to desorb the more strongly bound component. For the adsorption constants used, adsorption effects control the displacement.

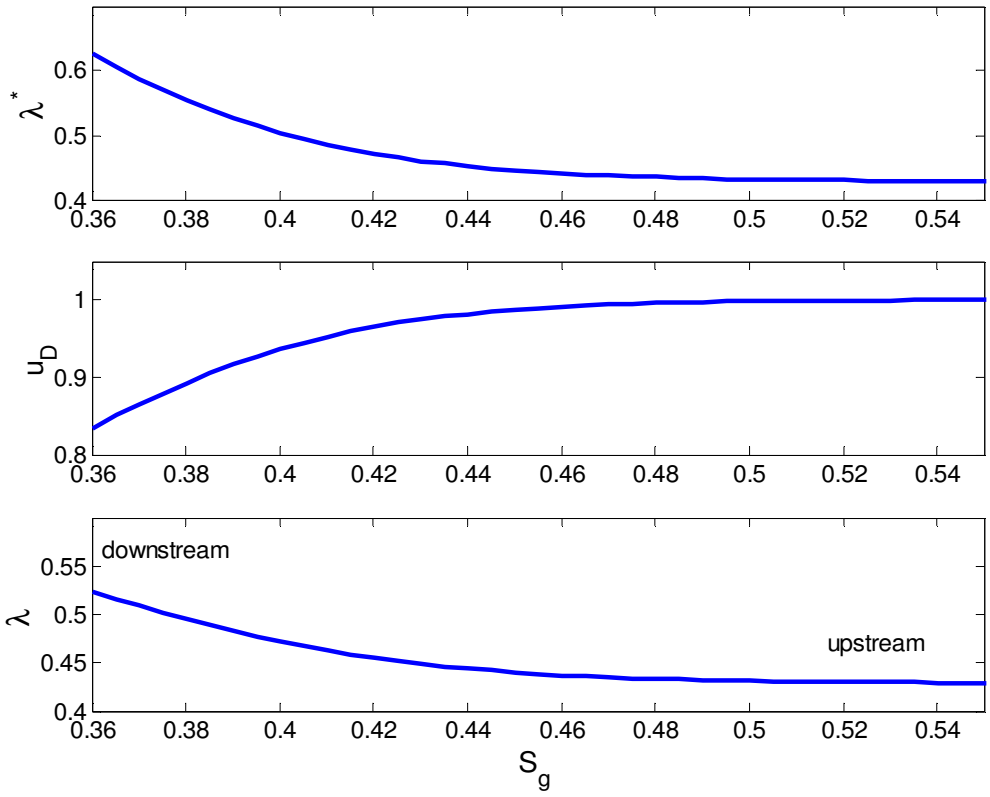

Figure 5-66: Variation of eigenvalues from injection tie line to initial tie line.

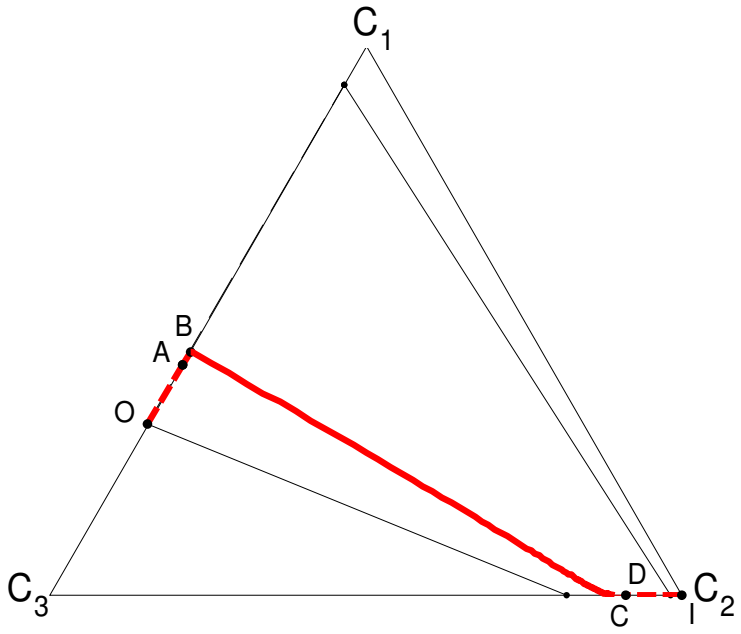

Figure 5-67: Composition path where the adsorption strength of C_1 is greater than the adsorption strength of C_2.

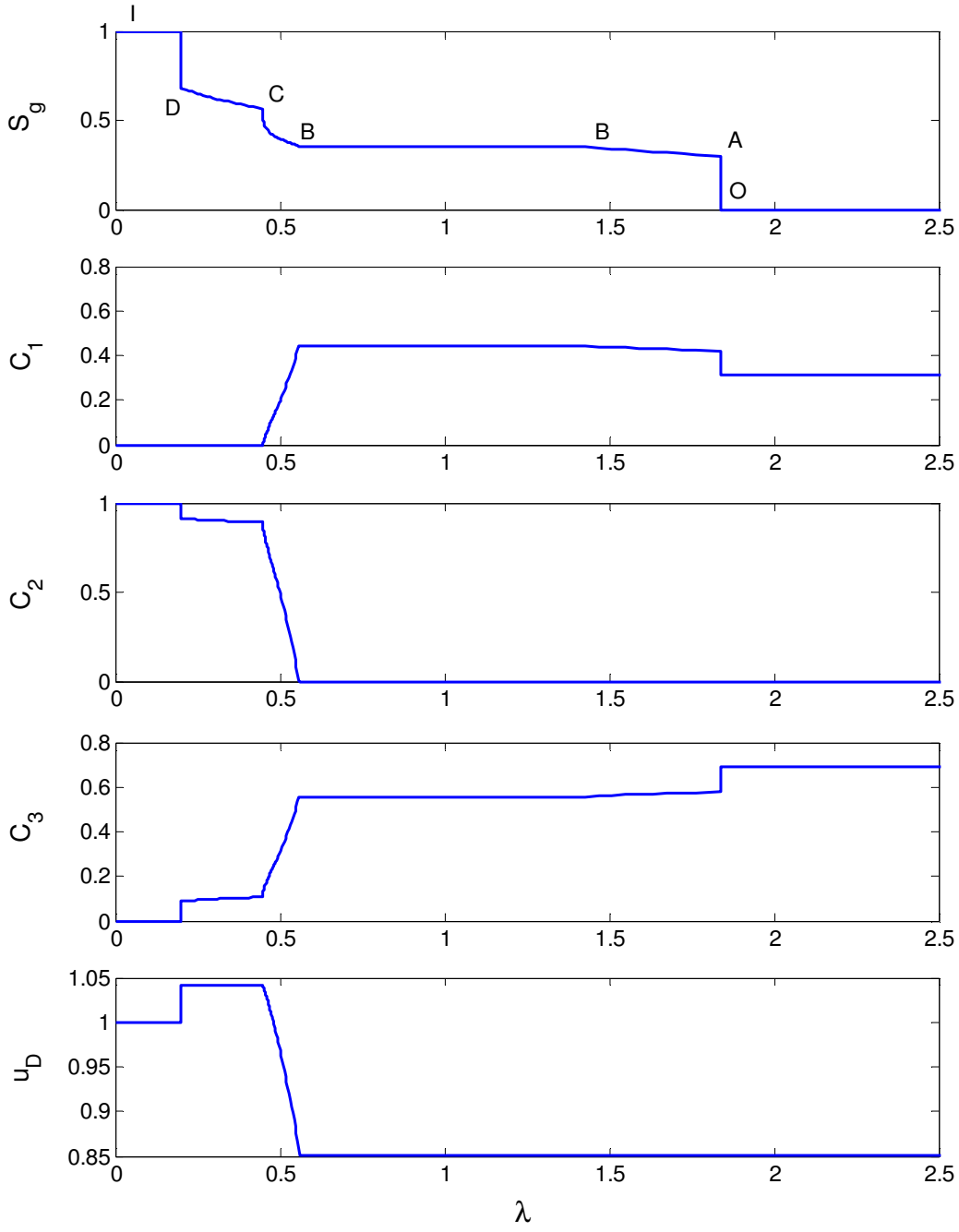

Figure 5-68: Solution profile where the adsorption strength of C_1 is greater than the adsorption strength of C_2.

Eigenvalue variation for a range of adsorption strengths is shown in Figure 5-69. When adsorption and volatility effects counteract each other, the resulting solution structure is a balance between these effects. For some combinations of adsorption strength and volatility, the composition paths are similar to nonadsorbing systems, while for other combinations, adsorption strength dominates and the solution structure is controlled by adsorption.

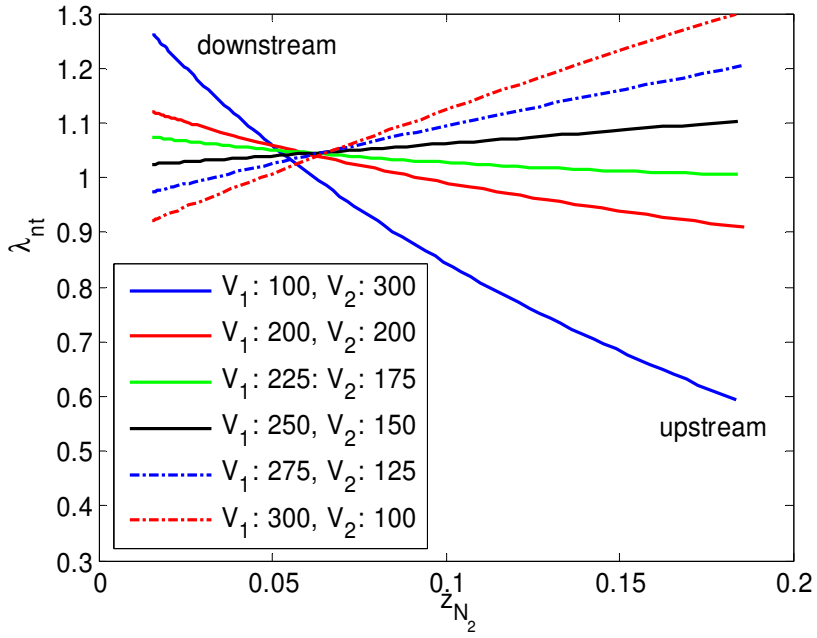

Figure 5-69: Variation of nontie-line eigenvalues from injection tie line to initial tie line.

5.9. Sorption Hysteresis

Adsorption hysteresis has been observed in pure gas adsorption in some coals (Harpalani and Zhao, 1989, Bell and Rakop, 1986). This phenomenon is attributed to surface heterogeneities (Seri-Levy and Avnir, 1993). As gas is adsorbed onto the coal surface, matrix swelling occurs, reducing pore size. On desorption, matrix shrinkage results in increasing the openings of the pore throats.

These changes in the matrix as components adsorb and desorb from the surface can create surface heterogeneities that affect the amount of gas adsorbed. This effect is manifest as desorption curves where the loading of gas on coal surfaces is greater than adsorption at the same pressure. To incorporate sorption hysteresis in the analytical model, additional conditions on the sorption constants are required:

$$a_{iD} = a_{iD}^{desorb}, \quad \frac{dy_i}{d\eta} < 0 \tag{5.1}$$

$$a_{iD} = a_{iD}^{adsorb}, \quad \frac{dy_i}{d\eta} > 0 \tag{5.2}$$

$$a_{iD}^{desorb}\left(y_i^{max}\right) = a_{iD}^{adsorb}\left(y_i^{max}\right). \tag{5.3}$$

Adsorption and desorption constants are summarised in Table 5-13. Corresponding isotherms are shown in Figure 5-70. To illustrate the effect of sorption hysteresis on displacement behaviour, a mixture of 0.9 N_2 0.1 CO_2 was injected into a coalbed with initial conditions of 0.3103 CH_4 and 0.6987 H_2O. Figure 5-71 compares solution profiles for displacements with and without sorption hysteresis.

Table 5-13: Adsorption and desorption constants used to model adsorption hysteresis effects.

component	adsorption		desorption	
	V_{mi} (scf/ton)	B_i (psi^{-1})	V_{mi} (scf/ton)	B_i (psi^{-1})
N_2	272	0.0024	226	0.0053
CH_4	811	0.0024	609	0.0148
CO_2	1760	0.0052	1510	0.0292

Adsorption hysteresis affects breakthrough and bank arrival times, and shifts overall component concentrations. Because initial and injection compositions are

fixed, key tie lines remain the same and the solution profiles are merely stretched or compressed relative to the case where hysteresis is not considered. When sorption hysteresis is considered, N_2 adsorption strength increases and the propagation speed on N_2 through the coalbed is decreased. This effect is shown in the broader bank where N_2 desorbs CH_4, compared to the system without hysteresis. More CH_4 is bound on the coal on the desorption path than on the adsorption path, therefore, more CH_4 molecules are added to the flowing phase as CH_4 is desorbed than when the adsorption path is used in the displacement. This results in a greater increase in local flow velocity and a faster leading segment. In the solution presented, when hysteresis effects are considered, the solution structure remains unchanged, but the velocities are adjusted relative to changes in adsorption strength.

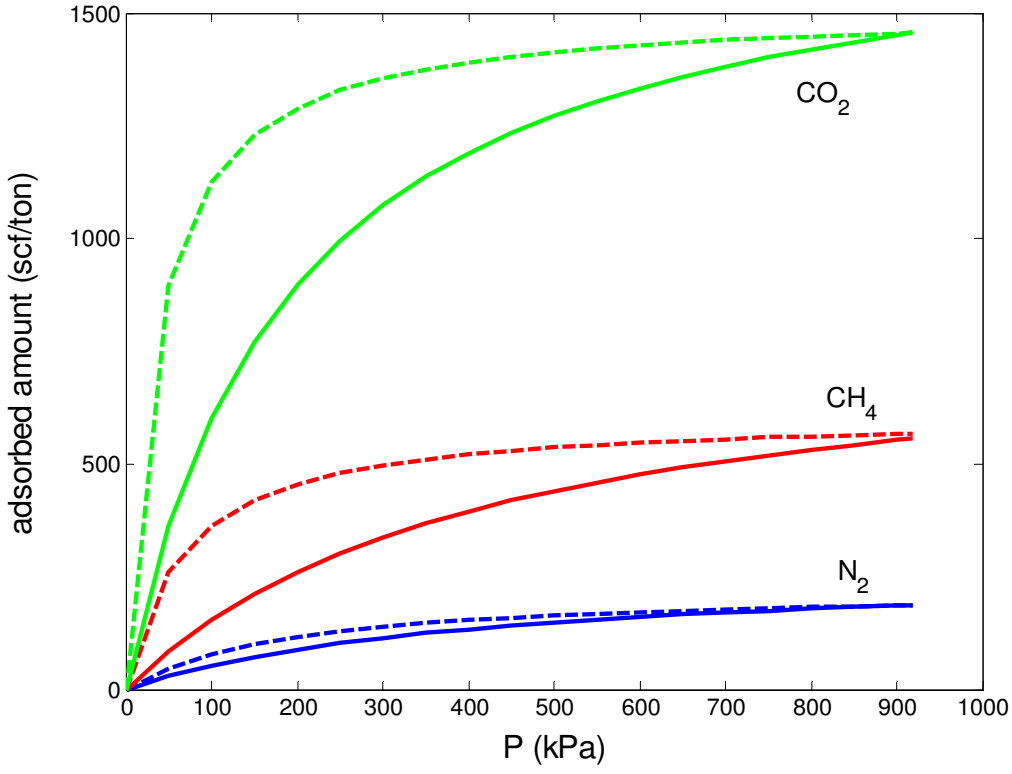

Figure 5-70: Adsorption and desorption isotherms used to model adsorption hysteresis.

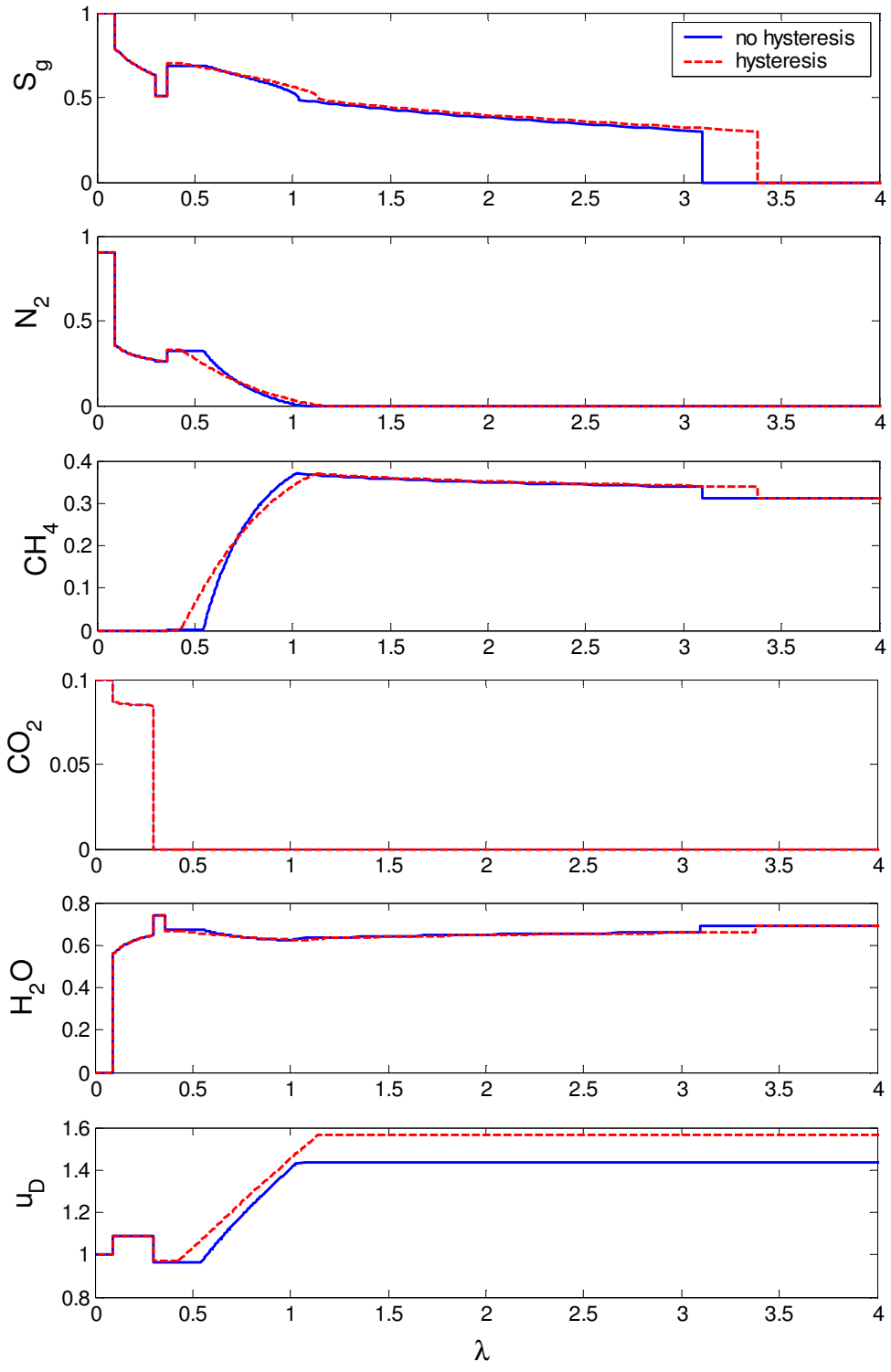

Figure 5-71: Solutions profiles for displacement with and without adsorption hysteresis.

5.10. Realistic Phase Behaviour

Solutions presented thus far do not reflect realistic behaviour of component partitioning between gas and aqueous phases. In this section, the initial assumption of constant K-values to evaluate component partitioning between aqueous and gaseous phases is relaxed. The Peng-Robinson equation of state (Peng and Robinson, 1976) was used to evaluate phase densities. Thermodynamic parameters are summarised in Table 5-14. A constant mobility ratio was assumed (M = 18.5). Injection of a mixture of 0.5 N_2 and 0.5 CO_2 into a coalbed saturated with CH_4 and H_2O at 3000 kPa and 30ºC is considered.

Composition path and solution profiles are presented in Figures 5-72 and 5-73. Table 5-15 presents equilibrium compositions for a variety of total molar compositions. Gas components have very low solubilities in the aqueous phase and H_2O has low volatility in the gas phase. The difference in K values between H_2O and gas components results in the phase boundaries expanding to occupy almost the entire quaternary space. Composition paths are compressed towards the H_2O vertex. However, the solution structure remains the same as the constant K value solutions presented earlier. Due to the low solubility of H_2O in the gas phase, many pore volumes of CO_2 are required to vaporise all the H_2O in the coalbed. CH_4 recovery is determined by the nontie-line eigenvalue of the landing point of the crossover tie line.

Table 5-14: Thermodynamic properties of components used in example solutions.

	P_c (kPa)	T_c (ºK)	ω	κ_{ij}			
				N_2	CH_4	CO_2	H_2O
N_2	3399	126.1	0.037	0	0.0278	-0.0315	0
CH_4	4599	190.6	0.011	0.0278	0	0.0933	0
CO_2	7377	304.1	0.224	-0.0315	0.0933	0	0.0737
H_2O	22064	647.3	0.344	0	0	0.0737	0

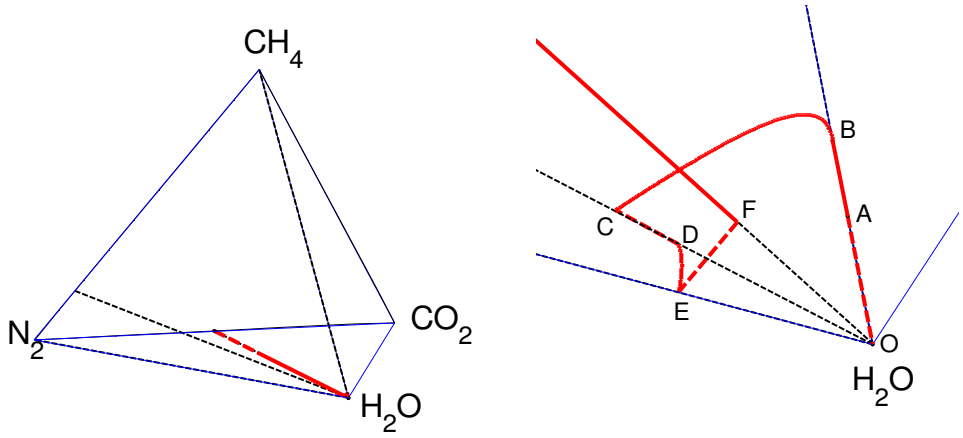

Figure 5-72: Composition path for injection of 0.5 N_2 and 0.5 CO_2 (full quaternary space shown on left, enlargement of H_2O apex shown on right).

Table 5-15: Equilibrium compositions for a variety of mixtures in the $N_2/CH_4/CO_2/H_2O$ system. There is low solubility of gases in the water phase. K values do not change significantly.

z				y				K			
N_2	CH_4	CO_2	H_2O	N_2	CH_4	CO_2	H_2O	N_2	CH_4	CO_2	H_2O
0.10	0.05	0.10	0.75	0.400	0.200	0.399	0.002	417492	50150	1733	0.0015
0.40	0.05	0.10	0.45	0.726	0.091	0.182	0.001	423062	50266	1703	0.0014
0.80	0.05	0.10	0.05	0.841	0.053	6.2×10^{-5}	0.999	424217	50221	1691	0.0014
0.50	0.05	0.40	0.05	0.526	0.053	0.420	0.001	418047	50013	1731	0.0014

Presence of the additional degenerate tie line does not affect the technique developed by Wang (1998) for the analytical determination of minimum miscibility pressure. Miscibility occurs when one of the key tie lines is a critical tie line. The degenerate tie line is bounded by the crossover and initial tie lines. The size of the phase envelope varies monotonically from crossover tie line to initial tie line. Of the three tie lines, the degenerate tie line will always have the intermediate length. Therefore, the degenerate tie line will never be a critical tie line, and the presence of the degenerate tie line does not affect development of miscibility in flue gas injection for enhanced oil recovery, such as N_2 and CO_2 injection in reservoir containing CH_4 and C_{10}.

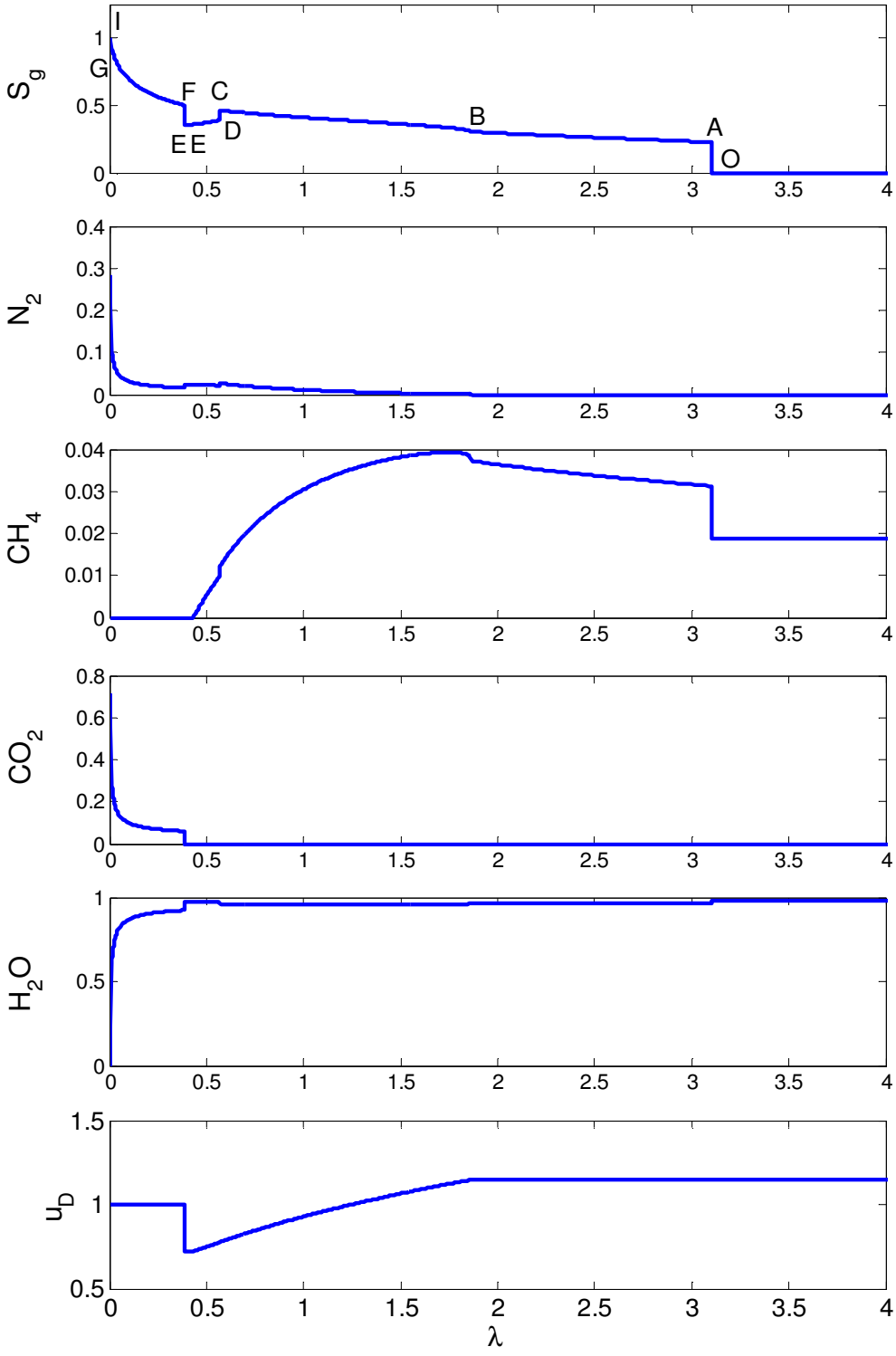

Figure 5-73: Solution profile for injection of 0.5 N_2 and 0.5 CO_2.

5.11. Summary

The theory for multicomponent, multiphase gas injection has been extended to model four-component, two-phase flow in systems with adsorption and volume change on mixing. Four-component systems are of interest, because they are the simplest representation of flue gas injection into a water-saturated coalbed. A range of gas injection conditions spanning the composition space was considered. Solution construction in the four-component system is an extension of that in the ternary systems.

New components of the solution structure were identified when mixtures of the most volatile gas component and least volatile intermediate gas component are injected. The first solution structures that use the $\frac{\partial \lambda_{nt}}{\partial S} > 0$ branch of the nontie-line path, nontie-line paths that do not utilise the equal-eigenvalue point, path switches between two nontie-line paths and a degenerate shock are presented. These structures are also present in absence of adsorption. However they were not observed by previous researchers because flue gas injection was not investigated systematically.

Chromatographic separation of the injection gas mixture occurs as the gas propagates through the coal. More strongly adsorbing components propagate through the coal at a slower rate than weakly adsorbing components. When N_2 is present in the injection gas, it will travel quickly through the coal and contaminate the gas produced, requiring an additional separation prior to sales.

Chapter 6

Conclusions

The analytical theory for multicomponent, multiphase flow was extended to model systems with adsorption and volume change on mixing. These solutions can be applied to model CO_2 sequestration and ECBM in water-saturated coals, providing insight into the interplay among phase behaviour, convection and gas adsorption/desorption from the coal surface. The main contributions of this work are:

- The first solutions for two-phase, four-component flow with adsorption and volume change as components transfer between gas and liquid phases were developed. Solutions for a variety of injection and initial conditions are presented.

- A new solution structure involving a path switch between two nontie-line paths was discovered. This occurs in special cases of two phase injection mixtures. The analysis for the entropy condition for two nontie-line paths connected by a degenerate shock is presented in ternary systems with

constant K-values. These structures also occur in nonadsorbing systems under similar injection conditions.

- The presence of the degenerate tie line does not affect miscibility development in systems without adsorption. In the cases presented, the degenerate tie line is bound between the initial tie line and the crossover tie line. Because tie line lengths vary monotonically between these key tie lines, the degenerate tie line will be of intermediate length and will never be a critical tie line.

6.1. Conclusions

Solutions to binary, ternary and quaternary systems with adsorption were presented. Conclusions from this analysis are divided into two categories: those applicable to ECBM and CO_2 sequestration operations, and those that are more general to the analytical theory for gas injection.

6.1.1. ECBM and CO_2 Sequestration

The analytical theory for gas injection with adsorption and volume change on mixing is useful for understanding ECBM recovery processes and CO_2 sequestration in deep, unminable coal seams. An extended Langmuir isotherm was used to model adsorption and desorption of gases onto and from the coal surface. The resulting solutions are similar to those without adsorption. Solutions were constructed for a range of gas injection mixtures pertinent to ECBM and CO_2 sequestration applications. Analysis of these solutions leads to the following conclusions:

- Solution construction theory developed for multicomponent, multiphase flow can be extended to systems with adsorption and desorption of components from a solid surface. Analytical theory was previously developed to model multiphase, multicomponent

flow in polymer systems, but did not consider changes in volume as components transferred between gas and liquid phases (Johansen and Winther, 1989), and for ECBM in gas phase systems (Zhu, 2003). In the solutions presented by Zhu, compositions varied along distinct paths in the single phase region. In gas-water systems, multiphase effects dominate solution structure in ECBM systems and paths in the single phase region are replaced by shocks into and out of the two-phase region.

- Adsorption reduces characteristic wave velocities. Solution structures in cases with adsorption are the same as those found in the nonadsorbing case, but are stretched or compressed according to the adsorption strength.

- Solution structures are influenced by relative adsorption strength and volatility. In systems where components that adsorb more strongly and are less volatile displace components that are less strongly adsorbed and more volatile (CO_2 injection to displace CH_4), solutions exhibit shocks between equilibrium states (Type I). In systems where a weakly adsorbing component displaces a strongly adsorbing component (N_2 injection to displace CH_4), a rarefaction connects equilibrium states (Type II). The balance between adsorption strength and volatility can lead to solution structures different from those observed in corresponding nonadsorbing systems.

- Similar to the single phase solutions reported by Zhu (2003), volume change associated with gas species removed from the mobile phase as they are adsorbed onto the coal surface or when gas species are added to the mobile phases as they are desorbed from the coal surface can produce significant changes in local flow

velocity as compositions evolve through the displacement in multiphase systems. In cases where there is significant adsorption of gas injected (high concentration CO_2 in the injection gas), multivalued compositions may result if the standard solution construction procedures for nonadsorbing systems are applied (Types III-C and III-D solutions). In these situations, the crossover tie line lies only in the ruled surface of the initial tie line, not in the ruled surfaces of both the injection and initial tie lines which is the case in nonadsorbing systems. Conservation of mass and the velocity rule constraint still apply to solution construction, and segments of variation must obey these constraints.

- When gas mixtures are injected, gases chromatographically separate based on their relative adsorption strength and volatility. Components that are more strongly adsorbing and less volatile propagate more slowly than components that are less strongly adsorbing and more volatile. Surface adsorption properties of coal and phase behaviour act as a chromatograph to separate injection gas mixtures, which may be useful in applications for CO_2 sequestration and acid gas sweetening.

- Gas injection into coalbeds drives the partial pressure of CH_4 to zero, resulting in efficient recovery of CH_4 is achieved when gas is injected into a coalbed. Gas mixtures that are rich in N_2 recover CH_4 faster than gas mixtures rich in CO_2. Because CH_4 is more strongly adsorbing than N_2, there is a increase in local flow velocity when N_2 is injected. When CO_2 is injected, there is a decrease in local flow velocity because CH_4 is less strongly adsorbing than CO_2. N_2-rich displacements propagate faster through the coal than CO_2-rich displacements. For all gas injection mixtures presented,

CH_4 was recovered within less than three pore volumes injected. Depending on the goal of the gas injection scheme, acceleration of CH_4 production or delay of CO_2 breakthrough, injection gas composition can be tailored to meet the objectives of the gas injection project.

- Displacement in undersaturated coalbeds is slower than in saturated coals due to the additional volume change associated with the phase change shock from two-phase conditions to single phase initial conditions. In undersaturated systems, additional gas is required to bring the coal to saturated conditions. Breakthrough time of the leading shock is greater than one pore volume injected. This delay in breakthrough compared to saturated systems makes CO_2 sequestration in undersaturated coals more attractive than in saturated coals.

6.1.2. Analytical Theory of Gas Injection

The new composition paths observed in this dissertation also occur in systems without adsorption. Analysis of these solutions yields the following conclusions:

- In systems where initial or injection conditions are undersaturated, if nonlinear functions are present in the accumulation term of the governing equation, phase change shocks entering and leaving the two-phase regions do not occur along a tie line extension, as they do in nonadsorbing systems. The tie-line extension analogue in these systems is found by solving for equilibrium concentration that satisfies the Rankine-Hugoniot with the undersaturated state.

- A new shock structure, the degenerate shock, which connects two nontie-line paths, was found. The conditions under which this

structure occurs in ternary and quaternary systems are delineated. In ternary systems, the degenerate shock occurs when two-phases are simultaneously injected. This situation arises when the gas saturation associated with the gas fractional flow of the injected fluid is low enough that the gas saturation increases from upstream to downstream conditions. The specific gas saturation is determined by the mobility ratio and phase behaviour. In quaternary systems, this structure can occur when mixtures of the most strongly adsorbing and least volatile component and the least strongly adsorbing and most volatile component are injected. If enough of the more strongly adsorbing gas is removed from the flowing phase, a two-phase mixture with low mobile gas saturation is created in the displacement resulting in a nontie-line path variation which follows the $\frac{\partial \lambda_{nt}}{\partial S} > 0$ variation up to the degenerate tie line.

- When the degenerate shock is present in the solution structure, N_c key tie lines are required to construct a composition path connecting injection and initial states that obeys the velocity rule and entropy condition. The N_c key tie line structure also occurs in nonadsorbing systems.

- The degenerate structure introduces another composition path which pulls the path further away from the dilution line, making it difficult for numerical schemes to resolve. Higher order numerical methods which have the goal of modelling CO_2 sequestration and flue gas injection must be capable of accurately and efficiently resolving the degenerate structure. The degenerate structure occurs over a small velocity range relative to the continuous variation

features. Adaptive refinement within this region would efficiently capture this structure.

- A new allowable composition path which follows the $\frac{\partial \lambda_{nt}}{\partial S} > 0$ branch of the nontie-line path from the crossover tie line to the initial tie line without passing through the equal-eigenvalue point on the initial tie line is presented. This path occurs in two-phase ternary injection and quaternary gas injection scenarios when the upstream gas saturation on the injection tie line (in the two-phase ternary system) or crossover tie line (in the quaternary system) is less than the gas saturation of the landing point of the $\frac{\partial \lambda_{nt}}{\partial S} > 0$ branch traced from the equal-eigenvalue point of the initial tie line. Although gas saturation increases as components vaporise into the gas phase, in this displacement, the gas saturation is so low that it remains the least mobile phase, resulting in a slow displacement.

6.2. Extensions and Future Work

The simplified mathematical model to describe transport in ECBM only focuses on the interaction between convection and equilibrium between the solid, gas and aqueous phases. As a consequence, the results presented are only applicable to well-cleated coals where gravitational and capillary forces are neglected. The use of the method of characteristics to solve the transport problem imparts other restrictions on the applicability of the model to coal systems, such as constant injection and initial conditions, one-dimensional flow, constant pressure for evaluation of phase behaviour and homogenous properties of the porous medium.

A simple representation of flue gas injection is handled by the quaternary system. However, many impurities, such as SO_x, CO and NO_x, may also be present in flue gas mixtures, depending on combustion conditions and fuel source.

Sulphur compounds have significantly higher adsorption affinities and different phase properties from carbon and nitrogen based impurities and should not be lumped with those components. Extending solution structures to more components would allow more realistic representation of injection gas compositions. A comprehensive survey of injection and initial states is required to delineate all possible solution structures.

For the quaternary system, a full analysis of possible composition paths encountered in gas injection applications is documented in this dissertation. This work focuses on the practical aspects of gas injection for ECBM, therefore, only gas injection into water saturated coalbeds was considered. Complementary composition paths for aqueous phase injection into gas reservoirs should be analysed to define completely the solution structures encountered in the flue gas system. Experimental verification of the new compositions paths through slim tube displacements should be performed.

These solutions to the Riemann problems provide the building blocks for solutions to more general initial boundary value problems. The general solutions from a Riemann solver can be coupled with streamline simulation techniques to model ECBM and CO_2 sequestration in three dimensional systems with variable reservoir properties. Quantification of the modelling errors due to simplification of the physical mechanisms, such as gravity and capillary crossflow, is required to delineate the reservoir and fluid parameters where the analytical solutions presented are reasonable representations of transport processes in coals and under what conditions additional techniques (Bratvedt *et al.*, 1996, Batycky, 1997) to account for supplemental physics is necessary.

Nomenclature

Roman

a = amount adsorbed per unit of volume coal
B = Langmuir constant for a specified temperature
C = concentration
D = diffusion coefficient
f = volumetric fractional flow
G = overall molar concentration
H = overall molar flux
k = permeability
K = gas-liquid partition coefficient
L = length
M = mobility ratio
n = Corey exponent
p = partial pressure
P = reservoir pressure
Pe = Peclet number
r = radius
R = radius of spherical system
S = saturation
t = time
T = temperature
u = local flow velocity

v = interstitial velocity
V_m = Langmuir constant
x = mole fraction
y = mole fraction in the gas phase
z = total mole fraction

Greek

ξ = dimensionless distance
η = similarity variable
$\kappa_{i,j}$ = binary interaction coefficient of component i and component j
λ = wave velocity
λ^* = wave velocity scaled by local flow velocity
Λ = shock velocity
μ = viscosity
ω = acentric factor
ϕ = porosity
ρ = molar density
τ = dimensionless time
θ = fractional coverage of species on coal surface

Subscript

a = aperture width
c = critical
D = dimensionless
eff = effective
EV = equivelocity
f = fracture
g = gas
gc = critical gas
GD = dimensionless variable in the gas phase
i = i^{th} component

inj = injection
j = j^{th} phase
LD = dimensionless in the liquid phase
nt = nontie line
o = previous time step value
Pe = Peclet number
r = solid phase
rg = relative to the gas phase
rgo = end point relative to the gas phase
rw = relative to the water phase
rwo = end point relative to the water phase
ST = standard conditions
t = tie line
wr = water residual

Superscript

d = downstream
D = downstream
I = single phase
II = two-phase
$init$ = initial
inj = injection
u = upstream
U = upstream

Bibliography

Arri, L. E., Yee, D., Morgan, W. D., Jeansonne, M. W. "Modeling Coalbed Methane Production with Binary Gas Sorption," paper SPE 24363 presented at the Rocky Mountain Regional Meeting, Casper, WY, 18-21 May 1992.

Ayers, W. B. Jr. "Coalbed Gas Systems, Resources and Production and a Review of Contrasting Cases from the San Juan and Powder River Basins," *AAPG Bulletin* (2002) **86**, no. 11, 1853-1890.

Batycky, R. P. "A Three-Dimensional Two-Phase Field Scale Streamline Simulator," Ph.D dissertation, Stanford University, Stanford CA (1997).

Bell, G. J., Rakop, K. C. "Hysteresis of Methane/Coal Sorption Isotherms," paper SPE 15454 presented at the 61st Annual Technical Conference and Exhibition New Orleans, LA, 5-8 October 1986.

Bratvedt, F., Glimse, T., Tegnander, C. "Streamline Computations for Porous Media Flow Including Gravity," *Transport in Porous Media* (1996) **25**, 63-78.

Brooks, R. H., Corey, A. T. "Hydraulic properties of porous media," Hydrology Papers, Colorado State University, Fort Collins, CO (1964).

Buckley, S. E., Leverett, M. C. "Mechanism of Fluid Displacement in Sands," *Trans. AIME* (1941) **249**, 107-116.

Carbon Dioxide Information Analysis Centre. *Trends Online: A Compendium of Data on Global Change*. Oak Ridge National Laboratory, U.S. Department of Energy, Oak Ridge, TN (2003).

Carothers, W. W., Kharaka, Y. K. "Stable carbon isotopes of HCO_3- in oil-field waters: implications for the origin of CO_2," *Geochimica et Cosmochimica Acta*, (1980) **44**, 323-332.

Cervik, J. "Behavior of Coal-Gas Reservoirs," USBM Tech. Progress Report 10, (1969).

Chaback, J. J., Morgan, W. D., Yee, D. "Sorption Irreversibilities and Mixture Compositional Behavior during Enhanced Coalbed Methane Recovery Processes," paper SPE 35622 presented at the Gas Technology Conference, Calgary, AB, 28 April-1 May 1996.

Chaturvedi, T. "Spontaneous Imbibition and Wettability Characteristics of Powder River Basin Coal," Master's report, Stanford University, Stanford CA (2006).

Chen, G., Harpalani, S. "Study of fracture network in coal," In: Myer, L. R., Cook, N. G. W., Goodman, R. E., Tsang, C. -F. (Eds.), *Fractured and Jointed Rock Masses*. Balkema, Rotterdam (1995) 431-434.

Close, J. C. *AAPG Studies in Geology: Natural Fractures in Coal*. (1993) **38**, 119-132.

Close, J. C., Mavor, M. J. "Influence of Coal Composition and Rank of Fracture Development in Fruitland Coalbed Natural Gas Reservoirs of San Juan Basin," In:

Schowochow, S. D., Murray, D. K., Fahy, M. F. (Eds.), *Coalbed Methane of Western North America*. Denver, CO, Rocky Mountain Association of Geologists (1991) 109-121.

Colombo, U., Gazzarrini, F., Gonfiantini, R., Kneuper, G., Teichmuller, M., Teichmuller, R. "Carbon isotope study on methane from German coal deposits," In: Hobson, G. D., Speers, G. C. (Eds.) *Advances in organic geochemistry*. Oxford, Pergamon Press (1966) 1-26.

Computer Modelling Group. *CMG-GEM User's Manual*. Calgary, AB (2005).

Cui, X., Bustin, R. M., Dipple, G. "Differential Transport of CO_2 and CH_4 in Coalbed Aquifers: Implications for coalbed gas distribution and composition," *AAPG Bulletin* (2004) **8**, 1149-1161.

Cui, X., Bustin, R. M. "Volumetric strain associated with methane desorption and its impact on coalbed gas production from deep coal seams," *AAPG Bulletin* (2005) **89**, 1181-1202.

Dahl, O., Johansen, T., Tveito, A., Winther, R. "Multicomponent Chromatography in a Two Phase Environment," *SIAM J. Appl. Math*. (1992) **52**, no. 1, 65-104.

De Bruin, R., Lymann, T. "Coalbed Methane in Wyoming," In: W. R. Miller, (Ed.) *Coalbed Methane and the Tertiary Geology of the Powder River Basin, Wyoming and Montana*. Wyoming Geological Association, **50**, 61-72.

Diamond, W. P., La Scola, J. C., Hyman, D. M. "Results of direct-method determination of the gas content of U. S. coalbeds," U.S. Department of the Interior, Bureau of Mines Information Circular 9067 (1986).

Dindoruk, B. "Analytical Theory of Multiphase, Multicomponent Displacement in Porous Media," Ph. D. dissertation, Stanford University, Stanford CA (1992).

Dindoruk, B., Johns, R. T., Orr, F. M., Jr. "Analytical Solutions for Four Component Gas Displacements with Volume Change on Mixing," Third European Conference on the Mathematics of Oil Recovery, Delft, Netherlands, June 1992.

Dumore, J. M., Hagoort, P., Risseeuw, A. S. "An Analytical Model for One-Dimensional, Three-Component Condensing and Vaporizing Gas Drives," *SPEJ* (1984) **4**, 169-179.

Energy Information Administration. *International Energy Outlook, 2003*. Energy Information Administration, U.S. Department of Energy, Washington, D. C. (2003).

Ermakov, P. "Analytical Solutions for 1D Oil Displacement by Gases," Master's report, Stanford University, Stanford CA (2000).

Flores, R. "Coalbed Methane in the Powder River Basin, Wyoming and Montana: An Assessment of the Tertiary-Upper Cretaceous Coalbed Methane Total Petroleum System," In: *Total Petroleum System and Assessment of Coalbed Gas in the Powder River Basin Province, Wyoming and Montana*. USGS Digital Data Series DDS-60-C. US Department of the Interior, Denver, CO (2004).

Gamson, P. D., Beamish, B. B., Johnson, D. P. "Coal Microstructure and Micropermeability and Their Effects on Natural Gas Recovery," *Fuel* (1993) **72**, 87-99.

Gan, H., Nandi, S., Walker, P. L., Jr. "Nature of Porosity in American Coals," *Fuel* (1972) **51**, 272-277.

Gash, B. W. "The effects of cleat orientation and confining pressure on cleat porosity, permeability and relative permeability in coal," *Log Anal.* (1992) **33**, 176-177.

Gonzalez, M., Araujo, M. "Use of the Method of Characteristics to Study Three-Phase Flow," paper SPE 75168 presented at the 2002 SPE/DOE Improved Oil Recovery Symposium, Tulsa, OK, 13-17 April 2002.

Gray, I. "Reservoir Engineering in Coal Seams: Part 1—The Physical Process of Gas Storage and Movement in Coal Seams," *SPERE* (1987) **12**, 28-34.

Greaves, K. H., Owen, L. B., Olszewski, A. "Multi-Component Gas Adsorption-Desorption Behavior of Coal," proceedings International Coalbed Methane Symposium, Birmingham, AL, 17-21 May 1993.

Harpalani, S.; Schraufnagel, R. A. "Shrinkage of coal matrix with release of gas and its impact on permeability of coal," *Fuel* (1990) **69**, no. 5, 551-556.

Harpalani, S., Zhao, X. "An Investigation of the effect of gas desorption on coal permeability," presented at The Coalbed Methane Symposium, University of Alabama, Tuscaloosa, AB, 17-20 April 1989.

Helferrich, F. G. "Theory of Multicomponent, Multiphase Displacement in Porous Media," *SPEJ* (1981) **2**, 51-62.

Hirasaki, G, J. "Application of the Theory of Multicomponent, Multiphase Displacement to Three-Component, Two-Phase Surfactant Flooding," *SPEJ* (1981) **4**, 191-204.

Hunt, J. M. *Petroleum Geochemistry and Geology*. W. H. Freeman and Co., San Francisco, USA (1979).

Intergovernmental Panel on Climate Change. *Third Assessment Report of the Intergovernmental Panel on Climate Change*. Cambridge University Press, New York, USA (2001).

Isaacson, E. L. "Global Solution of a Riemann Problem for a Non-Strictly Hyperbolic System of Conservation Laws Arising in Enhanced Oil Recovery," The Rockefeller University, New York, NY (1980).

Jeffrey, A. *Quasilinear Hyperbolic Systems and Waves*. Pitman Publishing, London, UK (1976).

Jessen, K. R., Wang, Y., Ermakov, P., Zhu, J., Orr, F. M., Jr. "Fast, Approximate Solutions for 1D Multicomponent Gas Injection Problems," paper SPE 56608, presented at the 2002 SPE Annual Technical Conference and Exhibition, San Antonio, TX, September 29-October 2 2002.

Johansen, T., Winther, R. "The Solution of the Riemann Problem for a Hyperbolic System of Conservation Laws Modeling Polymer Flooding," *SIAM J. Math. Anal.* (1988) **5**, 541-566.

Johansen, T., Winther, R. "The Riemann Problem for Multicomponent Polymer Flooding," *SIAM J. Math. Anal.* (1989) **7**, 908-929.

Johns, R. T. "Analytical Theory of Multicomponent Gas Drives with Two-Phase Mass Transfer," Ph. D. dissertation, Stanford University, Stanford CA (1992).

Johns, R. T., Dindoruk, B., Orr, F. M., Jr. "Analytical Theory of Combined Condensing/Vaporizing Gas Drives," *SPE Advanced Technology Series* (1993) **5**, no. 2, 7-16.

Johns, R. T., Fayers, F. J., Orr, F. M., Jr. "Effect of Gas Enrichment and Dispersion on Nearly Miscible Displacements in Condensing/Vaporizing Drives," *SPE Advanced Technology Series* (1993) **2**, no. 2, 25-34.

Johns, R. T., Orr, F. M., Jr. "Miscible Gas Displacement of Multicomponent Oils," *SPEJ* (1996) **3**, 39-50.

Johns, R. T., Yuan, H., Dindoruk, B. "Quantification of Displacement Mechanisms in Multicomponent Gasfloods," *SPEJ* (2004) **9**, no. 3, 314-321.

Joubert, J. I., Grein, C. T., Bienstock, D. "Effect of moisture on the methane capacity of American coals," *Fuel* (1974) **53**, 186-191.

Juanes, R., Blunt, M. J. "Impact of Viscous Fingering on the Prediction of Optimum WAG Ratio," SPE 99721, presented at the 2006 SPE/DOE Symposium on Improved Oil Recovery, Tulsa, OK, 22-26 April, 2006.

Juanes, R., Patzek, T. W. "Analytical Solution to the Riemann Problem of Three-Phase Flow in Porous Media," *Transp. Porous Media* (2004) **55**, no. 1, 47-70.

Kissell, F. N., Bielicky, R. J. "An In-Situ Diffusion Parameter for the Pittsburgh and Pocahontas No. 3 Coalbeds," Bureau of Mines Report of Investigations No. 7668, Pittsburgh, PA (1972).

Kotarba, M. "Isotopic geochemistry and habitat of the natural gases from the Upper Carboniferous Zacler coal-bearing formation in Nowa Ruda coal district (Lower Silesia, Poland)," In: Durand, B., and Behar, F., (Eds.), *Advances in organic geochemistry*. Oxford, Pergamon Press, (1989) **1**, 549-560.

Kuuskraa, V. A. *Encyclopaedia of Energy*. Elsevier, Cleveland, USA (2004).

Kuuskraa, V. A., Boyer II, C.M., Kelafant, J. A. "Hunt for quality basins goes abroad," *Oil and Gas Journal* (1992) **90**, 49-54.

LaForce, T., Johns, R. T. "Analytical solutions for surfactant-enhanced remediation of nonaqueous phase liquids," *Water Resour. Res.* (2005) **41**.

Larson, R. G. "The Influence of Phase Behavior on Surfactant Flooding," *SPEJ* (1979) **12**, 411-422.

Larson, R. G., Hirasaki, G. J. "Analysis of the Physical Mechanisms in Surfactant Flooding," *SPEJ* (1979) **12**, 411-422.

Law, B. E. "The Relationship Between Coal Rank and Cleat Spacing: Implications for the Prediction of Permeability in Coal," paper 9341 presented at the 1993 International Coalbed Methane Symposium, Birmingham, AB, 17-21 May 1993.

Levine, J. R. *AAPG Studies in Geology: Coalification: The Evolution of Coal as a Source Rock and Reservoir Rock for Oil and Gas.* (1993) **38**, 39-77.

Lin, W. "Gas Permeability of Coal Beds and Thermochemical Recovery of Viscous Oil," Master's Report, Stanford University, Stanford CA (2006).

Markham, E. C., Benton, A. F. "The Adsorption of Gas Mixtures by Silica," *J. Amer. Chem. Soc.* (1931) **53**, 497-507.

Mavor, M.J. and Vaughn, J.E.: "Increasing Coal Absolute Permeability in the San Juan Basin Fruitland Formation," *SPERE* (1998) 6, 201-206.

Mazumder, S., Plug, W.-J., Bruning, H. "Capillary Pressure and Wettability Behaviour of Coal-Water-Carbon Dioxide System," SPE 84339, presented at the SPE Annual Technical Conference and Exhibition, Denver, CO, 5-8 October 2003.

McKee, C. R., Bumb, A. C., Koenig, R. A. "Stress-dependent Permeability and Porosity of Coal and Other Geologic Formations," *SPEFE* (1988) **3**, 81-91.

Meissner, F. F. "Cretaceous and lower Tertiary coals as sources for gas accumulations in the Rocky Mountain area," In: Woodward, J., Meissner, F.F., and Clayton, J.L. (Eds.), *Hydrocarbon source rocks of the greater Rocky Mountain region*. Rocky Mountain Association of Geologists, (1984) 401-431.

Monroe, W. W., Silva, M. K., Larson, L. L., Orr, F. M., Jr. "Composition Paths in Four-Component Systems: Effect of Dissolved Methane on 1D CO_2 Flood Performance," *SPERE* (1990) **8**, 423-432.

Orr, F. M., Jr. *Theory of Gas Injection Processes*. Tie Line Publications, Copenhagen, Denmark (2007).

Palmer, I., Mansoori, J. "How Permeability Depends on Stress and Pore Pressure in Coalbeds: A New Model," *SPEREE* (1998) **12**, 539-544.

Pashin, J.C. "Regional analysis of the Black Creek-Cobb coalbed-methane target interval, Black Warrior basin, Alabama," *Geological Survey of Alabama Bulletin* (1991) **145**, 127.

Pekot L. J., Reeves, S. R. "Modeling Coal Matrix Shrinkage and Differential Swelling with CO_2 Injection for Enhanced Coalbed Methane Recovery and Carbon Sequestration Applications," US Department of Energy Topical Report, November 2002.

Peng, D. Y., Robinson, D. B. "A New Two-Constant Equation of State," *Ind. Eng. Chem. Fund.* (1976) **15**, 59-64.

Petroleum Technology Transfer Council. "*Past, Present and Future of Coal Bed Methane in the Rocky Mountains*." PTTC Rocky Mountain Regional Workshop, Denver, CO, 22 June 1999.

Pollard, D. D., Aydin, A. *GSA Bulletin: Progress in Understanding Jointing Over the Past Century*. (1988) **100**, no. 8, 1181-1204.

Pollard, D. D., Fletcher, R. C. *Fundamentals of Structural Geology*. Cambridge University Press, Cambridge, UK (2005).

Pope, G. A. "The Application of Fractional Flow Theory to Enhanced Oil Recovery," *SPEJ* (1980) **6**, 191-205.

Pope, G. A., Lake, L. W., Helfferich, F. G. "Cation Exchange in Chemical Flooding: Part 1—Basic Theory Without Dispersion," *SPEJ* (1978) **12**, 418-434.

Puri, R., Evanoff, J. C., Brugler, M. L. "Measurement of Coal Cleat Porosity and Relative Permeability Characteristics," paper SPE 21491 presented at the 1991 SPE Gas Technology Symposium, Houston, TX, 23-25 January 1991.

Quattrocchi, F., Bencini, R., Basili, R., Cara, R., Fandino, V., Giannelli, A., Pini, R., Sardu, G. "Feasibility study (I stage) of CO_2 geological storage by ECBM techniques in the Sulicis coal province (SW Sardinia, Italy)," presented at the 8th International Conference on Greenhouse Gas Control Technologies, Trondheim, Norway, 19-22 June 2006.

Rice, D. D. *AAPG Studies in Geology: Compositions and Origins of Coalbed Gas*. (1993) **38**, 159-184.

Reeves, S. "Geological Sequestration of CO_2 in Deep, Unminable Coalbeds: An Integrated Research and Commercial-Scale Field Demonstration Project," paper SPE 71749, presented at the SPE Annual Technical Conference and Exhibition. New Orleans, LA, 30 September-3 October 2001.

Reeves, S., Pekot, L. J. "Advanced Reservoir Modeling in Desorption-Controlled Reservoirs," paper SPE 71090, presented at the 2001 SPE Rocky Mountain Petroleum Technology Conference, Keystone, CO, 21-23 May 2001.

Rhee, H. K., Aris, R., Amundson, N. R. "On the Theory of Multicomponent Chromatography," *Phil. Trans. Royal Soc. London* (1970) **10**, 419-455.

Sams, W. N., Bromhal, G., Odusote, O., Jikich, S., Ertekin, T., Smith, D. H. "Simulating Carbon Dioxide Sequestration/ECBM Production in Coal Seams: Effects of Coal Properties and Operational Parameters," SPE 78691, presented at the SPE Eastern Regional Meeting, Lexington, KY, 23-25 October 2002.

Scott, A.R., Tyler,R. "Evaluating coalbed methane potential in Texas," *AAPG Bulletin* (2000) **84**, no. 10, 1691.

Seidle, J. P., Arri, L. E. "Use of Conventional Reservoir Models for Coalbed Methane Simulation," paper CIM/SPE 90-118, presented at The Canadian Institute of Mining/Society of Petroleum Engineers International Technical Meeting, Calgary, AB, 10-13 June 1990.

Seidel, J. P., Huitt, L. G. "Experimental Measurement of Coal Matrix Shrinkage Due to Gas Desorption and Implications for Cleat Permeability Increases," paper SPE 30010 presented at the International Meeting on Petroleum Engineering, Beijing, China, 14-17 November 1995.

Seri-Levy, A., Levy, D. "Effect of heterogeneous surface geometry on adsorption." *Langmuir*, (1993) **9**, pp. 3067-3076.

Seto, C. J., Jessen, K., Orr, F. M. Jr. "Compositional Streamline Simulation of Field Scale Condensate Vaporization by Gas Injection," paper SPE 79690 presented at the SPE Reservoir Simulation Symposium, Houston, TX, 3-5 February 2003.

Shi, J. Q., Durucan, S. "A bidisperse pore diffusion model for methane displacement desorption in coal by CO_2 injection," *Fuel* (2003) **82**, 1219-1229.

Smith, D. H., Bromhal, G., Sams, W. N., Jikich, S., Ertekin, T. "Simulating Carbon Dioxide Sequestration/ECBM Production in Coal Seams: Effects of Permeability Anisotropies and the Diffusion-Time Constant," *SPEREE* (2005) **4**, 156-163.

Smith, D. M., Williams, F. L. "Diffusional Effects in the Recovery of Methane From Coalbeds," *SPEJ* (1984) **10**, 529-535.

Smith, J. T., Ehrenberg, S. N. "Correlation of carbon dioxide abundance with temperature in clastic hydrocarbon reservoirs: relationship to inorganic chemical equilibrium," *Marine and Petroleum Geology* (1989) **6**, 129-135.

Srivastava, N. K. "Effects of Pressure Gradients on Displacement Performance for Miscible/Near Miscible Gas Floods," Master's report, Stanford University, Stanford CA (2004).

Stanton, R. W., Burruss, R. C., Flores, R. M., Warwick, P. D. "CO_2 Adsorption in Low-Rank Coals: Progress Toward Assessing the Nation-Wide Capacity to Store CO_2 in the Subsurface," presented at the 18th Annual International Pittsburgh Coal Conference, Newcastle, NSW, Australia, 3-7 December 2001.

St. George, J. D., Barakat, M. A. "The change in effective stress associated with shrinkage from gas desorption in coal," *International Journal of Coal Geology* (2001) **45**, 105-113.

Tang, G. Q., Jessen, K., Kovscek, A. R. "Laboratory and Simulation Investigation of Enhanced Coalbed Methane Recovery by Gas Injection," paper SPE 95947 presented at the SPE Annual Technical Conference and Exhibition, Dallas, TX, 9-12 October 2005.

Tewes, F., Boury, F. "Formation and Rheological Properties of the Supercritical CO_2-Water Pure Interface," *J. Phys. Chem. B.* (2005) **109**, 3990-3997.

Tremain, C. M., Laubach, S. E., Whitehead, N. H. III. 1991. "Coal fracture (cleat) patterns in Upper Cretaceous Fruitland Formation, San Juan Basin, Colorado and New Mexico: Implications for coalbed methane exploration and development," In: Ayers, W. B., Jr., W. R. Kaiser, S. E. Laubach, W. A. Ambrose, R. W. Baumgardner, Jr., A. R. Scott, R. Tyler, J. Yeh, G. J. Hawkins, T. E. Swartz, D. D. Schultz-Ela, S. D. Zellers, C. M. Tremain, and N. H. Whitehead III, *Geologic and hydrologic controls on the occurrence and producibility of coalbed methane, Fruitland Formation, San Juan basin*. Gas Research Institute Topical Report. GRI-91/0072 (1991).

Thimons, B., Kissell, F. N. "Diffusion of methane through coal," *Fuel* (1973) **52**, 274-280.

United States Geological Survey. "Coalbed Methane—An Untapped Energy Resource and an Environmental Concern," USGS Fact Sheet FS-109-97, U. S. Geological Survey, Energy Resource Surveys Program (1997).

Unver, A. A., Himmelblau, D. M. "Diffusion Coefficients of CO_2, C_2H_4, C_3H_6, and C_4H_8 in Water from 6° to 65°C," *J. Chem. and Eng. Data* (1964) **9**, no. 3, 428-431.

U.S. Department of Energy and Environmental Protection Agency. *Carbon Dioxide Emissions from the Generation of Electric Power in the United States.* Department of Energy, Environmental Protection Agency, Washington, D. C. (2000).

van Bergen, F., Pagnier, H. "Field experiment of CO_2-ECBM in the Upper Silesian Basin of Poland," presented at the 8th International Conference on Greenhouse Gas Control Technologies, Trondheim, Norway, 19-22 June 2006.

van de Meer, B. "An Excellent Simulation Tool: SIMED II," *Information*. TNO-NITG. (2004) **5**, 12-14.

van Krevelen, D. W. *Coal—Typology, Chemistry, Physics and Constitution.* Elseveier, Amsterdam (1981).

Wang, Y. "Analytical Calculation of Minimum Miscibility Pressure," Ph. D. dissertation, Stanford University, Stanford CA (1998).

Warren, J. E., Root, P. J. "The Behavior of Naturally Fractured Reservoirs," *SPEJ, AIME* (1963) **228**, 245-255.

Welge, H. J. "A Simplified Model for Computing Oil Recovery by Gas or Water Drive," *Petroleum Trans., AIME* (1952) **195**, 91-98.

Wong, S., Law, D., Deng, X., Robinson, J., Kadatz, B, Gunter, B. Jianping, Y., Sanli, F., Zhiqiang, F. "Enhanced Coalbed Methane—Micro-Pilot Test at South Qinshui, Shanxi, China," presented at the 8th International Conference on Greenhouse Gas Control Technologies, Trondheim, Norway, 19-22 June 2006.

Wymann, R. E. "Gas resources in Elmsworth coal seams," AAPG Memoir (1984) **38**, 173-187.

Yang, R. T. *Gas Separation by Adsorption Processes.* Butterworths, Boston, MA (1987).

Yang, D., Tontiwachwuthikul, P., Yongan, G. "Dynamic Interfacial Tension Method for Measuring Gas Diffusion Coefficient and Interface Mass Transfer Coefficient in a Liquid," *Ind. Eng. Chem. Res.* (2006) **45**, 4999-5008.

Yee, D., Seidle, J. P., Hanson, W. P. *AAPG Studies in Geology: Gas Sorption on Coal and Measurement of Gas Content*. (1993) **38**, 203-218.

Zhu, J. "Multicomponent Multiphase Flow in Porous Media with Temperature Variation or Adsorption," Ph. D dissertation, Stanford University, Stanford CA (2003).

Zhu, J., Jessen, K., Kovscek, A. R., Orr, F. M., Jr. "Analytical Theory of Coalbed Methane Recovery by Gas Injection," *SPEJ* (2003) **12**, 371-379.

Zhu, J., Jessen, K., Orr, F. M., Jr. "Analytical Solution for Gas/Oil Displacement with Temperature Variation," paper SPE 89432 presented at the 2004 SPE/DOE Symposium on Improved Oil Recovery, Tulsa, OK, 17-21 April 2004.

Appendix A

Continuous Variation in the Binary Displacement

When S and u_D are taken as the independent variables, the system of equations in the two-phase region of the binary displacement becomes:

$$\begin{bmatrix} \frac{\partial H_1}{\partial S} & \frac{\partial H_1}{\partial u_D} \\ \frac{\partial H_2}{\partial S} & \frac{\partial H_2}{\partial u_D} \end{bmatrix} \begin{bmatrix} \frac{dS}{d\eta} \\ \frac{du_D}{d\eta} \end{bmatrix} = \lambda \begin{bmatrix} \frac{\partial G_1}{\partial S} & 0 \\ \frac{\partial G_2}{\partial S} & 0 \end{bmatrix} \begin{bmatrix} \frac{dS}{d\eta} \\ \frac{du_D}{d\eta} \end{bmatrix} \tag{A.1}$$

Substituting Eqs. 3.25 and 3.32 into the expressions for H_i and λ and following the decoupling procedure similar to that outlined in Dindoruk (1992), A.1 becomes:

$$\begin{bmatrix} \frac{\partial \alpha_1}{\partial S} - \frac{\alpha_1}{\alpha_2}\frac{\partial \alpha_2}{\partial S} - \lambda * \left(\frac{\partial G_1}{\partial S} - \frac{\alpha_1}{\alpha_2}\frac{\partial G_2}{\partial S} \right) & 0 \\ \frac{1}{\alpha_2}\frac{\partial \alpha_2}{\partial S} - \lambda * \left(\frac{1}{\alpha_2}\frac{\partial G_2}{\partial S} \right) & \frac{1}{u_D} \end{bmatrix} \begin{bmatrix} \frac{dS}{d\eta} \\ \frac{du_D}{d\eta} \end{bmatrix} = 0 \tag{A.2}$$

The subsystem for the variation of composition is

$$\frac{\partial \alpha_1}{\partial S} - \frac{\alpha_1}{\alpha_2}\frac{\partial \alpha_2}{\partial S} - \lambda^* \left(\frac{\partial G_1}{\partial S} - \frac{\alpha_1}{\alpha_2}\frac{\partial G_2}{\partial S} \right) = 0 , \tag{A.3}$$

and the resulting expression for the eigenvalue is

$$\lambda^* = \frac{\dfrac{\partial \alpha_1}{\partial S} - \dfrac{\alpha_1}{\alpha_2}\dfrac{\partial \alpha_2}{\partial S}}{\dfrac{\partial G_1}{\partial S} - \dfrac{\alpha_1}{\alpha_2}\dfrac{\partial G_2}{\partial S}} . \tag{A.4}$$

Because $\alpha = f(f)$ and $f = f(S)$,

$$\lambda^* = \frac{\dfrac{\partial \alpha_1}{\partial f}\dfrac{df}{dS} - \dfrac{\alpha_1}{\alpha_2}\dfrac{\partial \alpha_2}{\partial f}\dfrac{df}{dS}}{\dfrac{\partial G_1}{\partial S} - \dfrac{\alpha_1}{\alpha_2}\dfrac{\partial G_2}{\partial S}} . \tag{A.5}$$

The derivatives for α_i and G_i are:

$$\frac{\partial \alpha_i}{\partial f} = \rho_{GD} y_i - \rho_{LD} x_i , \tag{A.6}$$

$$\frac{\partial G_i}{\partial S} = \rho_{GD} y_i - \rho_{LD} x_i . \tag{A.7}$$

Substituting these expressions into Eq. A.5,

$$\lambda^* = \frac{\dfrac{df}{dS}\left[\left(\rho_{GD} y_1 - \rho_{LD} x_1\right) - \dfrac{\alpha_1}{\alpha_2}\left(\rho_{GD} y_2 - \rho_{LD} x_2\right) \right]}{\left(\rho_{GD} y_1 - \rho_{LD} x_1\right) - \dfrac{\alpha_1}{\alpha_2}\left(\rho_{GD} y_2 - \rho_{LD} x_2\right)} . \tag{A.8}$$

In the two phase region, continuous variation occurs along a tie line,

$$\lambda^* = \frac{df}{dS} . \tag{A.9}$$

In the single phase region, z_1 and u_D are the independent variables. The system of equations becomes:

$$\begin{bmatrix} \dfrac{\partial H_1}{\partial z_1} & \dfrac{\partial H_1}{\partial u_D} \\ \dfrac{\partial H_2}{\partial z_1} & \dfrac{\partial H_2}{\partial u_D} \end{bmatrix} \begin{bmatrix} \dfrac{dz_1}{d\eta} \\ \dfrac{du_D}{d\eta} \end{bmatrix} = \lambda \begin{bmatrix} \dfrac{\partial G_1}{\partial z_1} & 0 \\ \dfrac{\partial G_2}{\partial z_1} & 0 \end{bmatrix} \begin{bmatrix} \dfrac{dz_1}{d\eta} \\ \dfrac{du_D}{d\eta} \end{bmatrix}. \tag{A.10}$$

The same procedure as that used for the two-phase region for decoupling the local flow velocity from the composition is applied to the single phase problem. The system of equations becomes

$$\begin{bmatrix} \dfrac{\partial \alpha_1}{\partial z_1} - \dfrac{\alpha_1}{\alpha_2}\dfrac{\partial \alpha_2}{\partial z_1} - \lambda * \left(\dfrac{\partial G_1}{\partial z_1} - \dfrac{\alpha_1}{\alpha_2}\dfrac{\partial G_2}{\partial z_1} \right) & 0 \\ \dfrac{1}{\alpha_2}\dfrac{\partial \alpha_2}{\partial z_1} - \lambda * \left(\dfrac{1}{\alpha_2}\dfrac{\partial G_2}{\partial z_1} \right) & \dfrac{1}{u_D} \end{bmatrix} \begin{bmatrix} \dfrac{dz_1}{d\eta} \\ \dfrac{du_D}{d\eta} \end{bmatrix} = 0. \tag{A.11}$$

The subsystem for composition variation in the single phase region is

$$\frac{\partial \alpha_1}{\partial z_1} - \frac{\alpha_1}{\alpha_2}\frac{\partial \alpha_2}{\partial z_1} - \lambda * \left(\frac{\partial G_1}{\partial z_1} - \frac{\alpha_1}{\alpha_2}\frac{\partial G_2}{\partial z_1} \right) = 0. \tag{A.12}$$

Because the mole fractions sum to 1, α_2 and G_2 become:

$$\alpha_2 = \rho(1 - z_1), \tag{A.13}$$

$$G_2 = \rho(1 - z_1) + \left(\frac{1-\phi}{\phi} \right) a_2. \tag{A.14}$$

The derivatives of α_i and G_i are:

$$\frac{\partial \alpha_1}{\partial z_1} = \rho, \tag{A.15}$$

$$\frac{\partial \alpha_2}{\partial z_1} = -\rho, \tag{A.16}$$

$$\frac{\partial G_1}{\partial z_1} = \rho + \left(\frac{1-\phi}{\phi} \right) \frac{\partial a_1}{\partial z_1}, \tag{A.17}$$

$$\frac{\partial G_2}{\partial z_1} = -\rho - \left(\frac{1-\phi}{\phi}\right)\frac{\partial a_2}{\partial z_1}. \tag{A.18}$$

When Eqs. A.15 to A.18 are substituted into Eq. A.12, λ^* is

$$\lambda^* = \frac{\rho\left(1+\frac{z_1}{z_2}\right)}{\rho\left(1+\frac{z_1}{z_2}\right)+\left(\frac{1-\phi}{\phi}\right)\left(\frac{\partial a_1}{\partial z_1}-\frac{z_1}{z_2}\frac{\partial a_2}{\partial z_1}\right)}. \tag{A.19}$$

If we assume that H_2O, component 2, does not adsorb,

$$\frac{\partial a_2}{\partial z_1} = 0, \tag{A.20}$$

Eq. A.20 becomes

$$\lambda^* = \frac{\rho\left(1+\frac{z_1}{z_2}\right)}{\rho\left(1+\frac{z_1}{z_2}\right)+\left(\frac{1-\phi}{\phi}\right)\frac{\partial a_1}{\partial z_1}}. \tag{A.21}$$

In this analysis, the adsorption function is chosen to be positive concave (e.g. Langmuir type isotherm). Therefore, the eigenvalue in the single phase region will always be greater than 0. At the phase boundary, the eigenvalue is 0. Continuous variation into and out of the two-phase region violates the velocity rule and shock is required for compositions when a phase change occurs.

Continuous Variation in the Ternary Displacement

This section formulates the eigenvalue problem in the two-phase region for the ternary displacement. In this analysis, S, y_I and u_D are taken as the independent variables:

$$\begin{bmatrix} \frac{\partial H_1}{\partial S} & \frac{\partial H_1}{\partial y_1} & \frac{\partial H_1}{\partial u_D} \\ \frac{\partial H_2}{\partial S} & \frac{\partial H_2}{\partial y_1} & \frac{\partial H_2}{\partial u_D} \\ \frac{\partial H_3}{\partial S} & \frac{\partial H_3}{\partial y_1} & \frac{\partial H_3}{\partial u_D} \end{bmatrix} \begin{bmatrix} \frac{dS}{d\eta} \\ \frac{dy_1}{d\eta} \\ \frac{du_D}{d\eta} \end{bmatrix} = \lambda \begin{bmatrix} \frac{\partial G_1}{\partial S} & \frac{\partial G_1}{\partial y_1} & \frac{\partial G_1}{\partial u_D} \\ \frac{\partial G_2}{\partial S} & \frac{\partial G_2}{\partial y_2} & \frac{\partial G_2}{\partial u_D} \\ \frac{\partial G_3}{\partial S} & \frac{\partial G_3}{\partial y_1} & \frac{\partial G_3}{\partial u_D} \end{bmatrix} \begin{bmatrix} \frac{dS}{d\eta} \\ \frac{dy_1}{d\eta} \\ \frac{du_D}{d\eta} \end{bmatrix}. \tag{A.22}$$

Applying a decoupling procedure similar to Dindoruk (1992) to the 2x2 subsystem for the normalised eigenvalue gives:

$$\begin{bmatrix} \frac{\partial \alpha_1}{\partial y_1} - \frac{\alpha_1}{\alpha_3}\frac{\partial \alpha_3}{\partial y_1} - \lambda^*\left(\frac{\partial G_1}{\partial y_1} - \frac{\alpha_1}{\alpha_3}\frac{\partial G_3}{\partial y_1}\right) & \frac{\partial \alpha_1}{\partial S} - \frac{\alpha_1}{\alpha_3}\frac{\partial \alpha_3}{\partial S} - \lambda^*\left(\frac{\partial G_1}{\partial S} - \frac{\alpha_1}{\alpha_3}\frac{\partial G_3}{\partial S}\right) \\ \frac{\partial \alpha_2}{\partial y_1} - \frac{\alpha_2}{\alpha_3}\frac{\partial \alpha_3}{\partial y_1} - \lambda^*\left(\frac{\partial G_2}{\partial y_1} - \frac{\alpha_2}{\alpha_3}\frac{\partial G_3}{\partial y_1}\right) & \frac{\partial \alpha_2}{\partial S} - \frac{\alpha_2}{\alpha_3}\frac{\partial \alpha_3}{\partial S} - \lambda^*\left(\frac{\partial G_2}{\partial S} - \frac{\alpha_2}{\alpha_3}\frac{\partial G_3}{\partial S}\right) \end{bmatrix} \begin{bmatrix} \frac{\partial y_1}{\partial \eta} \\ \frac{\partial S}{\partial \eta} \end{bmatrix} = \bar{0}. \tag{A.23}$$

Defining the variables γ_i , β_i and δ_i as

$$\gamma_i = \rho_G y_i - \rho_L x_i \quad , \tag{A.24}$$

$$\beta_i = \rho_L x_i \,, \tag{A.25}$$

$$\delta_i = \frac{1-\phi}{\phi} \frac{V_{m_i} \rho_r \rho_{iST} B_i p_i}{1 + \sum_{j=1}^{n_c} B_j p_j} \,, \tag{A.26}$$

and substituting them into Eq. A.23, the elements become:

$$\begin{aligned} &\frac{\partial \alpha_1}{\partial y_1} - \frac{\alpha_1}{\alpha_3}\frac{\partial \alpha_3}{\partial y_1} - \lambda^*\left(\frac{\partial G_1}{\partial y_1} - \frac{\alpha_1}{\alpha_3}\frac{\partial G_3}{\partial y_1}\right) \\ &\quad = \left(f - \lambda^* S\right)\left(\frac{\partial \gamma_1}{\partial y_1} - \frac{\alpha_1}{\alpha_3}\frac{\partial \gamma_3}{\partial y_1}\right) + \left(1 - \lambda^*\right)\left(\frac{\partial \beta_1}{\partial y_1} - \frac{\alpha_1}{\alpha_3}\frac{\partial \beta_3}{\partial y_1}\right) + \lambda^*\left(-\frac{\partial \delta_1}{\partial y_1} + \frac{\alpha_1}{\alpha_3}\frac{\partial \delta_3}{\partial y_1}\right), \end{aligned} \tag{A.27}$$

$$\begin{aligned} &\frac{\partial \alpha_2}{\partial y_1} - \frac{\alpha_2}{\alpha_3}\frac{\partial \alpha_3}{\partial y_1} - \lambda^*\left(\frac{\partial G_2}{\partial y_1} - \frac{\alpha_2}{\alpha_3}\frac{\partial G_3}{\partial y_1}\right) \\ &\quad = \left(f - \lambda^* S\right)\left(\frac{\partial \gamma_2}{\partial y_1} - \frac{\alpha_2}{\alpha_3}\frac{\partial \gamma_3}{\partial y_1}\right) + \left(1 - \lambda^*\right)\left(\frac{\partial \beta_2}{\partial y_1} - \frac{\alpha_2}{\alpha_3}\frac{\partial \beta_3}{\partial y_1}\right) + \lambda^*\left(-\frac{\partial \delta_2}{\partial y_1} + \frac{\alpha_2}{\alpha_3}\frac{\partial \delta_3}{\partial y_1}\right), \end{aligned} \tag{A.28}$$

$$\frac{\partial \alpha_1}{\partial S} - \frac{\alpha_1}{\alpha_3}\frac{\partial \alpha_3}{\partial S} - \lambda^*\left(\frac{\partial G_1}{\partial S} - \frac{\alpha_1}{\alpha_3}\frac{\partial G_3}{\partial S}\right) = \left(\frac{df}{dS} - \lambda^*\right)\left(\gamma_1 - \frac{\alpha_1}{\alpha_3}\gamma_3\right), \tag{A.29}$$

$$\frac{\partial \alpha_2}{\partial S} - \frac{\alpha_2}{\alpha_3}\frac{\partial \alpha_3}{\partial S} - \lambda^*\left(\frac{\partial G_2}{\partial S} - \frac{\alpha_2}{\alpha_3}\frac{\partial G_3}{\partial S}\right) = \left(\frac{df}{dS} - \lambda^*\right)\left(\gamma_2 - \frac{\alpha_2}{\alpha_3}\gamma_3\right). \tag{A.30}$$

The following variables are defined to simplify the elements of A.23:

$$A_1 = \frac{\partial \gamma_1}{\partial y_1} - \frac{\alpha_1}{\alpha_3}\frac{\partial \gamma_3}{\partial y_1}, \tag{A.31}$$

$$A_2 = \frac{\partial \gamma_2}{\partial y_1} - \frac{\alpha_2}{\alpha_3}\frac{\partial \gamma_3}{\partial y_1}, \tag{A.32}$$

$$B_1 = \frac{\partial \beta_1}{\partial y_1} - \frac{\alpha_1}{\alpha_3}\frac{\partial \beta_3}{\partial y_1}, \tag{A.33}$$

$$B_2 = \frac{\partial \beta_2}{\partial y_1} - \frac{\alpha_2}{\alpha_3}\frac{\partial \beta_3}{\partial y_1}, \tag{A.34}$$

$$C_1 = -\frac{\partial \delta_1}{\partial y_1} + \frac{\alpha_1}{\alpha_3}\frac{\partial \delta_3}{\partial y_1}, \tag{A.35}$$

$$C_2 = -\frac{\partial \delta_2}{\partial y_1} + \frac{\alpha_2}{\alpha_3}\frac{\partial \delta_3}{\partial y_1}, \tag{A.36}$$

$$D_1 = \gamma_1 - \frac{\alpha_1}{\alpha_3}\gamma_3, \tag{A.37}$$

$$D_2 = \gamma_2 - \frac{\alpha_2}{\alpha_3}\gamma_3, \tag{A.38}$$

and the subsystem for the normalised eigenvalue becomes:

$$\begin{bmatrix} \left(f - \lambda^* S\right)A_1 + \left(1 - \lambda^*\right)B_1 + \lambda^* C_1 & \left(\frac{df}{dS} - \lambda^*\right)D_1 \\ \left(f - \lambda^* S\right)A_2 + \left(1 - \lambda^*\right)B_2 + \lambda^* C_2 & \left(\frac{df}{dS} - \lambda^*\right)D_2 \end{bmatrix} \begin{bmatrix} \frac{\partial y_1}{\partial \eta} \\ \frac{\partial S}{\partial \eta} \end{bmatrix} = \overline{0}. \tag{A.39}$$

Setting the determinant of Eq. A.39 to zero gives the following expressions for the the normalised eigenvalues:

$$\lambda^* = \frac{df}{dS}, \frac{f + \chi_1}{S + \chi_1 + \chi_2}, \tag{A.40}$$

where

$$\chi_1 = \frac{B_1 D_2 - B_2 D_1}{A_1 D_2 - A_2 D_1}, \tag{A.41}$$

and

$$\chi_2 = \frac{C_2 D_1 - C_1 D_2}{A_1 D_2 - A_2 D_1}. \tag{A.42}$$

χ_1 and χ_2 Along a Tie Line

To demonstrate that χ_1 and χ_2 are constants for a given tie line, the following variables are defined:

$$\gamma_i = \rho_{GD} y_i + \rho_{LD} x_i, \tag{A.43}$$

$$b_i = \frac{\rho_{LD}}{K_i} \frac{\partial y_i}{\partial y_1}, \tag{A.44}$$

$$g_i = \left(\rho_{GD} - \frac{\rho_{LD}}{K_i} \right) \frac{\partial y_i}{\partial y_1}, \tag{A.45}$$

$$c_i = \frac{\partial \delta_i}{\partial y_1}, \tag{A.46}$$

and

$$\alpha_i = \gamma_i f + \beta_i. \tag{A.47}$$

Expanding A_i, B_i, and D_i gives

$$A_1 = \frac{(g_1\gamma_3 - g_3\gamma_1)f + g_1\beta_3 - g_3\beta_1}{\gamma_3 f - \beta_3}, \tag{A.48}$$

$$A_2 = \frac{(g_2\gamma_3 - g_3\gamma_2)f + g_2\beta_3 - g_3\beta_2}{\gamma_3 f - \beta_3}, \tag{A.49}$$

$$B_2 = \frac{(b_2\gamma_3 - b_3\gamma_2)f + b_2\beta_3 - b_3\beta_2}{\gamma_3 f - \beta_3}, \tag{A.50}$$

$$B_1 = \frac{(b_1\gamma_3 - b_3\gamma_1)f + b_1\beta_3 - b_3\beta_1}{\gamma_3 f - \beta_3}, \tag{A.51}$$

$$D_1 = \frac{\gamma_1\beta_3 - \gamma_3\beta_1}{\gamma_3 f + \beta_3}, \tag{A.52}$$

and

$$D_2 = \frac{\gamma_2\beta_3 - \gamma_3\beta_2}{\gamma_3 f + \beta_3}. \tag{A.53}$$

Substitution of these expressions into Eq. A.41 (χ_1) gives

$$\begin{aligned}&\frac{B_1D_2 - B_2D_1}{A_1D_2 - A_2D_1}\\ &= \frac{[(b_1\gamma_3 - b_3\gamma_1)f + b_1\beta_3 - b_3\beta_1](\gamma_2\beta_3 - \gamma_3\beta_2) - [(b_2\gamma_3 - b_3\gamma_2)f + b_2\beta_3 - b_3\beta_2](\gamma_1\beta_3 - \gamma_3\beta_1)}{[(g_1\gamma_3 - g_3\gamma_1)f + g_1\beta_3 - g_3\beta_1](\gamma_2\beta_3 - \gamma_3\beta_2) - [(g_2\gamma_3 - g_3\gamma_2)f + g_2\beta_3 - g_3\beta_2](\gamma_1\beta_3 - \gamma_3\beta_1)}.\end{aligned} \tag{A.54}$$

The denominator simplifies to

$$\begin{aligned}&A_1D_2 - A_2D_1\\ &= (f\gamma_3 + \beta_3)\rho_{LD}\rho_{GD}\left[g_1y_2y_3\left(\frac{1}{K_3} - \frac{1}{K_2}\right) + g_2y_1y_3\left(\frac{1}{K_1} - \frac{1}{K_3}\right) + g_3y_1y_2\left(\frac{1}{K_2} - \frac{1}{K_1}\right)\right],\end{aligned} \tag{A.55}$$

and the numerator simplifies to

$$\begin{aligned}&B_1D_2 - B_2D_1\\ &= (f\gamma_3 + \beta_3)\rho_{LD}\rho_{GD}\left[b_1y_2y_3\left(\frac{1}{K_3} - \frac{1}{K_2}\right) + b_2y_1y_3\left(\frac{1}{K_1} - \frac{1}{K_3}\right) + b_3y_1y_2\left(\frac{1}{K_2} - \frac{1}{K_1}\right)\right].\end{aligned} \tag{A.56}$$

The dependence on fractional flow cancels, and χ_1 is a function of equilibrium composition

$$\frac{B_1D_2 - B_2D_1}{A_1D_2 - A_2D_1} = \frac{b_1 y_2 y_3\left(\frac{1}{K_3} - \frac{1}{K_2}\right) + b_2 y_1 y_3\left(\frac{1}{K_1} - \frac{1}{K_2}\right) + b_3 y_1 y_2\left(\frac{1}{K_2} - \frac{1}{K_1}\right)}{g_1 y_2 y_3\left(\frac{1}{K_3} - \frac{1}{K_2}\right) + g_2 y_1 y_3\left(\frac{1}{K_1} - \frac{1}{K_2}\right) + g_3 y_1 y_2\left(\frac{1}{K_2} - \frac{1}{K_1}\right)}. \quad \text{(A.57)}$$

If a similar substitution is made into χ_2,

$$\begin{aligned}&\frac{C_2D_1 - C_1D_2}{A_1D_2 - A_2D_1}\\ &= \frac{[(c_3\gamma_2 - c_2\gamma_3)f + c_3\beta_2 - c_2\beta_3](\gamma_1\beta_3 - \gamma_3\beta_1) - [(c_3\gamma_1 - c_1\gamma_3)f + c_3\beta_1 - c_1\beta_3](\gamma_2\beta_3 - \gamma_3\beta_2)}{[(g_1\gamma_3 - g_3\gamma_1)f + g_1\beta_3 - g_3\beta_1](\gamma_2\beta_3 - \gamma_3\beta_2) - [(g_2\gamma_3 - g_3\gamma_2)f + g_2\beta_3 - g_3\beta_2](\gamma_1\beta_3 - \gamma_3\beta_1)}.\end{aligned} \quad \text{(A.58)}$$

The numerator simplifies to

$$\begin{aligned}&C_2D_1 - C_1D_2\\ &= \beta_3\rho_{LD}\rho_{GD}\left[c_1 y_2 y_3\left(\frac{1}{K_3} - \frac{1}{K_2}\right) + c_2 y_1 y_3\left(\frac{1}{K_1} - \frac{1}{K_2}\right) + c_3 y_1 y_2\left(\frac{1}{K_2} - \frac{1}{K_1}\right)\right].\end{aligned} \quad \text{(A.59)}$$

Using the previous simplification of $A_1D_2 - A_2D_1$ shows that χ_2 is a also a function of equilibrium composition

$$\frac{C_2D_1 - C_1D_2}{A_1D_2 - A_2D_1} = \frac{c_1 y_2 y_3\left(\frac{1}{K_3} - \frac{1}{K_2}\right) + c_2 y_1 y_3\left(\frac{1}{K_1} - \frac{1}{K_3}\right) + c_3 y_1 y_2\left(\frac{1}{K_2} - \frac{1}{K_1}\right)}{g_1 y_2 y_3\left(\frac{1}{K_3} - \frac{1}{K_2}\right) + g_2 y_1 y_3\left(\frac{1}{K_1} - \frac{1}{K_3}\right) + g_3 y_1 y_2\left(\frac{1}{K_2} - \frac{1}{K_1}\right)}. \quad \text{(A.60)}$$

Phase Change Shocks in the Ternary Displacement

The shock balance from the single phase region to the two-phase region is written as

$$\Lambda = \frac{H_i^I - H_i^{II}}{G_i^I - G_i^{II}}, \quad i = 1 \ldots N_c . \tag{A.61}$$

Substitution of the definitions for G_i^p and H_i^p into Eq. A.43 gives

$$\Lambda = \frac{u_D^I x_i^I \rho_D^I - u_D^{II}\left[f^{II}\left(y_i^{II}\rho_{GD}^{II} - x_i^{II}\rho_{LD}^{II}\right) + x_i^{II}\rho_{LD}^{II}\right]}{x_i^I \rho_D^I + \frac{1-\phi}{\phi}a_i^I - \left[S^{II}\left(y_i^{II}\rho_{GD}^{II} - x_i^{II}\rho_{LD}^{II}\right) + x_i^{II}\rho_{LD}^{II} + \frac{1-\phi}{\phi}a_i^{II}\right]}. \tag{A.62}$$

Rearranging Eq. A.44 to solve for x_i^I gives a relationship between the equilibrium phase compositions and the initial composition,

$$x_i^I = \frac{1-\phi}{\phi}\Lambda\frac{a_i^{II} - a_i^I}{\rho_D^I\left(\Lambda - u_D^I\right)} + x_i^{II}\rho_{LD}^{II}\frac{\Lambda\left(1 - S^{II}\right) + \left(u_D^{II}f^{II} - 1\right)}{\rho_D^I\left(\Lambda - u_D^I\right)} + y_i^{II}\rho_{LD}^{II}\frac{\Lambda S^{II} + u_D^{II}f^{II}}{\rho_D^I\left(\Lambda - u_D^I\right)}. \tag{A.63}$$

Entry from the single phase region into the two phase region occurs along a tie line extension for two cases:

- The adsorption function is linear, or
- $a_i^{II} = a_i^I$, thereby cancelling the adsorption contribution. If the isotherm is a function of equilibrium phase composition, along a tie line, the adsorbed concentration is constant, and the adsorption cancels.

Continuous Variation in the Quaternary Displacement

This section formulates the eigenvalue problem in the two-phase region for the quaternary displacement. Taking S, y_1, y_2 and u_D as the independent variables, the system of equations becomes:

$$\begin{bmatrix} \frac{\partial H_1}{\partial S} & \frac{\partial H_1}{\partial y_1} & \frac{\partial H_1}{\partial y_2} & \frac{\partial H_1}{\partial u_D} \\ \frac{\partial H_2}{\partial S} & \frac{\partial H_2}{\partial y_1} & \frac{\partial H_2}{\partial y_2} & \frac{\partial H_2}{\partial u_D} \\ \frac{\partial H_3}{\partial S} & \frac{\partial H_3}{\partial y_1} & \frac{\partial H_3}{\partial y_2} & \frac{\partial H_3}{\partial u_D} \\ \frac{\partial H_4}{\partial S} & \frac{\partial H_4}{\partial y_1} & \frac{\partial H_4}{\partial y_2} & \frac{\partial H_4}{\partial u_D} \end{bmatrix} \begin{bmatrix} \frac{dS}{d\eta} \\ \frac{dy_1}{d\eta} \\ \frac{dy_2}{d\eta} \\ \frac{du_D}{d\eta} \end{bmatrix} = \lambda \begin{bmatrix} \frac{\partial G_1}{\partial S} & \frac{\partial G_1}{\partial y_1} & \frac{\partial G_1}{\partial y_2} & \frac{\partial G_1}{\partial u_D} \\ \frac{\partial G_2}{\partial S} & \frac{\partial G_2}{\partial y_1} & \frac{\partial G_2}{\partial y_2} & \frac{\partial G_2}{\partial u_D} \\ \frac{\partial G_3}{\partial S} & \frac{\partial G_3}{\partial y_1} & \frac{\partial G_3}{\partial y_2} & \frac{\partial G_3}{\partial u_D} \\ \frac{\partial G_4}{\partial S} & \frac{\partial G_4}{\partial y_1} & \frac{\partial G_4}{\partial y_2} & \frac{\partial G_4}{\partial u_D} \end{bmatrix} \begin{bmatrix} \frac{dS}{d\eta} \\ \frac{dy_1}{d\eta} \\ \frac{dy_2}{d\eta} \\ \frac{du_D}{d\eta} \end{bmatrix}. \tag{A.64}$$

Applying the decoupling similar to that outlined in Dindoruk (1992), the system of equations becomes:

$$\left(\begin{bmatrix} \frac{\partial \alpha_1}{\partial S} - \frac{\alpha_1}{\alpha_4}\frac{\partial \alpha_4}{\partial S} & \frac{\partial \alpha_1}{\partial y_1} - \frac{\alpha_1}{\alpha_4}\frac{\partial \alpha_4}{\partial y_1} & \frac{\partial \alpha_1}{\partial y_2} - \frac{\alpha_1}{\alpha_4}\frac{\partial \alpha_4}{\partial y_2} & 0 \\ \frac{\partial \alpha_2}{\partial S} - \frac{\alpha_2}{\alpha_4}\frac{\partial \alpha_4}{\partial S} & \frac{\partial \alpha_2}{\partial y_1} - \frac{\alpha_2}{\alpha_4}\frac{\partial \alpha_4}{\partial y_1} & \frac{\partial \alpha_2}{\partial y_2} - \frac{\alpha_2}{\alpha_4}\frac{\partial \alpha_4}{\partial y_2} & 0 \\ \frac{\partial \alpha_3}{\partial S} - \frac{\alpha_3}{\alpha_4}\frac{\partial \alpha_4}{\partial S} & \frac{\partial \alpha_3}{\partial y_1} - \frac{\alpha_3}{\alpha_4}\frac{\partial \alpha_4}{\partial y_1} & \frac{\partial \alpha_3}{\partial y_2} - \frac{\alpha_3}{\alpha_4}\frac{\partial \alpha_4}{\partial y_2} & 0 \\ \frac{1}{\alpha_4}\frac{\partial \alpha_4}{\partial S} & \frac{1}{\alpha_4}\frac{\partial \alpha_4}{\partial y_1} & \frac{1}{\alpha_4}\frac{\partial \alpha_4}{\partial y_2} & \frac{1}{u_D} \end{bmatrix} \cdots \right.$$
$$\left. - \lambda^* \begin{bmatrix} \frac{\partial G_1}{\partial S} - \frac{\alpha_1}{\alpha_4}\frac{\partial G_4}{\partial S} & \frac{\partial G_1}{\partial y_1} - \frac{\alpha_1}{\alpha_4}\frac{\partial G_4}{\partial y_1} & \frac{\partial G_1}{\partial y_2} - \frac{\alpha_1}{\alpha_4}\frac{\partial G_4}{\partial y_2} & 0 \\ \frac{\partial G_2}{\partial S} - \frac{\alpha_2}{\alpha_4}\frac{\partial G_4}{\partial S} & \frac{\partial G_2}{\partial y_1} - \frac{\alpha_2}{\alpha_4}\frac{\partial G_4}{\partial y_1} & \frac{\partial G_2}{\partial y_2} - \frac{\alpha_2}{\alpha_4}\frac{\partial G_4}{\partial y_2} & 0 \\ \frac{\partial G_3}{\partial S} - \frac{\alpha_3}{\alpha_4}\frac{\partial G_4}{\partial S} & \frac{\partial G_3}{\partial y_1} - \frac{\alpha_3}{\alpha_4}\frac{\partial G_4}{\partial y_1} & \frac{\partial G_3}{\partial y_2} - \frac{\alpha_3}{\alpha_4}\frac{\partial G_4}{\partial y_2} & 0 \\ \frac{1}{\alpha_4}\frac{\partial G_4}{\partial S} & \frac{1}{\alpha_4}\frac{\partial G_4}{\partial y_1} & \frac{1}{\alpha_4}\frac{\partial G_4}{\partial y_2} & 0 \end{bmatrix} \right) \begin{bmatrix} \frac{dS}{d\eta} \\ \frac{dy_1}{d\eta} \\ \frac{dy_2}{d\eta} \\ \frac{du_D}{d\eta} \end{bmatrix} = \bar{0}. \tag{A.65}$$

The 3×3 subsystem for the normalised eigenvalue is:

$$\begin{bmatrix} F_{11}-\lambda^* G_{11} & F_{12}-\lambda^* G_{12} & F_{13}-\lambda^* G_{13} \\ F_{21}-\lambda^* G_{21} & F_{22}-\lambda^* G_{22} & F_{23}-\lambda^* G_{23} \\ F_{31}-\lambda^* G_{31} & F_{32}-\lambda^* G_{32} & F_{33}-\lambda^* G_{33} \end{bmatrix} \begin{bmatrix} \dfrac{dS}{d\eta} \\ \dfrac{dy_1}{d\eta} \\ \dfrac{dy_2}{d\eta} \end{bmatrix} = \bar{0}\,, \tag{A.66}$$

where:

$$F_{i1} = \frac{\partial \alpha_i}{\partial S} - \frac{\alpha_i}{\alpha_4}\frac{\partial \alpha_4}{\partial S}, \quad i = 1,\ldots,N_c - 1\,, \tag{A.67}$$

$$F_{i2} = \frac{\partial \alpha_i}{\partial y_1} - \frac{\alpha_i}{\alpha_4}\frac{\partial \alpha_4}{\partial y_1}, \quad i = 1,\ldots,N_c - 1\,, \tag{A.68}$$

$$F_{i3} = \frac{\partial \alpha_i}{\partial y_2} - \frac{\alpha_i}{\alpha_4}\frac{\partial \alpha_4}{\partial y_2}, \quad i = 1,\ldots,N_c - 1\,, \tag{A.69}$$

$$G_{i1} = \frac{\partial G_i}{\partial S} - \frac{\alpha_i}{\alpha_4}\frac{\partial G_4}{\partial S}, \quad i = 1,\ldots,N_c - 1\,, \tag{A.70}$$

$$G_{i2} = \frac{\partial G_i}{\partial y_1} - \frac{\alpha_i}{\alpha_4}\frac{\partial G_4}{\partial y_1}, \quad i = 1,\ldots,N_c - 1\,, \tag{A.71}$$

$$G_{i3} = \frac{\partial G_i}{\partial y_2} - \frac{\alpha_i}{\alpha_4}\frac{\partial G_4}{\partial y_2}, \quad i = 1,\ldots,N_c - 1\,. \tag{A.72}$$

The determinant of Eq. A.48 is set to zero to solve for the eigenvalues:

$$\begin{vmatrix} F_{11}-\lambda^* G_{11} & F_{12}-\lambda^* G_{12} & F_{13}-\lambda^* G_{13} \\ F_{21}-\lambda^* G_{21} & F_{22}-\lambda^* G_{22} & F_{23}-\lambda^* G_{23} \\ F_{31}-\lambda^* G_{31} & F_{32}-\lambda^* G_{32} & F_{33}-\lambda^* G_{33} \end{vmatrix} = 0\,, \tag{A.73}$$

and the eigenvalues for the quaternary displacement are:

$$\lambda^* = \frac{df}{dS}, \frac{-b \pm \sqrt{b^2 - 4ac}}{2a}\,, \tag{A.74}$$

where:

$$A_1 = G_{22}G_{33} - G_{23}G_{32}, \tag{A.75}$$

$$A_2 = G_{12}G_{33} - G_{13}G_{32}, \tag{A.76}$$

$$A_3 = G_{12}G_{23} - G_{13}G_{22}, \tag{A.77}$$

$$B_1 = F_{32}G_{23} + F_{23}G_{32} - F_{33}G_{22} - F_{22}G_{33}, \tag{A.78}$$

$$B_2 = F_{32}G_{13} + F_{13}G_{32} - F_{33}G_{12} - F_{12}G_{33}, \tag{A.79}$$

$$B_3 = F_{22}G_{13} + F_{13}G_{22} - F_{23}G_{12} - F_{12}G_{23}, \tag{A.80}$$

$$C_1 = F_{22}F_{33} - F_{23}F_{32}, \tag{A.81}$$

$$C_2 = F_{12}F_{33} - F_{13}F_{32}, \tag{A.82}$$

$$C_3 = F_{12}F_{23} - F_{13}F_{22}, \tag{A.83}$$

$$a = A_1\left(\gamma_1 y_1 - \frac{\alpha_1}{\alpha_4}\gamma_4 y_4\right) - A_2\left(\gamma_2 y_2 - \frac{\alpha_2}{\alpha_4}\gamma_4 y_4\right) + A_3\left(\gamma_3 y_3 - \frac{\alpha_3}{\alpha_4}\gamma_4 y_4\right), \tag{A.84}$$

$$b = B_1\left(\gamma_1 y_1 - \frac{\alpha_1}{\alpha_4}\gamma_4 y_4\right) - B_2\left(\gamma_2 y_2 - \frac{\alpha_2}{\alpha_4}\gamma_4 y_4\right) + B_3\left(\gamma_3 y_3 - \frac{\alpha_3}{\alpha_4}\gamma_4 y_4\right), \tag{A.85}$$

$$c = C_1\left(\gamma_1 y_1 - \frac{\alpha_1}{\alpha_4}\gamma_4 y_4\right) - C_2\left(\gamma_2 y_2 - \frac{\alpha_2}{\alpha_4}\gamma_4 y_4\right) + C_3\left(\gamma_3 y_3 - \frac{\alpha_3}{\alpha_4}\gamma_4 y_4\right). \tag{A.86}$$

Variation of Local Flow Velocity Along a Tie Line

Substituting the definitions for G_i and H_i into the conservation equations gives the following expressions:

$$\frac{\partial}{\partial\tau}\left[S(y_1\rho_{GD} - x_1\rho_{LD}) + x_1\rho_{LD} + \frac{1-\phi}{\phi}a_1\right] + \frac{\partial}{\partial\xi}\left[u_D\left(f(y_1\rho_{GD} - x_1\rho_{LD}) + x_1\rho_{LD}\right)\right] = 0, \tag{A.87}$$

and

$$\frac{\partial}{\partial\tau}\left[S(y_2\rho_{GD}-x_2\rho_{LD})+x_2\rho_{LD}+\frac{1-\phi}{\phi}a_2\right]+\frac{\partial}{\partial\xi}[u_D(f(y_2\rho_{GD}-x_2\rho_{LD})+x_2\rho_{LD})]=0\,. \quad \text{(A.88)}$$

For composition variation along a tie line, equilibrium phase compositions, adsorption concentration and phase densities remain constant. If we assume porosity is also constant, the conservation equations reduce to:

$$(y_1\rho_{GD}-x_1\rho_{LD})\frac{\partial S}{\partial\tau}+\frac{\partial}{\partial\xi}[u_D(f(y_1\rho_{GD}-x_1\rho_{LD})+x_1\rho_{LD})]=0\,, \quad \text{(A.89)}$$

and

$$(y_2\rho_{GD}-x_2\rho_{LD})\frac{\partial S}{\partial\tau}+\frac{\partial}{\partial\xi}[u_D(f(y_2\rho_{GD}-x_2\rho_{LD})+x_2\rho_{LD})]=0\,. \quad \text{(A.90)}$$

Eliminating $\frac{\partial S}{\partial\tau}$:

$$\frac{\partial u_D}{\partial\xi}\left(\frac{x_1\rho_{LD}}{(y_1\rho_{GD}-x_1\rho_{LD})}-\frac{x_2\rho_{LD}}{(y_2\rho_{GD}-x_2\rho_{LD})}\right)=0\,. \quad \text{(A.91)}$$

If we apply Henry's Law and substitute expressions for y_i into Eq. A.73, we get

$$\frac{\partial u_D}{\partial\xi}\rho_{LD}\left(\frac{1}{(K_1\rho_{GD}-\rho_{LD})}-\frac{1}{(K_2\rho_{GD}-\rho_{LD})}\right)=0\,. \quad \text{(A.92)}$$

In a two phase system, $K_1 \neq K_2$, therefore, for this equality to hold, $\frac{\partial u_D}{\partial\xi}=0$. Along a tie line, u_D is constant.

Appendix B

Analysis of Nonadsorbing Structures

Two-Phase Injection in Nonadsorbing Systems

In this appendix, analysis of Type III solution structures in analogue nonadsorbing systems is considered. This analysis is simplified to two-phase injection in a ternary system: $N_2/CH_4/C_{10}$. In practice, two-phase injection is unlikely. However, under certain injection conditions, quaternary displacements can create situations that mimic two-phase, ternary displacements. This appendix presents previously unreported solution structures. These solution structures were not discovered previously because two-phase injection conditions were of no practical significance in gas injection processes. Moreover, the model quaternary systems considered by earlier researchers limited their analysis to systems where K_1 and $K_2 > 1$ and K_3 and $K_4 < 1$. In flue gas injection, the model system is represented by K_1, K_2 and $K_3 > 1$ and $K_4 < 1$.

In this analysis, initial composition is fixed at 0.31 mol fraction CH_4 and 0.6 mol fraction C_{10}. Two-phase N_2/C_{10} binary injection mixtures are considered. The analysis presented is for constant K-values with no volume change effects because exact analytical expressions for composition paths are available. However, patterns presented remain the same for systems with variable K-values and volume change effects. Table B-1 summarises K-values and flow parameters used in this analysis.

Five types of solution structures are possible. These are dependent on the injection gas saturation relative to the landing points of the nontie-line paths traced from the equal-eigenvalue point of the initial equilibrium tie line (Figure B-1). Corresponding solution profiles are summarised in Figure B-2. Figure B-3 shows the location of key points that delineate the categories of composition paths encountered in two-phase injection systems. S_{gA} is the landing point on the injection tie line of the $\frac{\partial \lambda_{nt}}{\partial S} < 0$ branch of the nontie-line path traced from the initial tie line. S_{gB} is the landing point on the injection tie line of the $\frac{\partial \lambda_{nt}}{\partial S} > 0$ branch of the nontie-line path traced from the initial tie line. S_{gEV} is the saturation of the equivelocity point on the injection tie line.

Table B-1: Summary of K-values and flow parameters used in the $N_2/CH_4/C_{10}$ system.

K_{N2}	8
K_{CH4}	3.5
K_{C10}	0.01
M	15

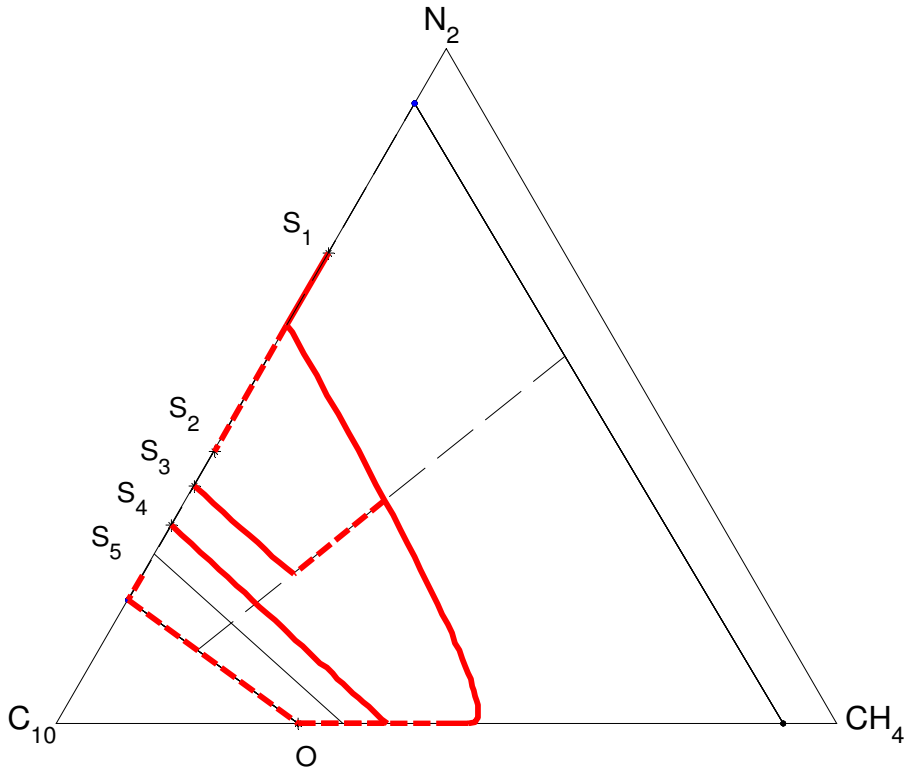

Figure B-1: Composition paths for two-phase injection compositions.

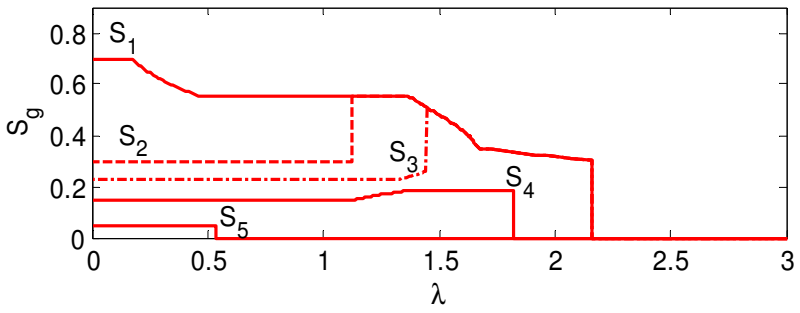

Figure B-2: Solution profiles for two-phase injection conditions.

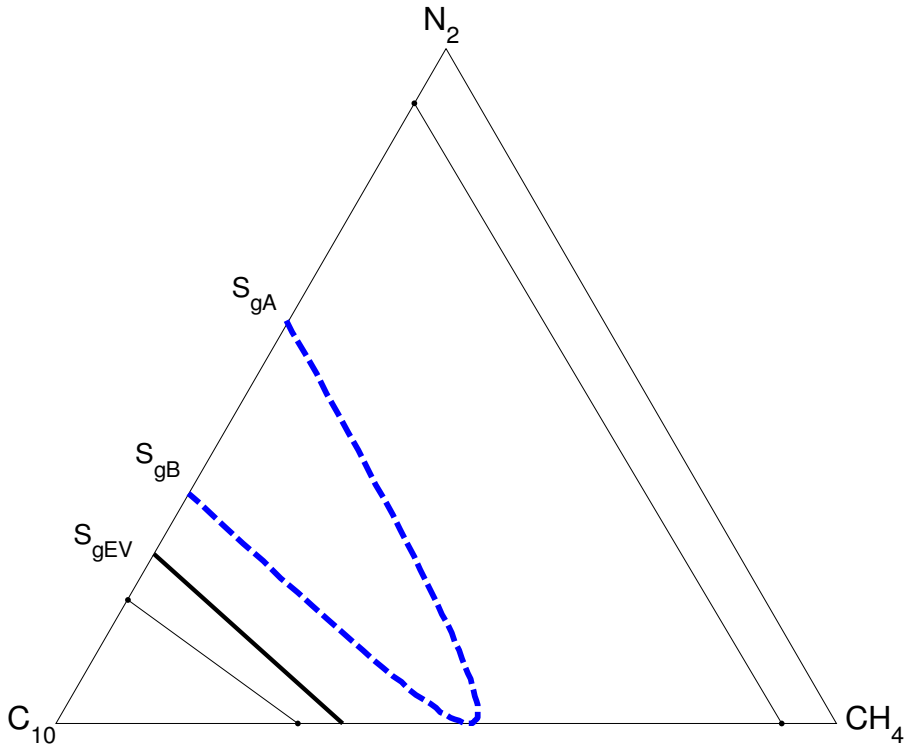

Figure B-3: Location of key points delineating solution structures in composition space.

S_1: $S_g > S_{gA}$

For high S_g injection conditions, gas saturation decreases monotonically from the injection to initial state. The composition path and solution profile for this type of solution are shown in Figures B-4 and B-5. Solution construction for these systems follows traditional construction for ternary systems. The initial tie line is the shortest tie line; construction starts at that tie line. A tangent shock along the initial tie line is required for the composition path to enter the two-phase region from the initial composition. This shock is followed by a tie-line rarefaction to the equal-eigenvalue point. At the equal-eigenvalue point, the path switches from a tie-line path to a nontie-line path. This nontie-line variation connects initial and injection tie lines.

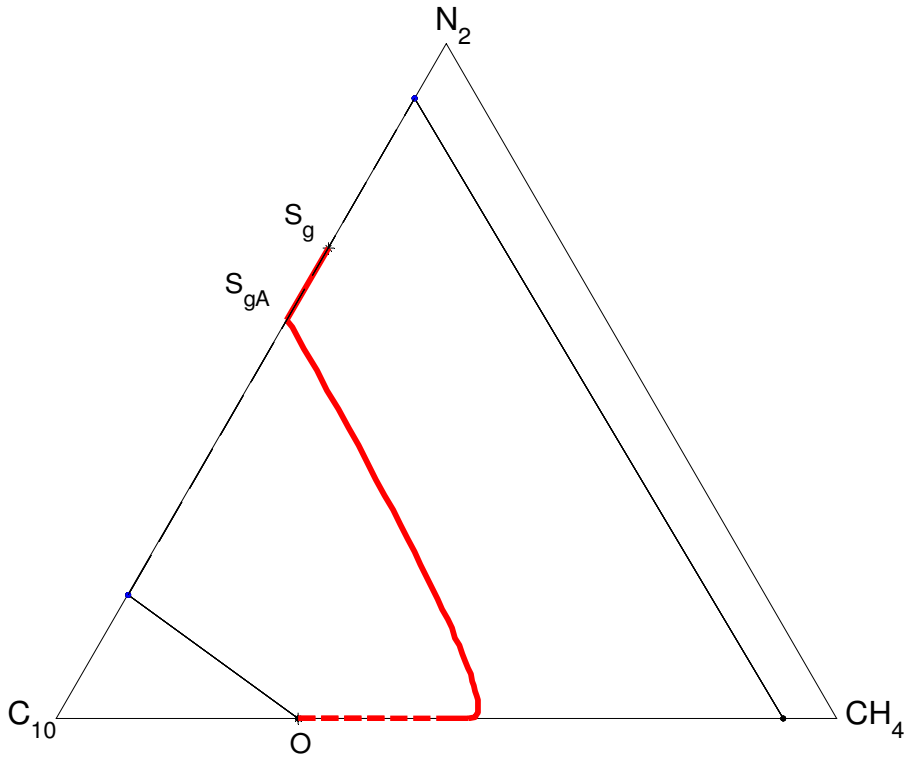

Figure B-4: Composition path for S_1 structure.

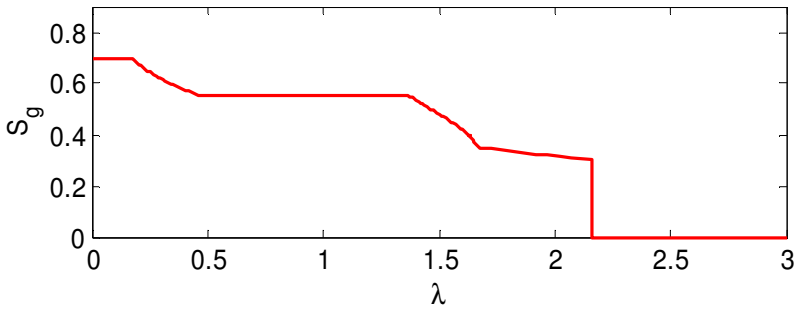

Figure B-5: Solution profile for S_1 structure.

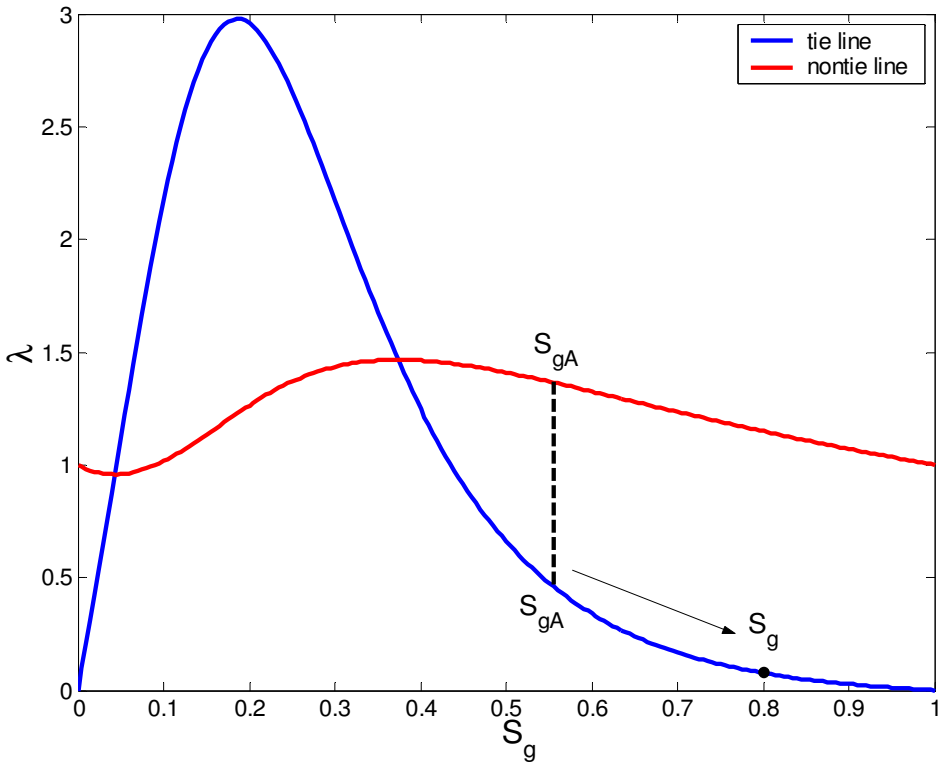

Figure B-6: Path switch from nontie-line path to tie-line path at the injection tie line.

Figure B-6 shows the location of the eigenvalue of the landing point of the nontie-line path on the injection tie line relative to the injection saturation. The nontie-line eigenvalue is greater than the tie-line eigenvalue for the same saturation, and a path switch is allowed. This switch corresponds to a zone of constant state in the solution profile. In this example, the landing point of the nontie-line path has a faster wave velocity than that of the injection condition. A tie-line rarefaction connects the landing point and injection state.

S_2: S_g bounded by S_{gA} and S_{gB}, and $\Lambda < \lambda_{ntA}$

Composition path and solution profile for this injection condition are shown in Figures B-7 and B-8. Solution construction for injection conditions where $S_{gB} < S_g < S_{gA}$ follows a similar construction procedure as for the previous solution. Continuous variation along the injection tie line from S_{gA} to S_g violates the velocity rule, and a shock is necessary (Figure B-9). A genuine shock along the injection tie line connects the nontie-line landing point to the injection condition.

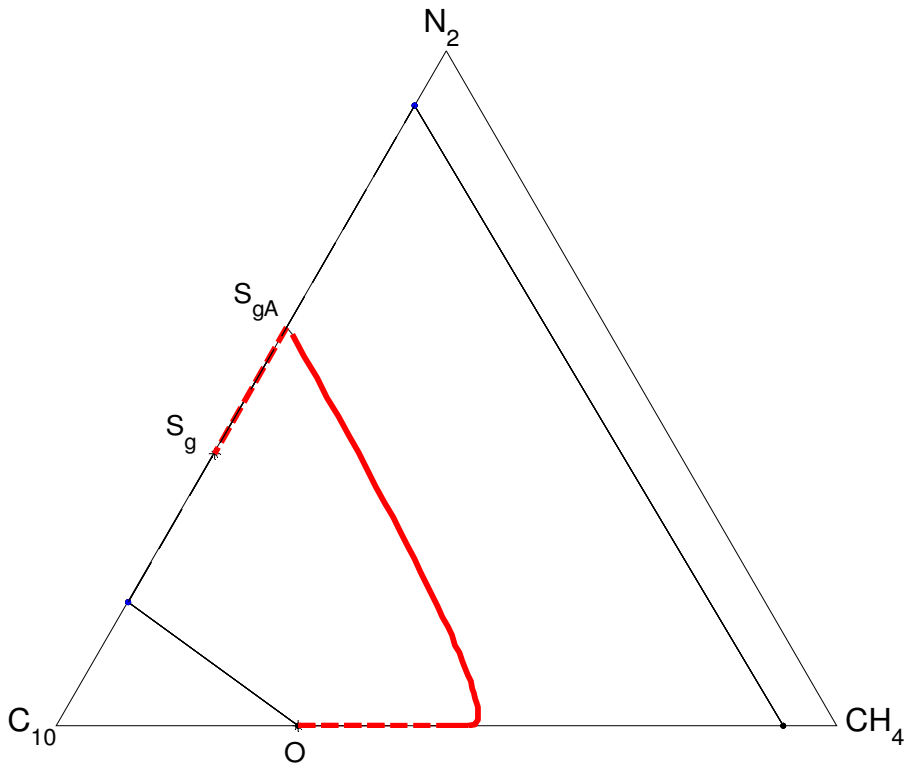

Figure B-7: Composition path for S_2 structure.

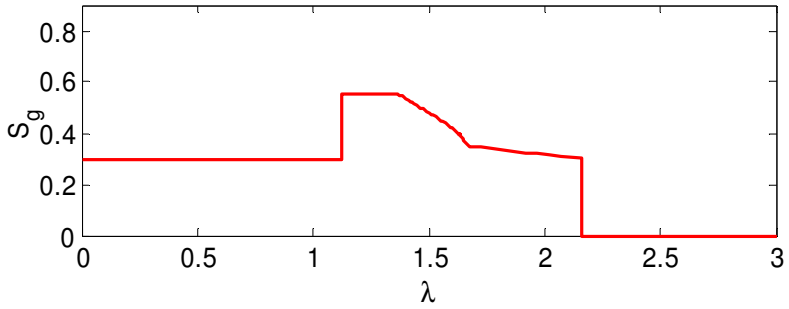

Figure B-8: Solution profile for S_2 structure.

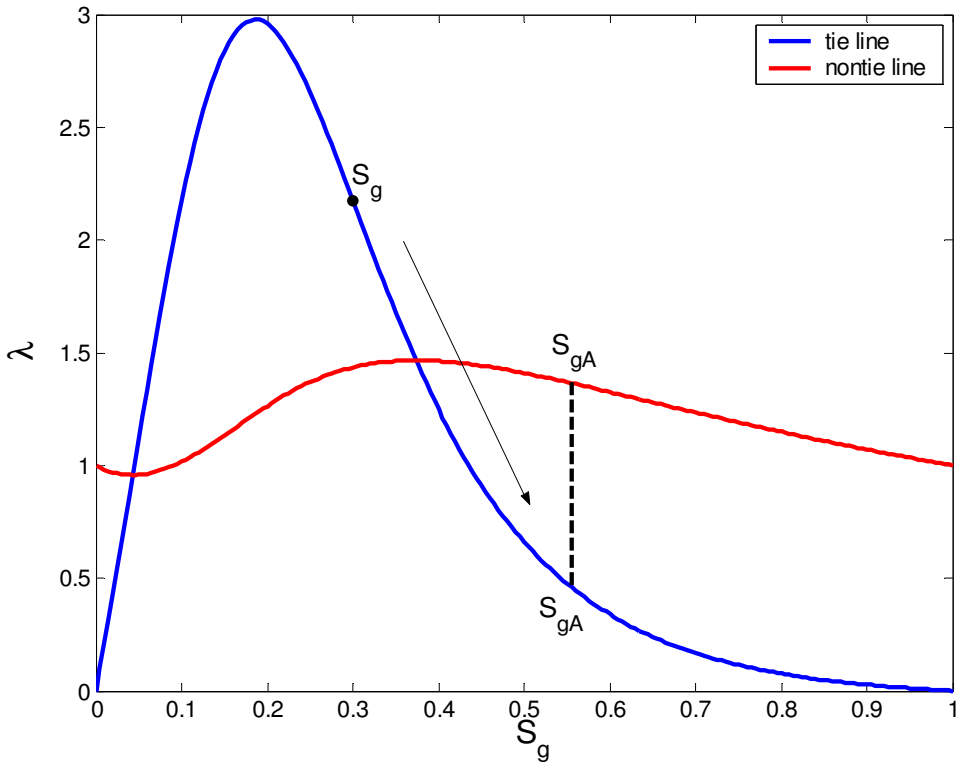

Figure B-9: Tie-line variation from S_{gA} to S_g violates the velocity rule.

To analyse this solution structure, the parameterisation presented in Wang (1998) is used. -*P* (Eq. B.1) is the overall volume fraction on the envelope curve (Dindoruk, 1992)

$$P = \frac{K_1 - K_2}{K_2 - 1}\frac{K_1 - K_3}{1 - K_3}x_1^2 . \tag{B.1}$$

The slope of the line segment from *P* to S_{gA} (Figure B-10, Eq. B.2) is the nontie-line eigenvalue at S_{gA} on the injection tie line

$$\lambda_{nt} = \frac{F_1 + P}{C_1 + P}. \tag{B.2}$$

The velocity of the genuine shock connecting the injection condition and the nontie-line path traced from the initial tie line (S_g to S_{gA} in Figure B-7) is given by the slope of the chord connecting S_g and S_{gA} in Figure B-10.

The limit of this solution structure occurs when $S_g = S_g^*$, where S_g^* is the intersection of the line segment from *P* to S_{gA} with the overall fractional flow function for the injection tie line. If $S_g < S_g^*$, the velocity of the genuine shock is greater than the nontie-line eigenvalue, and the velocity rule is violated. The next section shows the new structure required to connect injection and initial states for $S_g < S_g^*$.

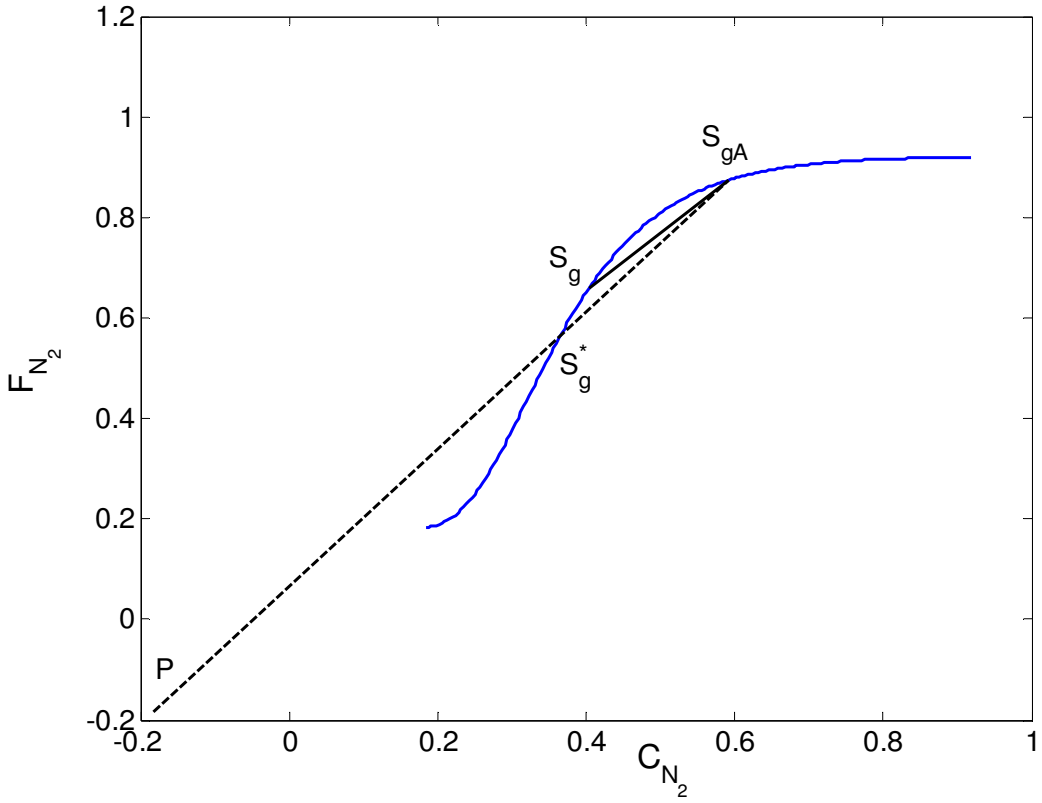

Figure B-10: Stability of genuine shock from S_g to S_{gA}.

S_3: S_g bounded by S_{gA} and S_{gB}, and $\Lambda > \lambda_{ntA}$

The composition path and solution profile for this injection condition are presented in Figures B-11 and B-12. Figure B-13 shows the allowable points that satisfy the Rankine-Hugonoit condition for an injection saturation bounded by the two landing point saturations of the nontie-line path from the equal-eigenvalue point on the injection tie line (S_{gA} and S_{gB}) . The Hugoniot locus for a shock from the injection composition does not intersect the initial tie line. Therefore, a shock from the injection condition to the initial tie line is not allowed. For two-phase injection conditions where $S_g < S_g^*$, injection and initial segments are constructed independently. For this injection condition, the nontie-line path is taken. This

composition path requires the use of both $\frac{\partial \lambda_{nt}}{\partial S} < 0$ and $\frac{\partial \lambda_{nt}}{\partial S} > 0$ branches of the nontie-line paths. Previously reported solutions only considered nontie-line variation where $\frac{\partial \lambda_{nt}}{\partial S} < 0$.

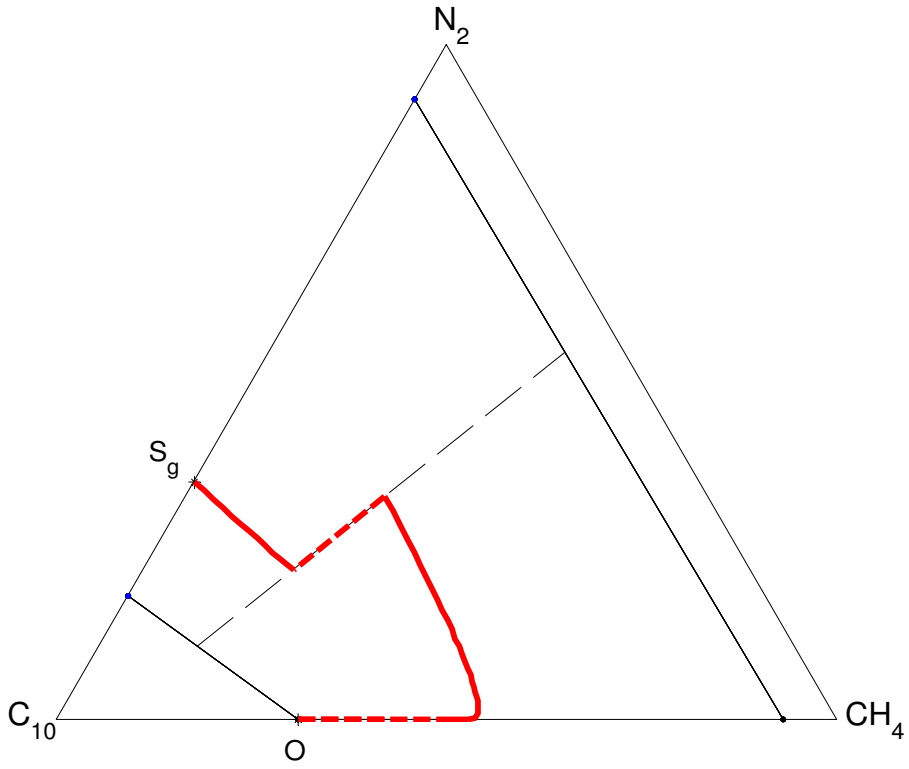

Figure B-11: Composition path for S_3 structure.

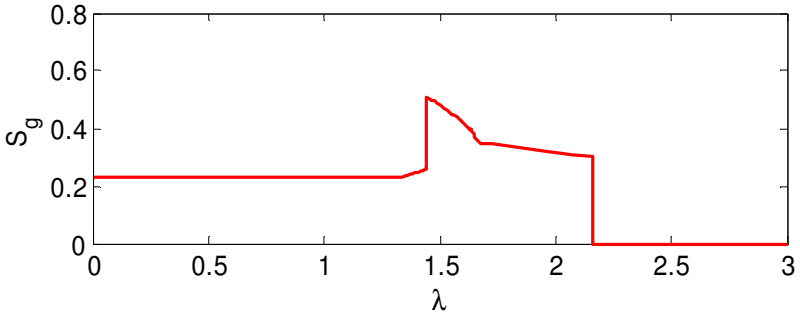

Figure B-12: Solution profile for S_3 structure.

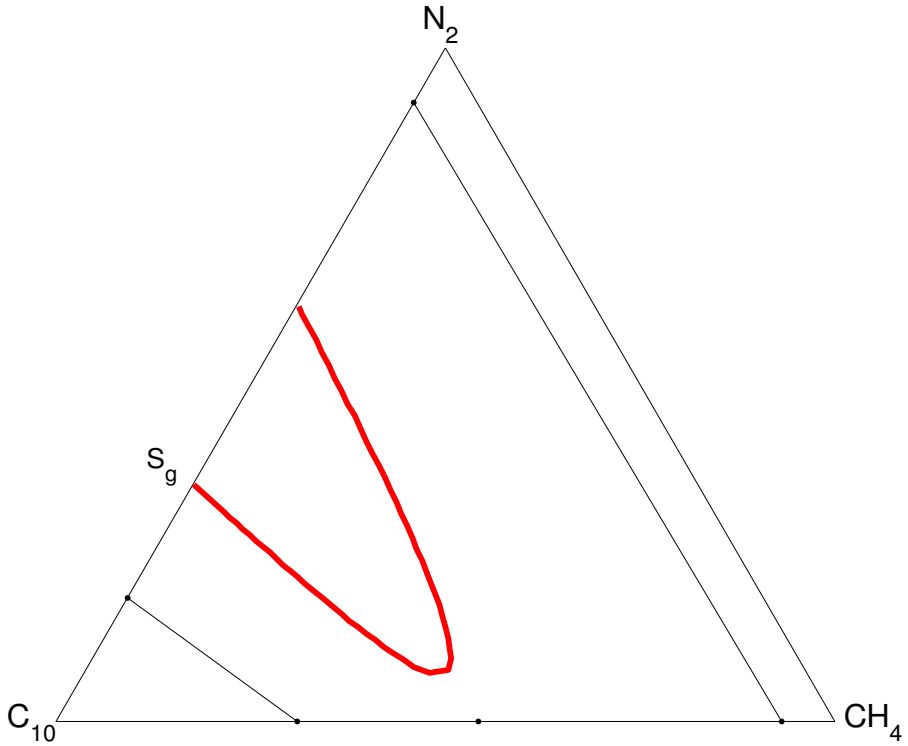

Figure B-13: Hugoniot locus traced from S_g

The nontie-line path traced from the injection conditions, S_g, is nested in the nontie-line path traced from the equal-eigenvalue point of the initial tie line (Figure B-14). A shock is necessary to connect the injection and initial nontie-line paths. When the nontie-line eigenvalue is traced from the injection tie line to the initial tie line (Figure B-15), there is a tie line where the nontie-line eigenvalue of the injection nontie-line path is equal to the nontie-line eigenvalue of initial nontie-line path. Figure B-16 illustrates that path switches from the nontie-line path to this tie line are allowable on both sides of the shock. Because the eigenvalue decreases from the injection landing point to the initial landing point, continuous variation along the tie line violates the velocity rule. A shock along this tie line is required to facilitate the switch from the injection nontie-line path to the initial nontie-line path.

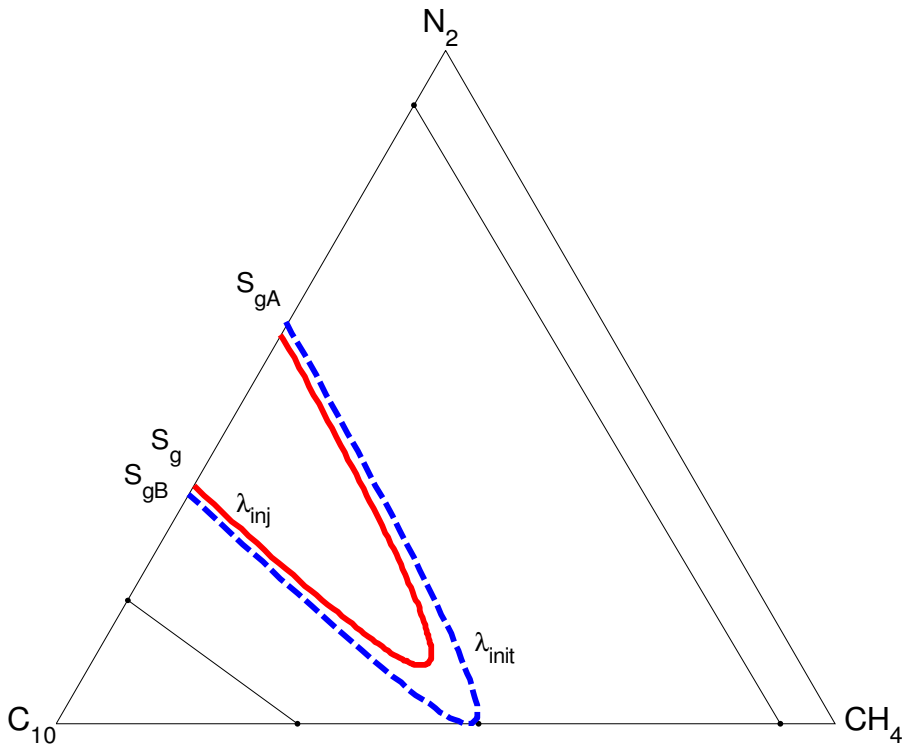

Figure B-14: The injection nontie-line path is nested in the initial nontie-line path.

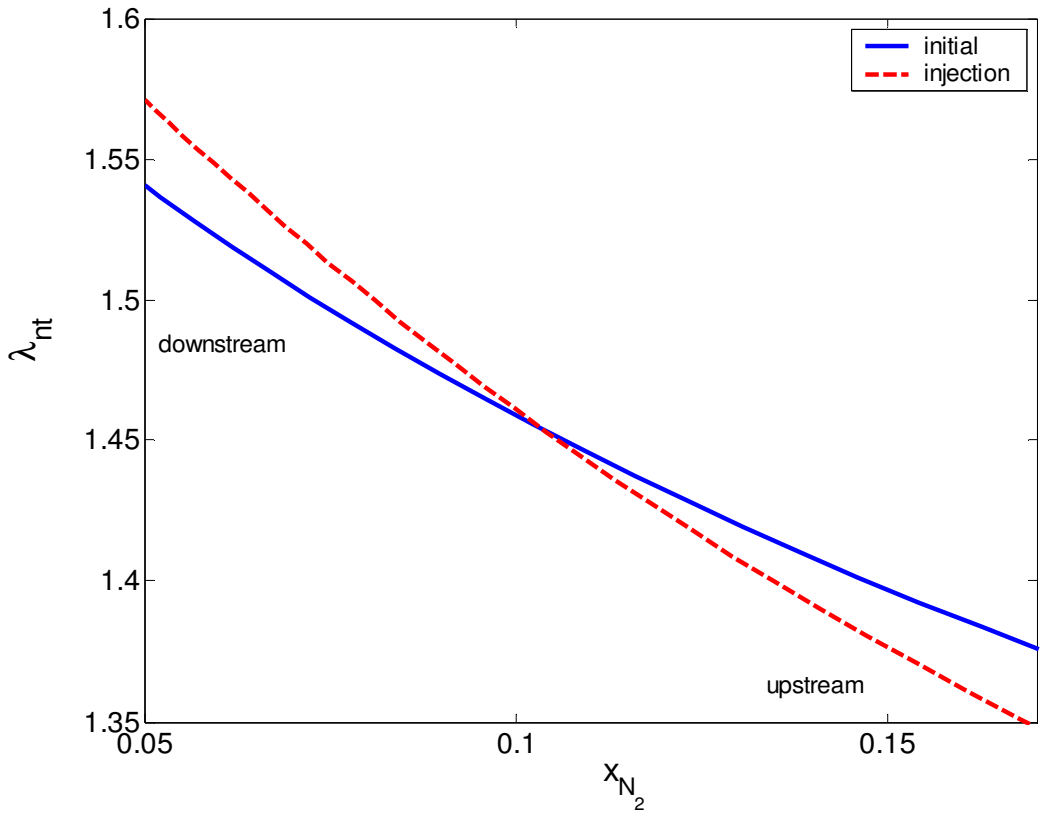

Figure B-15: Variation of nontie-line eigenvalues from injection to initial tie-lines.

For this shock to remain stable throughout the displacement, the velocity of the shock must be equal to the velocities immediately upstream and downstream of the shock. Jeffrey (1976) classifies this type of shock as a degenerate shock. This tie line is designated the degenerate tie line. Figures B-17 and B-18 show a composition path and solution profile and for a tie-line shock shorter than the degenerate tie line. This solution construction is not allowed because the wave velocities on the injection segment are faster than the shock velocity, violating the velocity rule (Figure B-19) although the velocity rule is satisfied on the initial segment (Figure B-20). Figures B-21 and B-22 show a composition path and solution profile for a tie-line shock along a tie line longer than the degenerate tie line. This solution construction is also not allowed due to a violation of the velocity rule. In this case, the velocity rule violation occurs with eigenvalues on

the initial branch. On the injection segment, the eigenvalues are slower than the shock velocity and structure is stable (Figure B-24). However, on the initial branch, the shock velocity is faster than the nontie-line eigenvalue (Figure B-23). For tie lines that are longer than the degenerate tie line, the shock velocity will overtake the wave velocities of the initial branch as the displacement proceeds.

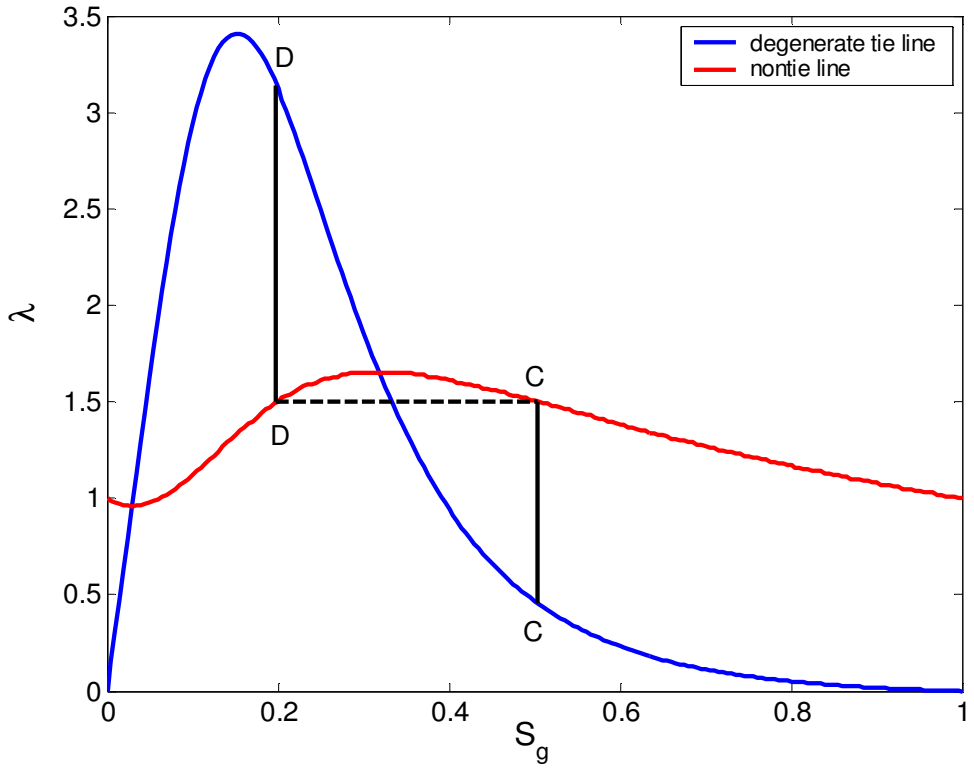

Figure B-16: Path switches from the nontie-line paths to the degenerate tie line obey the velocity rule.

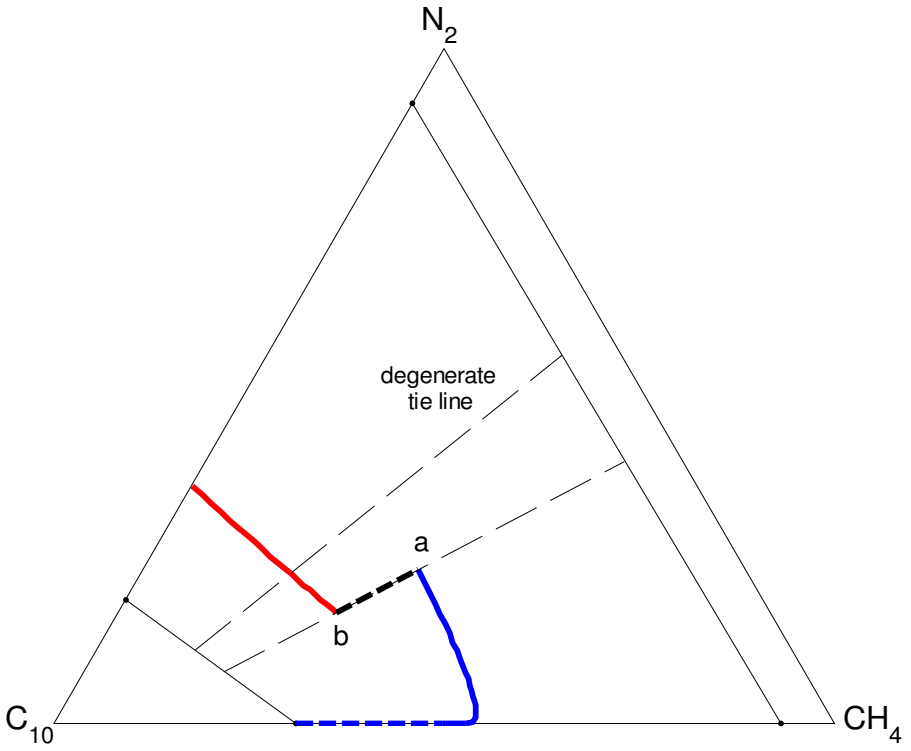

Figure B-17: Composition path of a tie-line shock shorter than the degenerate tie line.

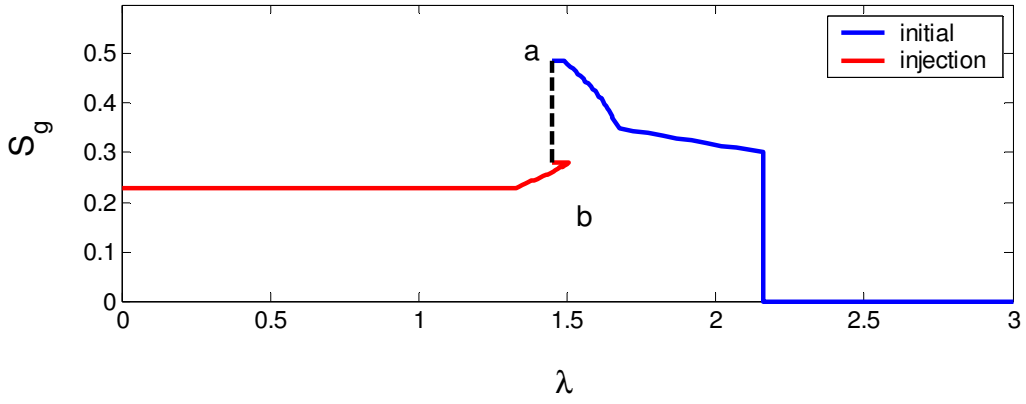

Figure B-18: Solution profile of a tie-line shock shorter than the degenerate tie line.

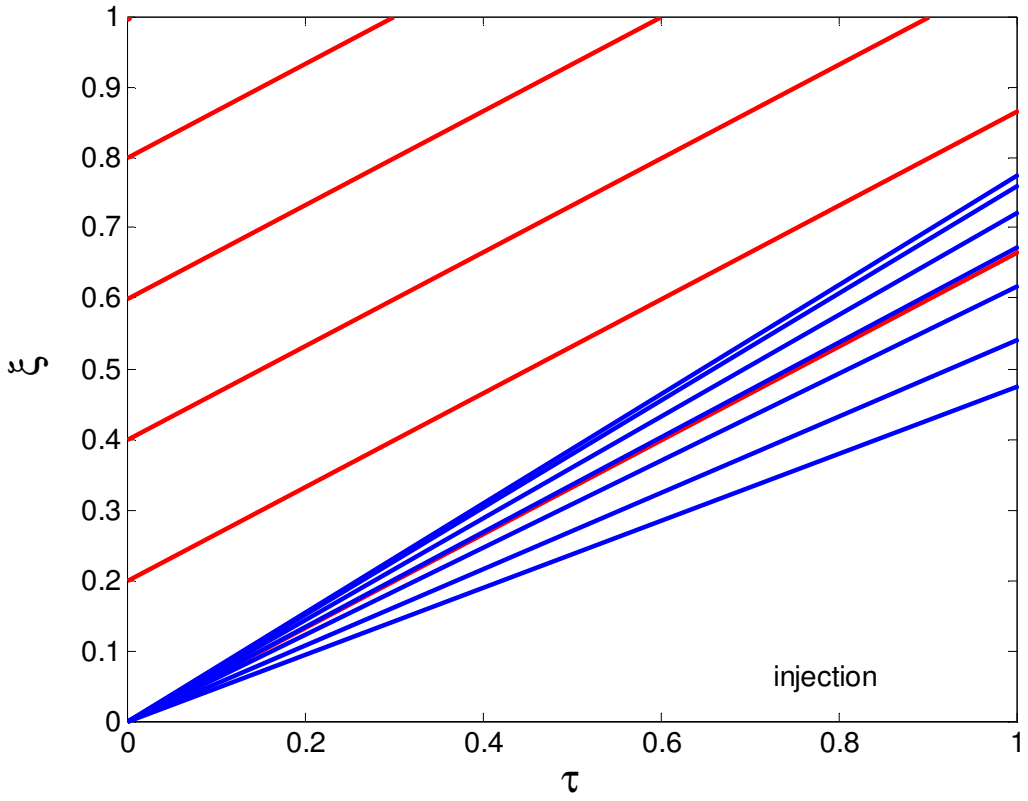

Figure B-19: ξ-τ diagram of injection characteristics upstream (blue) of a tie-line shock (red) along a tie line shorter than the degenerate tie line.

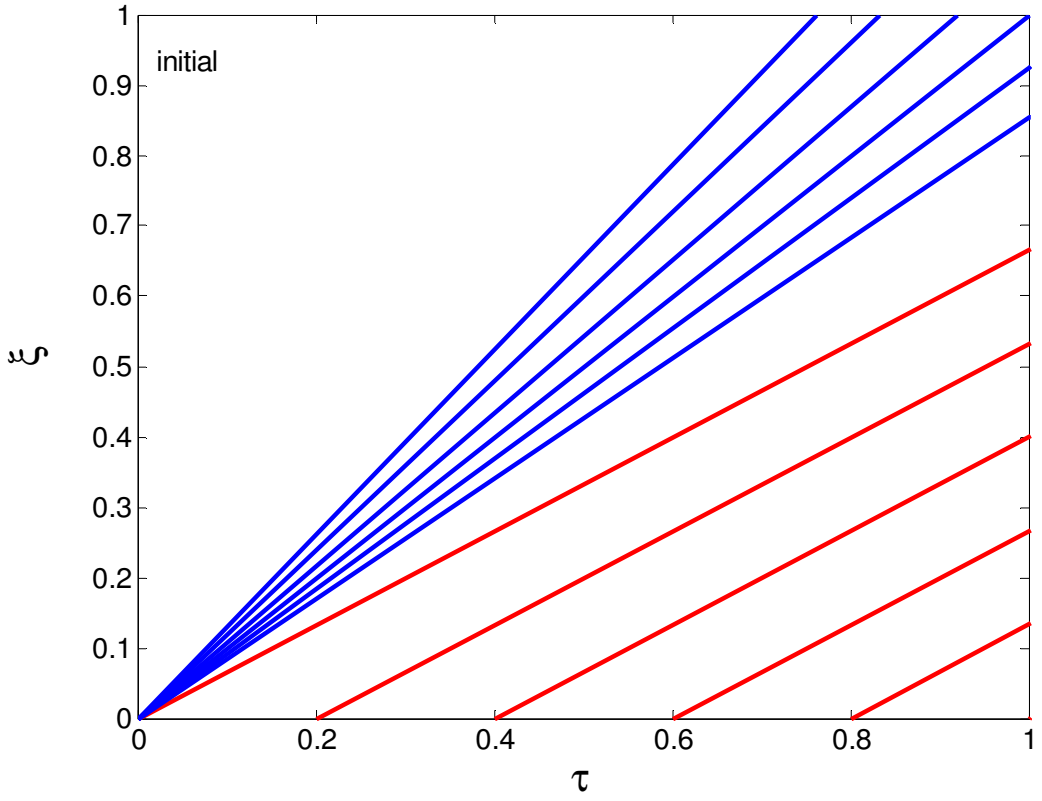

Figure B-20: ξ-τ diagram of initial characteristics downstream (blue) of a tie line shock (red) along a tie line shorter than the degenerate tie line.

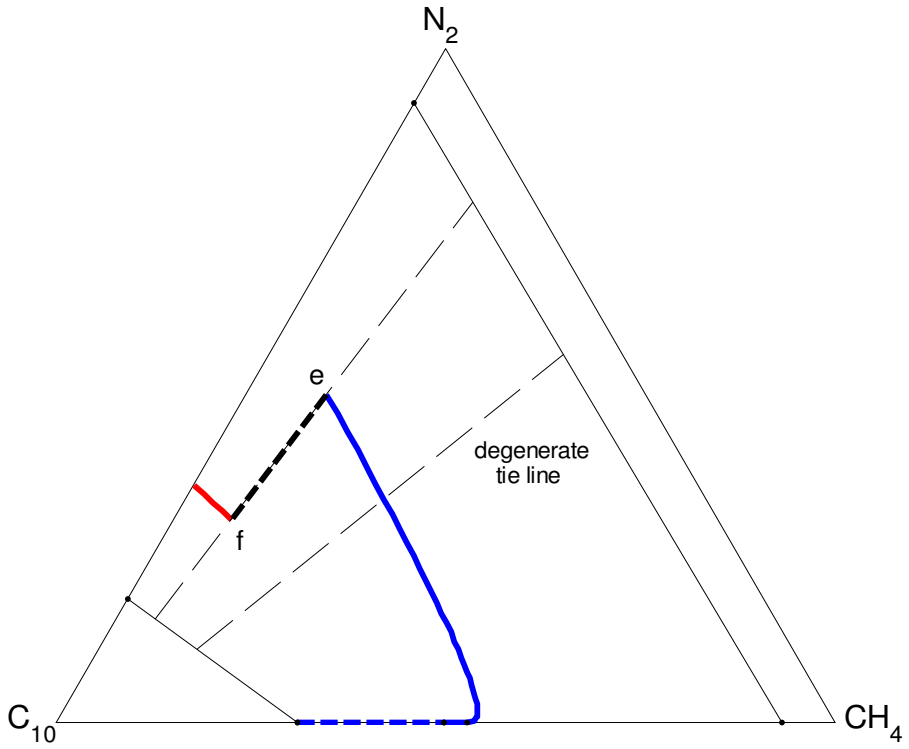

Figure B-21: Composition path of a tie-line shock longer than the degenerate tie line.

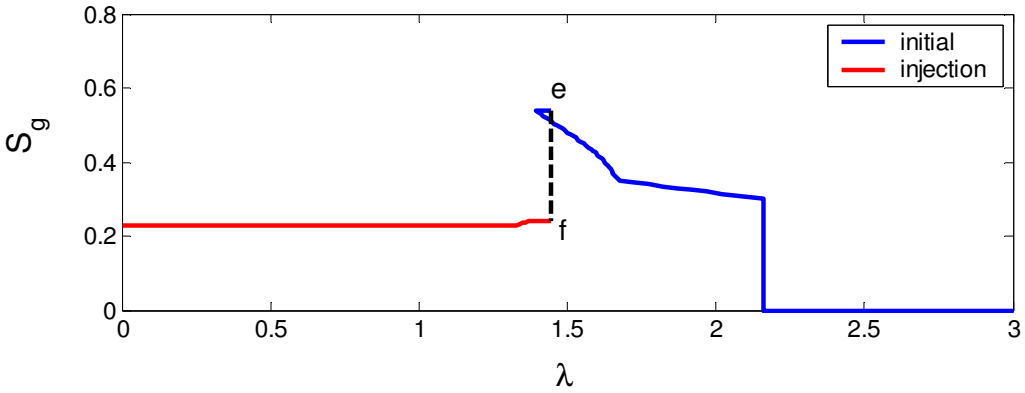

Figure B-22: Solution profile of a tie line shock longer than the degenerate tie line.

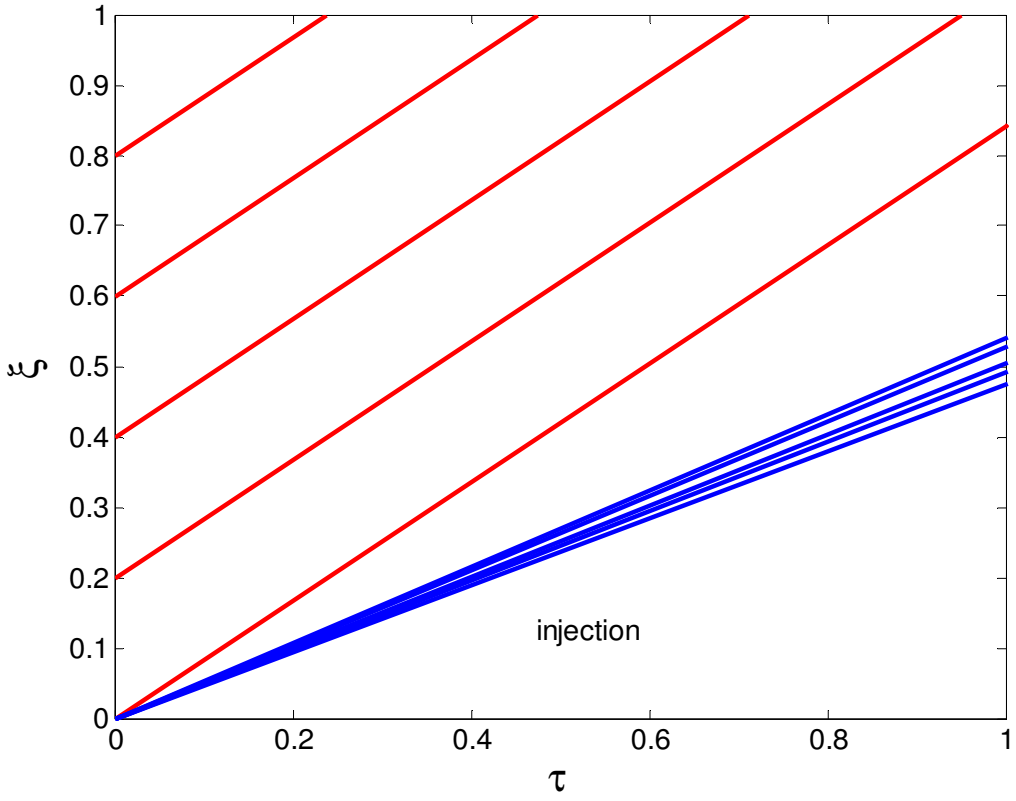

Figure B-23: ξ-τ diagram of injection characteristics upstream (blue) of a tie-line shock (red) along a tie line longer than the degenerate tie line.

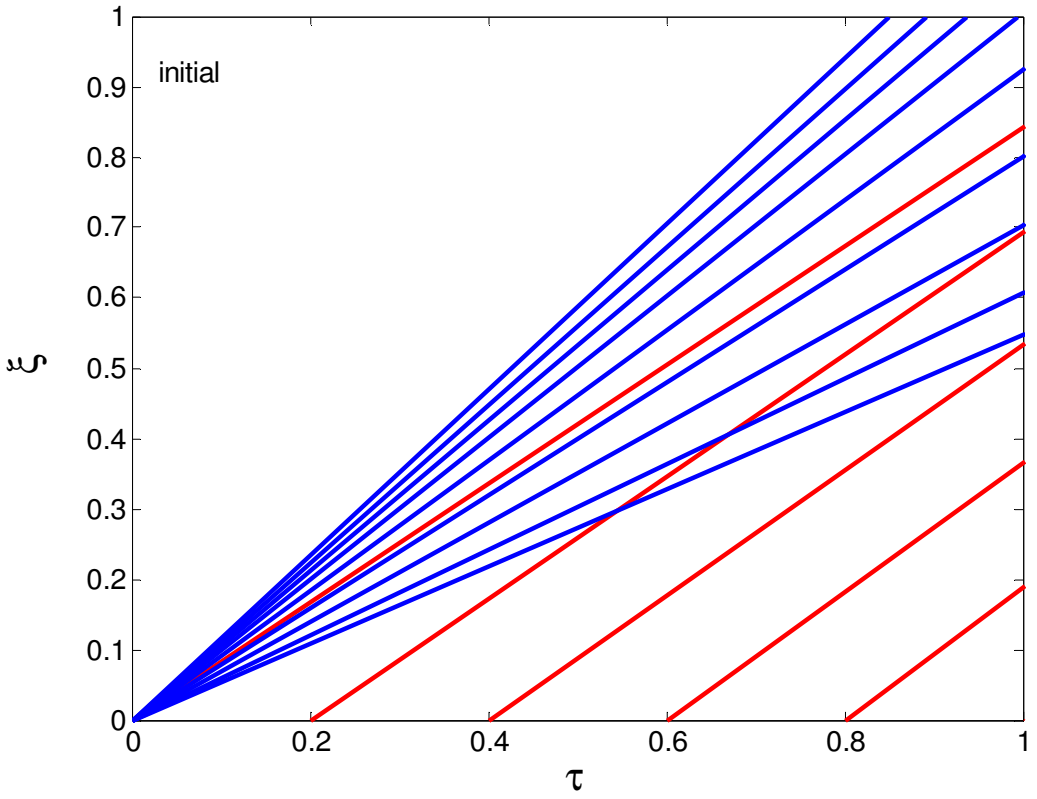

Figure B-24: ξ-τ diagram of initial characteristics downstream (blue) of the tie-line shock (red) along a tie line longer than the degenerate tie line.

Figure B-25 illustrates another representation of this path switch. The slope of the characteristics of the injection nontie-line path increase as the nontie-line is traced path up towards the degenerate tie line, while the slope of the characteristics from the initial nontie-line path decrease tracing the nontie-line path down towards the degenerate tie line. At the degenerate tie line, the injection characteristic is equal to the initial characteristic. A compatible set of waves is traced along the injection and initial nontie-line paths.

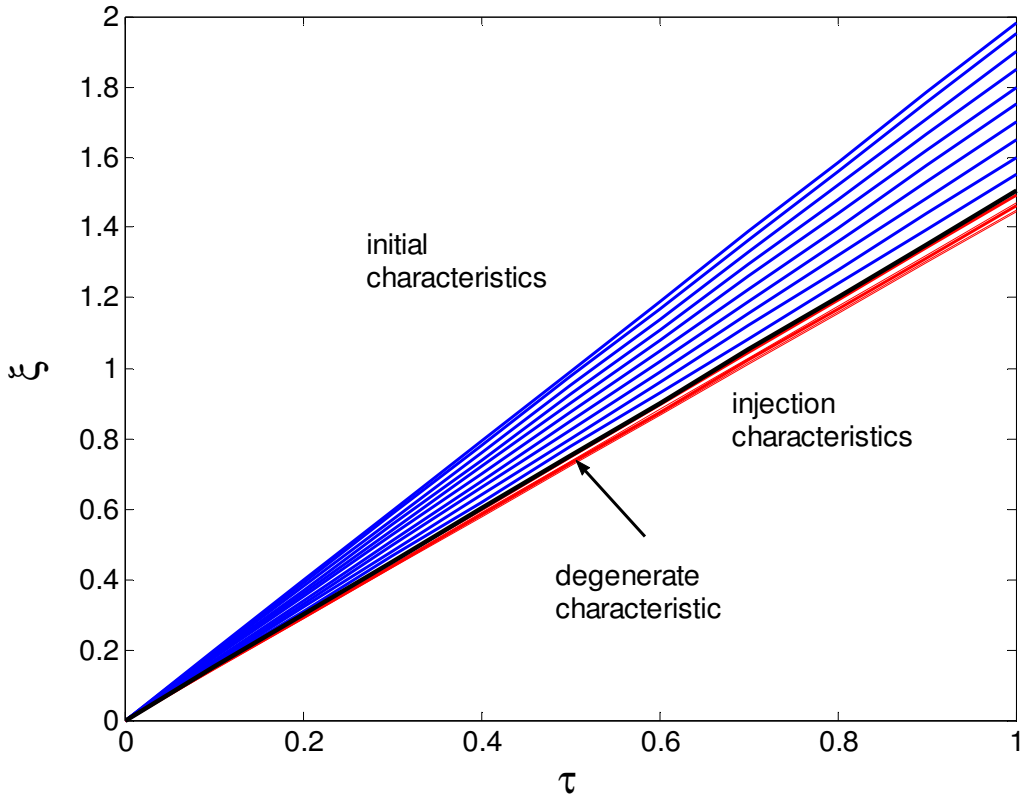

Figure B-25: Variation of characteristics from injection tie line (red) to initial tie line (blue). The degenerate shock is shown in black.

Figure B-26 demonstrates that the degenerate shock is stable as it propagates through the displacement. The degenerate shock is represented by the slope of the chord connecting C and D

$$\Lambda_{deg} = \frac{F_C - F_D}{C_C - C_D}. \tag{B.3}$$

The slope of the line segment from C to P_D represents the nontie-line eigenvalue immediately downstream of the shock

$$\lambda_{nt}^{D} = \frac{F_C + P_D}{C_C + P_D}. \tag{B.4}$$

The slope of the line segment connecting D to P_D represents the nontie-line eigenvalue upstream of the shock,

$$\lambda_{nt}^{U} = \frac{F_D + P_D}{C_D + P_D}. \tag{B.5}$$

From Figure B-26, both the nontie-line eigenvalues immediately upstream and downstream of the degenerate shock are equal to the degenerate shock.

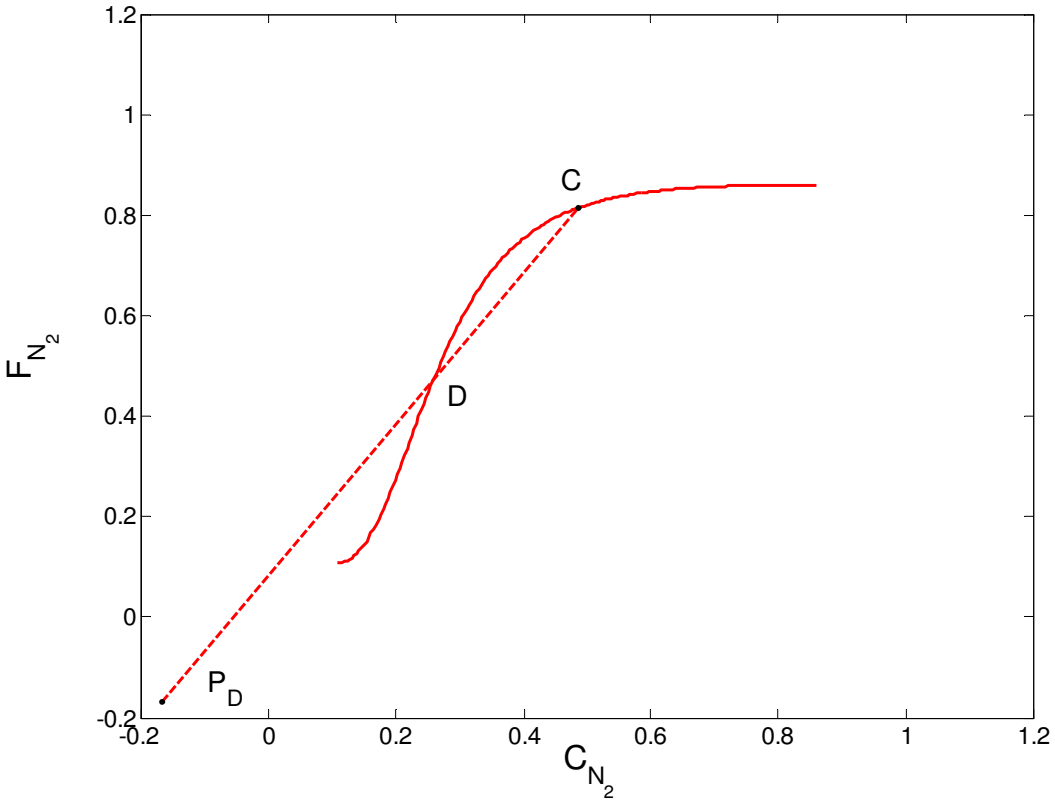

Figure B-26: Geometric interpretation of the degenerate shock and the nontie-line eigenvalues immediately upstream and downstream of the shock.

Nontie-line eigenvalues upstream of the shock are given by the following expression

$$\lambda_{nt}^{L} = \frac{F_L + P_L}{C_L + P_L}. \tag{B.6}$$

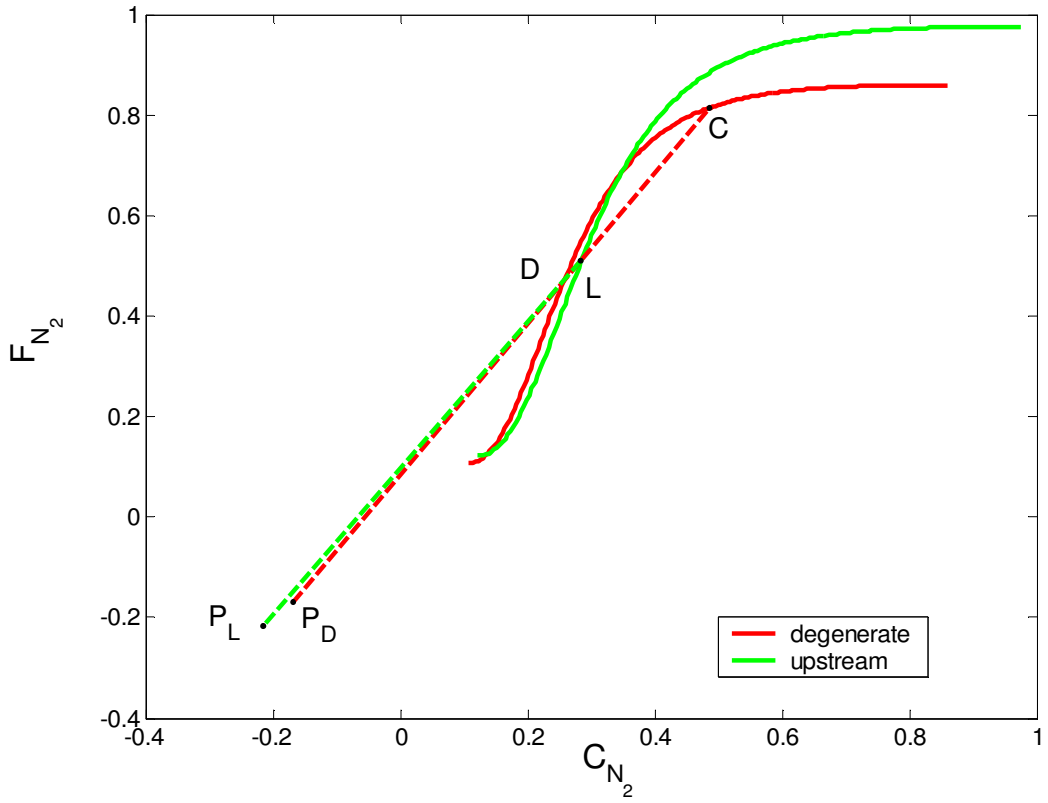

Figure B-27: Geometric interpretation of the degenerate shock relative to a nontie-line eigenvalue approaching from the upstream side.

Figure B-27 shows the geometric interpretation of the degenerate shock and nontie-line eigenvalues approaching the degenerate shock from the upstream side. Tie lines upstream of the degenerate tie line are longer than the degenerate tie line, therefore, $P_L < P_D$. Gas saturation upstream of the degenerate tie line is less than the gas saturation of the gas saturation of the injection branch at the degenerate tie

line: $F_L < F_{deg}$ and $C_L > C_{deg}$. For the nontie-line eigenvalues upstream of the degenerate tie line, the denominator of ${\lambda_{nt}}^L$ is greater than denominator of ${\lambda_{nt}}^U$, and the numerator of ${\lambda_{nt}}^L$ is less than ${\lambda_{nt}}^U$. As we move further upstream from the degenerate tie line, the denominator increases while the numerator decreases. Therefore, eigenvalues upstream of the shock will always be less than the velocity of the degenerate shock.

Nontie-line eigenvalues downstream of the shock are given by

$$\lambda_{nt}^R = \frac{F_R + P_R}{C_R + P_R}. \tag{B.7}$$

Figure B-28 shows the geometric interpretation of the degenerate shock relative to a nontie-line eigenvalue approaching the degenerate tie line from the downstream side. Tie lines downstream of the degenerate tie line are shorter than the degenerate tie line: $P_R > P_D$. Gas saturation of the initial nontie-line branch increases approaching the degenerate tie line: $F_R > F_{deg}$ and $C_R < C_{deg}$. The denominator of ${\lambda_{nt}}^R$ is less than the denominator of ${\lambda_{nt}}^D$, and the numerator of ${\lambda_{nt}}^R$ is greater than ${\lambda_{nt}}^D$. As the path is traced downstream from the degenerate tie line, the denominator decreases while the numerator increases. Wave velocities of the nontie-line path increase on the downstream side of the shock and will always be greater than the shock velocity. For this injection condition, the velocity rule and the entropy condition are satisfied on both sides of the shock.

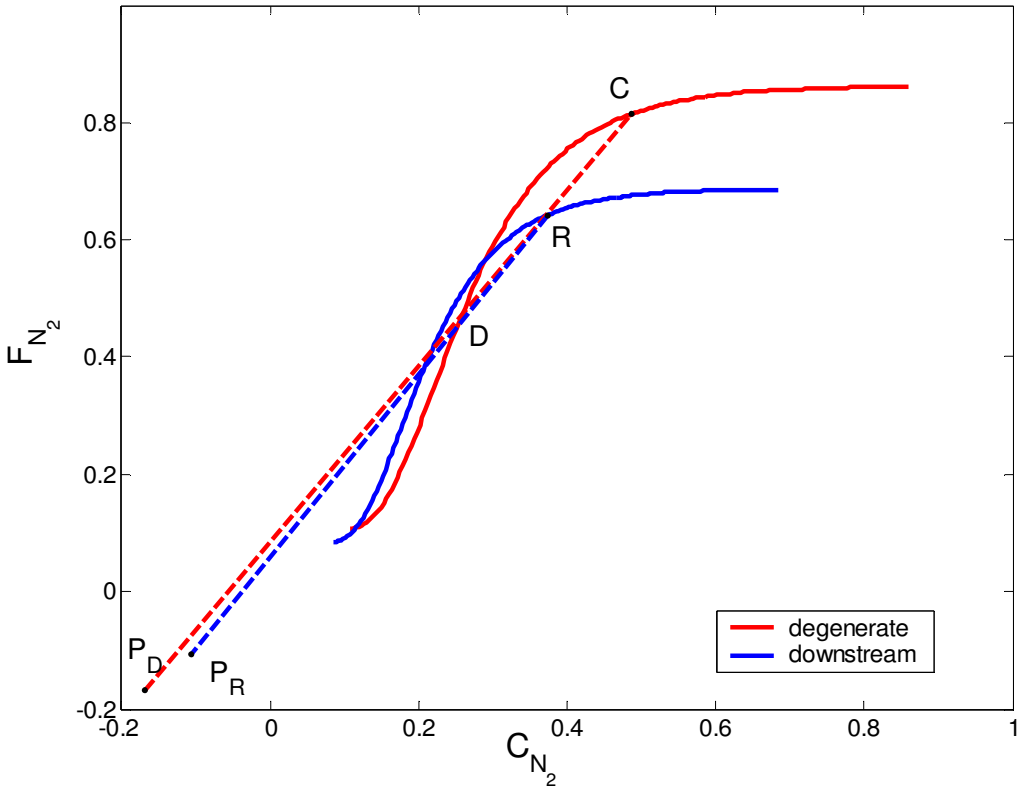

Figure B-28: Geometric interpretation of the degenerate shock relative to a nontie-line eigenvalue approaching from the downstream side.

Thus, for two-phase injection conditions where $S_{gB} < S_g < S_{gA}$ and $S_g < S_g^*$, an additional key tie line is required to complete the solution. When S_g is decreased further, the degenerate shock velocity increases, and the location of the degenerate tie line moves closer to the initial tie line, creating a family of solutions that vary smoothly from the injection tie line to the initial tie line (Figures B-29, B-30 and B-31).

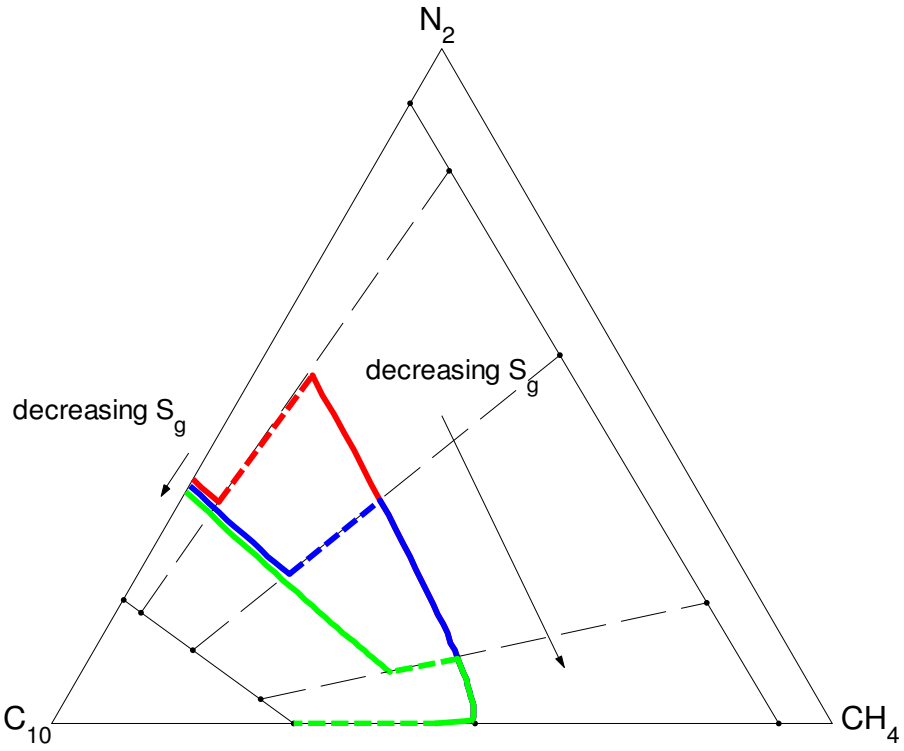

Figure B-29: Change in composition path for decreasing S_g.

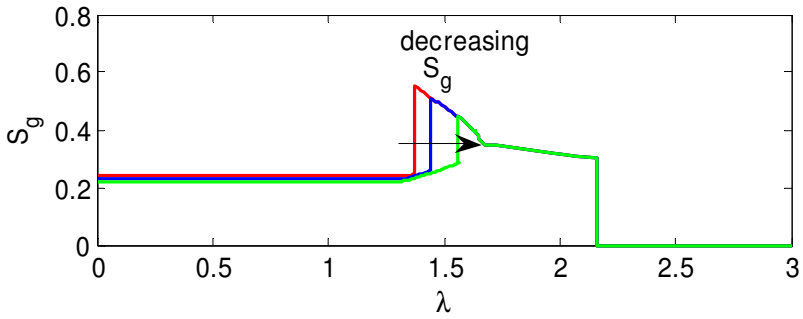

Figure B-30: Change in solution profile for decreasing S_g.

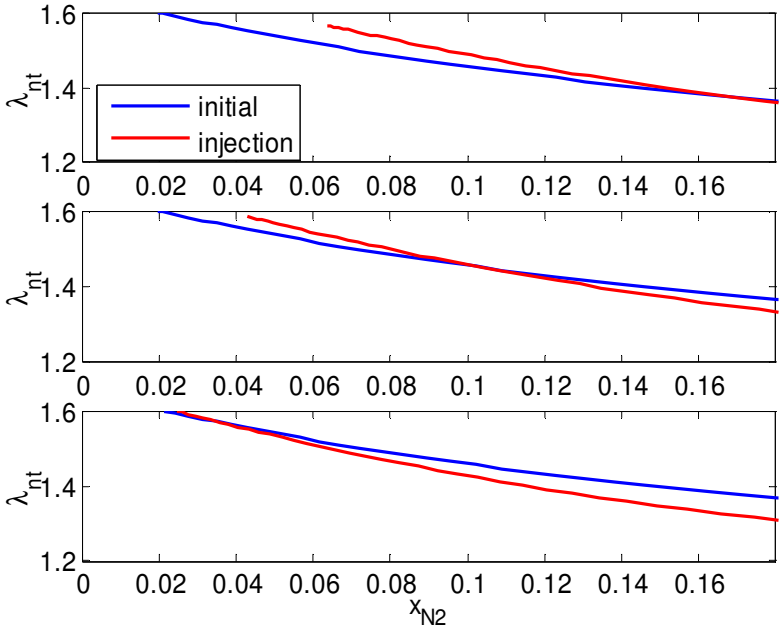

Figure B-31: Change in degenerate tie-line location for decreasing S_g. At lower injection saturations, the equal-eigenvalue point between nontie-line eigenvalues shifts towards upstream conditions.

S_4: $S_g < S_{gB}$ and $S_g > S_{gEV}$

The composition path and solution profile for this injection condition are presented in Figures B-32 and B-33. As S_g is further decreased, the nontie-line path traced from the injection condition is no longer nested within the nontie-line path traced from the equal-eigenvalue point of the initial tie line (Figure B-34). Continuous variation from the injection condition up to the initial tie line is allowable, as is the path switch from the nontie-line path to the initial tie line (Figure B-35). Continuous variation along the initial tie line is followed by a genuine shock from the switch point to the initial conditions, completing the composition path.

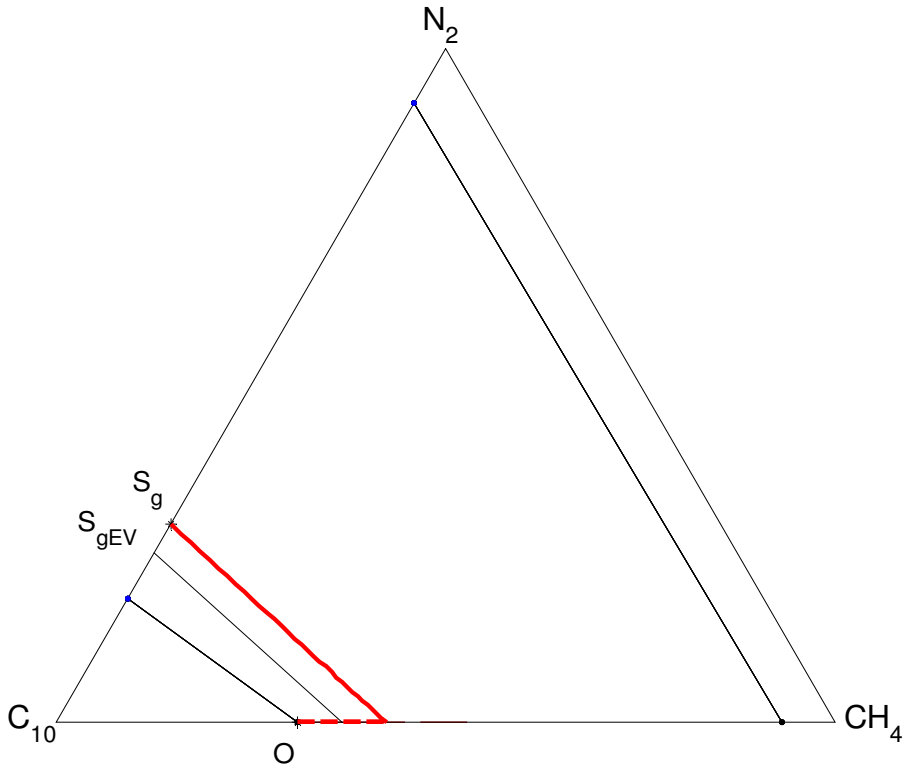

Figure B-32: Composition path for S_4 structure.

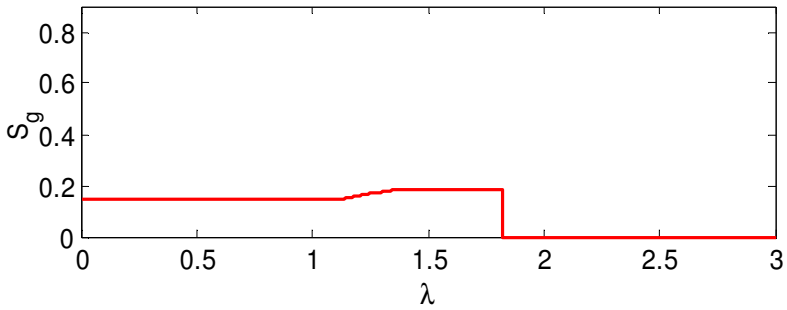

Figure B-33: Solution profile for S_4 structure.

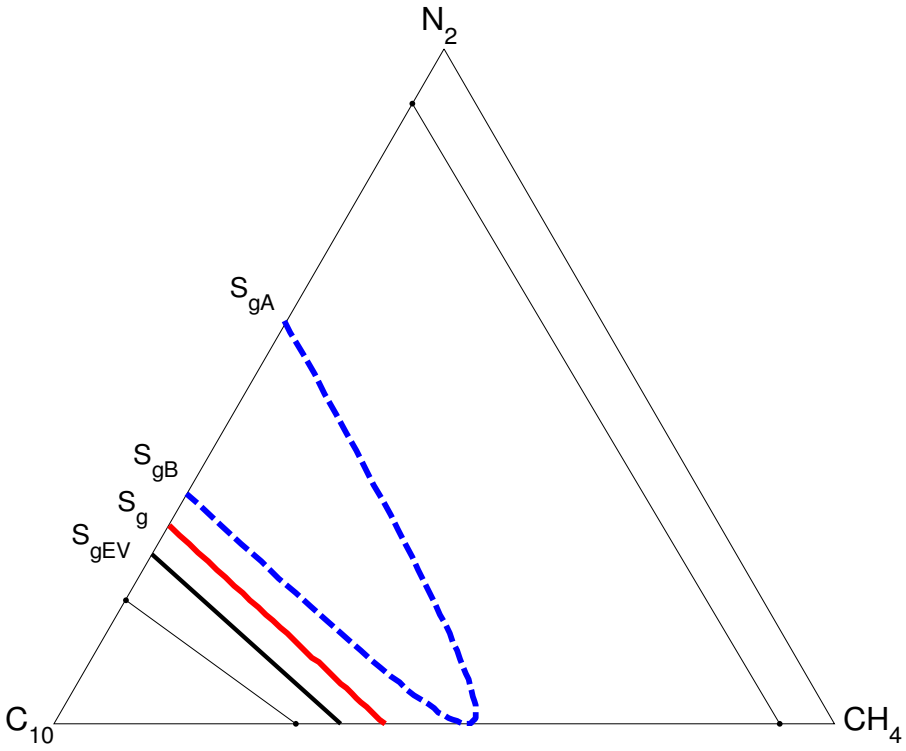

Figure B-34: Nontie-line paths of injection and initial branches.

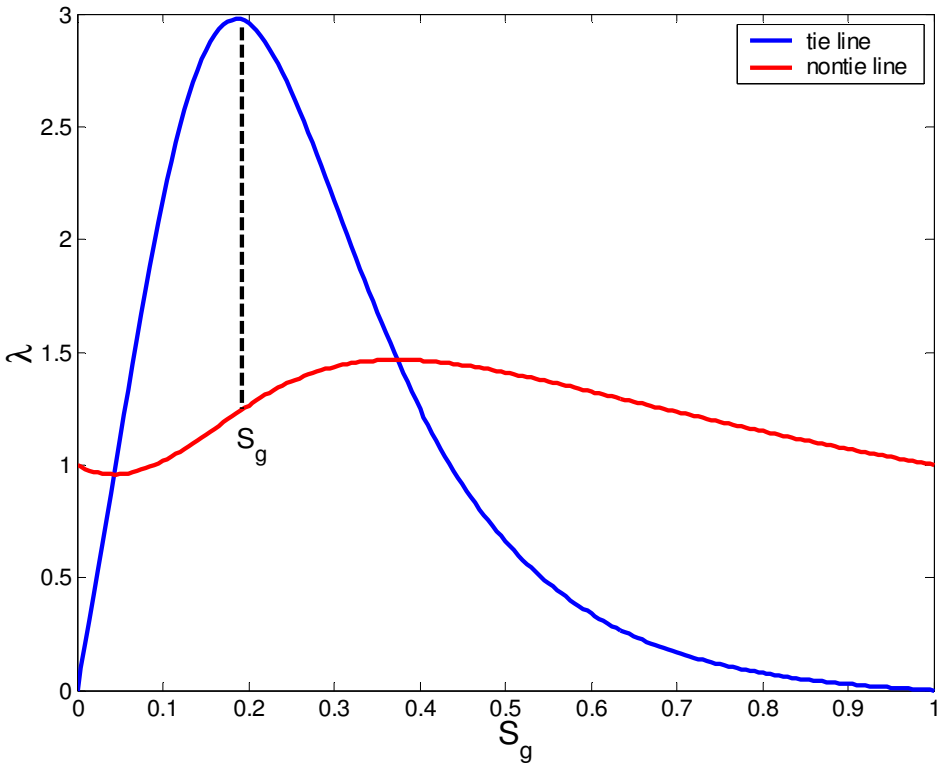

Figure B-35: Path switch from the nontie-line path to the initial tie line obeys the velocity rule.

S_5: $S_g < S_{gEV}$

The composition path and solution profile for an injection condition where the gas saturation is less than the saturation of the equivelocity point are presented in Figures B-36 and B-37. For $S_g < S_{gEV}$, both continuous variation along the tie line and a path switch from tie-line to nontie-line path violate the velocity rule (Figure B-38). Eigenvalues decrease for nontie-line paths traced from the injection tie line to the initial tie line (Figure B-39). Continuous variation along a nontie-line path violates the velocity rule, therefore a shock is necessary. Injection and initial states are connected by shock from injection state along the injection tie line to the

liquid phase boundary. At the phase boundary, $f_g = S_g$; therefore, $F_1 = C_1$, and the nontie-line eigenvalue is unity, and the phase boundary is a path. From the phase boundary of the injection tie line, the composition path follows the phase boundary to initial conditions, creating an indifferent wave to complete the solution.

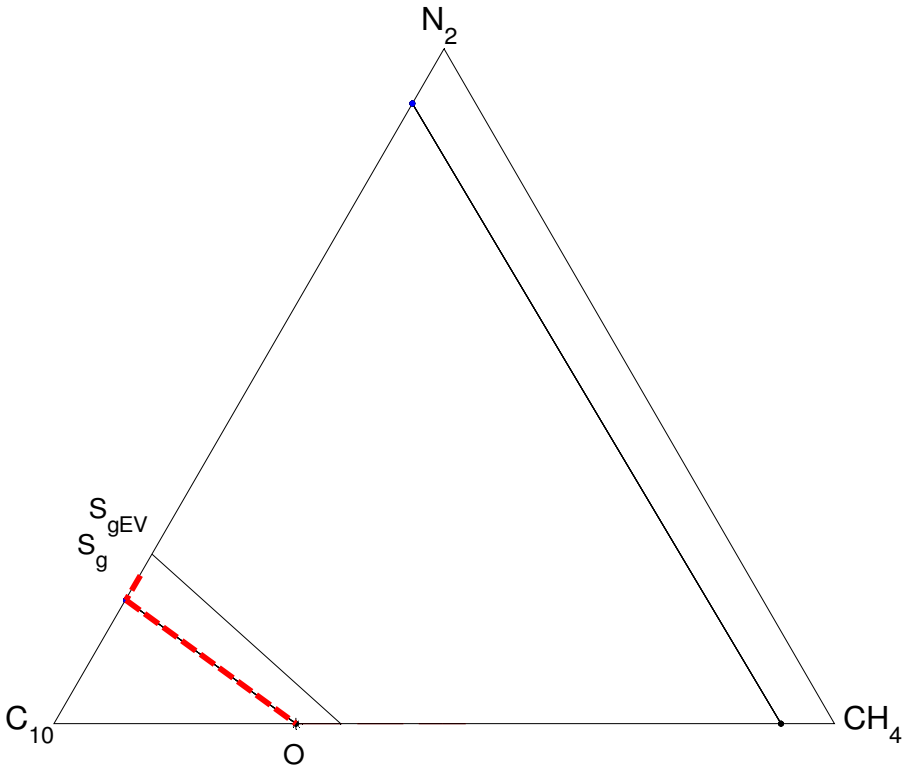

Figure B-36: Composition path for S_5 structure.

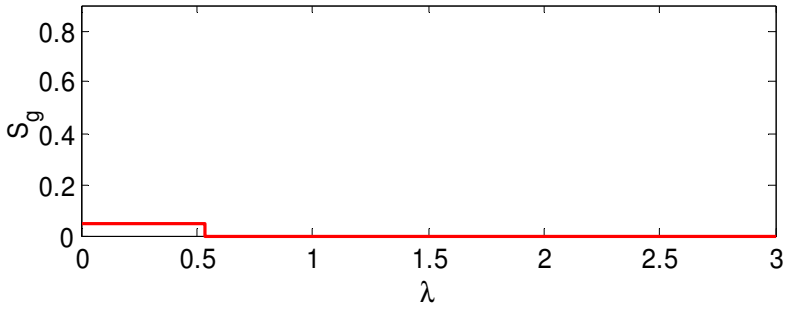

Figure B-37: Solution profile for S_5 structure.

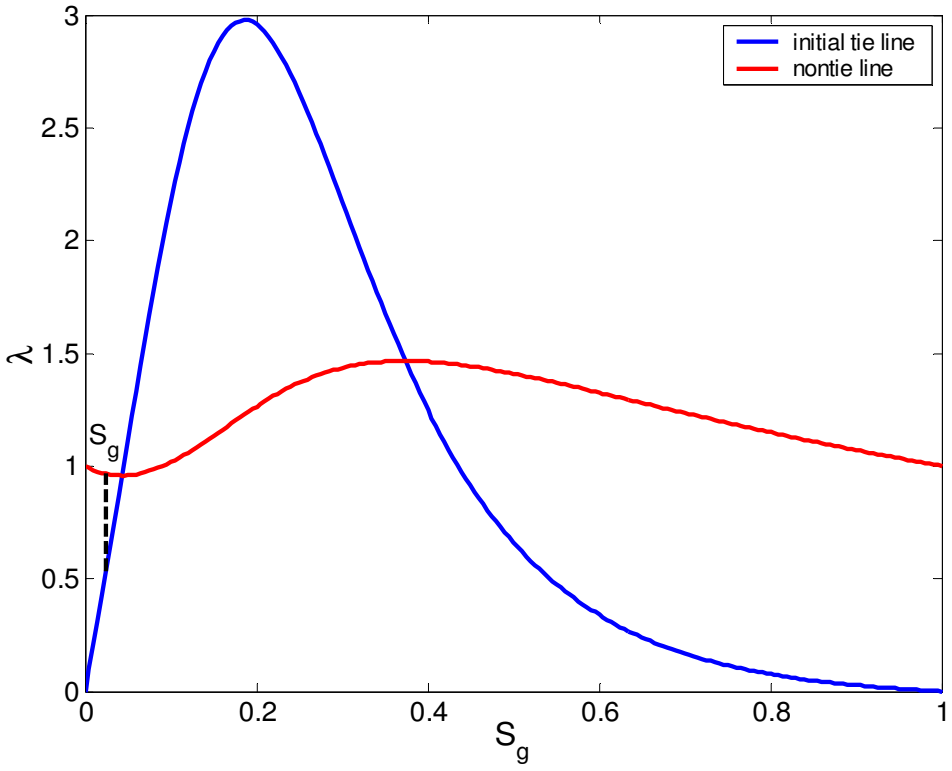

Figure B-38: Switch from nontie-line path to tie-line path violates the velocity rule.

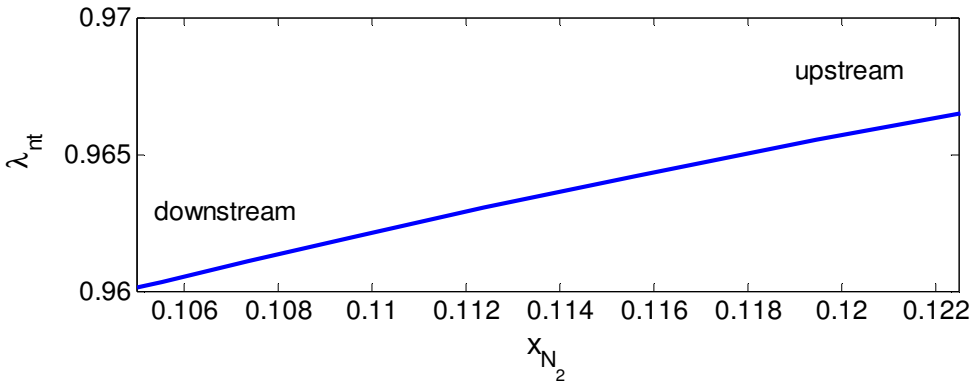

Figure B-39: Variation of eigenvalues from injection tie line to initial tie line along a nontie-line path for saturations below the equivelocity gas saturation.

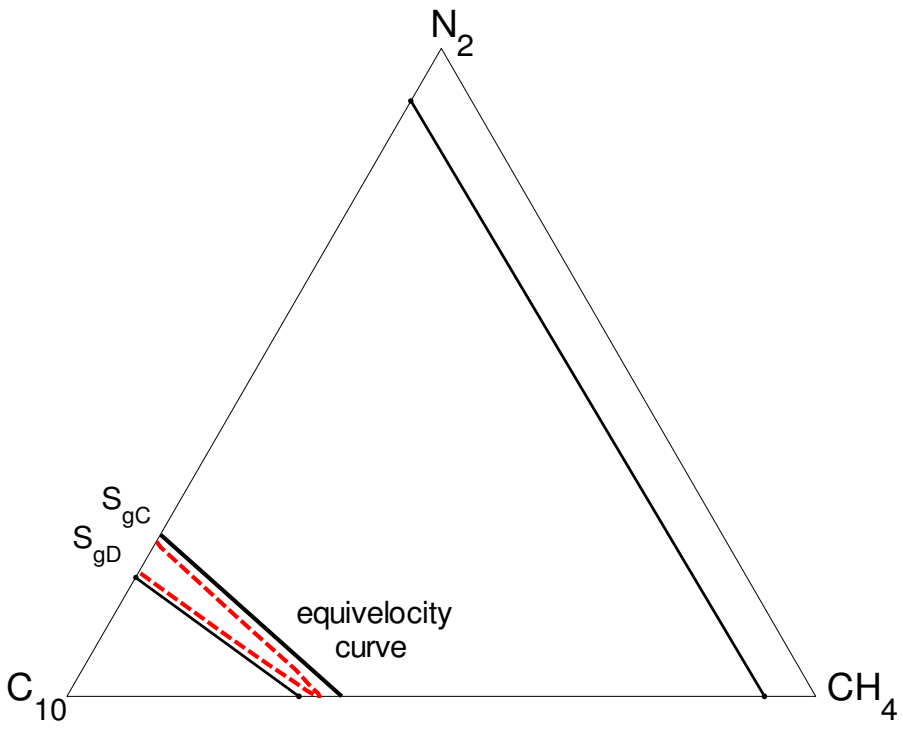

Figure B-40: Location of S_{gC} and S_{gD} relative to the equivelocity curve and liquid phase boundary.

Outside the saturations bounded by S_{gC} and S_{gD} (Figure B-40), the region bounded by the landing points on the injection tie line of the nontie-line path traced by the equal-eigenvalue point on the initial tie line, a shock from injection conditions to a location on the initial tie line satisfies the Rankine-Hugoniot condition. However, the velocity of the genuine shock connecting the landing point to initial condition is slower than the shock connecting injection and initial tie lines. Shock constructions on the injection and initial fractional flow curves are shown in Figure B-41. The slope of the line segment connecting S_{inj} to S_{land} represents the velocity of the shock connecting injection and initial tie lines. The slope of the line segment connecting S_{land} to S_{init} represents the velocity of the genuine shock to initial conditions. Because the line segment connecting injection and initial tie lines lies above the diagonal and the initial condition lies on the diagonal, the slope of the line segment connecting injection and initial line segments will always be greater than the line segment representing the genuine shock. Therefore, solutions for saturations below the equivelocity saturation must follow a construction beginning with a shock to the phase boundary. Table B-2 summarises velocities for a shock from a gas saturation below the equivelocity curve.

Table B-2: Summary of shock velocities from an injection saturation of 0.0538 to the initial tie line.

landing saturation on initial tie line	Λ, injection saturation, 0.0538, to initial tie line	Λ, landing point to initial conditions
0.0219	0.9623	0.3434
0.0381	0.9623	0.6046

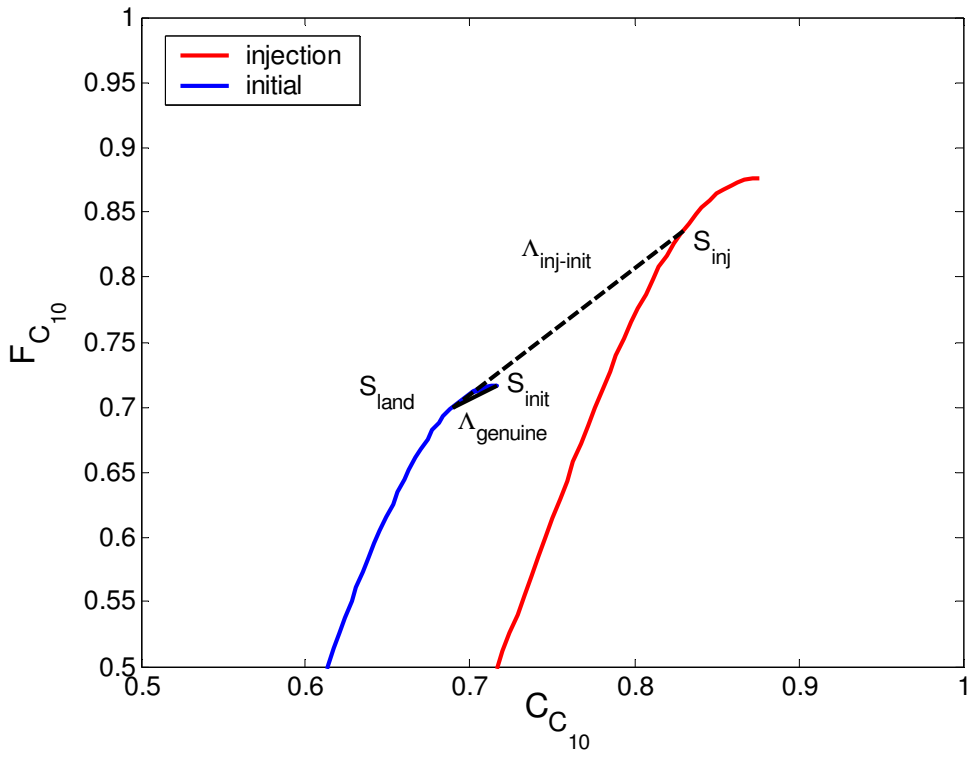

Figure B-41: Enlargement of fractional flow shock construction from injection tie line to initial tie line. The velocity of the shock connecting the injection and initial tie lines is greater than the velocity of the genuine shock to initial conditions.

The equivelocity saturation represents the limit between the S_4 and S_5 solution structures. Figures B-42 and B-43 show composition paths and solution profiles for this an injection condition. At the equivelocity saturation, f_g is equal to S_g, making F_1 and C_1 are equal and therefore, the nontie-line eigenvalue is unity. Saturations along the equivelocity curve all have a velocity of unity and travel as an indifferent wave. At the landing point on the initial tie line, the shock velocity is also unity, since $F_1^{init} = C_1^{init}$ and $F_1^{EV} = C_1^{EV}$, and the denominator is equal to the numerator.

At the equivelocity saturation, the S_5 structure: a shock from injection conditions as the equivelocity saturation to the liquid phase boundary followed by a nontie-line path up the phase boundary, also satisfies these boundary conditions. The velocity of the shock from injection conditions to the phase boundary is unity since f_g (S_g = 0) = 0 and therefore, F_1 (f_g = 0) = C_1 (S_g = 0). The nontie-line path along the phase boundary from the injection tie line to the initial tie line is also unity since F_1 and C_1 are equal at the phase boundary. The shock and the nontie-line path travel as a set of indifferent waves.

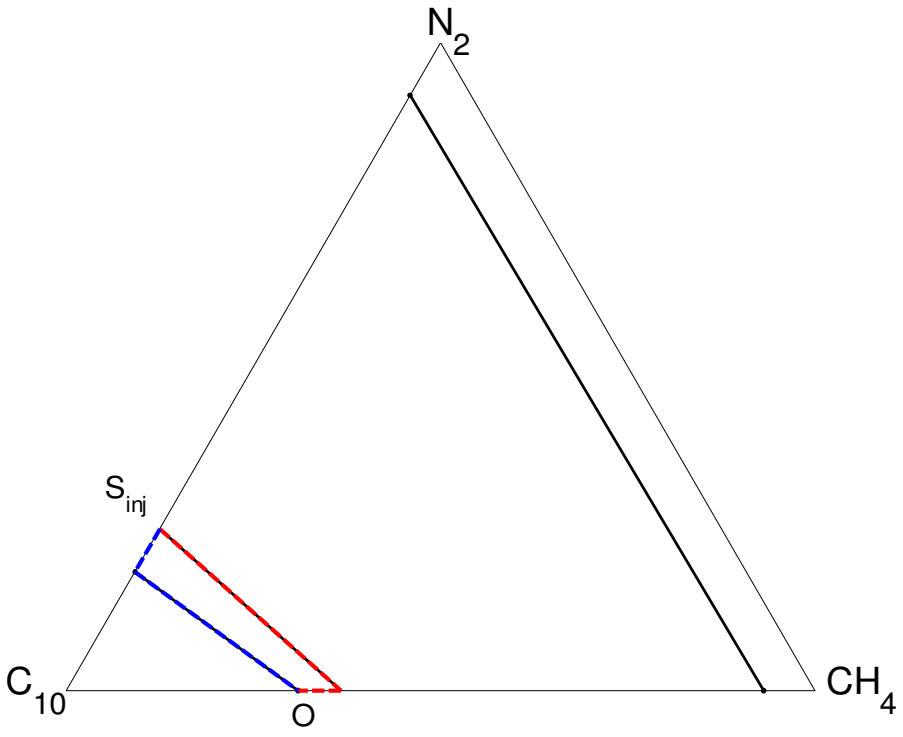

Figure B-42: Both the S_4 and S_5 structures satisfy boundary injection conditions at the equivelocity saturation on the injection tie line.

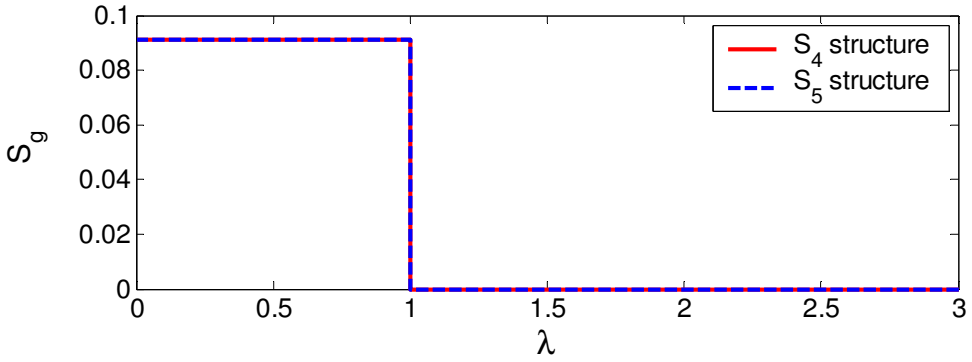

Figure B-43: Saturation profile for injection conditions at the equivelocity saturation are identical for the S_4 and S_5 structures.

As gas saturations decrease towards the equivelocity gas saturation, the region of the continuous variation connecting the injection and initial tie lines shrinks and velocity of the leading shock decreases to unity. As gas saturations increase towards the equivelocity gas saturation, the velocity of the shock from injection conditions to the phase boundary increases to an indifferent wave of unity. These transitions are shown in Figures B-44 and B-45. A similar bifurcation between solutions is observed in analytical solutions for water-alternating gas systems (Juanes and Blunt, 2006).

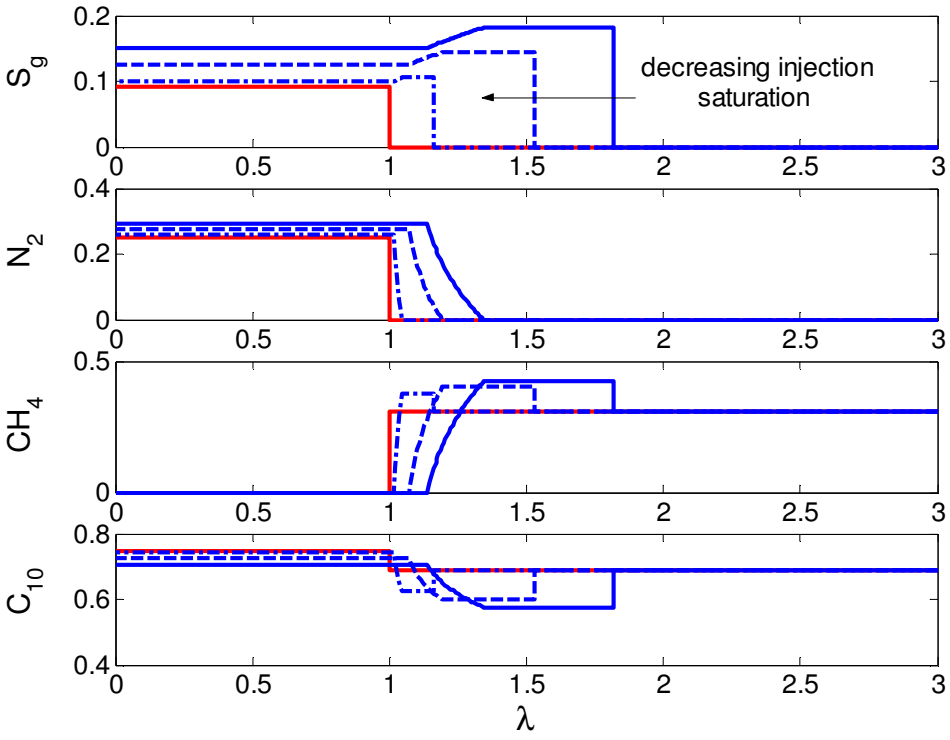

Figure B-44: Solution profiles for injection saturations decreasing towards the equivelocity gas saturation.

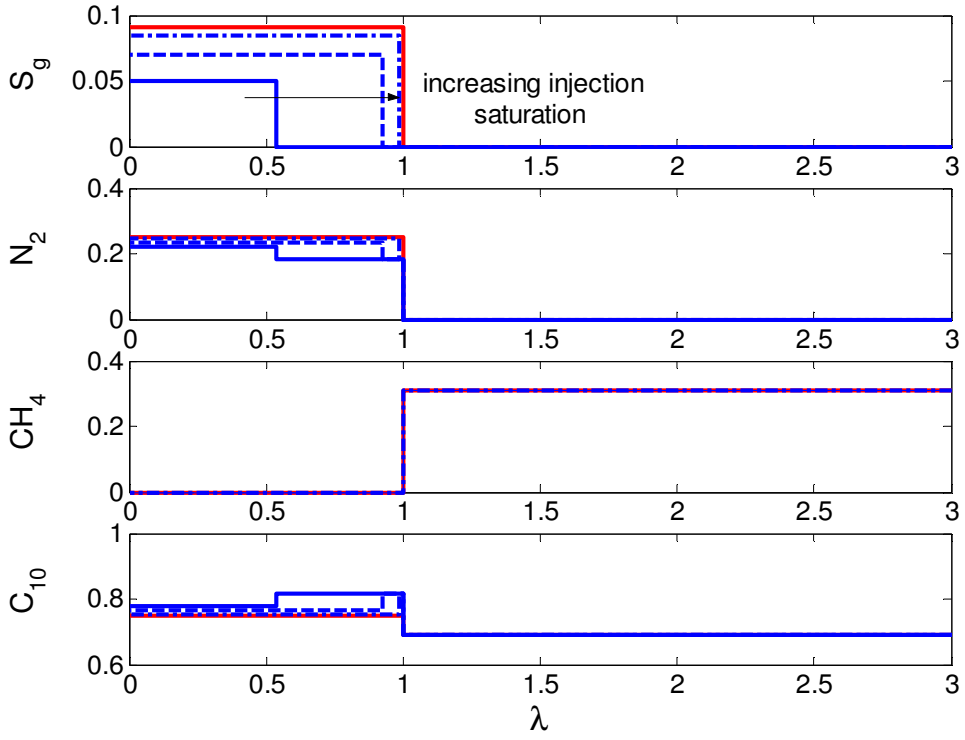

Figure B-45: Solution profiles for injection saturations increasing towards the equivelocity gas saturation.

Example of S_3 Structure in a Quaternary Displacement

When a mixture of the most volatile gas component and the least volatile intermediate component is injected, it is possible to create an intermediate composition where the landing point on the crossover tie line is less than S_g^*. An example of the S_3 solution structure is illustrated with injection of a mixture of 0.5 N_2 and 0.5 CO_2 to displace and oil containing 0.2837 CH_4 and 0.7163 C_{10} at 10 000 kPa and 70°C. Parameters are summarised in Table B-3.

Solution construction starts with the procedure outlined in Monroe *et al.* (1990). In this system, the crossover tie line is the longest tie line. Solution paths from the injection tie line to the crossover tie line and initial tie line to the crossover tie line are constructed independently. At point E, sufficient gas is removed from the mobile phase such that the gas saturation of the landing point is lower than the saturation of the equal-eigenvalue point of the crossover tie line. A path switch from the landing point of the tangent shock (F-E) to the $\frac{\partial \lambda_{nt}}{\partial S} > 0$ branch of the nontie-line path is taken, and the S_3 structure connects the crossover tie line to the initial tie line. The composition path and solution profile for this displacement are shown in Figures B-46 and B-47.

Table B-3: Summary of model parameters used in quaternary displacement illustrating S_3 structure.

K_{N2}	8
K_{CH4}	3.5
K_{CO2}	2
K_{H2O}	0.01
M	15.04

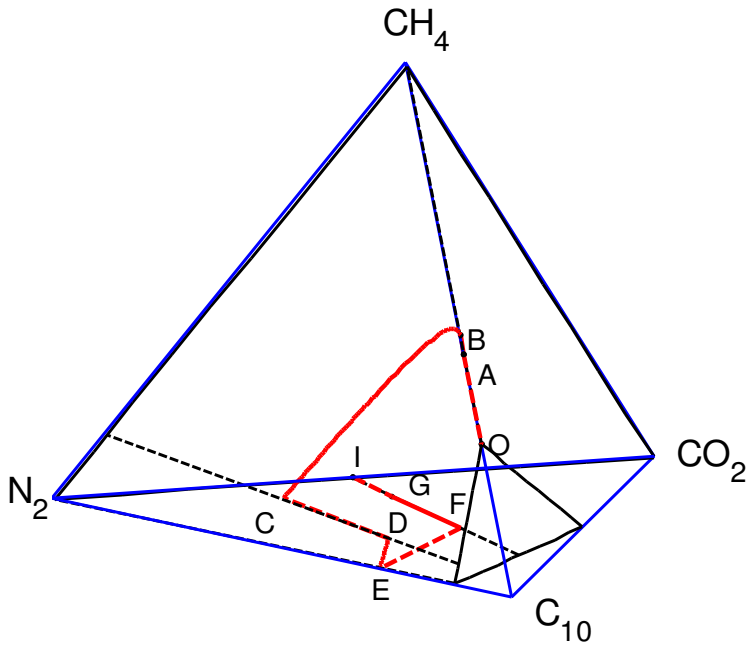

Figure B-46: Composition path of quaternary displacement with S_3 solution structure.

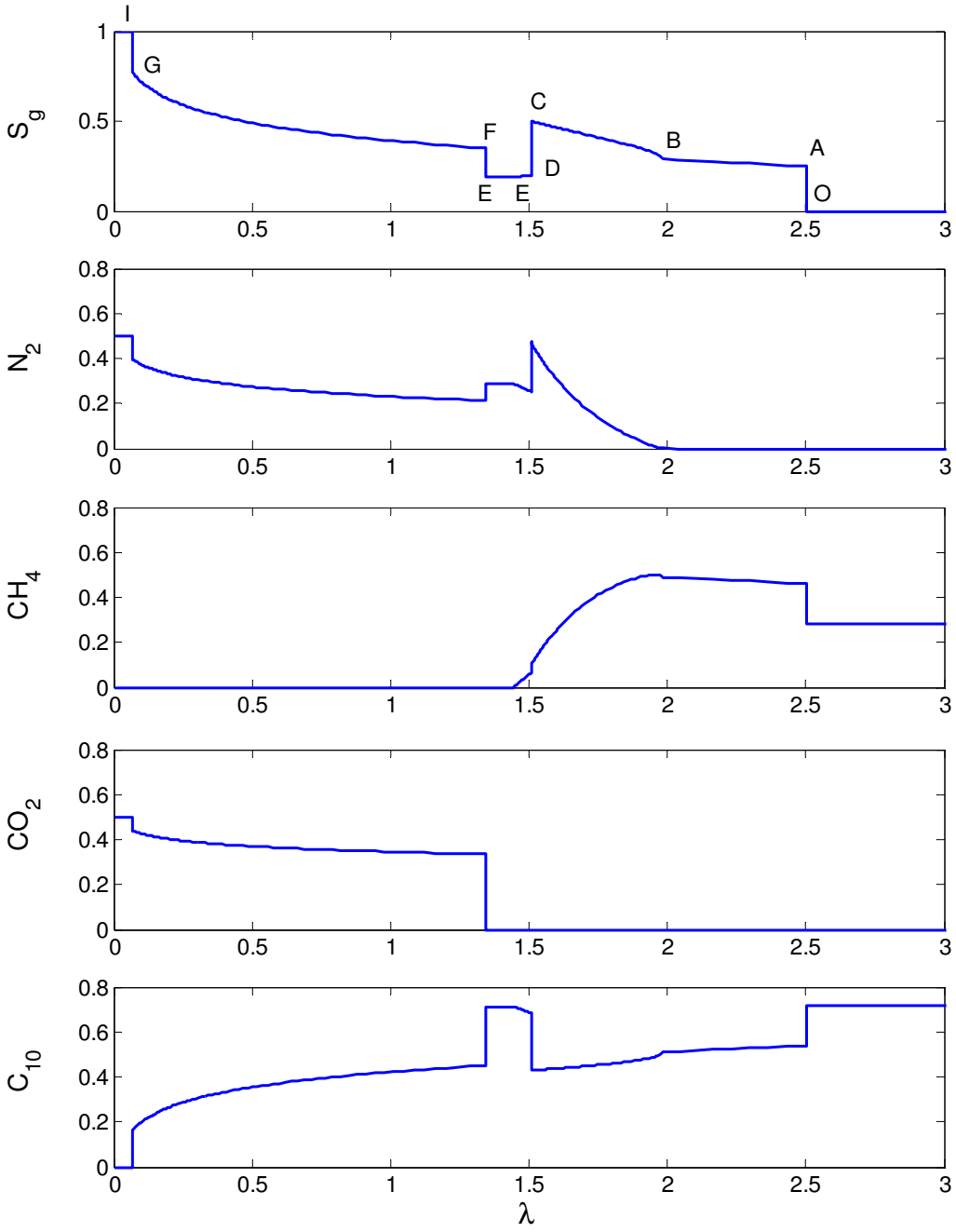

Figure B-47: Solution profile of quaternary displacement with S_3 solution structure.

Two-Phase Initial Conditions

Two-phase initial conditions are of interest because they are commonly the starting point in surfactant flood applications. Composition paths are constructed by applying the velocity rule and entropy condition to ensure coherence of all solution segments. Similar solution structures occur in systems with two-phase initial conditions, with modifications to the leading edge of the displacement. Two examples are presented demonstrating the solution structure in systems with two-phase initial conditions.

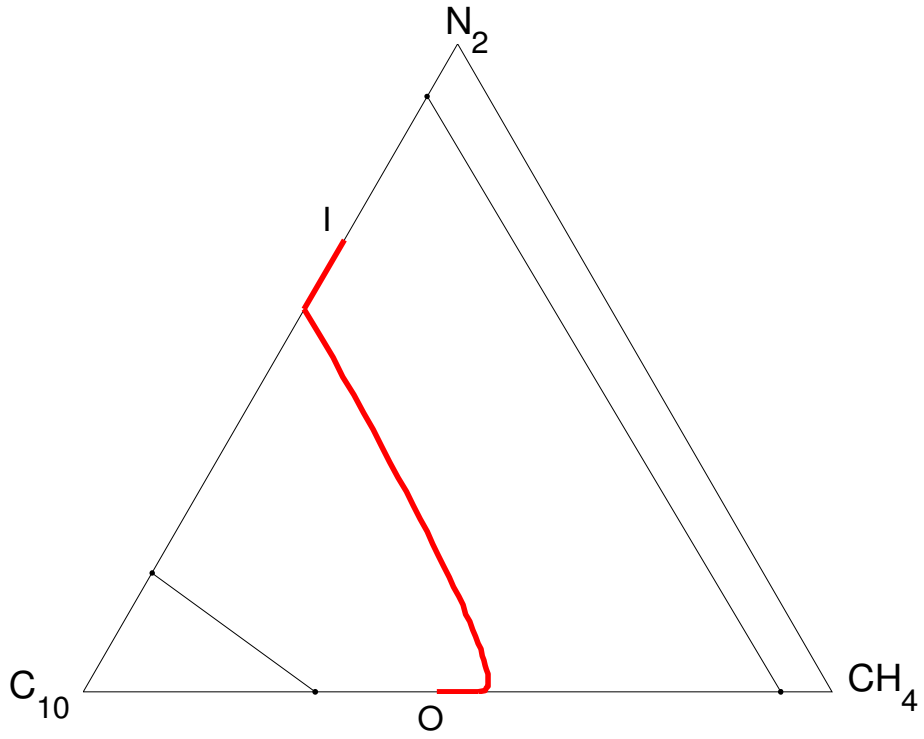

Figure B-48: Composition path for two-phase initial conditions less than the equal eigenvalue gas saturation.

The first example considers initial gas saturations that lie between the $\frac{df}{dS}$ maximum and the equal eigenvalue point (Figures B-48 and B-49). The leading edge of displacement is constructed with a tie line rarefaction from the initial condition to the equal eigenvalue point.

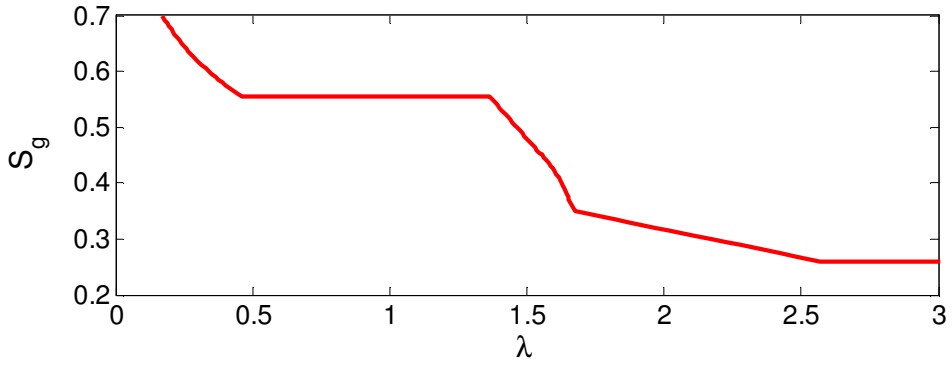

Figure B-49: Saturation profile for a two-phase initial condition less than the equal eigenvalue gas saturation.

If initial gas saturations are less than the saturation at which the $\frac{df}{dS}$ maximum occurs, continuous variation along the tie line violates the velocity rule and a shock is required (Figure B-50). The leading edge consists of a tangent shock from the initial condition along the initial tie line, analogous to solutions with single phase initial conditions.

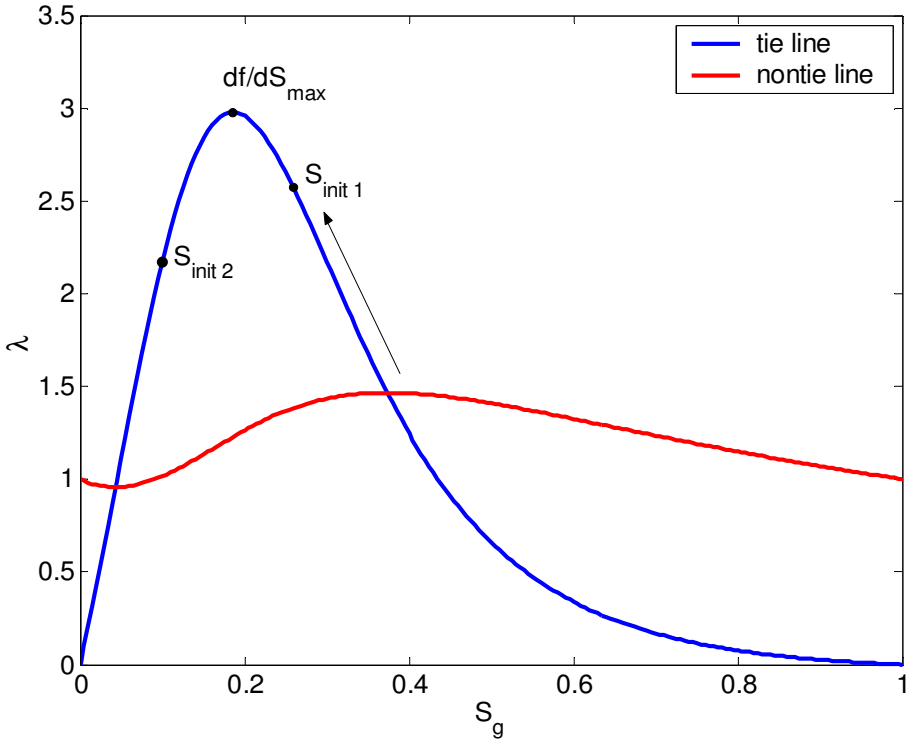

Figure B-50: Continuous variation to gas saturations below the maximum violate the velocity rule. A tangent shock along the tie line from initial conditions completes the leading edge of the displacement.

If the initial gas saturation is greater than the equal eigenvalue point, the initial segment of the solution is taken directly from the nontie-line path. Figures B-51 and B-52 shows the composition path and solution profiles for this initial condition.

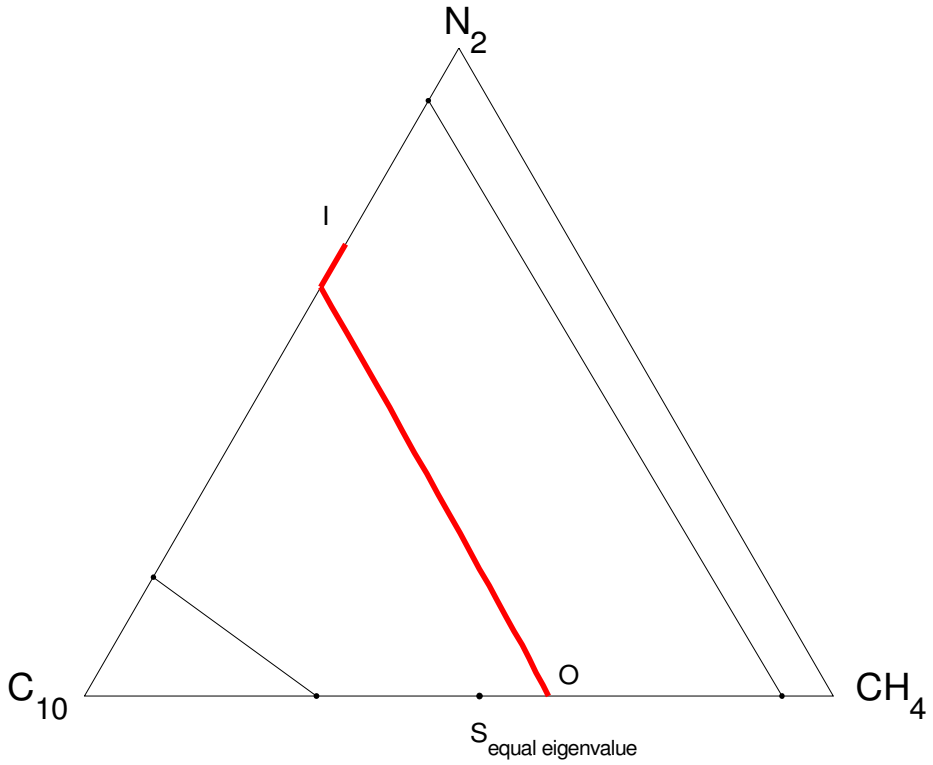

Figure B-51: Composition path for initial gas saturation greater than the equal eigenvalue gas saturation.

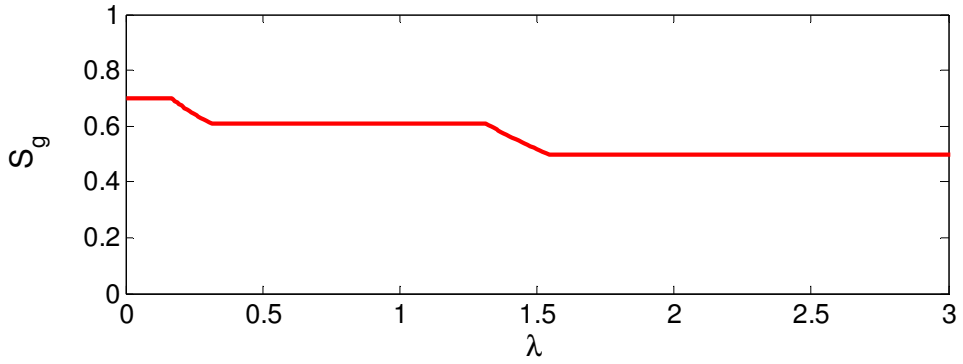

Figure B-52: Saturation profile for an initial gas saturation greater than the equal eigenvalue gas saturation.

Summary of Two-Phase Injection Solutions

Composition paths connecting two-phase injection conditions to a single phase initial condition can be composed of combinations of tie line rarefactions (R_{tl}), nontie-line rarefactions, utilising the $\frac{\partial \lambda_{nt}}{\partial S} < 0$ branch of the nontie-line path (R_{ntl}^{-}), nontie-line rarefactions utilising the $\frac{\partial \lambda_{nt}}{\partial S} > 0$ branch of the nontie-line path (R_{ntl}^{+}) and shocks along and between tie lines (S_{tl} and S_{ntl}). By applying the velocity rule and the entropy condition, five types of composition paths spanning the two-phase injection space were identified. These paths are summarised in Table B-4.

In systems with adsorption, nontie-line paths are functions of both phase behaviour and adsorption. At the phase boundary and the equivelocity saturation, the nontie-line eigenvalue is not equal to unity, and are no longer paths. For saturations below the equivelocity saturation, the composition path resembles the S_4 structures. With the exception of the S_5 structure, the composition paths presented in this appendix also apply to systems with adsorption. In systems with adsorption, the nontie-line eigenvalue is a function of phase behaviour and adsorption strength. The solution structures remain the same, but the location of shocks and rarefactions are scaled relative to both adsorption and phase behaviour.

Table B-4: Summary of composition path configurations for vaporising drives with two-phase injection. Injection conditions refer to Figure B-1.

injection condition	configuration	construction initiated at:
S_1	$R_{tl} \rightarrow R_{ntl}^{-} \rightarrow R_{tl} \rightarrow S_{tl}$	shortest tie line (initial)
S_2	$S_{tl} \rightarrow R_{ntl}^{-} \rightarrow R_{tl} \rightarrow S_{tl}$	shortest tie line (initial)
S_3	$R_{ntl}^{+} \rightarrow S_{tl} \rightarrow R_{ntl}^{-} \rightarrow R_{tl} \rightarrow S_{tl}$	longest tie line (injection)
S_4	$R_{ntl}^{+} \rightarrow S_{tl}$	longest tie line (injection)
S_5	$S_{tl} \rightarrow S_{ntl}$	longest tie line (injection)